SPATIOTEMPORAL MAPPING OF OXYGEN IN MODEL POROUS MEDIA BIOFILMS USING ^{19}F MAGNETIC RESONANCE OXIMETRY

by

Jeffrey William Simkins

A dissertation submitted in partial fulfillment
of the requirements for the degree

of

Doctor of Philosophy

in

Chemical Engineering

MONTANA STATE UNIVERSITY
Bozeman, Montana

April 2019

DEDICATION

To family, friends, and the billions of bacteria that gave their lives for this project

ACKNOWLEDGEMENTS

This work is supported by the National Institutes of Health under award number R01GM109452. Some experiments were informed by work funded by the National Science Foundation's East Asian Pacific Summer Internships (EAPSI) program. Any opinions, findings and conclusions or recommendations expressed in this material are those of the author(s) and do not necessarily reflect the views of the NIH or NSF. Equipment funding was provided by the Murdock Charitable Trust and the National Science Foundation Major Research Instrumentation Program. The authors wish to thank Kayla Keepseagle, James Stangeland, and Betsey Pitts for assistance with bacterial culturing, and Mike Franklin for providing bacteria.

TABLE OF CONTENTS

TABLE OF CONTENTS - CONTINUED

TABLE OF CONTENTS - CONTINUED

TABLE OF CONTENTS - CONTINUED

LIST OF TABLES

Table Page

LIST OF FIGURES

Figure Page

LIST OF FIGURES – CONTINUED

Figure Page

LIST OF FIGURES – CONTINUED

Figure Page

ABSTRACT

Biofilms, microbial aggregates anchored to a surface using a sticky matrix of metabolic products called extracellular polymeric substances (EPS), are the dominant form of bacterial life and are widespread in nature, from glaciers to hot springs. The transition from the planktonic state to a biofilm is associated with striking changes to microbial phenotype which confer unique, biofilm-specific properties to resident cells that have important implications for medicine, industry, and environmental study. Many of these properties are caused in large part by oxygen transport limitation, which arises due to restriction of fluid flow in cell aggregates and consumption of oxygen for respiration. The balance of reactive and diffusive processes establishes strong spatial gradients in oxygen concentration which lead to profound spatial heterogeneity in bacterial species composition, growth yield, antimicrobial susceptibility, and reaction kinetics, among other traits. However, despite the importance of oxygen gradients in a host of highly-relevant biofilm phenomena, quantification of oxygen profiles in biofilms is difficult, both in the field and the lab, with the gold standard of measurement, the microelectrode, having significant limitations. ^{19}F Nuclear Magnetic Resonance (NMR) oximetry, a magnetic resonance-based technique for oxygen quantification that has been used to characterize oxygen usage in blood tissues and tumors, exploits the linear dependence of spin-lattice relaxation rate R_1 on local oxygen partial pressure for fluorine nuclei in perfluorocarbon (PFC) phases. In the current work, we apply ^{19}F NMR oximetry to a model packed bed biofilm system to generate novel insights into microbial oxygen usage and to introduce a complimentary oximetry tool for biofilm experimenters. We develop methodology for the introduction and fixation of a fluorinated oxygen sensor to facilitate long-term oxygen monitoring. We use ^{19}F oxygen distribution measurements in compliment to traditional NMR methods to correlate fluid flow with growth rate, generate spatial maps of oxygen utilization rate, identify differences in oxygen utilization behavior between different species, characterize infection persistence during antibiotic therapy, mathematically model macroscale oxygen sink development, and quantify local mass transfer phenomena.

CHAPTER ONE: INTRODUCTION

Biofilms are aggregates of microbes adhered to a surface using a self-secreted hydrogel matrix called extracellular polymeric substance (EPS) consisting of polysaccharides, DNA, proteins, and other metabolic products [1; 2]. The transition from the planktonic (free-floating) state to a biofilm is associated with profound changes to bacterial physiology and behavior, with many of the properties unique to biofilms explained by transport limitation of growth substrates [3]. Competition for essential nutrients establishes a reactive-diffusive equilibrium whereby strong concentration gradients are formed, and as a result individual cells exhibit striking spatial heterogeneity in phenotype to accommodate their unique chemical environment [4].

Molecular oxygen, by virtue of its pronounced impact on local chemistry and its indispensable role in respiration, is perhaps the most impactful of all nutrients, with oxygen availability dramatically affecting bacterial species composition and, even within a single species, microbial metabolic state [5-9]. As a result of its consumption, anoxic zones develop within cell aggregates [10-12] wherein resident cells undergo a transition to metabolic dormancy, among other changes, through marked alterations to gene expression. This phenotypic transformation confers a host of specific and high-relevance traits. For instance, oxygen-limited cells in pathogenic biofilms exhibit extraordinarily heightened tolerance to antimicrobials [8; 13] as well as host immune defenses [14]. The limitation of oxygen transport specifically is thus a critical criterion in the emergence of many properties unique to biofilms, which in turn have far-reaching implications across medical, industrial, and environmental contexts.

Despite its universal significance in biofilms, measurement of oxygen in these systems remains difficult whether in the field or the lab. The most widely-used method for quantifying oxygen gradients, the Clark microelectrode, provides high sensitivity and accuracy but is physically invasive [15] and limited to single-point data collection [16], necessitating lengthy acquisition times. Additionally, many experimental systems are inaccessible to microelectrode probing, such as those with closed walls. Measurement of oxygen in biofilms studies is therefore cumbersome but nonetheless imperative. This difficulty is exacerbated by the fact that biofilms do not possess simple planar geometry but rather form complex, three-dimensional structures separated by interstitial voids. These structures interact with localized fluid flow, producing complicated hydrodynamic behavior such as eddies, concentration boundary layers, and shear-induced streamers, which may vary wildly within a single biofilm [17]. As a result oxygen gradients exhibit extreme heterogeneity across even miniscule lengthscales, making spatial mapping of oxygen distribution with microelectrodes a daunting task. Nevertheless, these endeavors often yield invaluable insights, underscoring the importance of oxygen in biofilm systems.

^{19}F Nuclear Magnetic Resonance (NMR) Oximetry is a technique for oxygen measurement which exploits the linear relationship between ^{19}F spin-lattice relaxation rate R_1 and local oxygen concentration in perfluorocarbon (PFC) phases. Because molecular oxygen is paramagnetic, it hastens the relaxation of all nearby nuclei through a dipolar interaction known as hyperfine coupling, but the effect is modest or negligible for most nuclei. However, oxygen is highly soluble in PFC phases specifically, and the

resulting close proximity of oxygen atoms to PFC fluorine atoms facilitates much stronger coupling [18]. This in turn produces a strong dependence of ^{19}F relaxivity on local oxygen partial pressure pO_2 which can be used as an oxygen sensor. The technique has been used in the medical literature to quantify oxygenation in biological tissues [19-21], but has been limited by low PFC residence time in the body and ill-defined clearance pathways. One of the hallmark challenges of ^{19}F NMR oximetry, then, is introducing a fluorinated oxygen-sensor into the sample of interest without affecting system dynamics, and anchoring it to ensure constant spatial distribution, permitting long term measurement.

In the current work, ^{19}F NMR oximetry is applied to bacterial biofilms to provide novel insights into biofilm behavior and kinetics, and as well as to introduce a new tool into the biofilm experimenter's toolkit. We experimentally verify that incorporation of a PFC into a biofilm growth medium such as agarose or alginate does not fundamentally alter oxygen transport phenomenon or influence microbial growth. We develop methodology for dispersion and immobilization of a specific PFC, perfluorooctylbromide (PFOB), into alginate gel, a commonly-used growth scaffold for microbial studies, allowing for long-term monitoring of oxygen distribution. PFOB is emulsified in an aqueous phase containing sodium alginate, and the mixture is gelled by dripping into a calcium chloride solution, resulting in ~3.4 mm alginate gel beads with oxygen-sensing PFC dispersed throughout. These beads are used as the solid matrix in a packed bed column in the presence or absence of flow, and biofilm growth is stimulated by inoculating one of the beads with bacterial cells. The benefits of this experimental system

are two-fold. First, immobilization of the PFOB dispersion in the solid packing provides spatial fixation of the oxygen-sensor without affecting hydrodynamics or other column properties. Second, the packed bed column is a porous medium consisting of liquid flow amidst solid-like occlusions, and this complex geometry better approximates the growth conditions of real biofilms than traditional planar biofilm models and may thus better capture their behavior. We proceed to use ^{19}F NMR oximetry in combination with traditional NMR methods to generate novel insights into the nature of oxygen gradients in biofilms, with particular focus on the coupling of fluid flow and growth rate, oxygen consumption characteristics of different species, mathematical modeling of respiration kinetics, infection persistence under antibiotic challenge, and localized mass transport limitation.

Outline

Chapter 2 introduces the theory of Nuclear Magnetic Resonance (NMR), the phenomenon underpinning the experimental methodology used for this work. Particular focus is directed toward the quantum systems from which the phenomenon originates, the classical model which approximates its behavior, the procedure by which data are acquired, the methods for manipulation of signal including imaging and motion encoding, and the structure and function of relevant hardware. Chapter 3 discusses advanced NMR concepts and the experiments which exploit their physical and mathematical foundations to investigate molecular transport, such as general motion encoding and velocity imaging. Chapter 4 details the significance of oxygen gradients in bacterial biofilms with emphasis

on the mechanisms by which limitation of oxygen transport confers unique properties to resident microbes, and addresses the difficulty of measuring oxygen using traditional means.

Chapter 5 describes initial experiments demonstrating that incorporation of oxygen-sensing PFC into microbial growth media does not significantly impact oxygen transport phenomena, and outlines the general methodology by which oxygen mapping in model biofilms was achieved in the current work. In addition the results of several proof-of-concept applications are presented, such as correlation of fluid flow with local growth rate, spatial mapping of microbial oxygen consumption rate, and characterization of distinct oxygen-utilization behavior of different bacterial species. This work was published in *The Journal of Magnetic Resonance* and is featured on the front cover of its August 2018 issue [22]. Chapter 6 features the application of ^{19}F NMR oximetry to clinical biofilms. We use oxygen mapping to visualize infection persistence under prolonged antibiotic therapy and demonstrate that long-term administration of a broad-spectrum antimicrobial to an established biofilm imposes a pseudo-steady state which temporarily prevents oxygen sink expansion but is insufficient to inhibit respiration. This study is currently under review in *Magnetic Resonance in Medicine*. Chapter 7 transitions to engineering applications, with the method used to evaluate and mathematically model reactive-diffusive transport and to quantify localized external mass transfer resistance. This manuscript is under preparation and will be submitted to *Biotechnology and Bioengineering*.

References

[1] Characklis, W.G., and Marshall, K.C. (1990). Biofilms (Wiley).

[2] Donlan, R.M. (2002). Biofilms: microbial life on surfaces. Emerg Infect Dis *8*, 881.

[3] Stewart, P.S. (2003). Diffusion in biofilms. J Bacteriol *185*, 1485-1491.

[4] Stewart, P.S., and Franklin, M.J. (2008). Physiological heterogeneity in biofilms. Nature Reviews Microbiology *6*, 199-210.

[5] Xu, K.D., Stewart, P.S., Xia, F., Huang, C.-T., and McFeters, G.A. (1998). Spatial physiological heterogeneity inPseudomonas aeruginosa biofilm is determined by oxygen availability. Appl Environ Microbiol *64*, 4035-4039.

[6] Lee, W., Lewandowski, Z., Nielsen, P.H., and Hamilton, W.A. (1995). Role of sulfate-reducing bacteria in corrosion of mild steel: a review. Biofouling *8*, 165-194.

[7] Marteyn, B., Scorza, F.B., Sansonetti, P.J., and Tang, C. (2011). Breathing life into pathogens: the influence of oxygen on bacterial virulence and host responses in the gastrointestinal tract. Cell Microbiol *13*, 171-176.

[8] Borriello, G., Werner, E., Roe, F., Kim, A.M., Ehrlich, G.D., and Stewart, P.S. (2004). Oxygen Limitation Contributes to Antibiotic Tolerance of Pseudomonas aeruginosa in Biofilms. Antimicrob Agents Chemother *48*, 2659-2664.

[9] Prigent-Combaret, C., Vidal, O., Dorel, C., and Lejeune, P. (1999). Abiotic surface sensing and biofilm-dependent regulation of gene expression in Escherichia coli. J Bacteriol *181*, 5993-6002.

[10] Worlitzsch, D., Tarran, R., Ulrich, M., Schwab, U., Cekici, A., Meyer, K.C., Birrer, P., Bellon, G., Berger, J., and Weiss, T. (2002). Effects of reduced mucus oxygen concentration in airway Pseudomonas infections of cystic fibrosis patients. The Journal of clinical investigation *109*, 317-325.

[11] Cowley, E.S., Kopf, S.H., LaRiviere, A., Ziebis, W., and Newman, D.K. (2015). Pediatric cystic fibrosis sputum can be chemically dynamic, anoxic, and extremely reduced due to hydrogen sulfide formation. MBio *6*, e00767-00715.

[12] Kolpen, M., Hansen, C.R., Bjarnsholt, T., Moser, C., Christensen, L.D., van Gennip, M., Ciofu, O., Mandsberg, L., Kharazmi, A., and Döring, G. (2010).

Polymorphonuclear leukocytes consume oxygen in sputum from chronic Pseudomonas aeruginosa pneumonia in cystic fibrosis. Thorax *65*, 57-62.

[13] Kolpen, M., Lerche, C.J., Kragh, K.N., Sams, T., Koren, K., Jensen, A.S., Line, L., Bjarnsholt, T., Ciofu, O., and Moser, C. (2017). Hyperbaric oxygen sensitizes anoxic Pseudomonas aeruginosa biofilm to ciprofloxacin. Antimicrob Agents Chemother *61*, 1-9.

[14] Jesaitis, A.J., Franklin, M.J., Berglund, D., Sasaki, M., Lord, C.I., Bleazard, J.B., Duffy, J.E., Beyenal, H., and Lewandowski, Z. (2003). Compromised host defense on Pseudomonas aeruginosa biofilms: Characterization of neutrophil and biofilm interactions. J Immunol *171*, 4329-4339.

[15] Silver, I.A. (1973). Problems in the investigation of tissue oxygen microenvironment. In Chemical Engineering in Medicine (American Chemical Society), pp. 343-352.

[16] Davies, P.W., and Brink, F. (1942). Microelectrodes for measuring local oxygen tension in animal tissues. Rev Sci Instrum *13*, 524-533.

[17] Stewart, P.S. (2012). Mini-review: convection around biofilms. Biofouling *28*, 187-198.

[18] Delpuech, J.J., Hamza, M.A., Serratrice, G., and Stebe, M.J. (1979). Fluorocarbons as oxygen carriers. 1. An NMR study of oxygen solutions in hexafluorobenzene. J Chem Phys *70*, 2680-2687.

[19] Eidelberg, D., Johnson, G., Barnes, D., Tofts, P.S., Delpy, D., Plummer, D., and McDonald, W.I. (1988). ^{19}F NMR imaging of blood oxygenation in the brain. Magn Reson Med *6*, 344-352.

[20] Mason, R.P., Rodbumrung, W., and Antich, P.P. (1996). Hexafluorobenzene: A sensitive F-19 NMR indicator of tumor oxygenation. NMR Biomed *9*, 125-134.

[21] Liu, S., Shah, S.J., Wilmes, L.J., Feiner, J., Kodibagkar, V.D., Wendland, M.F., Mason, R.P., Hylton, N., Hopf, H.W., and Rollins, M.D. (2011). Quantitative tissue oxygen measurement in multiple organs using 19F MRI in a rat model. Magn Reson Med *66*, 1722-1730.

[22] Simkins, J.W., Stewart, P.S., and Seymour, J.D. (2018). Spatiotemporal mapping of oxygen in a microbially-impacted packed bed using 19 F Nuclear magnetic resonance oximetry. J Magn Reson *293*, 123-133.

CHAPTER TWO: INTRODUCTION TO NUCLEAR MAGNETIC RESONANCE

The phenomenon of nuclear magnetic resonance (NMR) was first observed in 1945 by Purcell, Torrey, and Pound at Harvard University [1], and independently by Bloch, Hansen, and Packard at Stanford University [2]. Beyond being a breakthrough validation of many of the predictions made in the field of quantum mechanics over the previous few decades, the discovery of magnetic resonance would also go on to provide revolutionary advancements to the fields of medicine, chemistry, engineering, and physics, due to the ability to noninvasively probe molecular environment. This chapter will introduce the basic concepts underlying the NMR phenomenon, while the next chapter will focus on the application of these ideas to facilitate more advanced experiments. Both chapters will rely heavily on reference texts by Paul Callaghan [3; 4], but will cite original references where applicable.

2.1 Quantum Mechanics

All nucleons (protons and neutrons) carry a property called *spin*, denoted with the letter *I*, an intrinsic form of angular momentum that shapes quantum mechanical behavior. As a result of the strong nuclear force, nucleons tend to bind each other, forming atomic nuclei which form the center of chemical elements. By virtue of the fact that nuclei are composed entirely of nucleons, the property of spin is extended to the nucleus. Nuclei with nonzero spin number (wherein the spin vectors of the constituent nucleons do *not* sum to zero) possess an associated magnetic moment μ with some spatial

orientation. Some NMR active nuclei, such as ^{1}H and ^{19}F which will be the focus here, possess a nuclear spin of ½. When angular momentum, *m*, of a spin is measured along an arbitrary reference axis, its value is restricted to discrete integer values in the range [-*I*, (-*I*+1), …, (*I*-1), *I*]. Thus, for ^{19}F and ^{1}H nuclei, m can only take on values +½ (spin up) or -½ (spin down).

The NMR experiment takes advantage of the fact that the intrinsic nuclear spin of atomic nuclei imparts a magnetic moment μ. In layman's terms, this means that the nucleus behaves as a tiny magnet which interacts with its electromagnetic environment. The ratio relating the strength of the magnetic moment μ relative to the angular momentum is given by $\mu = \gamma m$, where γ, called the gyromagnetic ratio, is a constant for a given nucleus [3]. ^{1}H and ^{19}F have the highest gyromagnetic ratios (2.675 and 2.517 x 10^{8} rad/(T s), respectively) of all NMR-active nuclei, and as a consequence provide the highest signal strength relative to a fixed magnetization.

The quantum state of a spin system containing a single basis state is described by:

$$A|a\rangle = a|a\rangle \qquad \text{(Eq 2.1)}$$

where *A* is an observable property of interest, the eigenvector $|a\rangle$ is a basis state of *A*, and the eigenvalue a is the observed value of measurement *A.* However, a fundamental principle of quantum mechanics states that, much like waves in classical physics, elementary particles and their composite bodies exist in a linear superposition of basis states, and collapse into a single basis state only when a measurement is taken due to an interaction between the system and the measurement equipment. The system may exist in a superposition of all allowed states $\{|a\rangle\}$ until a measurement is taken; this is referred to

as the spin state being "operated on" by the measurement *A*. The process of operating on an observable existing in a superposition of states is represented mathematically by taking the inner product (the projection of one vector onto the other), and results in the collapse of the wave function into one of the basis states [3].

Spin angular momentum is fundamentally quantum in nature, and manipulation of spin state will thus require the use of the above linear algebra-based notation, called "bra-ket" notation, to accurately describe the dynamics. Of particular interest to NMR, suppose that we wish to measure the component of angular momentum, $I = \overline{\langle I_x \rangle}\boldsymbol{i} + \overline{\langle I_y \rangle}\boldsymbol{j} + \overline{\langle I_z \rangle}\boldsymbol{k}$, about a particular axis, where $\boldsymbol{i}$, $\boldsymbol{j}$, and $\boldsymbol{k}$ are unit vectors along the *x*, *y*, and *z* vectors, respectively. The expectation value of the measurement is given by [3]:

$$\langle \Psi | I_z | \Psi \rangle = \sum_m |a_m|^2 \, m \qquad \text{(Eq 2.2)}$$

where the notation of the left-hand side denotes the inner product. I_z here is the operator for the measurement of angular momentum along a particular axis (*z* in this case), while the eigenvalue *m* is the result of an observation. During the act of measurement, the spin state wave function collapses to one of the allowed, quantized values, with the probability of each state weighted by $|a_m|^2$. With values of *m* restricted to ½ and -½, the expected value will be some linear combination of the probability densities of the two possible states. Other than the I_z operator associated with measurement of the angular momentum, two other operators form the basis of the quintessential NMR experiment:

$$I_+ = I_x + iI_y \qquad \text{(Eq 2.3)}$$

$$I_- = I_x - iI_y$$

These operators convert the -½ state to the ½ state, and vice versa. As we will see later, evolution of the NMR signal is on its most fundamental level a manipulation of the spin states via these operators using external magnetic fields.

2.2 The Zeeman Interaction

All quantum spin states have an energy level associated with them, just as position within a gravitational field confers an inherent potential energy. The energy of a spin state is measured using the Hamiltonian operator *H*. In the absence of a magnetic field, the two spin states have equal energy, and a nucleus' angular momentum vector will be oriented randomly in space. In this case, if one were to observe the spin state of an ensemble of nuclei, the expectation value would be zero (an individual measurement, of course, would still return either ½ or -½). However, in the presence of an external magnetic field $\boldsymbol{B_o}$, the interaction between the external field and the nucleus' intrinsic magnetic moment give rise to an energy difference between the two spin states, a phenomenon known as the Zeeman effect [3]. Specifically in this case, the spin +1/2 state (aligned *with* $\boldsymbol{B_o}$; denoted hereafter as "parallel" or "spin up") exhibits lower total energy than the spin -1/2 (aligned *against* $\boldsymbol{B_o}$; denoted as "antiparallel" or "spin down") orientation. The strength of the Zeeman Interaction is [3]:

$$H_{Zeeman} = -\gamma\hbar B_0 I_z \qquad \text{(Eq 2.4)}$$

corresponding to an energy difference between the two states (Figure 2.1) of:

$$\Delta E = \gamma\hbar\boldsymbol{B_o} \qquad \text{(Eq 2.5)}$$

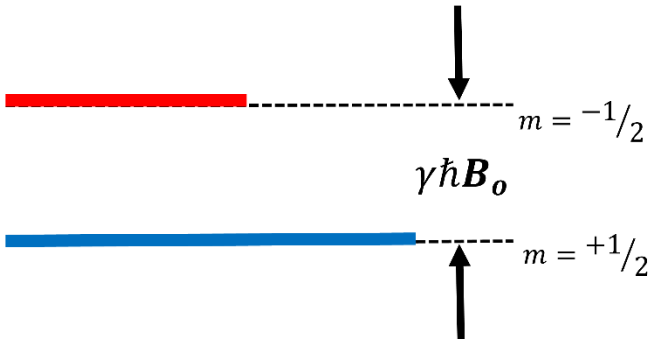

Figure 2.1. Energy level diagram for spins of I = ½ experiencing a Zeeman Interaction. The energy spacing for levels separated by m = ±1 is $\gamma\hbar B_o$. The bold colored lines exaggerate the population difference between the two states for an ensemble in thermal equilibrium.

Here $\hbar$ represents Plank's reduced constant, a proportionality constant that relates the quantized energy of a particle to the frequency of its associated electromagnetic wave (quantum mechanical theory asserts that all matter exhibits wave-like behavior to some extent). The quantity $\gamma \boldsymbol{B_o}$ has units of angular frequency and is referred to as the Larmor frequency, ω_o. The Larmor frequency represents the intrinsic frequency at which spins alternate between the two energy states. In classical mechanics, this corresponds to rotation about the external magnetic field axis (z by convention) due to a torque induced by the magnetic field on the spin angular momentum vector.

Due to the energy difference between states, there is a slight preference of nuclei to exist in the parallel configuration, which manifests in a bias in the number of nuclei occupying each state (Figure 2.1). The probability of occupying a parallel configuration is given by the Boltzmann distribution, a relationship derived from statistical mechanics [3]:

$$P_{+1/2} = \frac{exp(\frac{-\frac{1}{2}\gamma \boldsymbol{B_o} \hbar}{k_B T})}{exp(\frac{-\frac{1}{2}\gamma \boldsymbol{B_o} \hbar}{k_B T}) + exp(\frac{\frac{1}{2}\gamma \boldsymbol{B_o} \hbar}{k_B T})} \quad \text{(Eq 2.6)}$$

where T is the absolute temperature and k_B is the Boltzmann constant, a quantity relating the average kinetic energy of particles to their temperature. In words, the population difference between the two states represents a balance between the very small energy difference between spin up and spin down, and the intrinsic thermal energy (orders of magnitude greater) which pushes for equal populations due to random kinetic exchanges. The net effect is a miniscule population difference, with the parallel state having an excess of about one nucleus per million nuclei in each state. It is only the excess population in one state, called the net polarization, which is detected in the NMR experiment, making NMR a relatively insensitive spectroscopic technique. However, due to the staggering number of nuclei present in any sample (a mole of a compound contains over 6 x 10^{23} molecules!), there is ample signal for detection. Equation 2.6 makes it clear that net polarization is not a constant; increasing the magnetic field strength $\boldsymbol{B_o}$ or reducing temperature will augment the population asymmetry, leading to increased signal-to-noise during spin detection.

Explaining the magnetic resonance phenomenon through a quantum perspective becomes extremely cumbersome and unintuitive beyond the basics. Hereafter we will proceed using a classical perspective which makes the concepts much more accessible, although it should be noted that it is sometimes necessary to invoke quantum mechanics to account for some of the more peculiar results of magnetic resonance and to describe the behavior of nuclei possessing spin greater than ½ [5].

2.3 The Vector Model

While quantum mechanics fundamentally form the underlying basis of the NMR phenomenon, the behavior of ½ spins can be accurately and more intuitively expressed using classical physics due to the two-state nature of the ½ spin system and extensive smoothing of quantum behavior when moving from the particle scale to the continuum scale. Further, approaching the NMR experiment from a macroscale perspective can often generate novel insights due to mathematical simplicity. Such is the case in the representation of the summed angular momenta of an ensemble of nuclei as a magnetization vector $\boldsymbol{M}$, first introduced by Bloch in 1946 [2]. Conveniently, when we express the net polarization of a sample as a single vector, we observe that its behavior and evolution are consistent with macroscopic equations governing electromagnetism.

Electromagnetic induction is a macroscopic relationship between electricity and magnetism whereby the flow of current establishes a magnetic field and the presence of a magnetic field establishes the flow of current. Just as $\boldsymbol{B_o}$ is generated by running current through a metal solenoid, the magnetization vector (the sum of every spin's magnetization vector) acts as a magnet and is thus capable of generating a current inside a judiciously placed loop or coil of wire. However, at equilibrium, any current that would be induced by $\boldsymbol{M}$ is undetectable, as the strength of $\boldsymbol{M}$ is overwhelmingly drowned out by the much larger $\boldsymbol{B_o}$. To get the signal into a form that we can detect, we thus need to rotate $\boldsymbol{M}$ into the transverse plane where $\boldsymbol{B_o}$ has no contribution. Once this is achieved, a receiver coil oriented along the transverse plane will detect $\boldsymbol{M}$ via the current that it induces in the coil wire [3].

In the previous section it was mentioned that spins precess about the $\boldsymbol{B_o}$ field due to a torque between the two vectors. An alternate form of the Larmor frequency, this time in units of cyclical frequency, is given by [3]:

$$\omega_o = \frac{\gamma}{2\pi}\boldsymbol{B}_o \qquad \text{(Eq 2.7)}$$

and is typically on the order of tens to hundreds of megahertz for high-field NMR.

This observation, that magnetic fields exert a torque on spins, is exploited to rotate $\boldsymbol{M}$ out of the longitudinal plane. To do so, one must create a second magnetic field in the transverse plane, which we shall refer to as $\boldsymbol{B_1}$. This will then exert a torque on $\boldsymbol{M}$ and cause it to rotate into the transverse plane as dictated by the right hand rule.

The general differential equation governing the influence of the overall magnetic field $\boldsymbol{B}$ on $\boldsymbol{M}$ is expressed as [2]:

$$\frac{d\boldsymbol{M}}{dt} = \gamma \boldsymbol{M} \times \boldsymbol{B} \qquad \text{(Eq 2.8)}$$

Separated into *x*, *y*, and *z* components, considering contributions of the static magnetic field $\boldsymbol{B_o}$ and the pulsed magnetic field $\boldsymbol{B_1}$ separately, and applying the initial condition $\boldsymbol{M}(t) = M_o\mathbf{k}$, the behavior of the magnetization vector in the laboratory reference frame following excitation is given by [2]:

$$\begin{aligned} M_x &= M_0 sin(\omega_1 t) sin(\omega_0 t) \\ M_y &= M_0 sin(\omega_1 t) cos(\omega_0 t) \qquad \text{(Eq 2.9)} \\ M_z &= M_0 cos(\omega_1 t) \end{aligned}$$

where $\omega_1 = \gamma B_1$. The result is a vector that precesses both around $\boldsymbol{B_o}$ and $\boldsymbol{B_1}$, with frequencies ω_o and ω_1, respectively. Viewed in a static reference frame, the evolution of

M takes the form of a spiral which gradually approaches the transverse plane [3] (Figure 2.2).

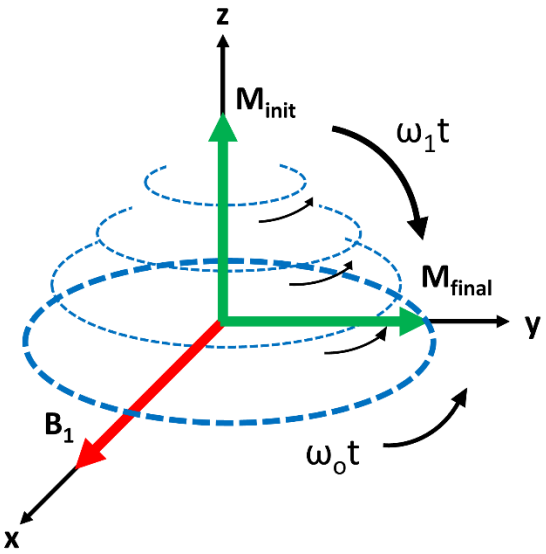

Figure 2.2. Time evolution of the magnetization vector *M* after application of a 90º rf excitation pulse. *M* precesses about B_o at ω_o and around B_1 at ω_1, resulting in a spiral-shaped approach toward the transverse plane.

It is now convenient to define and operate within a new coordinate system which we denote as the *rotating frame*, in contrast to the static *laboratory frame*. This reference frame takes the vantage point of the spins, precessing with them at the Larmor frequency ω_o. In this frame, the phase of precession for each spin is constant, and the *apparent* Larmor frequency is thus zero. If we can generate a transverse, time-invariant $\boldsymbol{B_1}$ field in this frame, the magnetization vector will precess about it and rotate directly into the transverse plane (Figure 2.3). To accomplish this, in the laboratory frame a gated pulse of current is applied, switching on and off at exactly the Larmour Frequency, generating a $\boldsymbol{B_1}$ field that appears static in the rotating frame. This frequency typically lies in the range

of radiowaves on the electromagnetic spectrum, and will thus be referred to hereafter as a radiofrequency (rf) pulse [3].

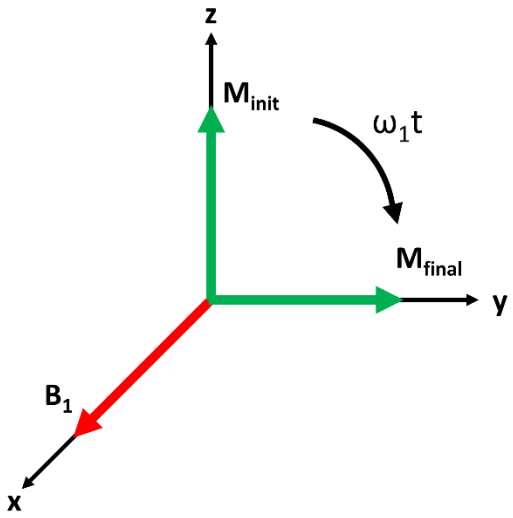

Figure 2.3. Time evolution of the magnetization vector *M* in the rotating frame. In these transformed coordinates, rotation about B_o is removed and only rotation about B_1 is apparent.

The general effect of applying a $\boldsymbol{B_1}$ field at a nonzero frequency ω_{off} is to introduce a frequency offset to the ω_0 term [3]:

$$M_x = M_0 sin(\omega_1 t) sin((\omega_o - \omega_{off})t)$$

$$M_y = M_0 sin(\omega_1 t) cos\big((\omega_o - \omega_{off})t\big) \qquad \text{(Eq 2.10)}$$

$$M_z = M_0 cos(\omega_1 t)$$

As the experimenter can choose freely the frequency at which the $\boldsymbol{B_1}$ field is pulsed, a judicious selection $\omega_{off} = \omega_o$ causes the entire second term of each $\boldsymbol{M}$ component to assume a constant value, removing $\boldsymbol{B_o}$'s contribution to the time evolution of $\boldsymbol{M}$. Thus, from this reference frame, application of a $\boldsymbol{B_1}$ results only in the tipping of $\boldsymbol{M}$ directly into the transverse plane, with no precession about the *z* axis (Figure 2.3).

The angle of rotation or tip angle that $\boldsymbol{M}$ undergoes in response to the $\boldsymbol{B_1}$ field pulse is given by:

$$\beta = \gamma \boldsymbol{B_1} t_p \qquad \text{(Eq 2.11)}$$

where t_p is the duration of the applied pulse. Any desired tip angle can be achieved, depending on application, with 90 and 180° of rotation being routine.

With $\boldsymbol{M}$ now partially or entirely in the transverse plane and with $\boldsymbol{B_1}$ turned off, $\boldsymbol{M}$ will now precess about the $\boldsymbol{B_o}$ axis, inducing an oscillating current in the receiver coil which is digitized at regular intervals and recorded [3]. This signal dissipates over time; the underlying reasons are the topic of the next section.

2.4 Relaxation

The act of tipping $\boldsymbol{M}$ into the transverse plane *excites* the nuclei in the sample, at which point the magnetization will continue to evolve in a process called relaxation. There are two fundamental mechanisms of relaxation which differ in their molecular origins; both act simultaneously on $\boldsymbol{M}$. The process by which the net magnetization decays in the transverse plane is termed spin-spin relaxation or T_2 relaxation, and is most intuitively understood as the timescale of loss of phase coherence across the spin ensemble due to stochastic and irreversible molecular interactions experienced by each spin. The second relaxation mechanism characterizes the timescale by which $\boldsymbol{M}$ re-establishes its thermal equilibrium in the longitudinal plane, and is termed spin-lattice relaxation or T_1 relaxation. T_1 relaxation originates from the release of energy from excited spins to the surrounding environment (the thermal lattice), leading to the

regrowth of the equilibrium magnetization vector along the *z* axis. All microscale processes causing T_1 relaxation also inherently cause T_2 relaxation; for this reason, T_2 is always less than or equal to T_1 [3].

Both relaxation mechanisms are ultimately descriptions of the time-dependent evolution of the magnetization vector due to stochastic effects, and are thus best understood in terms of the autocorrelation function. Consider a variable of interest, *A*, that varies stochastically with time. The autocorrelation function is given by:

$$G(t) = \int_0^\infty A(t')A(t'+t)dt' \qquad \text{(Eq 2.12)}$$

The function *G(t)* expresses the strength to which *A* remains correlated to its initial value. A further useful characteristic of many NMR-relevant stochastic variables is that these variables are often stationary, meaning the probabilities associated with different ensembles states do not fluctuate with time, and thus the absolute coordinates (beginning and end) of the observed time range are irrelevant; only the time interval itself is important. In stationary systems, it is generally further assumed that the long-time average of the stochastic variable is equivalent to the instantaneous spatial average for that variable, a property known as ergodicity. This property allows for the extrapolation of the autocorrelation function to the ensemble [3]:

$$G(t) = < A(0)A(t) > \qquad \text{(Eq 2.13)}$$

At time $t = 0$, *G(t)* is simply equal to the mean squared value of *A*, $<A(0)^2>$. As time increases, the association between the initial and final state of *A* decays as stochastic events accumulate, and system memory is lost. Normalizing the autocorrelation to its

initial value of $<A(0)^2>$, and taking its integral over time, we derive the correlation time, τ_c:

$$\tau_c = \frac{\int_0^\infty <A(0)A(t)>dt}{<A(0)^2>} \qquad \text{(Eq 2.14)}$$

Where τ_c is a measure of the characteristic timescale over which stochastic variables lose their correlation. In NMR parlance, excitation of the magnetization vector causes the constituent spins to become highly correlated, and relaxation is the measure by which the correlation among the spins degenerates due to stochastic interactions and collisions on the molecular scale. T_1 and T_2 are thus the correlation times associated with the macroscale return to equilibrium $\boldsymbol{M_z}$ and loss of $\boldsymbol{M_{xy}}$, respectively, during the NMR experiment [3]. The molecular interactions which cause them, of course, will have their own associated correlation times. These will turn out to have profound impact on T_1 and T_2.

2.5 Spectral Density Functions

Relaxation ultimately derives from the individual dipolar interactions between ½ spins, due essentially to each spin acting as a miniscule magnet. Each interaction is associated with a particular energy, just as the interaction between a spin and an external field. The dipolar Hamiltonian may take many forms depending on the type of interaction, but always depends strongly on the distance between dipoles and the time associated with the interaction, which is, in fact, the correlation time τ_c (spins are said to be correlated while they are interacting). This correlation time is bounded by the timeframe over which the two spins retain the required spatial orientation to facilitate the

dipolar interaction, and thus relaxation is intimately tied to molecular motion. In the simple case of free, isotropic molecular tumbling in a liquid phase, a range of molecular rotation times will exist due to random thermal effects. Taking the Fourier transform of the distribution of molecular rotation times, we obtain the spectrum of molecular rotation *frequencies*, which we term the spectral density function, *J(ω)*. As it turns out, *J(ω)* directly describes the nature and extent of the dipolar interactions, and thus governs what relaxation times will be observed. For spin-½ nuclei in the presence of a static magnetic field (*i.e.* experiencing the Zeeman Interaction), there are three potential outcomes for interacting spins, with the first given by [3]:

$$J^{(0)}(\omega) = \frac{24}{15r_{ij}^6}\frac{\tau_c}{1+\omega^2\tau_c^2} \qquad \text{(Eq 2.15)}$$

where r_{ij} is the distance between spin *i* and *j.* This corresponds to a situation in which neither spin experiences a change in spin state. As we will see briefly, this relation is secular, meaning it does not depend on the Larmor frequency ω_o [6]. Because there is no change of spin state, there is no net release of energy from the system. As we will see soon, the secular interaction results in T_2 relaxation but not T_1 relaxation, which occurs only when energy is released to the surrounding environment.

The second interaction results in one of the two spins changing its energy state, and is given by [3]:

$$J^{(1)}(\omega) = \frac{4}{15r_{ij}^6}\frac{\tau_c}{1+\omega^2\tau_c^2} \qquad \text{(Eq 2.16)}$$

Finally, if both spins flip energy states, we obtain:

$$J^{(2)}(\omega) = \frac{16}{15r_{ij}^6}\frac{\tau_c}{1+\omega^2\tau_c^2} \qquad \text{(Eq 2.17)}$$

In the above cases, the process of spin state reversal leads to net energy release to the environment.

A direct relation between T_1 relaxation time and the spectral density functions is given by the equation [3]:

$$\frac{1}{T_1} = \left(\frac{\mu_0}{4\pi}\right)^2 \gamma^4 \hbar^2 \frac{3}{2} I(I+1)\left[J^{(1)}(\omega_0) + J^{(2)}(2\omega_0)\right] \qquad \text{(Eq 2.18)}$$

The dependence of the two spectral density functions on ω_o and $2\omega_o$ respectively, indicates clearly what we have suggested above: these interactions occur only when the molecular tumbling frequency is equal to the Larmor frequency, or an integer multiple of it. We see further from the nonzero orders of the Bessel functions *J* that both of these are associated with spin state evolution, which we know now results in energy release to the surroundings. This is the basis by which we designate T_1 spin-lattice relaxation; the process of energy emission to the thermal lattice is in and of itself a relaxation process. The net effect is the re-establishment of the equilibrium polarization along the *z* axis.

The dependence of T_2 on the spectral density functions is given by [3]:

$$\frac{1}{T_2} = \left(\frac{\mu_0}{4\pi}\right)^2 \gamma^4 \hbar^2 \frac{3}{2} I(I+1)\left[\frac{1}{4}J^{(0)}(0) + \frac{5}{2}J^{(1)}(\omega_0) + \frac{1}{4}J^{(2)}(2\omega_0)\right] \qquad \text{(Eq 2.19)}$$

Here, we observe that T_2 exhibits sensitivity to Larmor-Frequency facilitated energy exchange interactions, similar to T_1. Additionally, however, T_2 is also sensitive to the secular $J^{(o)}$ term, which has no dependence on the Larmor frequency. Thus, secular, zero-frequency interactions induce T_2 but not T_1 relaxation, and as a natural consequence, T_1 is always greater than or equal to T_1.

We now have all the tools required to explain what relaxation tells us about molecular environment. A plot of the relationship between the relaxation time constants

and the dipolar coupling correlation time is shown in Figure 2.4. For short correlation times, characteristic of low viscosity fluids, dipolar couplings are short-lived. Furthermore, the high rate of molecular tumbling results in each spin sampling a large number of spin interactions over the course of the NMR experiment. These stochastic interactions tend to average out in accordance with the central limit theorem, resulting in slow loss of phase coherence. Put another way, the time-averaged autocorrelation of the magnetic field experienced by each spin is higher than it would be if spins were stationary. This phenomenon is called motional narrowing. In non-viscous liquid samples, T_2 is on the order of seconds [3].

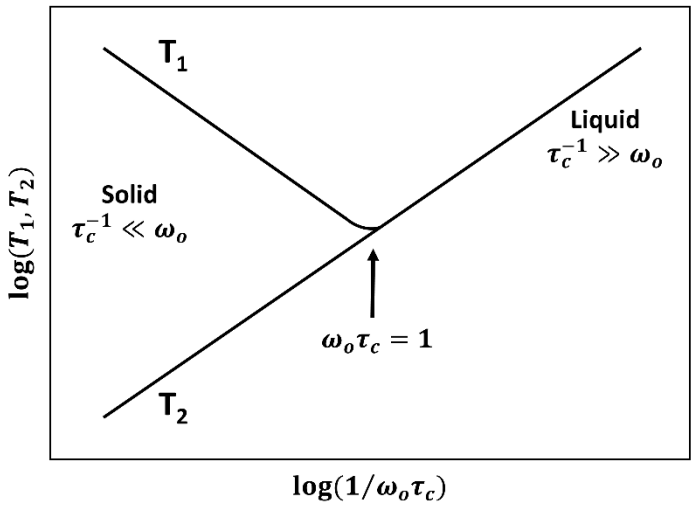

Figure 2.4. T_1 and T_2 relaxation as a function of correlation time τ_c at fixed Larmor frequency ω_o. Reproduced from [4].

As correlation time increases (*i.e.* when molecular tumbling is slow, as in the case for viscous fluids), the amount of interactions each spin samples in a given time period lessens, and the influence of motional narrowing diminishes, leading to a more rapid loss

of phase coherence. In systems with very large correlation times, such as solids with fixed molecular lattices, phase coherence is lost almost instantly as the molecular interactions become static. Each spin is essentially locked into a particular molecular environment and the strong dipolar interactions it experiences fail to average out over time. The spins will rapidly fall out of phase, and transverse relaxation may disappear in a matter of microseconds.

T_1 in contrast, exhibits a nonlinear dependence on correlation time [3]. A counterintuitive result, this observation is nonetheless easily explained by plotting the spectral density function (Figure 2.5), which, as we recall, simply denotes the distribution of molecular tumbling rates. For non-viscous liquids (fast motion), there is a very wide spectrum of molecular tumbling rates, with a significant part of the distribution falling well above the Larmor frequency. T_1 relaxation occurs only when rotational tumbling is on resonance, *i.e.* equal to the Larmor frequency, and therefore only the proportion of spins experiencing this specific tumbling rate (marked as A) will relax. As random thermal motion decreases (intermediate motion), perhaps due to a reduction in temperature or for a different compound with different chemical properties, the distribution is pulled towards zero as average kinetic energy decreases. As the total amount of spins is constant, this now means that the proportion of spins tumbling exactly at the Larmor frequency has increased (B), and thus relaxation will proceed faster. However, for samples with very long correlation times (slow motion), such as solids, the entire molecular tumbling distribution may fall well below the Larmor frequency. Due to the randomness of thermal vibrations, there will always be some tiny proportion of spins

that will end up rotating at the Larmor frequency, if only briefly, and only these spins will relax (*C*), resulting in an extremely long T_1 over the macroscale. For free water, T_1 is on the order of 5 seconds, while for truly solid compounds such as diamond, T_1 is on the order of months to years.

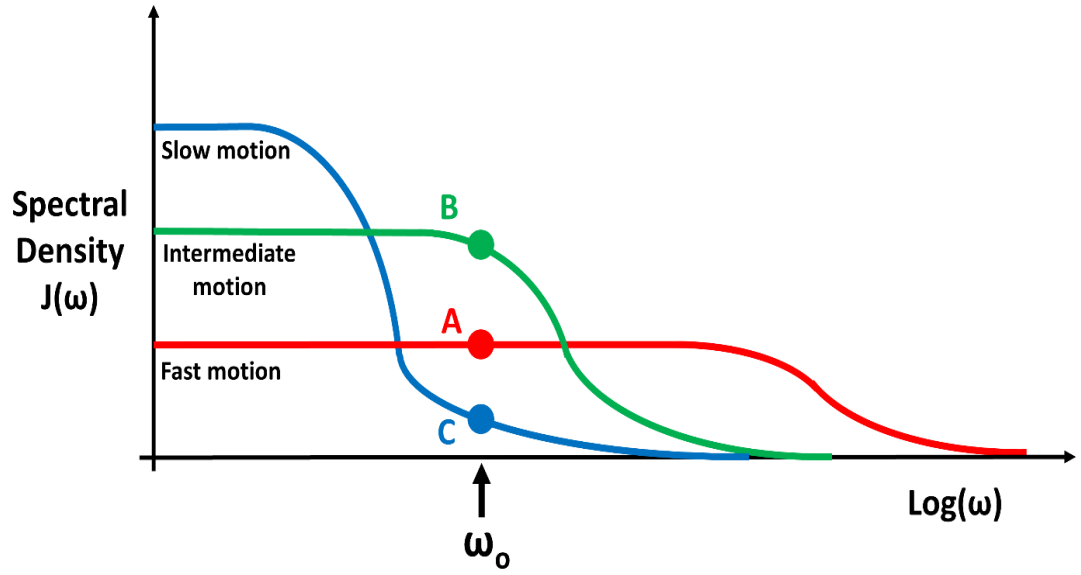

Figure 2.5. Spectral density function (distribution of molecular tumbling rates) for slow, intermediate, and fast motional regimes. Only spins exhibiting a molecular tumbling frequency exactly equal to the Larmor frequency will undergo spin-lattice relaxation, resulting in a nonlinear dependence of T_1 on molecular tumbling rate ω ($= 1/\tau_c$). Reproduced from [7].

We have now described the molecular basis by which relaxation results in the time-dependent evolution of the magnetization vector. What is the mathematical form of this evolution? To analyze the contributions of T_1 and T_2 on the magnetization, we first separate the magnetization into longitudinal and transverse components, recognizing that

T_1 acts on the longitudinal portion and T_2 acts on the transverse portion. The governing equation for the longitudinal component of $\boldsymbol{M}$ is given by [3]:

$$\frac{dM_z}{dt} = -\frac{M_z - M_0}{T_1} \qquad \text{(Eq 2.20)}$$

where M_o is the equilibrium magnetization. T_1 is typically measured by inverting the magnetization into the $-z$ plane using a 180º pulse, and then sampling the magnetization strength after waiting a variable recovery period (called the inversion time or TI) by tipping the developing M_z vector into the transverse plane. This pulse sequence is called Inversion Recovery (IR), and imposes the initial condition $M_z(0) = -M_o$. A schematic of the pulse sequence is shown in Figure 2.6. The solution is [3]:

$$M_z = M_o[1 - 2\exp(^{-t}/_{T_1})] \qquad \text{(Eq 2.21)}$$

By fitting the magnitude of M_z after variable TI to the above equation, a value for T_1 is obtained.

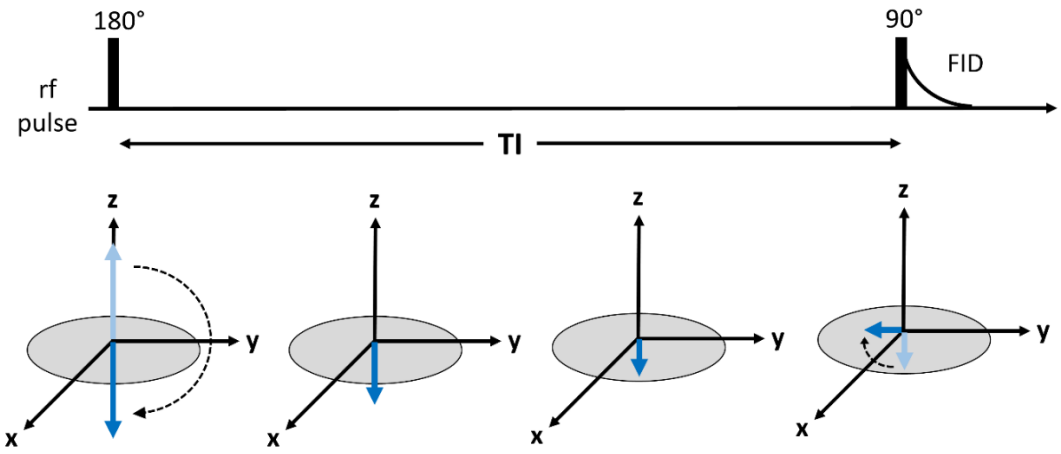

Figure 2.6. Inversion Recovery pulse sequence along with associated time evolution of the magnetization vector. Systematic variation of the inversion time (TI) allows for the timescale of return to thermal equilibrium to be samples and characterized.

The influence of T_2 on the transverse component of the magnetization vector is described by:

$$\frac{dM_{x,y}}{dt} = -\frac{M_{x,y}}{T_2} \qquad \text{(Eq 2.22)}$$

with initial condition $M_{xy}(0) = M_o$. The solution is easily obtained as:

$$M_{x,y}(t) = M_o \exp\left(-\frac{t}{T_2}\right) \qquad \text{(Eq 2.23)}$$

Thus, both T_1 and T_2 take the form of exponentials. These terms are easily incorporated into the Bloch equations [2], essentially acting as sources or sinks to a conservation equation for magnetization:

$$\frac{dM_x}{dt} = \gamma M_y B_o - \frac{M_x}{T_2}$$

$$\frac{dM_y}{dt} = \gamma M_z B_1 - \gamma M_x B_o - \frac{M_y}{T_2} \qquad \text{(Eq 2.24)}$$

$$\frac{dM_z}{dt} = -\gamma M_y B_1 - \frac{M_z - M_0}{T_1}$$

We have now explained the phenomenological reasons why relaxation occurs on the molecular scale, formulated mathematical solutions for the macroscale relaxation constants that result, and incorporated their influence into the governing equations that dictate the evolution of the magnetization vector. As we have shown, T_1 and T_2 provide a window into the molecular environments experienced by the spins; the specific information they provide is heavily dependent on the pulse sequence used. We will return to the general capabilities of relaxometry in a future section. However, of specific importance to this work, we must note the particular relevance of a special type of dipolar interaction called the Hyperfine Structure, also called Hyperfine Coupling, on spin-lattice relaxation [8]. This interaction occurs not between the two spins of adjacent nuclei, but between a nucleus and an unpaired electron of a nearby molecule.

An unpaired electron refers to an electron that occupies an orbital of an atom singly, rather than as part of an electron pair. This is also known as a degenerate orbital. The process of electron pairing is energetically favorable, and thus unpaired electrons occur infrequently in chemistry. However, certain molecules, such as molecular oxygen (O_2), are able to maintain stability despite containing one or more unpaired electrons. In the case of oxygen specifically, the outer valence shell (2p) contains two unpaired electrons which spin in the same direction, resulting in a strongly dipolar molecule [9].

The Hyperfine Coupling of an NMR-active, spin ½ nucleus and an unpaired electron takes different forms depending on the nature of the molecular contact by which the interaction is facilitated. Assuming a continuous translational diffusion model, as we

have done above, the dependence of relaxation on the Hyperfine Structure is given by [8]:

$$\frac{1}{T_1} = \frac{1}{2} g_N^2 g_e^2 \beta_e^2 \beta_N^2 I(I+1)\left[3J^{(1)}(\omega_I) + 7J^{(1)}(\omega_o)\right] \qquad \text{(Eq 2.25)}$$

where g_N and g_e represent Landé g-factors for nuclear and electronic spin, respectively, β_N and β_e represent nuclear and electronic magnetons, respectively, and ω_I represents the resonant frequency of the electronic spin [8]. The Hyperfine Structure is a powerful interaction, and as a consequence, a very efficient stimulator of T_1 relaxation. The presence of molecules containing unpaired electrons such as oxygen in a sample therefore hasten the rate of T_1, a property called paramagnetism. The solubility of oxygen in most solvents, however, is low, and the total effect on sample relaxation may go unnoticed. This is the case for water and most other commonly used solvents in NMR In certain solvents, however, the translational diffusion model fails to accurately describe the dynamics of dissolved oxygen. This is the case for liquid perfluorocarbons (PFCs), aliphatic or aromatic organic molecules with some or all hydrogens replaced with fluorine atoms. As the interaction between paramagnetic oxygen and the ^{19}F spin of PFCs form the basis of the current study, we will now briefly describe the molecular dynamics that underlie this special case.

In 1979 Delpuech et al. demonstrated that the interaction between ^{19}F nuclei of the PFC hexafluorobenzene (HFB) and the unpaired electrons of molecular oxygen can be explained not by continuous diffusion but by discontinuous diffusion of oxygen by stepwise migration to vacancies in the liquid lattice of the perfluorinated solvent [8]. This behavior is analogous to the formation of a solvation shell around a charged ion, *e.g.*

water bound to the surface of a chlorine atom through hydrogen bonding. It is believed that the geometry of the carbon-fluorine bond permits for a much closer proximity between the ^{19}F nucleus and the unpaired electrons of oxygen, in turn facilitating a powerful interaction between the two. Much like the continuous diffusion case, the secular terms turns out to be negligible; however, the dipolar contribution takes a unique form:

$$\frac{1}{T_1} = \frac{2\,x\,10^{-14}\mu_I^2\gamma_I^2\tau_c}{15r_I^6}\left(\frac{3}{1+\omega_I^2\tau_c^2} + \frac{7}{1+\omega_O^2\tau_c^2}\right) \qquad \text{(Eq 2.26)}$$

where μ_I is the electronic spin moment of oxygen and γ_I is the electronic gyromagnetic ratio [8]. This form of the Hyperfine Coupling, arising from the discontinuous lattice hopping behavior of oxygen in HFB, exhibits significantly higher strength than the continuous diffusion case. The effect of this is twofold: first, the lack of stereohindrance allows for dissolution of a high number of oxygen molecules in the PFC while still retaining energetic favorability. Oxygen is therefore highly soluble in PFC's, exhibiting a solubility of about an order of magnitude higher than for water ([10]). Second, the anomalous diffusion behavior of oxygen in these solvents increases the strength of the Hyperfine Structure, meaning the paramagnetic effect is amplified. The net effect is that the presence of oxygen in PFC systems results in a dramatically heightened rate of T_1 relaxation [11]. It should be noted that, while Delpuech's derivation is specifically applicable to HFB alone, it is thought that the same geometric considerations apply to other PFCs, thus explaining the high solubility of oxygen across a wide spectrum of fluorocarbons. As we will see later, the strong linear dependence of the relaxation rate $1/T_1$ of PFC ^{19}F nuclei can be exploited to directly measure oxygen concentration.

Moving forward, we will often refer to the *rate* constant of spin-lattice relaxation rather than the *time* constant; this is simply the inverse of the time constant ($R_1 = 1/T_1$) and the substitution is made because it is the rate that scales directly with local oxygen partial pressure (pO_2), not the time.

2.6 NMR Experimental Equipment:

Before we can explore the techniques by which we can manipulate spin behavior and encode them for desired observables, we must first understand the equipment used for the manipulations and the mathematical forms by which the signal presents.

On its most rudimentary level, exploitation of the NMR phenomenon requires a static magnetic field $\boldsymbol{B_o}$, a method of delivery radiofrequency pulses including a spectrometer and transmission coil, and a receiver coil. The $\boldsymbol{B_o}$ field historically was generated by placing the sample adjacent to a dedicated electromagnet, *e.g.* a block of ferromagnetic material (iron). Overall field homogeneity is a critical priority, and these electromagnets fared poorly in this metric due to field lines exhibiting significant spatial gradients. This issue was partially overcome with the use of 'shims', manually introduced shunts of magnetic material to compensate for the spatial variability in magnetic strength and direction. A significant breakthrough in NMR was the introduction of the superconducting magnet, a long and narrow wire solenoid comprised of a metallic material with the useful property of exhibiting zero electrical resistance at near-absolute zero temperature [12]. This coil is immersed in a bath of liquid helium which is itself immersed in liquid nitrogen, with the vacuum-filled gaps between each dewar. This

allows the superconducting coil to remain at near-zero absolute temperature for extended periods so long as the helium and nitrogen are refilled intermittently. The magnet is 'charged' once at the beginning of its life, and after being disconnected from the power source, current will cycle through indefinitely, generating a strongly homogeneous magnetic field in the solenoid's interior. The magnet's homogeneity is further augmented by the use of 'active' shims, accessory coils overlaid on top of the primary solenoid which correct for minor $\boldsymbol{B}$ gradients by running small amounts of current through. The shape of each shim coil determines the shape of the correction, with the most common corrections between linear in x, y, and z, and quadratic in z. The length, makeup, and density of the main solenoid are the primary determinants of overall $\boldsymbol{B_0}$. The strength of the magnet used in the present work produces a field strength of 7 T, corresponding to a Larmor frequency of 300 MHz for ^{1}H and 282 MHz for ^{19}F. The bore of the magnet is approximately 52 mm, and can thus accommodate samples up to 30 mm in width. Gradient coils are also present, allowing the spatial profile of the magnetic field to be altered strategically to encode spins for desired information; this will be discussed in a later section.

Excitation is accomplished using a coil of wire closely surrounding the sample, which is provided current by the NMR spectrometer. A power source outputs rf frequency current which is gated by the pulse programmer to match the desired frequency (Larmor frequency) and shaped to produce the desired excitation profile. The excited magnetization vector will then induce an oscillating current in a concentric detection coil. In modern NMR hardware, the transmission coil is also used as the detection coil. This

adjustment makes for simpler and less crowded design but requires the inclusion of a brief period where current is neither transmitted nor received while the coil switches mode of operation.

Typically, NMR coils utilize either a 'birdcage' design, although other configurations (such as the saddle coil) are not uncommon. The coil is oriented orthogonally to the *z* axis such that only transverse magnetization results in electromagnetic induction, and a references axis is chosen against which the oscillating signal is measured. The phase of the signal often provides critical information regarding the behavior of the spins, and it is thus necessary to measure both the real and imaginary components of ***M***. This is accomplished using a process called heterodyning [3], whereby voltage from the sample is mixed with two different reference voltages with a 90º phase difference, and the sum frequency term is removed, leaving only the difference term:

$$S(t) = \frac{1}{2} S_0 [cos(\omega_0 t - \omega t) - i\, sin(\omega_0 t - \omega t)] \qquad \text{(Eq 2.27)}$$

rewriting this in terms of the complex exponential, and including relaxation as an additional magnetization evolution term [13], we obtain:

$$S(t) = S_o\, exp(i\Phi)\, exp(i\Delta\omega t)\, exp\left(\frac{-t}{T_2}\right) \qquad \text{(Eq 2.28)}$$

where Φ is the receiver phase (this can be removed during signal processing), ω is the reference frequency, and $\Delta\omega = \omega_o - \omega$ is the offset frequency, *i.e*. the *apparent* frequency of the signal. Equation 2.28 indicates that the signal both oscillates and degenerates, as shown in Figure 2.7, and for this reason it is called the free induction decay (FID).

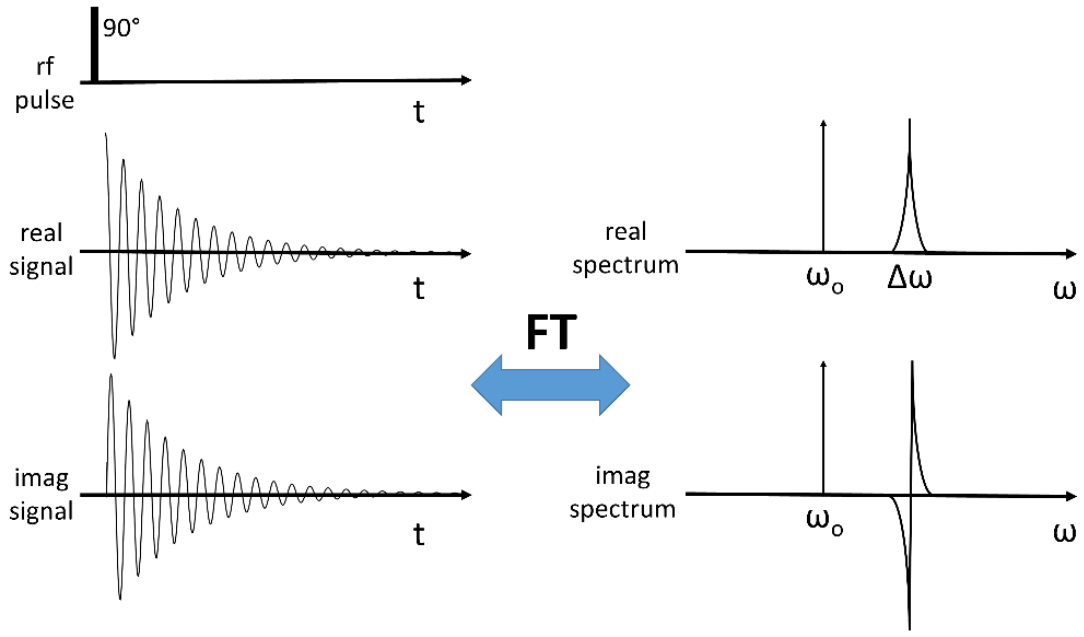

Figure 2.7. Appearance of the NMR signal after an excitation pulse. The rotating magnetization vector is visualized as a complex, exponentially-damped oscillation in the time domain which becomes a Lorentzian peak when Fourier transformed to the frequency domain.

To get the NMR signal into a useful form, it is necessary to employ a mathematical operation known as the Fourier transform (FT). The FT of a function in the time domain or spatial domain is an alternate representation of the same function in the frequency domain [14]. The mathematical formulation of the FT is given by:

$$\mathcal{F}\{g(t)\} = G(F) = \frac{1}{\sqrt{2\pi}}\int_{-\infty}^{\infty} g(t)e^{-i\omega t}dt \qquad \text{(Eq 2.29)}$$

$$\mathcal{F}\{G(F)\} = g(t) = \frac{1}{\sqrt{2\pi}}\int_{-\infty}^{\infty} G(F)e^{i\omega t}d\omega$$

In layman's terms, the FT of some arbitrary function is the distribution of frequencies (sines and cosines) needed to represent that function. In NMR, valuable data

generally comes in the form of frequency information: slight differences in Larmor frequency between different nuclei is used to identify constituent molecules and imposed spatial variation of Larmor frequency allows a sample to be imaged. However, the data is inherently acquired in the time domain where it may be uninterpretable. Fourier transformation of the data neatly pulls out the constituent frequencies, allowing for further processing and analysis.

Application of the FT to Eq. 2.28 results in a spectrum of frequencies, which for a single constituent nucleus within a spatially homogeneous magnetic field, will appear as a single peak (Figure 2.7). The shape of these peaks take the mathematical form of the Lorentzian function, the FT of the exponential function. A relevant property of FTs is time scaling, which observes that functions that are narrow in the time domain become wider in the frequency domain; this is because high-frequency oscillations are required to represent sharp features. As a result, samples undergoing fast relaxation (a small FID envelop), will exhibit wide peaks in the frequency domain, while samples undergoing slow relaxation will have sharp peaks, *i.e.* motional narrowing. The full-width-at-half-maximum (FWHM) of the Lorentzian peak is directly related to relaxation rate by $FWHM = {}^{1}/_{\pi T_2{}^*}$. The T_2 with the associated asterisk is referred to as 'T_2 star', and it is the time constant associated with the FID. In addition to relaxation effects caused by irreversible stochastic molecular interactions (true T_2 processes), dephasing is also induced by static inhomogeneities in the $\boldsymbol{B_o}$ field, as spins will assume different Larmor frequencies not only due to spin couplings but simply due to their different positions. This additional dephasing term is not indicative about molecular interactions, but rather

an artifact caused by either imperfections in $\boldsymbol{B_0}$ or sample geometry (susceptibility). As we will discover in the next section, there is a method with which we can circumvent T_2^*-related signal dephasing and hone in on true T_2 processes alone [3].

In practice, the NMR signal is not continuously recorded but must be sampled at a discrete, regular interval called the dwell time (DW), in a process termed digitization. The rate of sampling can have a strong impact on the integrity of the processed signal; too slow of digitization will result in the signal being assigned a spuriously low frequency, as will be discussed in a later section. Additionally, the frequency domain data set will have a spectral width (range of frequencies that can be detected) inverse to the dwell time.

2.7 Pulse Sequences

The NMR experiment is only valuable insofar as the experimenter has carefully manipulated the spins to yield something meaningful. These manipulations include rotation of the magnetization vector with rf pulses and encoding spins for position, displacement, or other properties with magnetic field gradients. With a small toolkit, the repertoire of possible measurements to be made seem small; however, this could not be further from the truth. The modularity of pulse and gradient design, combined with the sensitivity of NMR parameters such as relaxation on a wide spectrum of physio-chemical characteristics, allows for almost limitless potential for inquiry.

NMR experiments are typically mapped out using a pulse sequence diagram, which features time along the *x* axis and multiple lines, each representing the timing of

one of the experimental elements such as rf pulse transmission and detection, and gradient along some axis. A basic pulse sequence is ultimately designed to encode for some desired observable, and pulse sequences can be combined to result in a compound measurement. For instance, a pulse sequence that measures T_2 can be combined with an imaging sequence to generate an image where each pixel outputs the T_2 value for that region [15]. We have previously discussed the Inversion Recovery sequence which is used to measure T_1; we will now introduce some other simple pulse sequences.

2.8 Spin Echo

Previously it was mentioned that inherent $\mathbf{B_0}$ inhomogeneity results in additional spin dephasing, and that the resulting T_2* dependent spreading of peaks in the spectral domain can obscure the features of interest such as true T_2. No magnet is perfectly homogeneous, and thus this problem remains despite significant improvements to NMR hardware over the past several decades. Fortunately, this issue can be overcome using the spin echo, also called the Hahn echo after its introduction by Erwin Hahn in 1950 [16]. The technique works to reverse the dephasing effects of $\boldsymbol{B_0}$ inhomogeneity by applying a 180º pulse about the transverse plane at some time τ after the excitation pulse, when the magnetization vector has already decayed to zero (Figure 2.8). This is, in effect, simply reversing the direction of precession without influencing the distribution of frequencies. Because each spin continues to precess at its own frequency, the reversal of direction will ultimately result in all the spins reconverging to their state of coherence at 2τ, regardless of the spatially-dependent variance in Larmor frequency. The reconvergence is observed

as a reversed FID (*i.e.* a positive exponential) which reaches a maximum at exactly 2τ, and then decays again to zero (normal FID). This phenomenon is referred to as the spin echo. Because true T_2 dipolar coupling processes occur throughout this period, the maximum achieved will be less than the initial FID amplitude, *i.e.* only static spatial differences in magnetic field strength can be refocused. Typically, the NMR experiment will collect the echo rather than the FID, not just due to removal of unwanted inhomogeneous effects but also because the evolution period between excitation and the acquisition of the echo allows the spins to be encoded for desired variables.

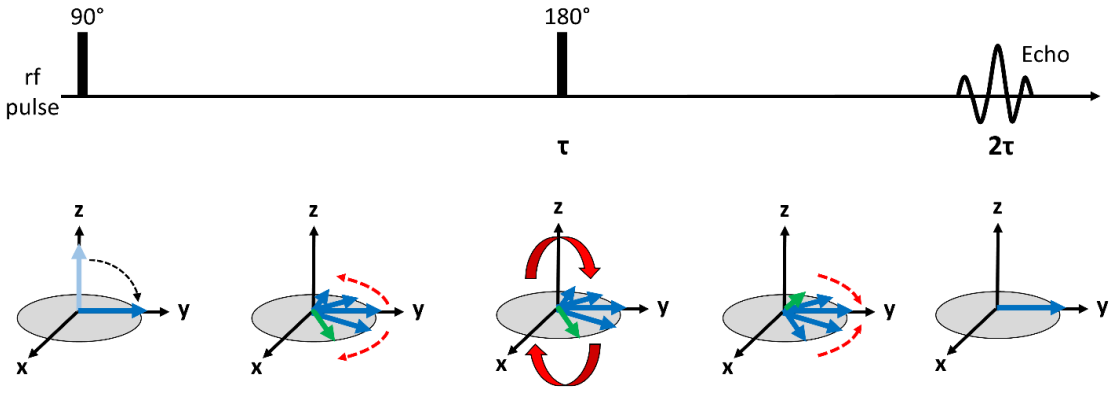

Figure 2.8. The spin echo pulse sequence along with the associated time evolution of the magnetization vector. A 180° refocusing pulse is applied at time τ after excitation, causing a reversal of dephasing effects due to B_o inhomogeneity. At time 2τ, the spins reconverge on their initial phase after excitation, resulting in an echo.

2.9 CPMG Echo Train

As the spin echo refocuses static inhomogeneity effects but not true T_2 processes, the rate of true T_2 decay is most easily determined by applying a chain of consecutive

180º pulses, as first demonstrated by Carr and Purcell in 1954 and refined by Meiboom and Gill 4 years later [15; 17]. An echo is acquired between each refocusing pulse, with the amplitude of each echo decaying exponentially according to the T_2 governing equation, with no interference from static $\boldsymbol{B_o}$ inhomogeneities. Fitting the monoexponential decay to the T_2 equation produces a fit value for T_2 (Figure 2.9).

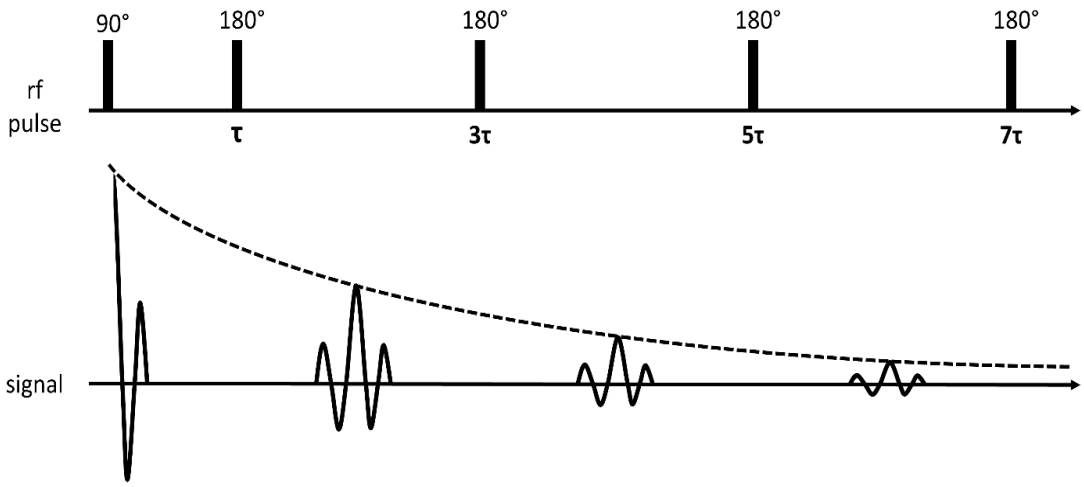

Figure 2.9. The CPMG pulse sequence, featuring a train of 180° refocusing pulses alternating with echo acquisitions. Because the amplitude of each consecutive echo decreases according to T_2 processes, this sequence is used to measure T_2 relaxation.

2.10 Phase Cycling

Although we typically describe the NMR experiment in terms of conventional Newtonian physics, occasionally the true quantum basis of spin behavior appears to rear its ugly head, resulting in unanticipated and peculiar results. This is the case with unwanted coherences, whereby the application of standard pulses stimulates an unwanted response in a subset of spins. Due to the fundamental randomness of the spin

superposition state, ensembles of spins can fail to experience a given pulse, or experience a different pulse strength than intended, leading to an incorrect tip angle. The error will then be carried forward for future pulses, culminating in ensembles of spins that follow an unintended spin evolution pathway. Because these pathways are coherent, they will contribute to the signal in various ways, causing spurious echoes and anomalies in phase and amplitude that may obscure the information encoded into the correct pathway. To remove these unwanted coherence pathways, the reference axes with which the quadrature detection channels define real and imaginary signal are shuffled for each acquisition, and the phases of the rf pulses are likewise rotated. The net effect is that the signal following the intended evolution pathway constructively adds to itself, while unwanted coherence pathways destructively cancel [18]. These phase cycle operations are coded into the pulse sequence; however, the experimenter must ensure that the experimental parameters being used satisfy a complete phase cycle.

2.11 Signal Averaging

Signal averaging is critical not just for the removal of unwanted coherence pathways but also in compensating for the signature limitation of NMR as an imaging and microscopy technique: insensitivity. Due to the miniscule net polarization of a spin ensemble even at high fields, NMR is inherently an insensitive technique. In high-resolution applications, the amplitude of thermal noise in the receiver coil may be on the same order of magnitude as the desired signal, leading to noisy, uninterpretable spectra. To improve signal-to-noise ratio, each signal acquisition is repeated multiple times, and

the signal from each iteration is added. Signal contribution from nuclei will scale linearly with N, the number of averages, while noise, assumed to be incoherent and following a Gaussian distribution with mean zero, will scale with $\sqrt{N}$ due to random cancellation [3]. Thus, signal to noise ratio ultimately scales as:

$$SNR \propto \frac{N}{\sqrt{N}} = N^{1/2} \qquad \text{(Eq 2.30)}$$

2.12 Magnetic Resonance Imaging

Frequency information has long been used as a molecular fingerprint that can be used to identify a sample's constituent compounds. However, arguably the most important innovation made in the field of magnetic resonance, occurring over three decades after the discovery of the NMR phenomenon, was the demonstration that frequency information could be used to map the position of nuclei in a sample (i.e. generate an image) [19; 20]. As introduced earlier, variation of magnetic field strength across a sample leads to a spread in the range of frequencies exhibited by different ensembles, thus broadening the peaks in the frequency domain. In magnetic resonance imaging (MRI), we exploit this phenomenon to provide a window intro the distribution of spins' positions by intentionally imposing a linear gradient in magnetic field strength across the sample. In the presence of the gradient, a spin's frequency of precession will correspond directly to its spatial position. In such a circumstance, we refer to the gradient as 'encoding' the spins for position. With prior knowledge of the gradient amplitude and duration, we can translate the frequency profile into a spatial map of $\rho(\mathbf{r})$, the spin density of the sample.

2.13 Gradients and k-Space

Let us define the gradient vector as the slope of the *z*-component of the $\boldsymbol{B_o}$ field as a function of position $\boldsymbol{r}$, that is, $\boldsymbol{G} = \nabla B_z$ (Figure 2.10). Applying a $\boldsymbol{G}$ which is linear with respect to position in an arbitrary direction across the sample results in a local Larmor frequency representing the sum of the $\boldsymbol{B_o}$ and $\boldsymbol{G}$ contributions:

$$\omega_0(\boldsymbol{r}) = \gamma(B_0 + \boldsymbol{r} \cdot \boldsymbol{G}) \qquad \text{(Eq 2.31)}$$

The signal produced by this sample is given by:

$$S(t) = \iiint \rho(\boldsymbol{r})\, exp(-i\gamma \boldsymbol{r} \cdot \boldsymbol{G}t) d\boldsymbol{r} \qquad \text{(Eq 2.32)}$$

where we observe via comparison to Equation 2.29 the existence of an apparent Fourier relation between the spin density $\rho(\boldsymbol{r})$ and the quantity $\gamma t\boldsymbol{G}$ [4]. To provide clarity for the Fourier pair variables, we introduce the variable $\boldsymbol{k}$, a vector that represents spatial frequency [4]:

$$\boldsymbol{k} = \frac{\gamma t \boldsymbol{G}}{2\pi} \qquad \text{(Eq 2.33)}$$

Substitution of $\boldsymbol{k}$ into our signal expression yields:

$$S_N(\boldsymbol{k}) = \int \rho(\boldsymbol{r})\, exp(-i\boldsymbol{k} \cdot \boldsymbol{r})\, d\boldsymbol{r} \qquad \text{(Eq 2.34)}$$

$$\rho(\boldsymbol{r}) = \frac{1}{2\pi} \int S(\boldsymbol{k})\, exp(i\boldsymbol{k} \cdot \boldsymbol{r})\, d\boldsymbol{k}$$

indicating a direct Fourier relationship between the spin density, and the obtained signal in the reciprocal space (spatial frequency) domain. This informs us that the complex signal we collect, *S*, can be directly Fourier transformed to produce a visual representation of the spin density, i.e. an image. This implies that the data we collect is a direct function of spatial frequency $\boldsymbol{k}$.

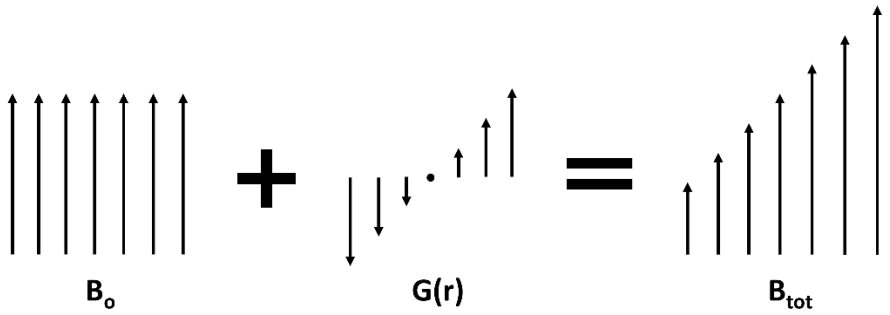

Figure 2.10. Application of a magnetic field gradient produces a combined magnetic field that varies linearly with position along the gradient axis. The strength of the gradient is greatly exaggerated for illustrative purposes.

2.14 Imaging Gradients

A gradient applied along an arbitrary axis causes spins to dephase as their Larmor frequency is tied to their position. The amount of dephasing is of course linearly proportional to both the strength of the gradient (how much incremental $\boldsymbol{B}$ is gained for a given change in position $\boldsymbol{r}$), and the time over which the spins experience the gradient. Spins will begin to 'lap' each other with respect to phase, resulting in the establishment of a 'helix of phase' which tightens up as long as the gradient remains on (Figure 2.11) [4]. Much like any other wave, the tightness of the phase helix can be characterized by its wavelength, λ, or by its inverse, the scalar frequency k. It is this spatial frequency that the wavevector $\boldsymbol{k}$ refers, and its dependence on both the strength of the gradient and the time over which it is applied is made clear by Eq 2.33.

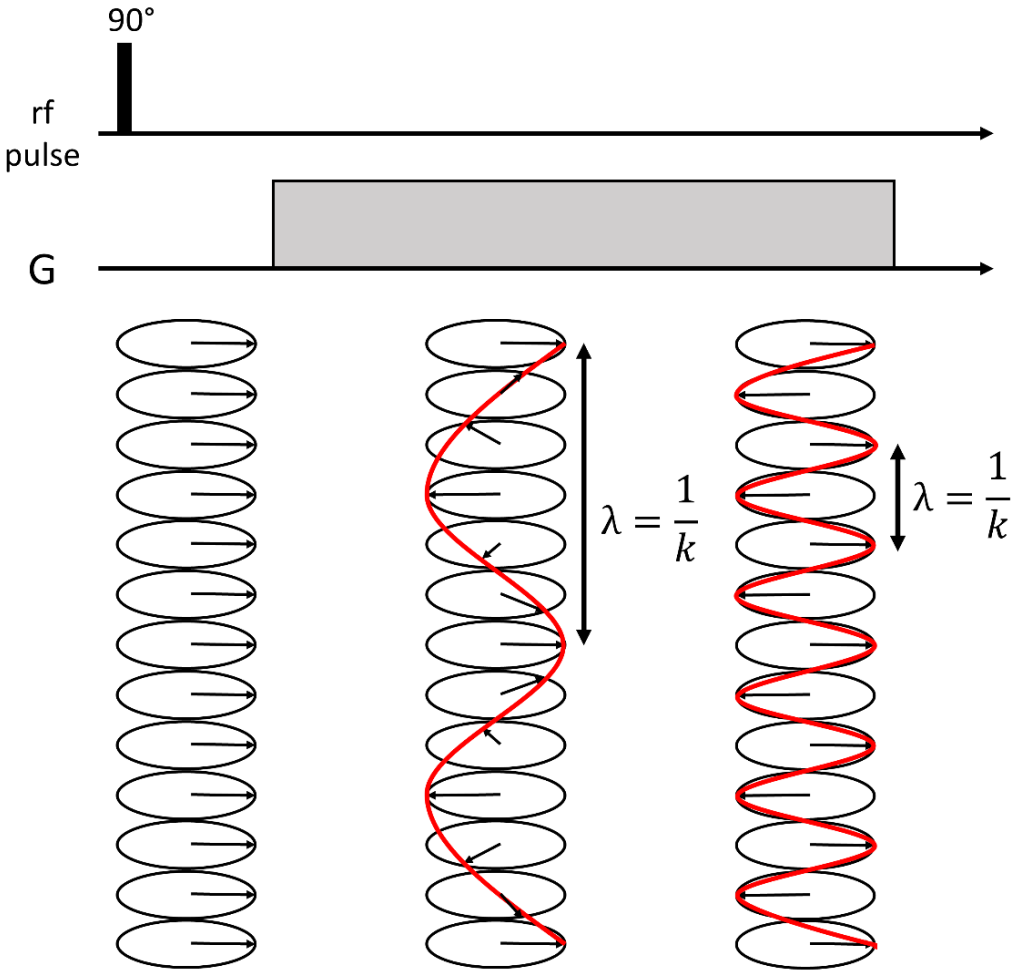

Figure 2.11. Evolution of spin phase under the influence of a magnetic field gradient, *G*, following an excitation pulse. A helix of phase is established which winds up (increases in spatial frequency) over time [4].

Of course, with all spins fully dephased we will not obtain any signal; observation of signal requires the echo condition be met. To achieve this, we apply a gradient of equal and opposite sign to refocus the spins, either by changing the direction of the current through the gradient coils, or by employing a 180º pulse to produce a spin echo (Figure 2.12).

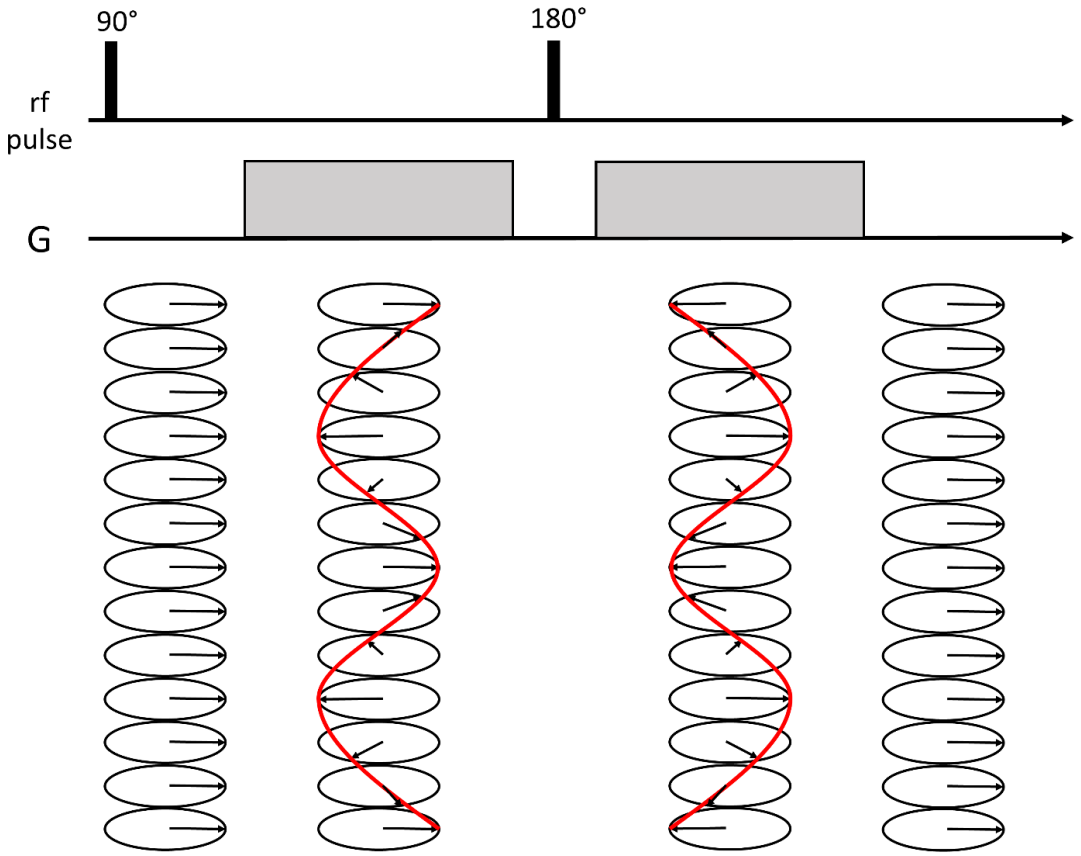

Figure 2.12. Incorporating a 180° refocusing pulse between two gradients of equal area rephrases the spins to produce an echo. The spin echo approach to spin rephrasing also has the added benefit of rephrasing incoherences due to B_o field inhomogeneities [4].

As we have so far shown, applying gradients in field strength after excitation produces a spatial helix of frequency which depends linearly on the gradient strength and time applied. The time-domain signal then naturally becomes a direct function of spatial frequency $\boldsymbol{k}$. We therefore state that the signal in this case is acquired in the *k*-space domain, and as gradient strength and/or duration increases in magnitude (i.e. as the phase helix tightens), we move away from the origin of *k*-space which is the zero gradient point.

It is evident from the form of $\boldsymbol{k}$ that we may traverse $\boldsymbol{k}$ in two different ways: first, by changing the gradient duration during signal acquisition, and second, by changing gradient amplitude during signal phase evolution. The first method is referred to as frequency encoding, with the associated gradient referred to as the 'read gradient,' G_{read} or G_{FE}. The second method is termed phase encoding, with associated 'phase gradient', G_{PE}. When a gradient is left on, we naturally traverse $\boldsymbol{k}$-space along whatever dimension G_{FE} is applied. It is thus reasonable to acquire data continuously (digitizing at regular short intervals as always), to facilitate rapid data collection. This is the reason why frequency encoding is referred to as the 'readout' dimension, and it is accomplished by applying a steady gradient during the acquisition of the echo signal.

To fill in the phase-encode dimension of $\boldsymbol{k}$-space, we must use an alternative approach, as applying a frequency encode gradient in both dimensions during acquisition of the echo will confound the contributions of the x and y positions of each spin on the observed signal. Instead, sometime after excitation a gradient of fixed duration and variable strength G_{PE} is applied along the phase encode axis before acquisition. Each iteration of the pulse sequence uses a different G_{PE} strength, such that we are shifted up or down along the phase encode dimension of $\boldsymbol{k}$-space. In this way, we traverse a new line in 2D $\boldsymbol{k}$-space with each acquisition.

Most basic imaging sequences use frequency encoding in one dimension, phase encoding in a second dimension, and spin echo refocusing to generate a 2D image (Figure 13). However, depending on the requirements of the experiment, other sequences may be used. For example, time constraints during a hospital MRI (patients find long

MRI acquisition times to be stressful) have led to the predominance of gradient echo sequences, which allow for the acquisition of all of ***k***-space in one excitation following a zig-zag trajectory [21]. This dramatically reduces experiment time at the cost of an increase in imaging artifacts, which will be addressed later. In samples with extremely short T_2 times, such as rock, frequency encode gradients are applied in both directions simultaneously during the excitation pulse, varying the strength of each independently, such that **k**-space is traversed via polar coordinates [22]. This results in an absence of data near the center of ***k***-space and necessitates reconstruction of the ***k***-space data in Cartesian space to facilitate Fourier transformation, but allows for collection of the rapidly-vanishing signal. There are endless ways to traverse ***k***-space, and it is up to the experimenter to determine which is most appropriate for the application at hand. In all cases, the meaning of ***k***-space is the same: the center of ***k***-space contains the bulk features of the image (low frequencies), while the peripheral regions contain the fine details and edge contrasts (high frequencies) [3]. Because data in ***k***-space ultimately tells you what distribution of frequencies is needed to reproduce your sample image, loss of data for a single coordinate in ***k***-space affects all parts of the resulting image.

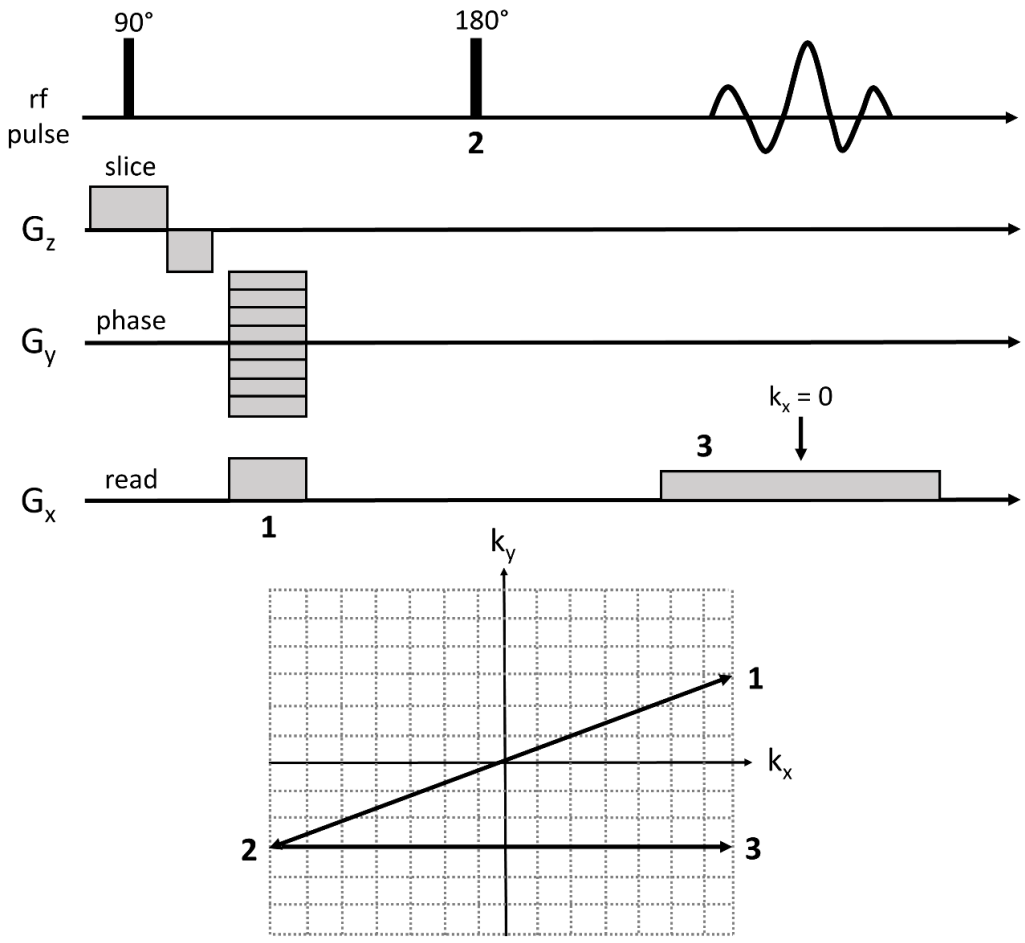

Figure 2.13. Two-dimensional imaging pulse sequence featuring phase encoding in the first dimension, frequency encoding in the second, and spin echo refocusing, along with associated *k*-space trajectory. After excitation, a combination of phase and read gradients traverse to a specific starting point in *k*-space (1). A 180° refocusing pulse inverts the *k*-space coordinate to (2). The applied read gradient then slides the signal across a row in *k*-space while the data is acquired (3). The strength of the phase gradient is varied between each acquisition such that a different line of *k*-space is acquired each time [4].

2.16 Slice-Select Gradient and Chemical Selective Excitation

Different chemical functional groups have unique chemical shifts associated with them, which generates different Larmor frequencies [23]. Because of this, a sample containing even a single solvent molecule may exhibit several peaks corresponding to

nonequivalent spin populations. A commonly encountered example in medicine is water and fat. The protons of water possess a different Larmor frequency than the long-chain hydrocarbon protons of fatty acids. ^{19}F nuclei exhibit extremely strong chemical shifts, with interpeak distances ranging from tens to hundreds of parts-per-million (ppm). In NMR, we frequently wish to probe the environment of only one of the constituent peaks, for instance if we wanted to image the distribution of fatty tissues in the human brain to find the location of a tumor. This is accomplished using chemical selective excitation, whereby only a range of frequencies within the sample are excited.

Pulse duration exhibits a Fourier relationship with frequency bandwidth, while the same is not true of pulse *strength*. The relation $\beta = \gamma \boldsymbol{B_1} t_p$ thus indicates that the distribution of frequencies about the center frequency which will be excited by an rf pulse can be controlled by altering the pulse duration while adjusting $\boldsymbol{B_1}$ strength to retain the desired tip angle. The implication of the Fourier pair is that the pulse time is inversely proportional to the bandwidth, or spectrum of excited frequencies, which is succinctly stated as $\omega_{rf} = 1/t_p$. Short time duration pulses (also called 'hard pulses') produce wide excitation bandwidths, exciting all frequencies in the spectrum, while long duration pulses (called 'soft pulses') produce narrow excitation bandwidths which are used to excite only a certain peak within the distribution.

Control over the distribution of excited frequencies is further augmented by the ability to shape pulses to produce the desired excitation bandwidth shape. Typically, we want an excitation profile wherein a subset of frequencies experience complete, uniform excitation (so all spins have the same tip angle), and all other frequencies experience no

excitation whatsoever. This profile, characterized by a constant value over a finite range and zero elsewhere, is called a hat function. To produce this, it is necessary to form the excitation pulse into the shape of the hat's FT, the sinc function (Figure 2.14) [4]. The true sinc function possesses lobes of decreasing amplitude that stretch infinitely in the time domain, and therefore we can only approach its shape. However, a 3-lobed approximation is generally sufficient to generate a reasonably-uniform excitation profile.

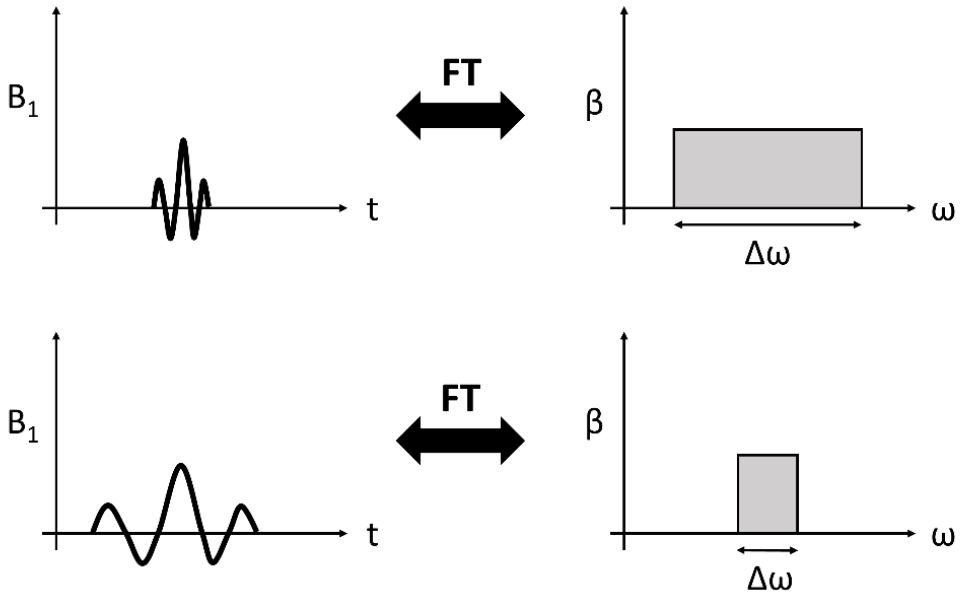

Figure 2.14. Sinc-shaped pulses are used to excite a range of frequencies with uniform tip angle β. The pulse duration is inversely proportional to the width of the distribution of excited frequencies. When combined with a slice-select gradient, selective excitation allows for a single desired slice of sample to be imaged.

Selective excitation is also a key component of 2D imaging. So far we have discussed position encoding in two dimensions. The sequence as described thus far would resolve position in the phase-encode and readout dimension, but as the excitation step

would affect all spins in the sample, the result would produce image voxels with a depth of the entire sample. Such an image may be of little use when there are features of interest in the third dimension, as they would be averaged out. To circumvent this, the experimenter applies a gradient along the third dimension (*i.e.* not the phase encode nor readout axis) during excitation, resulting in a linear distribution of Larmor frequencies determined by position along that axis. The experimenter then tunes the frequency of the $\boldsymbol{B_1}$ pulse to excite the Larmor frequency corresponding to the geometric coordinate of interest. Further, the duration of the pulse is chosen to intentionally select the range of frequencies corresponding to the desired width of the segment of sample that is to be investigated (the 'slice'). This process is called 'slice selection', and allows full control over both the location and width of the slice that will be imaged (Figure 2.13) [4].

2.17 Imaging Artifacts

We have now established the building blocks that are used to image samples, and must now turn our attention to the ways in which the imaging methodology interacts with the final result, the image. Acquisition of the ***k***-space signal involves the convergence of a multitude of parameters, some originating from the sample itself (its geometry, chemistry, or position) and some originating from the experimental hardware (its method of signal transmission, detection, and processing), and all of these factors contribute to the final product. Error of one or more component or failure to compensate for NMR imaging limitations will produce artifacts in the image, and it is critical for the experimenter to become acquainted intimately with the relationships between the image

and the acquisition protocol. Here we describe some of the commonly encountered NMR imaging artifacts, and their basis. This list is by no means exhaustive.

2.18 Chemical Shift

As described earlier, different molecules and even different functional spin populations within a single molecule exhibit different Larmor frequencies due to slight differences in magnetic field, a phenomenon called chemical shift. The resulting peak separation is linearly field strength dependent. At 7 T, for instance, the Larmor frequencies of fat and water differ by about 1000 Hz. This becomes a complicating factor during imaging, as the spectrometer associates a given frequency ω with a specific position $\boldsymbol{r}$. The spectrometer is unaware that there is an additional frequency present in the sample, and will interpret this peak as a spatial offset from the origin (Figure 2.15). The end result is the signal from the side peak will mismatch to the wrong voxel, visualized as a bright band adjacent to a dark band on the image [23]. This occurs purely in the readout direction as the resulting extra phase of nuclei from the side peak relative to the main peak does not accumulate from one phase-encoding step to the next, and thus the differential phase shift between the two peaks is constant at a given location between successive phase-encoding steps.

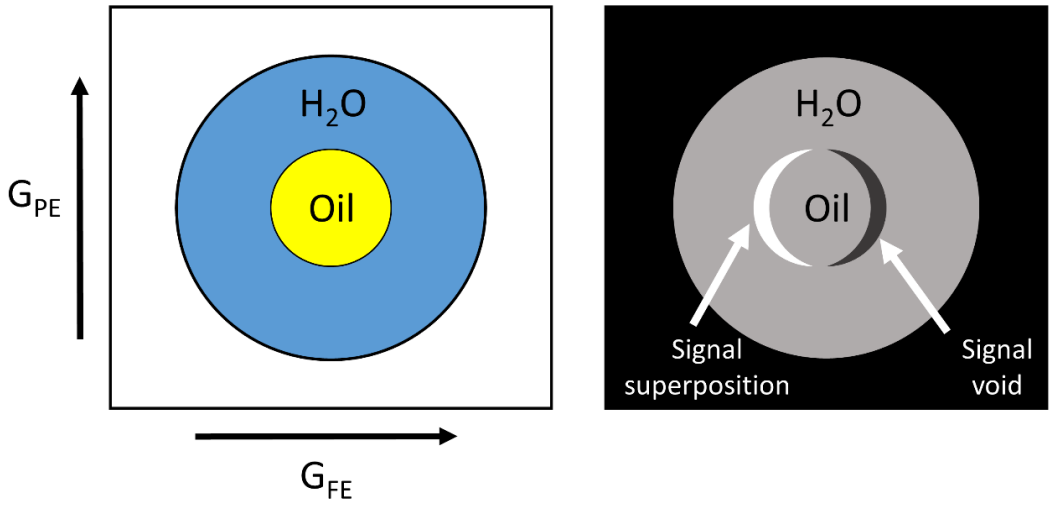

Figure 2.15. Chemical shift artifact exhibiting characteristic bright and dark bands where a side peak was misregistered as a spatial offset.

There are several methods that can mitigate chemical shift artifacts. The first is to switch the PE and FE dimensions, as the artifact does not manifest in the PE direction, although this will only switch the axis along which the artifact occurs. As peak separation depends directly on field strength, use of a lower field strength will reduce the magnitude of the artifact [23]. A final approach is to increase the amount of bandwidth per pixel. When we apply a frequency encode gradient, we specify its strength, which in turn determines the frequency difference exhibited by spins at different positions in conjunction with the dwell time. For a fixed dwell time, a strong gradient might correspond to a frequency difference (called sweep width) of 5000,000 Hz across the sample, while a weak gradient might correspond to a difference of 5,000 Hz. Discrete ranges of frequencies are assigned to different pixels according to $\Delta\omega = FOV_f/N_f$, where FOV_f is the width of the field-of-view (FOV) in the readout direction and N_f is the number of points digitized. A higher overall receiver bandwidth increases the spectrum of

frequencies that are binned within a single pixel for a fixed G_{FE}, which reduces the overall spatial shift associated with the frequency mismatch that results from chemical shift. There is a drawback to this approach however; as noise occurs throughout the frequency spectrum, raising the total receiver bandwidth causes an increase in noise in the signal, leading to marginal SNR losses. Notably, chemical shift can also occur in the slice-select dimension, leading to image blurriness. The solution in this case is the same: use of a strong slice-select gradient will reduce the magnitude of the chemical shift artifact.

2.19 Magnetic Susceptibility

The susceptibility artifact has a similar appearance to the chemical shift artifact (adjacent bright and dark bands in the readout direction), but differs in its mechanistic origin. Tied to the phenomenon of paramagnetic compounds inducing T_1 relaxation is their macroscopic property of distorting the overall $\boldsymbol{B_0}$ field. This, in turn, modulates the Larmor frequencies of nearby nuclei. In MRI, this phenomenon manifests itself as bright and dark bands or distortions in the readout direction that appear at surface junctions, such as along glass walls, metal objects, and liquid-solid or liquid-air interfaces (air contains paramagnetic O_2). Mitigating magnetic susceptibility artifacts follows the same protocol as chemical shift artifacts [3].

2.20 DC Offset

The direct current offset is visualized as a bright spot at the exact center of the image, and occurs when there is some constant voltage present in the electronic circuits even in the absence of signal. Constant voltage in the ***k***-space domain adds to the usual FID or echo, and when Fourier transforms, manifests as a delta function at the origin (the intuitive explanation for this Fourier pair is that only a single zero-frequency term is required to represent a constant value) [14]. This artifact is not hugely problematic as the offending central point can simply be removed.

2.21 Zebra Stripes (Noise Spike)

The aptly-named zebra stripes artifact is visualized as a wave of increased and decreased signal across the image [24]. It occurs when a glitch occurs during acquisition of one or more points in ***k***-space. The magnitude of a particular point in ***k***-space denotes how much of that spatial frequency is required to reproduce the spin density, and therefore loss of that information leads to the subtraction of that frequency from the image. Similarly, a random spike in the signal results in a high-amplitude wave being superimposed over the image. Described in terms of Fourier pairs, a spike in noise at a coordinate in ***k***-space is approximated as a delta function, which FTs to a complex sine/cosine wave [14]. The zebra stripe artifact can be compensated for either by reprocessing the data (filling in the spurious point with an interpolated value) or by re-running acquisition. With improvements to experimental hardware, noise spikes have become rare.

2.22 Gibbs' Ringing (Truncation Artifact)

Gibbs' ringing is observed as visible intensity overshoots and undershoot oscillations at high-contrast interfaces [24]. It originates as an inevitable consequence of using FTs to reconstruct sharp details. When we acquire data in ***k***-space, only a finite number of frequencies can be used to generate our image; the Fourier series is inherently truncated according to the number of discrete spatial frequency points we collect (***k***-space window). As a result, extremely high frequencies are omitted when performing the FT, and their absence is especially pronounced around sharp features. As this artifact is inherent to the FT itself, Gibbs' ringing appears in both the PE and FE dimensions. It can be reduced dramatically by increasing the matrix size with a fixed FOV, as an increase in resolution corresponds to a larger ***k***-space window [24]. This approach comes at the cost of increased acquisition time.

2.23 Data Clipping (ADC Overflow)

Commonly observed by inexperienced operators, data clipping manifests itself as distortions in the overall contrast and bulk features of the image, while leaving fine details unperturbed [24]. The artifact occurs when the signal exceeds the selected receiver gain of the experiment, *i.e.* the maximum amplitude to which the receiver exhibits sensitivity at its current setting. Because the echo signal is always highest at the center of **k**-space where there are no gradients dephasing the spins, it is these points that are clipped, resulting in a loss of low frequency information in the transformed image. Modern spectrometers typically output a warning automatically when this occurs, but

these cautions may be missed by the experimenter. The artifact is circumvented by re-running acquisition using a lower receiver gain setting.

2.24 Spatial Aliasing

Spatial aliasing, or wraparound artifact, occurs when part of the sample extends past the edge of the FOV specifically in the phase-encode dimension. In the first phase-encode step, for example, phase shifts between -180° and 180º encompass the field of view; that is, the gradient strength is selected such that spins at the bottom of the FOV obtain a phase of -180º while spins at the top of the FOV obtain a phase of 180º. Any part of the sample that extends past the edge of the FOV will have a phase offset that is higher in magnitude (for instance, an ensemble of spins may experience a phase shift of 270º). Because the phase encoding process requires all meaningful frequencies to be defined over a 360º window, the 270º phase shift is indistinguishable from a phase shift of -90º, and these spins will be interpreted as such and assigned the spatial position corresponding to the -90º phase shift [24]. This error affects each phase-encoding step linearly and propagates throughout the data acquisition process, with then end result manifesting as the folding over of features outside the FOV onto the opposite end of the FOV. This phenomenon technically also occurs in the readout direction, but is automatically corrected for in a process known as oversampling, a filtering effect related to the digitized bandwidth [3]. The only way to eliminate wraparound is to ensure that the FOV in the PE dimension is larger than the sample width.

2.25 Ghosting

A consequence of the time delay between phase encode steps, ghosting is visualized as either general blurriness in the case of non-periodic motion or discrete visual replications ('ghosts') of an image feature appearing at regular spatial intervals along the phase-encode axis in the case of periodic or one-time motion [24]. For the periodic or one-time case, the phenomenon can be illustrated simply: a single point of mass (delta function) moves from one location along the PE axis to another halfway through the acquisition of an image (*i.e.* after completion of half the phase-encode steps). The bottom half ***k***-space representation will be a sine/cosine wave with some frequency, while the top half will be a sine/cosine wave with some other frequency. When summed together, the PE dimension of ***k***-space contains two truncated oscillations (*i.e.* oscillations multiplied by hat functions). When transformed into the image space, the FT of the echo (the image), is convoluted with the FT of the hat function (the sinc), resulting in a sinc function where each lobe maximum contains a representation of the image [24]. In the case of nonperiodic motion, each individual motion instigates a truncation of the echo, and when summed together, the sincs interfere destructively leading to incoherent blurring of the signal. Ghosting can be combated in a number of ways, such as swapping the PE and FE axes relative to the direction of sample motion so that ghosting does not obscure the region of interest, preventing unwanted motion by securing the sample, or by synchronizing the repetition time with the periodic motion ('gating') [24].

2.26 NMR and Molecular Motion

Encoding spins for position opens the door not just for imaging, but also for the examination of molecular motion. Consider, for instance, a pair of position-encoding gradients featuring equal and opposite effective areas that are separated by some time, Δ [4]. For spins that have not experienced motion in this window, the position-dependent phase shift imparted by the first gradient will be exactly cancelled by the second, leading to perfect reconvergence of the spins back to their initial phase at the time of the echo. Spins that have experienced a net displacement along the gradient axis over Δ, however, will undergo a different phase shift during the second gradient application relative to the first. At the time of acquisition, these spins will exhibit a net phase shift which can be directly related to the displacement assuming *a priori* knowledge of the gradient parameters. The influence of this displacement encoding on the final signal depends on the nature of the motion. If all spins experience the same motion, summation over the ensemble will result in a macroscopically observable phase shift in the final signal. If the spins experience random displacements, for instance due to Brownian motion or dispersion across a non-uniform flow profile, the ensemble average will contain a distribution of phase shifts which cancel with each other, resulting in a decrease in signal amplitude [4]. Generally, the above types of motion can be categorized as 'coherent' or 'incoherent', and their contributions to the NMR signal considered separately. We will first turn our attention to coherent motion, *i.e*. bulk convection.

2.27 Displacement Space and the Normalized Echo Amplitude

The general effect of coherent motion is to introduce a coherent phase shift into the final NMR signal. Comparison of the signal under the influence of a displacement-encoding gradients to the signal in the absence of displacement encoding is represented mathematically by:

$$E(t) = \frac{M_+(z_0,t)}{M_+(z_0,0)} = exp(i\varphi(t)) \qquad \text{(Eq 2.35)}$$

where *E(t)* is the normalized echo signal, which depends on the accumulated phase shift at time *t* [4]. The accumulated phase is equal to the product of the gyromagnetic ratio and the dot product of the total gradient experienced and the spin displacement [4]. For coherent motion, spin displacement is the velocity multiplied by the time of motion, *Δ*. Thus we have:

$$E(\boldsymbol{g}) = \frac{S(\boldsymbol{g})}{S(0)} = exp(i\gamma\delta\boldsymbol{g}\cdot\boldsymbol{v}\Delta) \qquad \text{(Eq 2.36)}$$

where δ is the gradient duration and $\boldsymbol{g}$ the gradient strength [4]. Analogous to the spatial frequency variable $\boldsymbol{k}$, the displacement frequency variable $\boldsymbol{q}$ is given by:

$$\boldsymbol{q} = \frac{\gamma\delta\boldsymbol{g}}{2\pi} \qquad \text{(Eq 2.37)}$$

From the formulation of $\boldsymbol{q}$ above we note that $\boldsymbol{q}$ is functionally equivalent to $\boldsymbol{k}$, but with the distinction that $\boldsymbol{q}$ is used to denote displacement frequency rather than spatial frequency [5]. The information afforded by a displacement experiment is fundamentally different than its spatial counterpart, and it is thus reasonable to conceptually separate the two. Like $\boldsymbol{k}$-space, every point in $\boldsymbol{q}$-space contributes toward the overall measurable of

the NMR displacement experiment, which is not an image, but rather a histogram of displacement probabilities, called a propagator [4; 25].

2.28 Propagators and the PGSE experiment

As mentioned above, application of a pair of gradients with equal and opposite effective areas separated by time interval Δ results in each spin's phase encoding for its displacement over the time window. When summing over a spin ensemble, Equation 2.37 will reflect a range of phase shifts with each constituent phase shift weighted by its probability of occurring, *i.e.* the probability of a spin moving from $\boldsymbol{r}$ to $\boldsymbol{r'}$ over Δ. Introducing the dynamic displacement variable $\boldsymbol{R} = \boldsymbol{r'} - \boldsymbol{r}$, we note that the propagator of the spin ensemble characterized by initial distribution $\rho(\boldsymbol{r})$ is the probability density that spins have traveled a distance $\boldsymbol{R}$, accounting for all potential starting positions and paths [4]:

$$\boldsymbol{P}(\boldsymbol{R}, \Delta) = \int \rho(\boldsymbol{r})\, P(\boldsymbol{r}|\boldsymbol{r} + \boldsymbol{R}, \Delta) d\boldsymbol{r} \qquad \text{(Eq 2.38)}$$

The echo signal is then the integral of the product of the propagator and the resulting phase that is imparted to each displacement by the gradient pair (characterized by $\boldsymbol{q}$):

$$E(q, \Delta) = \int P(\boldsymbol{R}, \Delta)\, exp(iq \cdot \boldsymbol{R}) d\boldsymbol{R} \qquad \text{(Eq 2.39)}$$

We can see by comparison to Equation 2.34 that the echo signal has a direct Fourier relationship to the propagator. As a result, Fourier transformation of the signal along the gradient axis yields the probability distribution of spin displacement over the time interval Δ [4].

The propagator will necessarily contain information about coherent flow (whether present or not) and incoherent motion (*e.g.* Brownian diffusion), which is always present due to the random thermal motion of all nuclei. Incoherent motion during the gradient pair experiment, hereafter called the Pulse Gradient Spin Echo (PGSE), results in a distribution of phase shifts as shown in Figure 2.16, ultimately manifesting as loss of phase coherence and thus signal decay.

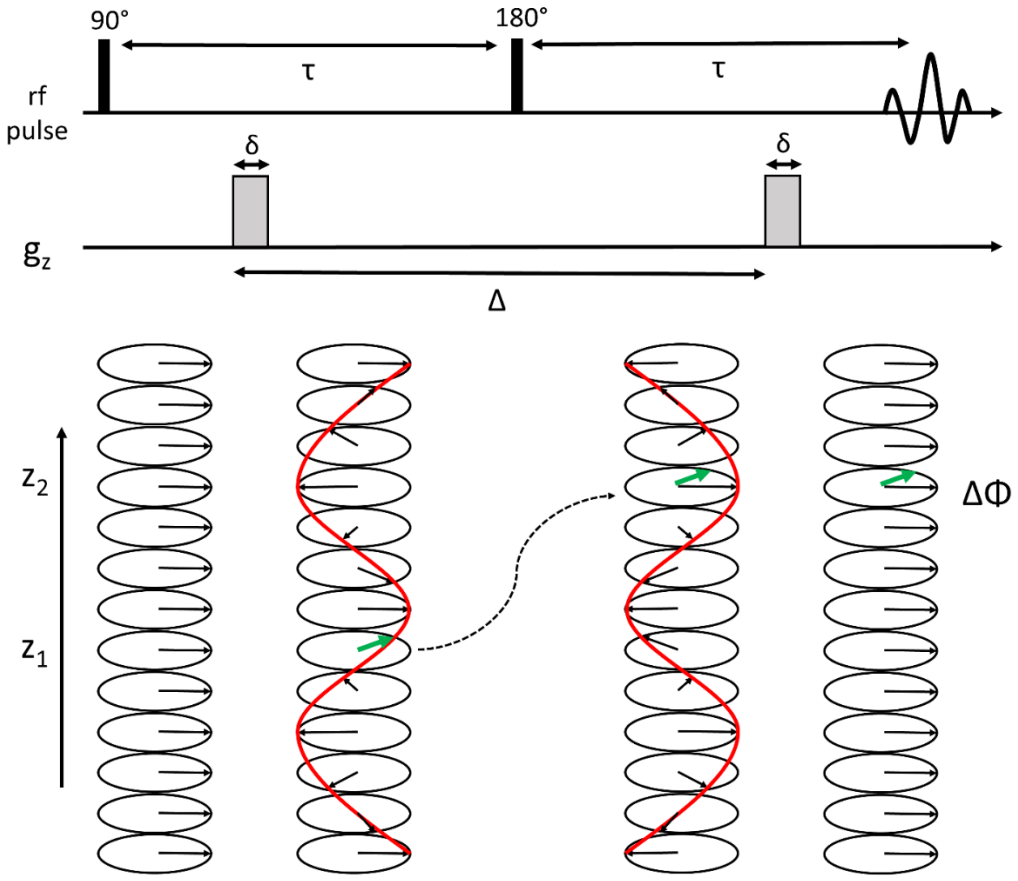

Figure 2.16. The PGSE pulse sequence along with phase evolution of spins due to the gradient pulses. Spins that have undergone no motion in the period between the two gradients, Δ, will recover their initial phase, while spins that have undergone motion during this window will exhibit a residual phase shift [4].

Figure 2.16 presents the gradient pulses as having very short duration. Why is this the case? If we wish to infer displacement from the discrete phase shifts imparted by each gradient application, any motion occurring *during* the presence of the gradients will confound results as each gradient in and of itself will introduce an unknown range of phase shifts, significantly increasing the complexity of the encoding process. This unwanted contribution can be mitigated by minimizing the gradient duration, and at sufficiently short δ it can be neglected altogether. This criteria is conventionally expressed as $\delta << \Delta$. When this requirement is satisfied, and for spins undergoing unrestricted diffusion, the normalized echo signal is given analytically by:

$$E(\boldsymbol{g}) = \frac{S(\boldsymbol{g})}{S(0)} = exp\left(-\gamma^2 g^2 \delta^2 D\left(\Delta - {}^{\delta}/_{3}\right)\right) \qquad \text{(Eq 2.40)}$$

The above result is the famed Stejskal-Tanner relationship, named after its discoverers [26]. Because each of the variables above either known physical constants or pre-selected pulse sequence parameters, the apparent self-diffusion coefficient *D* can be easily deduced by plotting the natural log of the normalized echo amplitude against the quantity $\gamma^2 g^2 \delta^2 (\Delta - {}^{\delta}/_{3})$.

We have now separately addressed the contributions of coherent and incoherent motion on the overall NMR signal with Equations 2.36 and 2.40, and note that the two can be combined to yield an expression for the normalized echo signal under general translational motion [4]

$$E(\mathbf{g}) = \exp\left(i\gamma\delta\mathbf{g}\cdot\mathbf{v}\Delta - \gamma^2 g^2 \delta^2 D\left(\Delta - {}^{\delta}/_{3}\right)\right) \qquad \text{(Eq 2.41)}$$

The above equation conveys the fundamental behavior of the NMR signal for the PGSE experiment, with coherent motion causing oscillations in phase and incoherent motion causing signal decay, both as a function of the applied gradient strength $\boldsymbol{g}$.

References

[1] Purcell, E.M., Torrey, H.C., and Pound, R.V. (1946). Resonance absorption by nuclear magnetic moments in a solid. Physical review *69*, 37.

[2] Bloch, F. (1946). Nuclear induction. Physical review *70*, 460.

[3] Callaghan, P.T. (1993). Principles of nuclear magnetic resonance microscopy (Oxford University Press on Demand).

[4] Callaghan, P.T. (2011). Translational dynamics and magnetic resonance: principles of pulsed gradient spin echo NMR (Oxford University Press).

[5] Blumich, B. (2000). NMR imaging of materials, Vol 57 (OUP Oxford).

[6] Slichter, C.P. (2013). Principles of magnetic resonance, Vol 1 (Springer Science & Business Media).

[7] Fukushima, E. (2018). Experimental pulse NMR: a nuts and bolts approach (CRC Press).

[8] Delpuech, J.J., Hamza, M.A., Serratrice, G., and Stebe, M.J. (1979). Fluorocarbons as oxygen carriers. 1. An NMR study of oxygen solutions in hexafluorobenzene. J Chem Phys *70*, 2680-2687.

[9] Halliwell, B., and Gutteridge, J. (1984). Oxygen toxicity, oxygen radicals, transition metals and disease. Biochem J *219*, 1.

[10] Navari, R.M., Rosenblum, W.I., Kontos, H.A., and Patterson, J.L. (1977). Mass transfer properties of gases in fluorocarbons. Res Exp Med (Berl) *170*, 169-180.

[11] Mason, R.P. (1994). Noninvasive physiology - 19F NMR of perfluorocarbons. Artificial Cells Blood Substitutes and Immobilization Biotechnology *22*, 1141-1153.

[12] Yntema, G. (1955). Superconducting winding for electromagnet. Paper presented at: Physical Review (American Physical Society One, College PK, MD 20740 USA).

[13] Torrey, H.C. (1956). Bloch equations with diffusion terms. Physical review *104*, 563.

[14] Brigham, E.O. (1988). The fast Fourier transform and its applications, Vol 448 (prentice Hall Englewood Cliffs, NJ).

[15] Carr, H.Y., and Purcell, E.M. (1954). Effects of diffusion on free precession in Nuclear Magnetic Resonance experiments. Physical Review *94*, 630-638.

[16] Hahn, E.L. (1950). Spin echoes. Physical Review *80*, 580-594.

[17] Meiboom, S., and Gill, D. (1958). Modified spin-echo method for measuring nuclear relaxation times. Rev Sci Instrum *29*, 688-691.

[18] Keeler, J. (2011). Understanding NMR spectroscopy (John Wiley & Sons).

[19] Lauterbur, P.C. (1973). Image formation by induced local interactions: examples employing nuclear magnetic resonance. Nature *242*, 190-191.

[20] Mansfield, P., and Grannell, P.K. (1973). NMR 'diffraction' in solids? Journal of Physics C: solid state physics *6*, L422-L426.

[21] Stehling, M.K., Turner, R., and Mansfield, P. (1991). Echo-planar imaging: magnetic resonance imaging in a fraction of a second. Science *254*, 43-50.

[22] Glover, G.H., Pauly, J.M., and Bradshaw, K.M. (1992). Boron-11 imaging with a three-dimensional reconstruction method. J Magn Reson Imaging *2*, 47-52.

[23] Brateman, L. (1986). Chemical shift imaging: a review. AJR Am J Roentgenol *146*, 971-980.

[24] Bellon, E.M., Haacke, E.M., Coleman, P.E., Sacco, D.C., Steiger, D.A., and Gangarosa, R.E. (1986). MR artifacts: a review. American Journal of Roentgenology *147*, 1271-1281.

[25] Kärger, J., and Heink, W. (1983). The propagator representation of molecular transport in microporous crystallites. Journal of Magnetic Resonance (1969) *51*, 1-7.

[26] Stejskal, E.O., and Tanner, J.E. (1965). Spin diffusion measurements: spin echoes in the presence of a time-dependent field gradient. The journal of chemical physics *42*, 288-292.

CHAPTER THREE: ADVANCED NMR TOPICS

In the early days of Nuclear Magnetic Resonance (NMR), measurements were limited by unavoidable inhomogeneities in the static magnetic field. Slight variation in $\boldsymbol{B_o}$ strength across the sample-containing region induced a spread in the Larmor frequencies of spins occupying different regions, causing a dramatic broadening of spectral lines. Information regarding relaxation due to molecular environment and separation and location of peaks was rendered inaccessible so long as hardware-dependent broadening was overlaid on top. However, as hardware capabilities improved and novel techniques were developed to eschew these limitations (*e.g*. the spin echo), it gradually became evident that the sensitivity of spin precession to slight inhomogeneities in field strength was also a fundamental strength of the NMR technique. Magnetic fields could be intentionally manipulated so as to impart a position-specific tag on the molecules of interest, and the resulting experiment would then generate insight into the mechanics of molecular motion. For instance, imposing a constant, known readout gradient during acquisition of an echo would lead to an echo wherein spectral frequency directly corresponds to position (*i.e.* a 1D image projection). Similarly, lobes of gradients with equal and opposite effective areas would encode information on the displacement experienced during the intra-gradient period into the residual phase shift of the individual spins, yielding invaluable information on coherent and incoherent motion. NMR's enduring utility as a probe of transport phenomena can be ascribed to the limitless potential afforded by the exploitation of magnetic field inhomogeneity as a tag of

molecular motion, and it is this capability that will be discussed in the following section. We will once again heavily rely on foundational texts by Paul Callaghan [1; 2].

3.1 Time-Varying Fields and Gradient Moments

Spatial drifting of spins during the NMR experiment lead to accumulated phase shifts which, when averaged over the sample or imaging voxel, lead to signal loss as out-of-phase vector components cancel. When a displacement measurement is desired, this phenomenon is manipulated by imposing quick 'pulses' of field inhomogeneity amidst a background of homogeneity. This is accomplished by activating gradients for short bursts. An initial gradient is employed for a brief duration, δ, and with strength $\boldsymbol{g}$, imparting a position-depending phase shift. After a mixing period, Δ, the same gradient is applied but with opposite direction (reversal in direction is either achieved by a 180º rf pulse during Δ or by inverting the direction of current through the gradient coils – the former option is generally preferred due to the added benefit of correcting signal loss due to static $\boldsymbol{B_o}$ inhomogeneities). At the end of the experiment, the integral of the gradient experienced by each spin is zero, and an echo is obtained at time 2τ, where τ is the time between excitation and the spin echo. This is in fact the requirement to achieve an echo, otherwise called the echo condition [2]:

$$\int_0^t \boldsymbol{g}^*(t')dt' = 0 \qquad \text{(Eq 3.1)}$$

In words, the zeroth moment of the gradient must be zero. Here the * denotes the effective direction of the gradient, and includes the impact of any 180° rf pulses.

In the absence of translational motion, the phase shifts induced by each gradient are perfectly cancelled and the echo amplitude is maximized. When a spin experiences a net displacement between the applications of the gradient pulses, the phase shifts do not entirely cancel and the spin acquires a residual phase shift. When motion is incoherent, such as in the case of Brownian motion, the residual phase shifts of different spins are completely uncorrelated due to the rapid timescale of molecular collisions compared with the NMR experiment timescale, leading to signal decay. When motion is coherent, such as in the case of constant velocity (plug flow), each spin has an identical displacement and therefore an identical residual phase shift, leading to no reduction in echo amplitude but instead a phase shift in the overall NMR signal [2].

In real systems, the displacement of spins may result from both diffusion and velocity, as well as from higher order terms such as acceleration and jerk. To formally disentangle the contributions of each of these terms, we can decompose the spin displacement, $\boldsymbol{r}$, into a function of position and its derivatives about the point $t = 0$, mathematically known as a Maclaurin series.

Using effective gradient notation, the residual phase shift, Φ, for spin j at time t is given by [2]:

$$\varphi_j(t) = \gamma \int_0^t \boldsymbol{g}^*(t') \cdot \boldsymbol{r}_j(t') dt' \qquad \text{(Eq 3.2)}$$

where $\boldsymbol{r_j(t)}$ represents the spin's current position. The dot product ensures that only displacement along the applied gradient axis results in phase accumulation. The Maclaurin series for the ensemble-average spin position is expressed as:

$$\overline{r(t')} = \bar{r}_0 + \frac{d\,\overline{r(t')}}{dt'}\bigg|_0 t' + \frac{1}{2!}\frac{d^2\overline{r(t')}}{dt'^2}\bigg|_0 t'^2 + \ldots \frac{1}{n!}\frac{d^n\overline{r(t')}}{dt'^n}\bigg|_0 t'^n \qquad \text{(Eq 3.3)}$$

As velocity is simply the time derivative of position, the second term corresponds to the contribution of velocity, or, equivalently stated, the first moment. Similarly, the second term represents acceleration, the third represents jerk, and all higher terms represent successive moments of the position series expansion [2]:

$$\overline{r(t')} = \bar{r}_0 + \bar{v}_0 t' + \frac{1}{2}\bar{a}_0 t'^2 + H.O.T. \qquad \text{(Eq 3.4)}$$

where H.O.T. denotes higher-order terms, which are typically neglected. With the contributions of velocity, acceleration, and higher order terms explicitly identified, we substitute Equation 3.4 and Equation 3.2 into Equation 2.36 which describes the normalized echo amplitude under flow conditions. The generalized result is [2]

$$E(t) = exp\left(i\gamma \boldsymbol{v} \cdot \int_0^t t' \boldsymbol{g}^*(t')dt' + i\gamma \boldsymbol{a} \cdot \int_0^t t'^2 \boldsymbol{g}^*(t')dt'\right) \qquad \text{(Eq 3.5)}$$

The echo condition ensures that the residual signal phase shift is insensitive to position; after application of the second gradient pulse, the integral of the gradient experienced (i.e. the zeroth moment) is zero:

$$m_0 = \int_0^t \boldsymbol{g}^*(t')dt' = 0 \qquad \text{(Eq 3.6)}$$

Each successive term, however, will impact the residual signal phase due to the additional *t* polynomial dependence of the higher moments. Specializing the general normalized echo amplitude formulation given by Equation 3.5 to the PGSE sequence, we obtain the following results for the first (velocity sensitive) moment:

$$m_1 = \int_0^t \boldsymbol{g}^*(t')t'dt' = g\delta\Delta \qquad \text{(Eq 3.7)}$$

Although the simple PGSE experiment exhibits dependence on velocity, this is not a fixed attribute of a translation-encoding sequence. In fact, the above equations indicate that the strength of the signal's dependence on the different moments can be

manipulated by judicious choice of gradient strength and timing. For instance, applying 3 gradient pairs, with the middle gradient twice the area of the other two as well as opposite sign, results in the first moment dropping to zero and thus eliminating all sensitivity to velocity. The concept of gradient moments can thus be applied to design pulse sequences which selectively measure position, velocity, acceleration, higher order terms, or some combination thereof [2].

3.2 Diffusion and Flow: Bloch-Torrey Derivation

Diffusion and flow analysis commonly uses the PGSE sequence or one of its variants due to the displacement encoding imparted by the gradient pair. For this reason, we must devote special attention to the sequence and the mathematical and molecular origins whereby the PGSE signal arises. In the previous chapter, we stated that the Stejskal-Tanner result of Equation 2.40, describing the behavior of the NMR signal as a function of the PGSE pulse sequence parameters, could be derived by evaluating the average propagator and relating its form to the NMR signal. The same result can be obtained via a conservation equation, with magnetization considered as a conserved quantity, as famously detailed in a landmark paper by [3]. In addition to validating the foundational Stejskal-Tanner result, the treatment of magnetization as a conserved quantity can also more generally yield novel insights into the behavior of the NMR signal during complex experiments and is thus a useful bridge between empirical results and NMR theory. For this reason, the Bloch derivation will be summarized in this section.

In Torrey's treatment, magnetization is considered to be a conserved quantity subject to Fick's Law, with relaxation incorporated as a sink term [3]. The 'transport of magnetization' equation is given by:

$$\frac{\partial M_x}{\partial t} = \gamma M_y\left(B_0 - {}^{\omega}/_{\gamma}\right) - \frac{M_x}{T_2} + \nabla \cdot \boldsymbol{D} \cdot \nabla M_x - (\boldsymbol{v} \cdot \nabla) M_x \qquad \text{(Eq 3.8)}$$

Assuming isotropic diffusion, moving to the rotating reference frame with a zero frequency offset, and introducing the transverse magnetization $M_+ = M_x + iM_y$ to combine M_x and M_y, we obtain [3]:

$$\frac{\partial M_+}{\partial t} = -i\gamma \boldsymbol{r} \cdot \boldsymbol{g}^*(t) M_+ - \frac{M_+}{T_2} + D\nabla^2 M_+ - (\boldsymbol{v} \cdot \nabla) M_+ \qquad \text{(Eq 3.9)}$$

In the absence of diffusion and inhomogeneity, the solution takes the form of a signal that decays exponentially due to T_2 relaxation and oscillates in phase due to rotation about $\boldsymbol{B_o}$ in the presence of a gradient. The initial condition implies that the coefficient of this solution which we call A, is a constant (assumed to be the initial magnetization $\boldsymbol{M_o}$). However, accounting for the diffusion term which depends on x only, A must now be permitted to be a function of t:

$$M_+(r,t) = A(t) exp\left(-i\gamma \boldsymbol{r} \cdot \int_0^t \boldsymbol{g}^*(t')dt'\right) exp\left({}^{-t}/_{T_2}\right) \qquad \text{(Eq 3.10)}$$

where $A(t)$ is referred to now as the modulation factor. Substitution of the above solution into the diffusion term of the original PDE and solving via separation of variables yields [3]:

$$A(t) = exp\left(-D\gamma^2 \int_0^t \left(\int_0^{t'} \boldsymbol{g}^*(t'')dt''\right)^2 dt'\right) exp\left(i\gamma \boldsymbol{v} \cdot \int_0^t \int_0^{t'} \boldsymbol{g}^*(t'')dt''dt'\right)$$

(Eq 3.11)

Specializing the general above result to the PGSE parameters, we successfully recover Equation 2.40. A useful insight of this treatment is that, under the echo condition $\int_0^t \boldsymbol{g}^*(t')dt' = 0$, *A(t)* simply becomes the normalized echo attenuation *E(t).* However, at all other times, an additional time-dependent attenuation factor remains which complicates signal interpretation, and thus the Stejskal-Tanner result is only valid for signal collected at the echo center. We may also observe that the inner integral of both terms of Equation 3.11 represents the zeroth moment of the magnetization, while the double integral over the second (but not the first) term produces our first moment, Equation 3.7. This portion of the phase modulation thus arises from coherent flow. The first term, a negative, real exponential, must inherently represent signal attenuation. This arises mathematically due to the squaring of the inner integral, which in effect measures phase evolution variance. It is this term which is quantified by the Stejskal-Tanner relationship, with the physical interpretation being that incoherent motion (random diffusion or dispersion) leads to signal attenuation [2].

3.3 Stejskal-Tanner, Diffusive Attenuation, and Restricted Diffusion

With the Stejskal-Tanner result [4] now validated by consideration of both magnetization conservation and the average propagator, we now turn our attention to the utility of the Stejskal-Tanner relationship as an experimental tool. The pulse sequence schematic for the PGSE experiment is shown in Figure 2.16. After excitation, spin position is encoded by the first gradient pulse of duration δ. The refocusing pulse at time τ has the effect of reversing the direction of precession such that the second gradient

pulse imparts an equal and opposite phase shift for all spins exhibiting a net displacement of zero over the evolution period Δ, and as a result an echo occurs at time 2τ. Spin displacement over Δ, of course, results in either attenuation or phase modulation of the signal depending on the nature of the transport.

Equation 2.40 makes it clear that there is a direct relationship between the height of the echo as a function of gradient strength and the spin diffusivity. As all variables in the equation are either known constants or pre-selected pulse sequence parameters, we can easily extract an apparent diffusion coefficient for the sample by taking the natural logarithm of the normalized echo amplitude *E(t)* and plotting it against the quantity $\gamma^2 g^2 \delta^2 (\Delta - {}^{\delta}/_{3})$, with the slope corresponding to $-D$ (Figure 1) [4]. However, there is significant nuance in the interpretation of diffusion as measured by the Stejskal-Tanner relationship or by other means.

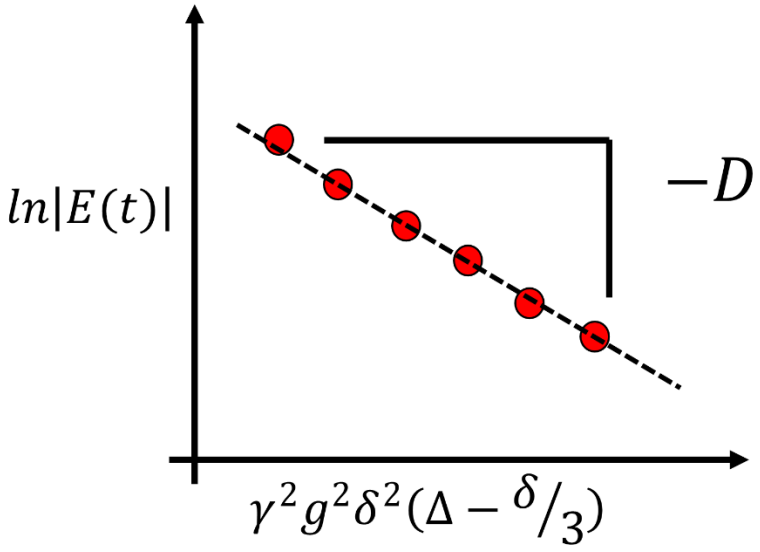

Figure 3.1. Fitting the natural log of the normalized echo amplitude to the Stejskal-Tanner relationship returns the apparent molecular diffusion coefficient.

For instance, suppose an ensemble of spins is constrained within an enclosed pore. Over short timescales we may expect a representative spin to freely diffusive through the bulk liquid phase. However, at longer timescales the same spin may collide with a wall such that increasing time will not result in a corresponding increase in mean squared displacement. If a PGSE sequence were run with a Δ time either near or beyond the timescale for spins to sample the wall, a Stejskal-Tanner fit would produce an apparent diffusion coefficient that did not contain information about the sample diffusivity, but rather the pore size and structure. In restricted diffusion cases such as this, and more broadly in conditions of generalized translational motion, there will be no analytical expression for the echo signal which is valid for the entire parameter space. Instead, the experimental conditions must be carefully considered to ensure that an experiment yields information that can be correctly interpreted. While this is often a

challenging endeavor with real samples, it is also a hallmark advantage of NMR: by fine-tuning the experiment to the specific characteristics and scales of the sample, a wide range of properties can be elucidated. In the example above, PGSE at short Δ could be used to measure bulk fluid diffusion, while PGSE at intermediate or long Δ could be used to measure pore size or pore connectivity [2].

The utility of NMR in the measurement of diffusion dynamics is vast, comprising of a variety of different pulse sequences designed to quantify various aspects of molecular motion such as pore length scale, tortuosity, pore site exchange rates, and velocity correlation. However, we will restrict our focus hereafter to velocity imaging, which is a key technique in the work presented in this dissertation.

3.4 Velocity Imaging

As discussed in the previous chapter, for the PGSE experiment the total phase shift of the acquired signal $E(\boldsymbol{q},\Delta)$ contains information about the average Eulerian velocity $\boldsymbol{v(r)}$ as well as diffusive attenuation. Conveniently, the PGSE pulse sequence is modular and can be combined with imaging sequences, resulting in an experiment that is collected in both $\boldsymbol{k}$- and $\boldsymbol{q}$-space [5]. When processed, the data yields an image where each voxel represents not the local spin density, but rather the average local velocity along the displacement-encoding axis (Figure 3.2).

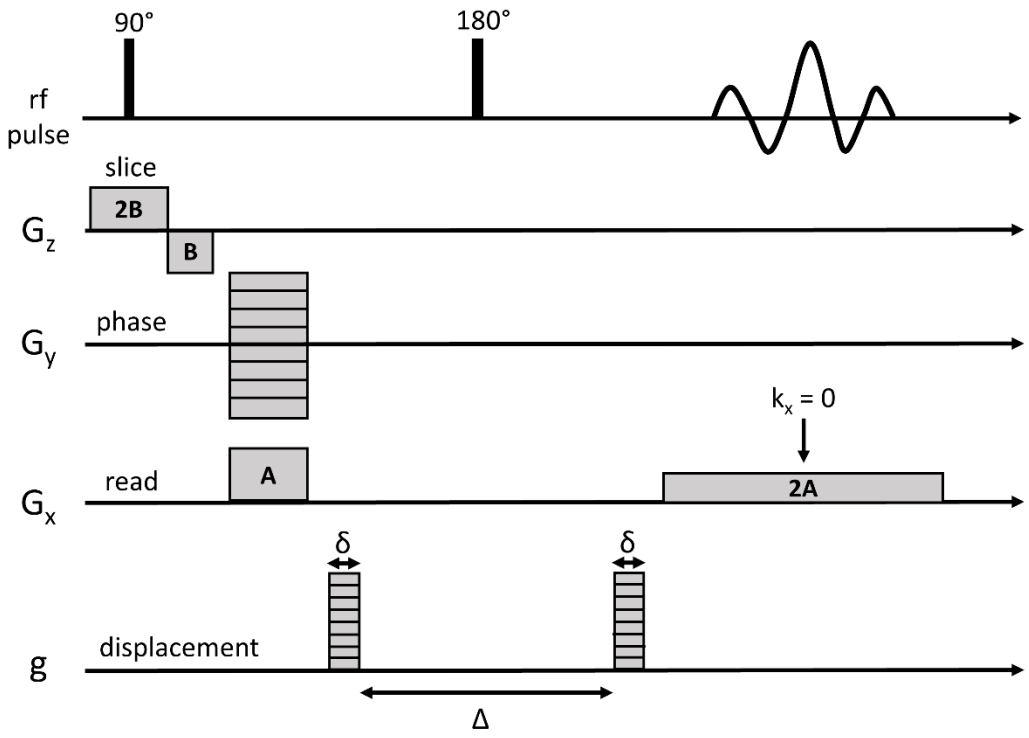

Figure 3.2. Velocity imaging pulse sequence incorporating both k- and q-space encoding. Sampling of the echo as a function of k-space provides an image which is further phase-encoded in q-space due to the PGSE gradients. The result is an image where each pixel contains the propagator for the associated sample region.

Spatial encoding is carried out via application of slice select, phase encode, and frequency encode gradients as shown in Figure 3.2. However, an additional pair of gradients (the displacement-encoding gradients of the PGSE experiment) are also included, separated by a refocusing pulse. The displacement axis may be chosen to be along any of the three dimensions, and the strength of the ***q***-space gradients are increased from zero to maximum value g_m in n_D steps with each acquisition of a full image. The data is visualized as a 3-dimensional matrix with $\boldsymbol{k}_{read}$ as the first dimension, $\boldsymbol{k}_{PE}$ as the second, and displacement ***q*** as the third. Fourier transformation along the spatial

frequency axes results in a stack of $\boldsymbol{q}$-encoded images, with the complex signal of pixel $\boldsymbol{r}$ of the nth $\boldsymbol{q}$ slice described by [2; 5]:

$$E(\boldsymbol{q}, \Delta, \boldsymbol{r}) = \rho(\boldsymbol{r}) exp[i(\gamma\delta v\Delta)(g_m/n_D)n] exp\,[-\gamma^2\delta^2(g_m/n_D)^2 Dn^2\Delta] \qquad \text{(Eq 3.12)}$$

Performing an N-point digital FT along the third dimension yields an image where each pixel contains the local average propagator with N displacement spectrum points between $\pm Z_{max}$, where $2Z_{max} = (2\pi n_D)/(\gamma\delta g_m)$. Given the product shown in Equation 3.12, the propagator takes the form of the convolution [2]:

$$\bar{P}(k/N, \Delta) = (\pi n_D^2/\gamma^2\delta^2 g_m^2 D\Delta)^{1/2} \exp[-\pi^2 k^2 n_D^2/\gamma^2\delta^2 g_m^2 N^2 D\Delta]$$
$$* \delta(k/N - \gamma\delta v\Delta\, g_m/2\pi n_D) \qquad \text{(Eq 3.13)}$$

where k is the digital value along the displacement axis, ranging from $-N/2$ to $N/2$-1. The peak center, whose shift away from $Z = 0$ gives the mean velocity of the corresponding pixel, occurs at the value

$$k_v = N\gamma\delta v\Delta\, g_m/2\pi n_D \qquad \text{(Eq 3.14)}$$

and so the mean molecular velocity is given by

$$v = 2\pi n_D k_v/N\gamma\delta\Delta g_m \qquad \text{(Eq 3.15)}$$

Diffusive and dispersive effects take the form of a general spreading of the propagator from its center, and can be quantified by observing the propagator's full-width-half-maximum (FWHM). Specifically, the value of the mean molecular self-diffusion coefficient takes the form [2]

$$D = (n_D k_{FWHM})^2 / [(4ln(2)/\pi^2)\gamma^2\delta^2 g_m^2 N^2\Delta] \qquad \text{(Eq 3.16)}$$

where k_{FWHM} represents the FWHM in digital units.

From the theoretical perspective, the lower limit to velocity resolution is the point at which stochastic motion competes with coherent motion, assuming available gradients are powerful enough to probe this regime. When diffusional displacement is on the order of velocity displacement over the evolution window, extensive spreading of the propagator is present, and there may be difficulty in evaluating the exact location of the peak. This issue is compounded by the digital nature of the collected data; the propagator contains only a finite number of probability values associated with discrete displacements, and thus binning error will also play a role. The exact error of the measurement, accounting for the above considerations, is computed by taking the derivative of the propagator near its peak with respect to small deviations in velocity δv, which gives the result [2]:

$$\delta v = \sqrt{\frac{2D}{\Delta}\frac{\delta P}{P}} \qquad \text{(Eq 3.17)}$$

where $\delta P/P$ is the noise-to-signal ratio of the propagator measurement. The maximum velocity resolution limit, of course, is governed by the coil dimension; excited spins must remain within the coil's active region by the time of acquisition or an echo will not be induced in the receiver:

$$v \leq l/TE \qquad \text{(Eq 3.18)}$$

where l is the coil dimension and TE is the echo time of the experiment.

Suppose that we wish to take an image of the average velocity of each pixel, but are unconcerned about diffusive effects. A full image of the propagator would be cumbersome due to the multiple $\boldsymbol{q}$-encoding steps, and any changes in the dynamics of the system over the course of the experiment would be obscured and blurred together in

the final image. In these cases a more efficient experimental scheme, featuring only a single $\boldsymbol{q}$-step, can be used. This is referred to as single-step phase-encoding. Although increasing the number of $\boldsymbol{q}$ values improves the precision of the velocity measurement, it is often beneficial to sacrifice some precision to facilitate the rapid collection of a full velocity image. In the two-step phase-encode experiment, the complex signal can be represented by [2]:

$$\frac{E(q_1,\Delta,\boldsymbol{r})}{E(0,\Delta,\boldsymbol{r})} = Aexp(i\emptyset) \qquad \text{(Eq 3.19)}$$

where $\emptyset = q_1 v\Delta$ and A is the attenuation factor due to diffusive effects. Provided that the diffusive attenuation is not so strong as to significantly deteriorate the $\boldsymbol{q}$-encoded image, the phase angle $\emptyset$ is easily calculated.

Of course, in order to obtain a robust, discrete numerical value for the velocity, we must still FT to the propagator space, which introduces a problem. The signal as presented contains only two points. When fed into a fast Fourier transform algorithm, the data is effectively truncated past the second $\boldsymbol{q}$ point, leading to broadening of the propagator due to convolution of the true propagator with a sinc function, the FT of the truncation function (hat). This is in fact true of *all* propagators generated from data that has not entirely attenuated, but it becomes an issue due to the small number of points [2]. Performing an *N*-point Fourier Transformation on a dataset (where *N* is the number of $\boldsymbol{q}$-steps) results in a spectrum with only two points, and it is of course not possible to identify the peak of the propagator*sinc spectrum with only these two points available. This limitation is remedied by introducing a number of false additional points to the signal dataset, all with value zero. When the augmented data is transformed, the resulting

displacement spectrum will contain an equal number of parts, providing shape to the propagator and allowing for determination of the point of maximum amplitude and therefore the velocity value. In effect, zero-filling allows the velocity resolution to be increased. The overall data analysis procedure for the velocity imaging pulse sequence is shown in Figure 3.3.

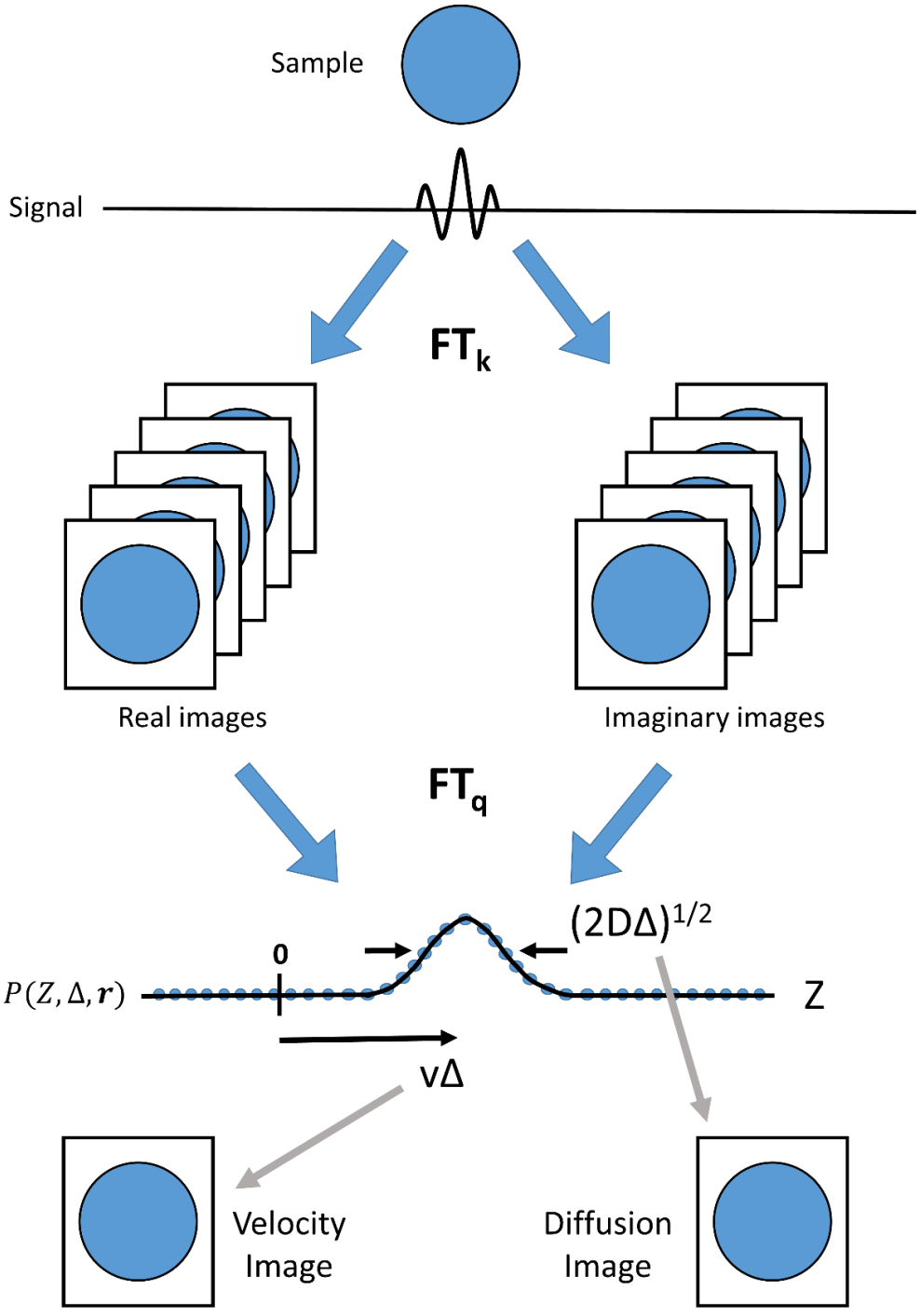

Figure 3.3. Flow chart for data processing in the velocity imaging NMR experiment. Reproduced from [2].

References

[1] Callaghan, P.T. (1993). Principles of nuclear magnetic resonance microscopy (Oxford University Press on Demand).

[2] Callaghan, P.T. (2011). Translational dynamics and magnetic resonance: principles of pulsed gradient spin echo NMR (Oxford University Press).

[3] Torrey, H.C. (1956). Bloch equations with diffusion terms. Physical review *104*, 563.

[4] Stejskal, E.O., and Tanner, J.E. (1965). Spin diffusion measurements: spin echoes in the presence of a time-dependent field gradient. The journal of chemical physics *42*, 288-292.

[5] Callaghan, P., Eccles, C., and Xia, Y. (1988). NMR microscopy of dynamic displacements: k-space and q-space imaging. Journal of Physics E: Scientific Instruments *21*, 820.

CHAPTER FOUR: INTRODUCTION TO OXYGEN IN BIOFILMS

A biofilm is defined as a community of bacteria in which cells adhere both to each other and to a surface, also called a substratum, through a self-secreted matrix of polysaccharides, proteins, nucleic acids, and other metabolic products collectively referred to as extracellular polymeric matrix. Although biofilms were first observed and described over three hundred years ago, it was not until the last few decades that the significance of the biofilm itself in a wide range of microbial phenomena began to be recognized.

In the mid 1600's, a largely self-taught Dutch scientist named Antonie van Leeuwenhoek became interested in lensmaking and over the next few decades made substantial improvements to optical technology, developing the first 300x single lens microscope sometime in the 1660's [1]. He applied his new invention to the microscopic world, scraping off plaque from his own teeth and tongue and documenting microscopic life in its contents, among other experiments. Referring to the microbes as "animalcules" ("tiny animals" in Latin), van Leeuwenhoek's description of the plaque-dwelling organism now known as *Selenomonad* was the first ever identification of a single-celled bacteria [2]. His discovery would go on to revolutionize the scientific community, paving the way for legendary experimentalists such as Louis Pasteur to elucidate the profound impact of microbial flora on everyday phenomena. As the field of microbial biology flourished over the next few hundred years, scientists developed myriad tools to explain and manipulate the physiology and behavior of microbial cells.

But van Leeuwenhoek had not just discovered bacterial cells; he had discovered a *biofilm*. And it was arguably not until the late 20th century that the importance of the biofilm itself, not merely the individual cells, began to be appreciated. Before then, scientists had largely strived to understand microorganisms at the level of the individual; what had been missed in van Leeuwenhoek's discovery was that the *organization* of the bacteria could be just as important as the individuals themselves. As it became increasingly evident in the late 20th century that these embedded microbial communities conferred unique properties *per se*, the term 'biofilm' appeared in the 1970's [3] as a means to stress the striking differences observed between the biofilm and planktonic (free-floating) microbial activity.

4.1 Biofilm Adaptations

Transition from the planktonic state to a biofilm is associated with several changes beneficial to participating cells. First and foremost, immobilization to a substrate in a desirable habitat via production of EPS allows cells to remain in that favorable environment [4]. EPS is sufficiently adhesive to resist shear forces that would easily sweep away freely suspended cells, and thus colony fixation is a means to augment resource availability [5]. The EPS matrix additionally provides protection to resident cells by presenting a physical barrier against predation, and also traps beneficial extracellular enzymes, increasing metabolic efficiency [6]. For the same reason, the EPS structure facilitates bacterial communication by entrapping communicatory signaling molecules which dictate microbial responses to environmental changes, a process called quorum

sensing [7]. Containment of metabolic products extends even to gene transfer, with genotypically distinct cells able to exchange useful genetic information [8]. This ability is further augmented by the fact that the establishment of EPS facilitates the recruitment of additional bacterial species to the biofilm which are not able to colonize a surface on their own but which may provide benefits to the existing residents [9], such as when two species possess complimentary metabolic pathways.

A final evolutionary benefit, of particular interest to the current work, is a substantial change in local transport processes. While convection dominates transport for freely suspended cells, within a biofilm EPS erects a convective barrier which dramatically limits the rate at which compounds permeate individual microcolonies, restricting molecular transport to diffusive processes alone [10]. This rate-limiting transport barrier establishes strong spatial gradients in the distribution of bulk compounds, creating localized microenvironments characterized by unique chemical makeup [11]. Although this may intuitively seem like a hindrance, as reduced nutrient delivery will invariably impede growth rate, it also provides a unique benefit. Spatial variability in chemical environment requires cells at different locations to alter their phenotype to suit their particular surroundings, leading to striking heterogeneity in microbial gene expression and physiology [12]. Much like larger organisms, phenotypic variability allows for greater flexibility during environmental change events by increasing the likelihood that at least a subset of organisms can respond appropriately. An example of high relevance is antibiotic tolerance: across a wide variety of species, cells in the basal layers of the biofilm where nutrient availability is limited display dramatically

increased tolerance to antibiotic compounds that would be universally lethal to a free-floating population [13]. This asset is, in fact, a direct result of the lack of nutrient access near the substratum; cells in this region exhibit little to no metabolic activity, and are thus unaffected by exposure to toxic compounds, which largely target bacterial growth pathways [14]. For this reason, biofilm-associated cells may be several orders of magnitude more tolerant to antimicrobials than their planktonic counterparts [15]. In the case of pathogenic bacteria, the same phenomenon confers tolerance to host immune defenses [16].

The unique evolutionary advantages provided by the biofilm state of growth have resulted in biofilms becoming ubiquitous across the microbial world. Nearly every species of microorganism have mechanisms by which they can adhere to surfaces and to each other [17], and it is estimated that biofilms represent the dominant form of bacterial growth, with up to 80% of bacteria on Earth's surface biofilm-associated [18-20]. They occur in environments as wide-ranging as glaciers [21] to geologic hot springs [22], and are visible to the layperson as dental plaque and slime found on rocks in rivers and ponds. Their prevalence is similarly pronounced in medicine, where 80% of bacterial infections are thought to be biofilm-associated [23]. In industry, biofilms can be a hindrance, for instance in the biofouling of filtration membranes [24], ship hulls [25], and petroleum pipelines [26], but are useful in other contexts, such as in bioremediation [27] or microbially-aided wastewater treatment [28].

4.2 Biofilm Development

Biofilm development proceeds in four steps: initial attachment, irreversible attachment, maturation, and dispersion (the maturation phase is sometimes subdivided into two steps) [29]. During initial attachment, free-floating microorganisms stochastically contact a substrate via gravitational forces or Brownian motion and associate with it, with initial adherence likely mediated through hydrophobic interactions and van der Waals forces [17; 30]. During irreversible attachment, cells anchor themselves more permanently to the surface using pili or other cell adhesion structures. Substrate contact and interaction triggers a cascade of regulatory changes which facilitate progression into the maturation phase [31]. Gene expression is altered to favor sessility and production of EPS. Quorum sensing signals are produced which stimulate cell division and the recruitment of new microbes at the site of colonization, as well as species-specific cell products which further induce the transition to the biofilm state. Microcolonies grow in a three-dimensional manner, with orientation of growth tightly regulated to produce distinct localized geometric patterns such as mushroom-shaped structures separated by interstitial voids containing little to no EPS [6]. These channels permit convection through the biofilm, increasing molecular transport between individual microcolonies, with the tortuous path imposed on the fluid flow induces turbulence, further augmenting nutrient delivery [32]. Finally, biofilm-embedded cells may enter the ultimate stage of biofilm development, dispersion, either due to mechanical shearing or deliberately in response to environmental cues such as alterations in nutrient availability [33] or increase of toxic products [34]. EPS production is downregulated and surfactant

molecules are produced which reduce surface-bacterial interactions [31]. Additional voids are created by programmed cell death, freeing resident live bacteria and allowing them to either slough off or emigrate autonomously using locomotion. Abandonment of the biofilm in sub-optimal conditions allows dispersing bacteria to then seek more favorable environments, reinitiating the biofilm formation process elsewhere.

Although a mature biofilm is constantly undergoing a complex web of metabolic and regulatory changes, overall structural growth occurs slowly relative to the timescales of molecular transport and thus a fully-developed biofilm is generally assumed to be pseudo-steady state when considering solute-biofilm interactions. This transition from unhindered growth to a pseudo-steady state biofilm is concomitant with the establishment of transport limitation. This is of course no surprise, as when nutrient availability becomes limited, growth rates will decrease overall as well as assume a spatial dependence as position within a microcolony begins to dictate chemical environment. We will consider both of these growth conditions separately, as they differ fundamentally with respect to the temporal development of both the biofilm and the concentration profile of relevant solutes.

4.3 Mathematics of Planktonic Growth

For planktonic cells suspended in a well-mixed solution, bacteria exhibit relatively simple growth behavior characterized by three phases: lag phase, exponential phase, and stationary phase. During the lag phase, bacteria adapt themselves to chemical and physical surroundings via synthesis of appropriate RNA, enzymes, and other

molecules. As cells prepare their phenotype for the local environment via gene regulation, no cell doubling occurs. The duration of lag phase is highly variable depending on species and the conditions of the medium, and can range from less than an hour to several days.

The exponential phase is characterized by cell doubling at a constant rate, with the rate of new bacteria appearing proportional to the current population. Mathematically, growth during this period can be derived with a biomass balance over a well-mixed volume of arbitrary size, where the rate of generation of biomass r_X is proportional to current biomass:

$$r_X = \mu X \qquad \text{(Eq 4.1)}$$

where X is the biomass density and μ is the maximum specific growth rate, which in the absence of nutrient limitation is a constant for a given species under constant conditions. The biomass balance over volume V yields:

$$\frac{d(XV)}{dt} = \mu XV \qquad \text{(Eq 4.2)}$$

Constant volume cancels, leaving a simple ordinary differential equation (ODE):

$$\frac{dX}{dt} = \mu X \qquad \text{(Eq 4.3)}$$

with solution:

$$X(t) = X_o \exp(\mu t) \qquad \text{(Eq 4.4)}$$

where X_o is the biomass initial condition. The above solution is valid when μ is independent of substrate concentration, called zero-order kinetics.

Considering the consumption of an arbitrary growth substrate, a separate rate constant r_C is introduced which is directly obtained from r_X:

$$r_C = \frac{-r_X}{Y_{XC}} \qquad \text{(Eq 4.5)}$$

where Y_{XC} is the yield coefficient, the ratio of biomass produced per substrate mass consumed. A mass balance on substrate over constant volume gives:

$$\frac{dC}{dt} = \frac{-r_X}{Y_{XC}} = \frac{-1}{Y_{XC}}\frac{dX}{dt} \qquad \text{(Eq 4.6)}$$

with solution:

$$C = C_o + \frac{1}{Y_{XC}}(X_o - X) \qquad \text{(Eq 4.7)}$$

From the above equation, we can determine the point at which substrate concentration reaches zero, which we will call t_C, by subbing in the known exponential form for X:

$$t_C = \frac{\ln(1+\frac{C_o Y_{XC}}{X_o})}{\mu} \qquad \text{(Eq 4.8)}$$

The time evolution of substrate concentration and biomass density are thus described by an exponential rise in biomass and concomitant exponential decay in substrate concentration. When available substrate is depleted (i.e. at timepoint t_C for the above model), or for other reasons such as the buildup of an inhibitory metabolic product, bacteria transition to stationary phase, wherein reduced growth causes death rate and growth rate to be equal, and biomass profile becomes flat.

It must be noted that the above formulation is only valid when the intrinsic growth rate is a constant, or when it can be approximated as a constant. As a general rule, μ will inevitably be a function of substrate availability, but in many cases only a minute substrate density is required to achieve the maximum μ, and in such cases divergence

from zero-order kinetics is negligible until substrate concentrations approach zero. One such situation may be encountered for the following specific growth rate dependence:

$$\mu = \frac{\mu_{max} C}{K_C + C} \qquad \text{(Eq 4.9)}$$

The above kinetic description, called the Monod equation, is empirically derived [35] and has been shown to be widely applicable for a variety of growth substrates and bacterial taxa. K_C is referred to as the half-saturation coefficient and represents the substrate concentration at which μ attains half its maximum value. Above this concentration, μ asymptotically approaches μ_{max}. When K_C is low relative to actual substrate densities, the zero-order growth model can be safely assumed. At substrate values near or under K_C, the full kinetic form must be accounted for. The effect of the Monod formulation is to introduce a long tail into the substrate decay plot at low C values, and to introduce a progressive blunting of the X growth curve which segues continuously into the flat slope corresponding to stationary phase. We note that other kinetic forms such as first order or product inhibition are common in the microbial world and require more complex treatment when the zero-order approximation cannot be safely assumed; however, we will largely restrict our focus here to zero-order kinetics which are relevant to the current work.

In the early phases of biofilm development, microbial growth mirrors the planktonic model. But as nutrient conditions deplete, the two biological states will diverge significantly in their behavior due to a key difference. In planktonic systems, the growth medium is sufficiently well-mixed so that chemical environment is assumed to be identical across the bacterial population [10]. As such, cells will progress to the next

phase of growth simultaneously. However, in a biofilm, cells are removed from the bulk fluid and thus their access to free-floating solutes depends on their spatial location. As cell density increases sufficiently as to prevent critical nutrients from fully penetrating the biofilm, a balance between reaction rate and diffusion rate develops which results in the establishment of a steady-state wherein the characteristics of solute profiles are dependent on both intrinsic bacterial physiology and environmental conditions.

4.4 Mathematics of Biofilm Growth and Diffusion Limitation

Many of the unique properties attributed to the biofilm state can be explained by the phenomenon of diffusion. The biofilm, characterized by high cell densities and a gel-like matrix of EPS, arrests flow and thus removes convective contributions to transport within the constituent microcolonies, leaving diffusion as the predominant transport process within cell aggregates [10]. Diffusive transport is described mathematically by Fick's second law:

$$\frac{\partial C}{\partial t} = \nabla \cdot (\boldsymbol{D_e}^* \nabla C) \qquad \text{(Eq 4.10)}$$

where C represents the concentration of a chemical species and $\boldsymbol{D_e}$ represents the effective diffusion tensor. The 'effective' terminology denotes that diffusion of solutes in a biofilm is typically reduced relative to the bulk fluid due to physical occlusion by cells and EPS, with the extent of this diminution dependent on a myriad of factors including solute size and polarity, and biofilm EPS volume fraction [36]. Assuming isotropic diffusion, and considering only diffusion along a single dimension, z, the equation simplifies to:

$$\frac{\partial C}{\partial t} = D_e \frac{\partial^2 C}{dz^2} \qquad \text{(Eq 4.11)}$$

Diffusion coefficient, the proportionality constant between lengthscale and timescale of diffusive motion, has unit length^2/time. This indicates that diffusive equilibration time scales with the square of the corresponding distance, which has profound impacts on the nature of molecular transport in a biofilm. For example, a biofilm that is 100 cells thick will exhibit a diffusion time 10,000 times longer than that of an individual cell [10]. The effect of this scaling law is that, as a biofilm microcolony grows in thickness, the ability of diffusion to deliver nutrients to cells near the substratum is eventually overwhelmed by its consumption in the upper layers. Penetration depth as a fraction of biofilm thickness progressively reduces until a steady state is achieved, characterized by temporally-static solute depth profiles and striking spatial heterogeneity in physiology, a property which, as mentioned above, is a critical contributor to the unique characteristics exhibited by biofilms. Once this balance has been achieved, changes to bulk fluid composition (such as a substantial increase in the concentration of an existing solute) only briefly perturb the system; within seconds to minutes, a new steady state solute profile is established [37]. This transience period is so short-lived because the biofilm thickness changes very slowly with respect to diffusive timescales, and can thus be neglected in these considerations.

Because the transience time of solute profile is ephemeral in response to changes to boundary condition, the steady state itself is of primary concern. For this case, the reactive-diffusive balance which is responsible for establishment of the substrate profile is given in one dimension by:

$$\frac{\partial C}{\partial t} = D_e \frac{\partial^2 C}{dz^2} - r = 0 \qquad \text{(Eq 4.12)}$$

When zero-order kinetics can be safely assumed, the balance becomes:

$$0 = D_e \frac{\partial^2 C}{dz^2} - \frac{\mu X}{Y_{XC}} \qquad \text{(Eq 4.13)}$$

To obtain a mathematical form for the substrate profile valid across systems of different lengthscale and concentration, z and C are non-dimensionalized:

$$u = \frac{C}{C_o} \qquad \text{(Eq 4.14)}$$

$$\xi = \frac{z}{L_f} \qquad \text{(Eq 4.15)}$$

where C_o is the substrate concentration at the biofilm surface and L_f is the biofilm thickness. The result is a simple second order ODE:

$$\frac{d^2 u}{d\xi^2} = 2\Phi^2 \qquad \text{(Eq 4.16)}$$

where Φ represents the collective constants:

$$\Phi = \left(\frac{\mu_{max} X_b L_f^2}{2 D_e Y_{XC} C_o}\right)^2 \qquad \text{(Eq 4.17)}$$

The above quantity is called the Thiele Modulus and is of high utility as it represents the ratio of reaction rate to diffusion rate [38]. At $\Phi \ll 1$, the relevant solute fully penetrates the biofilm with little concentration gradient, while at $\Phi \gg 1$, the penetration depth may be only a small fraction of the biofilm thickness. Its form will, of course, change according to the governing reaction kinetics.

For zero-order kinetics, the solution, representing the steady state distribution of substrate in the biofilm, is given by:

$$u = \Phi^2 \xi^2 - 2\Phi^2 \xi \frac{a}{L_f} + 1 \qquad \text{(Eq 4.18)}$$

where a, which we define as the penetration depth, arises from the zero-concentration boundary condition. We can then directly solve for a:

$$a = \left(\frac{2D_e Y_{XS} C_o}{\mu_{max} X_b}\right)^{1/2} \qquad \text{(Eq 4.19)}$$

4.5 External Mass Transfer Resistance

In the above formulations, it is implicitly assumed that the fluid immediately above the biofilm is sufficiently mixed to produce a uniform substrate concentration C_o regardless of position. Unfortunately, this is often not the case. The surface of the biofilm can be considered solid-like, and thus exerts a viscous effect on fluid above it, resulting in a general reduction of flowrate near the bulk-biofilm interface and a spatially-dependent velocity profile [39]. This in turn causes a reduction in streamline mixing which erects a barrier to solute transport in the fluid layer above the biofilm. This phenomenon, called a boundary layer or external mass transfer resistance, can significantly impact overall biofilm transport. Furthermore, its influence may be difficult to quantify as the exact distribution of fluid velocities may be unknown, and it is thus unclear what the relative contributions of diffusion and convection are in this layer. To make matters worse, biofilms do not exhibit planar geometry but rather a complicated three-dimensional structure with stochastic shapes and orientations, and therefore there may be dramatic spatial variability in the extent of external mass transfer resistance even at the microscale. Methods to evaluate the thicknesses of these boundary layers are extremely limited, and measurements are often restricted to either one-dimensional profiles which do not capture their true spatial distribution. Crude three dimensional

maps of external mass transfer resistance may be obtained by repeating such measurements over different locations or orientations but the timescales required for acquisition necessitate a tradeoff between signal-to-noise, time of measurement, and spatial resolution. It is clear, however, that boundary layers vary wildly across even minute distances, and that their influence on biofilm transport is often considerable.

External mass transfer resistance is typically quantified by assuming a constant, 'effective' boundary layer thickness wherein transport occurs by diffusion alone. Both the constant thickness and the 'no convection' assumption are of dubious validity, but such simplifications make the problem tractable, and in addition, any convective effects are accounted for via modulation of the 'effective' layer thickness. The flux through the boundary layer along a single dimension is then given by:

$$J = k_\delta (C_o - C_s) \qquad \text{(Eq 4.20)}$$

Where C_s is the substrate concentration at the biofilm surface and k_δ is an effective mass transfer coefficient, mathematically defined as:

$$k_\delta = \frac{D}{\delta} \qquad \text{(Eq 4.21)}$$

D is the diffusion coefficient in water (usually different than D_e) and δ is the effective thickness of the boundary layer. When k_δ is non-dimensionalized, it is referred to as the Sherwood number (Sh) [40]:

$$Sh = \frac{k_\delta L}{D} = \frac{-1}{1-u} = \left.\frac{\partial u}{\partial \xi}\right|_{\xi=0} \qquad \text{(Eq 4.22)}$$

where L denotes a system-specific characteristic dimension such as the diameter of a tube, or in this simplified planar geometry case, the depth of the fluid flowing over the top of the biofilm. Sherwood number is a particularly useful quantity as it represents the

ratio of convective mass transfer rate to diffusion mass transfer rate regardless of specific system size or magnitude of overall flux. For many applications, biofilm-related or otherwise, direct measurement of *Sh* is difficult or impractical, and instead correlational estimates are consulted which use theoretical and geometric considerations to provide an approximation of expected *Sh*. As it is inherently a measure of molecular mobility in the presence or absence of flow, *Sh* exhibits dependence on viscosity, density, velocity, and characteristic length. A particularly useful formulation of *Sh* is reached when these independent variables are compiled in such a way as to produce dimensionless ratios representing the relative strength of inertial forces to viscous forces, and the relative strength of viscous shear to molecular diffusivity. These dimensionless quantities are referred to as the Reynolds number (*Re*) [41] and Schmidt number (*Sc*) [42] respectively:

$$Re = \frac{\rho V L}{\mu} = \frac{inertial}{viscous} \qquad \text{(Eq 4.23)}$$

$$Sc = \frac{\mu}{\rho L} = \frac{momentum\ diffusivity}{mass\ diffusivity} \qquad \text{(Eq 4.24)}$$

Decomposition of mass transfer into the above dimensionless ratios allows for normalization across system size, facilitating the identification of patterns between these known or measurable quantities. It has been shown that across a wide and disparate variety of systems and geometries, *Sh* displays power law scaling with both *Re* and *Sc*, with the constant scaling factors dependent on local geometry and the relevant range of *Re* and *Sc*:

$$Sh = Sh_o + CRe^m Sc^n \qquad \text{(Eq 4.25)}$$

A wealth of literature is available providing optimized correlations for different systems [43; 44], and thus for a given geometry and range of *Re* and *Sc*, assumed to be

approximately known for an experimental system, a ballpark estimate of *Sh* can be obtained. For many macroscale processes such as chemical conversion, a reasonable estimate combined with iterative system adjustments to validate accuracy is sufficient. However, when microscale variation in external mass transfer resistance is important to system behavior, correlational estimates have significant limitations. Due to the intractable nature of measuring boundary layers across miniscule spatial scales, these limitations are difficult to circumvent, and development of novel methodologies to better obtain such measurements has long been an area of research with potentially wide-ranging relevance [45].

With boundary layer thickness (or, equivalently, *Sh*) known or approximated to satisfaction, substrate profile can then be characterized mathematically by employing a matching flux boundary condition, which states that molecular flux at the biofilm surface must be continuous. For zero-order kinetics, the imposed boundary condition is:

$$\frac{D}{\delta}(C_o - C_s) = \frac{\mu_{max} X}{Y_{XC}} a \qquad \text{(Eq 4.26)}$$

Rearranging, we obtain an equation which can be used to calculate the strength of external mass transfer resistance relative to internal resistance:

$$1 - \frac{C_s}{C_o} = 2\Phi\left(\frac{\delta D_e}{D L_f}\right)\left(\frac{C_s}{C_o}\right)^{\frac{1}{2}} = 2\Phi Bi\left(\frac{C_s}{C_o}\right)^{\frac{1}{2}} \qquad \text{(Eq 4.27)}$$

where we have introduced the Biot number (*Bi*), a dimensionless quantity relating the ratio of external resistance to internal resistance [46]. With knowledge of measurable parameters, the above equation is used to calculate the ratio of surface concentration to bulk concentration, directly identifying the impact of the boundary layer on substrate

delivery into the biofilm. The penetration depth can then be calculated using the known C_s boundary condition at the biofilm surface.

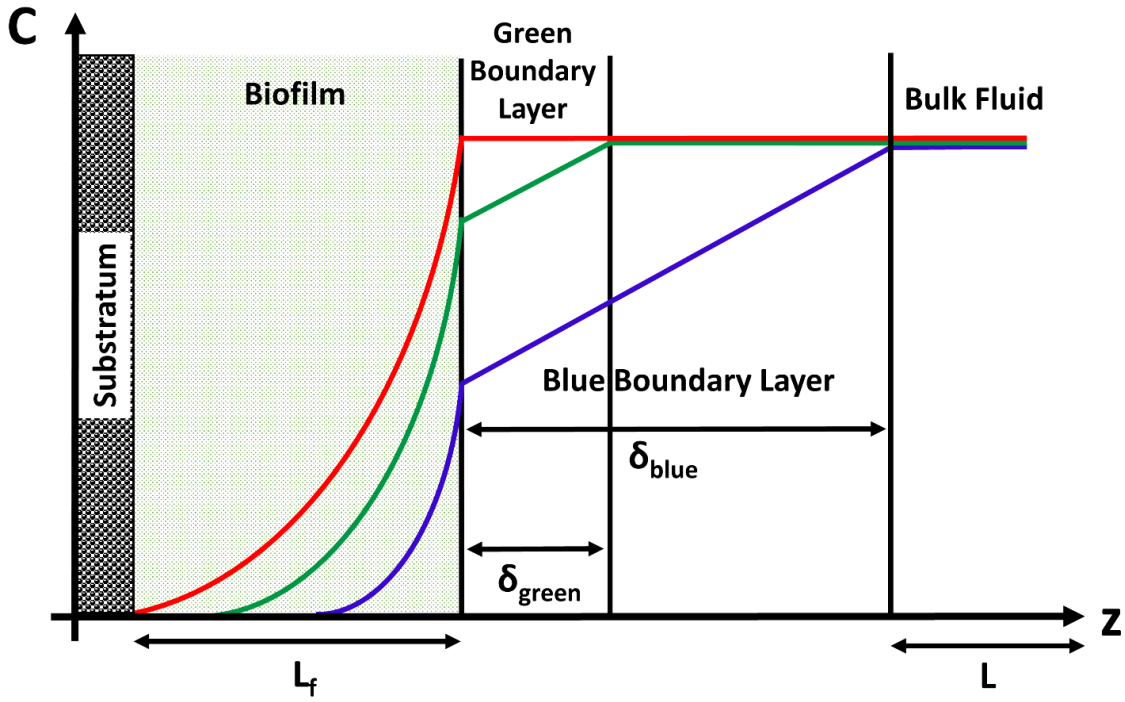

Figure 4.1. Theoretical concentration profiles for an arbitrary growth substrate characterized by zero-order kinetics with $\Phi = 1$, subjected to varying degrees of external mass transfer resistance.

Theoretical concentration profiles for an arbitrary growth substrate exhibiting zero-order kinetics with constant $\Phi = 1$ under varying degrees of external mass transfer resistance are shown in Figure 4.1. The red line represents a biofilm with no external mass transfer resistance. With reaction rate equal to diffusion rate, substrate concentration drops to zero precisely at the base of the biofilm. The exponential profile indicates increasingly reduced substrate flux with progressing depth into the biofilm as a result of bacterial consumption. The green line shows the same biofilm subjected to mild

external mass transfer resistance, with a C_s/C_o ratio of about 0.8, yielding $Bi \approx 0.11$ according to Eq 4.27. The blue line represents the biofilm subjected to substantial external mass transfer resistance, with a C_s/C_o ratio of about 0.5, corresponding to $Bi = 0.5$. For the systems exhibiting external mass transfer resistance, the flat slope in the boundary layer indicates constant flux into the biofilm which denotes the absence of reaction in this region, while the non-zero value of the slope signifies the absence of mixing and thus diffusive transport limitation. Because reaction rate is independent of substrate concentration for zero-order kinetics, the presence of a concentration boundary layer substantially reduces penetration depth into the biofilm. Note that the concentration profiles above are theoretically derived, generated from the assumption of a fixed boundary layer thickness characterized only by diffusion. In real biofilms, there typically exists a fluid flow velocity profile, with velocity magnitude gradually increasing with progressing distance from the biofilm. The effect of this flow distribution is a net flux that gradually grows as the biofilm is approached, i.e. the slope begins shallow near the bulk phase but becomes steeper with increasing proximity to the biofilm surface, asymptotically approaching the diffusive-only flux.

All the above mathematical treatments of the reactive-diffusive balance present in microbial aggregates aim to better elucidate the character of substrate penetration into a biofilm, as spatially-dependent chemical environment is perhaps the biggest predictor of biofilm presentation and behavior. Of course, not all chemical species are of equal importance. Nutrients that are rate-limiting or that strongly influence local chemistry can

dominate biofilm-environment interactions. In the next section, we discuss the specific impact of molecular oxygen, which meets both these criteria.

4.6 Oxygen in Biofilms

Molecular oxygen (O_2), also known as dioxygen or simply oxygen, constitutes about 21% of the Earth's atmosphere. Owing to its possession of unpaired electrons (called a degenerate electron configuration), oxygen is extremely reactive and slowly and spontaneously reacts with most organic molecules. The molecular mechanisms which induce this reactivity will not be described here but can be found in [47]. As a result of its long-term instability, oxygen cannot remain a free element in air without a source of continuous replenishment, and it is believed that free oxygen was virtually absent on earth for the first 2 billion years of its existence (4.5 to 2.5 billion years ago) [48]. Early life on earth, beginning between 3.5 and 4 billion years ago, evolved entirely in its absence, and indeed, exposure to even microaerophilic conditions would have been lethal due to oxidation of biomolecules to these obligate anaerobes. Around 2.3 billion years ago, however, a clade of organisms called cyanobacteria evolved the ability to form energy-dense sugars using carbon dioxide and light in a process called photosynthesis which produces oxygen as a reaction product. Initially, the generated oxygen was quickly absorbed and reduced by minerals in adjacent rock [49], but after these mineral sinks became saturated, oxygen rapidly began to accumulate in Earth's atmosphere and oceans, leading to what is likely the greatest mass extinction event in Earth's history [50]. However, a side effect of oxygen's reactive molecular structure is extreme

electronegativity, or tendency to attract electrons, a property which can be exploited to strip organic molecules of their electrons and extract massive amounts of energy using a metabolic pathway called oxidative phosphorylation. This biological process, in fact, can generate up to or above an order of magnitude more energy than anaerobic metabolism, depending on the anaerobic strategy used. Thus proliferation of oxygen on Earth instigated an extreme selection pressure for the ability to exploit oxygen in cellular machinery, resulting in unprecedented biological diversification.

The above account illustrates the profound influence of the presence of oxygen on local chemistry. This quality is especially pronounced in biofilms, where oxygen levels vary widely in comparison to its largely constant, ubiquitous distribution in the bulk atmosphere. With oxygen being variably lethal or indispensable for life for different organisms, it is arguably the most important growth substrate and its spatial distribution broadly shapes biofilm physiology.

Most intuitively, the presence or absence of oxygen dictates which microbial taxa may thrive in the biofilm. At the peripheries of cell clusters, where oxygen perfusion is high, aerobic microbes flourish, while the anoxic microniches they create foster the growth of obligate anaerobes. In the liminal zones between the two, microaerophilic bacteria such as *Helicobacter* may prosper. Facultative anaerobes such as *Staphylococcus epidermidis* and *Escherichia coli* may be found throughout the biofilm, with cells in the oxic layer growing rapidly and cells in the anoxic layer exhibiting lower growth yields. The reactive-diffusive balance of oxygen in a biofilm and the diffusion limitation it creates can therefore facilitate the development of a thriving consortium of different

species even at microscopic scales by establishing unique chemical microenvironments. As metabolic pathways for these organisms differ wildly, this habitat structuring also promotes widespread symbiosis, with the metabolic products of one organism being beneficial nutrients to another [51].

Even within single-species biofilms, the extensive physiological heterogeneity induced by differential oxygen availability has striking implications across medical, industrial, and environmental contexts. In medicine, the phenomenon of tolerance to antibiotics and host immune defenses mentioned at the beginning of this chapter is fundamentally linked to oxygen distribution. Oxygen-limited cells in pathogenic biofilms enter metabolic dormancy, conferring resilience to a wide spectrum of antimicrobials, as these compounds target biosynthetic pathways and are thus ineffective when such pathway is not being used. So while antibiotic challenge may exterminate the vast majority of the biofilm, surviving cells can simply resume growth and re-establish the colony once the compound has been cleared, a phenomenon called infection persistence. Oxygen distribution similarly aids in resistance from capture and killing by host immune defenses. For instance, respiratory competition for available oxygen mitigates the ability of neutrophils to initiate oxidative burst, an immune strategy whereby oxygen is converted to reactive oxygen species such as hydrogen peroxide which attack bacterial cellular structures [52; 53]. In some medical biofilms, such as those formed by *Pseudomonas aeruginosa*, the infection is able to immobilize and entrap neutrophils and efficiently convert the hydrogen peroxide they generate back into usable oxygen which can then be used for bacterial respiration [52; 54]. For the above reasons, oxygen

penetration into infected tissue is a strong predictor of clinical outcome [55], and therapies stimulating oxygen delivery into colonized wounds have proven effective [56].

In industry, biofilms may represent an obstacle to operation (e.g. biofouling), or may be useful (e.g. wastewater treatment or bioremediation). In all cases, oxygen availability is a critical determinant of microbial presentation which must be carefully and tightly controlled to produce the desired outcome. For instance, biofilm growth can significantly expedite corrosion of steel pipes, and the rate and extent this occurs is highly dependent on oxygen penetration depth, both because it determines which organisms are present (and therefore which surface reactions are present) and due to its intrinsic effect on local abiotic chemistry [57]. In separation membranes and membrane bioreactors, biofouling is strongly impacted by the extent of oxygen delivery to the membrane surface [58; 59]. Bioremediation, which uses stimulated microbial growth to degrade toxic compounds introduced into the ground or water as a result of industrial processes or unintentional spills, requires stringent control of oxygen delivery to select for desired microbes, with oxygen availability often rate-limiting for aerobic reactions [60; 61]. In microbial wastewater treatment processes, oxygen distribution largely determines the types of reactions undergone in biofilm flocs, thus shaping the macroscale conversions taking place [62; 63].

In environmental contexts, oxygen penetration depth shapes biofilm species composition, and as microbial life is a critical component of the base of the food chain, this influence has far-reaching effects for the local environment. For instance, in biofilms found in marine basis, stratified lakes, cyanobacterial mats, sulfur springs, and sediment

surfaces, incomplete oxygen penetration allows a diverse consortium of microbial species to thrive according to local oxic conditions [64]. In plant root biofilms, chemotaxis toward microaerophilic bands appears to be a key step in the association of nitrogen-fixing bacteria with the root rhizosphere [65], a symbiosis that is central to nutrient cycling and biological function in many plant species [66].

The above examples are by no means exhaustive but are intended to illustrate the universal relevance of oxygen gradients in biofilm systems. While oxygen distribution is inherently complex owing to its origin in complicated reaction-advection-diffusion phenomena, understanding the basis, characteristics, and impact of oxygen gradients is key to understanding biofilms themselves. On the microscale, the spatial extent of these gradients are often small due to high metabolic demand for oxygen and the high kinetic efficiency of bacterial oxidative phosphorylation, illustrated by the fact that the Monod half-saturation coefficient for oxygen consumption is well over an order of magnitude lower than saturation oxygen concentrations [67] and can be as low as on the order of μg/L [68] (the kinetics of oxygen consumption are thus accurately represented by zero-order models). At the scale of individual microcolonies, oxygen penetration depth into a single cell cluster is often on the order of only tens to hundreds of microns. However, the high spatial and temporal variance of biofilm growth and physiology often translates into oxygen concentration fluctuations on the macroscale, significantly impacting system behavior, for instance in industrial processes.

Unfortunately, measurement of oxygen distribution is difficult, whether in the lab, clinic, or field. By far the most-widely used method for oxygen quantification is the

Clark-type microelectrode [69], which enjoys the advantages of high precision and accuracy at the expense of significant drawbacks. The microelectrode consists of a needle-like sensor containing a silver anode, platinum cathode, and a thin oxygen-permeable Teflon membrane at the tip. When the electrode is introduced into the sample, oxygen freely permeates the membrane and becomes electrolytically reduced by the platinum cathode. The resulting electrochemical imbalance causes electrons from the anode to travel to the cathode, inducing an overall current in the electrode, at a rate linearly proportional to the oxygen partial pressure at the location of measurement. By calibrating the sensor to the salinity and temperature of the sample, the induced current can be directly related to localized oxygenation.

The microelectrode exhibits three characteristic limitations. First, measurement is restricted to a single spatial location at a time, making it extremely time consuming to collect spatial profiles [70]. The time penalty additionally makes dynamic tracking of oxygen in non-steady-state systems intractable. Second, microelectrodes are fundamentally invasive, requiring physical penetration to facilitate measurement, potentially altering oxygen concentration either by introduction of oxygen during electrode insertion or by interfering with natural flow paths above the biofilm [71]. Finally, some systems are inaccessible to microelectrode probing. For instance, introduction of the oxygen sensor to contained systems such as packed bed columns is cumbersome. Nevertheless, oxygen microelectrodes have remained popular over the decades and provided much invaluable insight into biofilm behavior as a result of their high accuracy, low cost, and, most fundamentally, due to the lack of competitive

alternatives. Development of alternative techniques could provide additional tools for biofilm researchers, potentially opening new doors in biofilm science.

References

[1] Mansuripur, M. (1999). The van Leeuwenhoek microscope. Optics and Photonics News *10*, 39-42.

[2] Smit, P., and Heniger, J. (1975). Antoni van Leeuwenhoek (1632–1723) and the discovery of bacteria. Antonie Van Leeuwenhoek *41*, 217-228.

[3] Mack, W., Mack, J., and Ackerson, A. (1975). Microbial film development in a trickling filter. Microb Ecol *2*, 215-226.

[4] Monds, R.D., and O'Toole, G.A. (2009). The developmental model of microbial biofilms: ten years of a paradigm up for review. Trends Microbiol *17*, 73-87.

[5] Rupp, C.J., Fux, C.A., and Stoodley, P. (2005). Viscoelasticity of Staphylococcus aureus biofilms in response to fluid shear allows resistance to detachment and facilitates rolling migration. Appl Environ Microbiol *71*, 2175-2178.

[6] Flemming, H.-C., and Wingender, J. (2010). The biofilm matrix. Nature reviews microbiology *8*, 623.

[7] Parsek, M.R., and Greenberg, E. (2005). Sociomicrobiology: the connections between quorum sensing and biofilms. Trends Microbiol *13*, 27-33.

[8] Madsen, J.S., Burmølle, M., Hansen, L.H., and Sørensen, S.J. (2012). The interconnection between biofilm formation and horizontal gene transfer. FEMS Immunol Med Microbiol *65*, 183-195.

[9] Sutherland, I.W. (2001). The biofilm matrix–an immobilized but dynamic microbial environment. Trends Microbiol *9*, 222-227.

[10] Stewart, P.S. (2003). Diffusion in biofilms. J Bacteriol *185*, 1485-1491.

[11] Stewart, P.S., Zhang, T., Xu, R., Pitts, B., Walters, M.C., Roe, F., Kikhney, J., and Moter, A. (2016). Reaction–diffusion theory explains hypoxia and heterogeneous growth within microbial biofilms associated with chronic infections. Npj Biofilms And Microbiomes *2*, 16012.

[12] Stewart, P.S., and Franklin, M.J. (2008). Physiological heterogeneity in biofilms. Nature Reviews Microbiology *6*, 199.

[13] Fux, C., Costerton, J.W., Stewart, P.S., and Stoodley, P. (2005). Survival strategies of infectious biofilms. Trends Microbiol *13*, 34-40.

[14] Tuomanen, E., Cozens, R., Tosch, W., Zak, O., and Tomasz, A. (1986). The rate of killing of Escherichia coli byβ-lactam antibiotics is strictly proportional to the rate of bacterial growth. Microbiology *132*, 1297-1304.

[15] Stewart, P.S., and Costerton, J.W. (2001). Antibiotic resistance of bacteria in biofilms. The lancet *358*, 135-138.

[16] Leid, J.G. (2009). Bacterial biofilms resist key host defenses. Microbe *4*, 66-70.

[17] Donlan, R.M. (2002). Biofilms: microbial life on surfaces. Emerg Infect Dis *8*, 881.

[18] Murphy, T.F., and Kirkham, C. (2002). Biofilm formation by nontypeable Haemophilus influenzae: strain variability, outer membrane antigen expression and role of pili. BMC Microbiol *2*, 7.

[19] Wimpenny, J., Manz, W., and Szewzyk, U. (2000). Heterogeneity in biofilms. FEMS Microbiol Rev *24*, 661-671.

[20] Flemming, H.-C., and Wuertz, S. (2019). Bacteria and archaea on Earth and their abundance in biofilms. Nature Reviews Microbiology, 17, 247-260.

[21] Smith, H.J., Schmit, A., Foster, R., Littman, S., Kuypers, M.M., and Foreman, C.M. (2016). Biofilms on glacial surfaces: hotspots for biological activity. npj Biofilms and Microbiomes *2*, 16008.

[22] Hall-Stoodley, L., Costerton, J.W., and Stoodley, P. (2004). Bacterial biofilms: from the Natural environment to infectious diseases. Nat Rev Micro *2*, 95-108.

[23] Akers, K.S., Mende, K., Cheatle, K.A., Zera, W.C., Yu, X., Beckius, M.L., Aggarwal, D., Li, P., Sanchez, C.J., and Wenke, J.C. (2014). Biofilms and persistent wound infections in United States military trauma patients: a case–control analysis. BMC Infect Dis *14*, 190.

[24] Herzberg, M., and Elimelech, M. (2007). Biofouling of reverse osmosis membranes: Role of biofilm-enhanced osmotic pressure. Journal of Membrane Science *295*, 11-20.

[25] Townsin, R.L. (2003). The ship hull fouling penalty. Biofouling *19*, 9-15.

[26] Rajasekar, A., Anandkumar, B., Maruthamuthu, S., Ting, Y.-P., and Rahman, P.K.S.M. (2010). Characterization of corrosive bacterial consortia isolated from petroleum-product-transporting pipelines. Appl Microbiol Biotechnol *85*, 1175-1188.

[27] Edwards, S.J., and Kjellerup, B.V. (2013). Applications of biofilms in bioremediation and biotransformation of persistent organic pollutants, pharmaceuticals/personal care products, and heavy metals. Appl Microbiol Biotechnol *97*, 9909-9921.

[28] Adav, S.S., Lee, D.-J., Show, K.-Y., and Tay, J.-H. (2008). Aerobic granular sludge: Recent advances. Biotechnology Advances *26*, 411-423.

[29] Monroe, D. (2007). Looking for chinks in the armor of bacterial biofilms. PLoS Biol *5*, e307.

[30] Beloin, C., Valle, J., Latour-Lambert, P., Faure, P., Kzreminski, M., Balestrino, D., Haagensen, J.A., Molin, S., Prensier, G., and Arbeille, B. (2004). Global impact of mature biofilm lifestyle on Escherichia coli K-12 gene expression. Mol Microbiol *51*, 659-674.

[31] Kostakioti, M., Hadjifrangiskou, M., and Hultgren, S.J. (2013). Bacterial biofilms: development, dispersal, and therapeutic strategies in the dawn of the postantibiotic era. Cold Spring Harb Perspect Med *3*, a010306.

[32] Melo, L. (2005). Biofilm physical structure, internal diffusivity and tortuosity. Water science and Technology *52*, 77-84.

[33] Sauer, K., Cullen, M., Rickard, A., Zeef, L., Davies, D.G., and Gilbert, P. (2004). Characterization of nutrient-induced dispersion in Pseudomonas aeruginosa PAO1 biofilm. J Bacteriol *186*, 7312-7326.

[34] Hong, S.H., Lee, J., and Wood, T.K. (2010). Engineering global regulator Hha of Escherichia coli to control biofilm dispersal. Microbial biotechnology *3*, 717-728.

[35] Monod, J. (1949). The growth of bacterial cultures. Annual Reviews in Microbiology *3*, 371-394.

[36] Stewart, P.S. (1998). A review of experimental measurements of effective diffusive permeabilities and effective diffusion coefficients in biofilms. Biotechnol Bioeng *59*, 261-272.

[37] De Beer, D., Srinivasan, R., and Stewart, P.S. (1994). Direct measurement of chlorine penetration into biofilms during disinfection. Appl Environ Microbiol *60*, 4339-4344.

[38] Thiele, E.W. (1939). Relation between catalytic activity and size of particle. Ind Eng Chem *31*, 916-920.

[39] Characklis, W.G. (1981). Bioengineering report: fouling biofilm development: a process analysis. Biotechnol Bioeng *23*, 1923-1960.

[40] Sherwood, T.K. (1959). Mass transfer between phases (Pennsylvania State University).

[41] Sommerfeld, A. (1909). Ein beitrag zur hydrodynamischen erklaerung der turbulenten fluessigkeitsbewegungen.

[42] Wilhelm, S.E.H. (1955). Production of steam under pressure (Google Patents).

[43] Gekas, V., and Hallström, B. (1987). Mass transfer in the membrane concentration polarization layer under turbulent cross flow: I. Critical literature review and adaptation of existing sherwood correlations to membrane operations. Journal of Membrane Science *30*, 153-170.

[44] Wang, G., Yuan, X., and Yu, K. (2005). Review of mass-transfer correlations for packed columns. Ind Eng Chem Res *44*, 8715-8729.

[45] Thompson, B. (1967). A critical review of existing methods of calculating the turbulent boundary layer (HM Stationery Office).

[46] Incropera, F.P., Lavine, A.S., Bergman, T.L., and DeWitt, D.P. (2007). Fundamentals of heat and mass transfer (Wiley).

[47] Valentine, J.S., Foote, C.S., Greenberg, A., and Liebman, J.F. (2012). Active oxygen in biochemistry, Vol 3 (Springer Science & Business Media).

[48] Bekker, A., Holland, H., Wang, P.-L., Rumble Iii, D., Stein, H., Hannah, J., Coetzee, L., and Beukes, N. (2004). Dating the rise of atmospheric oxygen. Nature *427*, 117.

[49] Anbar, A.D., Duan, Y., Lyons, T.W., Arnold, G.L., Kendall, B., Creaser, R.A., Kaufman, A.J., Gordon, G.W., Scott, C., and Garvin, J. (2007). A whiff of oxygen before the great oxidation event? Science *317*, 1903-1906.

[50] Dorado, G., Rey, I., Sánchez-Cañete, F.J.S., Luque, F., Jiménez, I., Morales, A., Gálvez, M., Sáiz, J., Sánchez, A., and Hernández, P. (2010). Biological mass extinctions on planet Earth. Archaeobios, 53.

[51] Phelan, V.V., Liu, W.-T., Pogliano, K., and Dorrestein, P.C. (2012). Microbial metabolic exchange—the chemotype-to-phenotype link. Nat Chem Biol *8*, 26.

[52] Liu, X., Roe, F., Jesaitis, A., and Lewandowski, Z. (1998). Resistance of biofilms to the catalase inhibitor 3-amino-1, 2, 4-triazole. Biotechnol Bioeng *59*, 156-162.

[53] Britigan, B.E., and Cohen, M.S. (1986). Effects of human serum on bacterial competition with neutrophils for molecular oxygen. Infect Immun *52*, 657-663.

[54] Jesaitis, A.J., Franklin, M.J., Berglund, D., Sasaki, M., Lord, C.I., Bleazard, J.B., Duffy, J.E., Beyenal, H., and Lewandowski, Z. (2003). Compromised host defense on Pseudomonas aeruginosa biofilms: Characterization of neutrophil and biofilm interactions. J Immunol *171*, 4329-4339.

[55] Schreml, S., Szeimies, R.M., Prantl, L., Karrer, S., Landthaler, M., and Babilas, P. (2010). Oxygen in acute and chronic wound healing. Br J Dermatol *163*, 257-268.

[56] Ueno, T., Omi, T., Uchida, E., Yokota, H., and Kawana, S. (2014). Evaluation of hyperbaric oxygen therapy for chronic wounds. Journal of Nippon Medical School *81*, 4-11.

[57] Lee, W., Lewandowski, Z., Nielsen, P.H., and Hamilton, W.A. (1995). Role of sulfate-reducing bacteria in corrosion of mild steel: a review. Biofouling *8*, 165-194.

[58] Drews, A., Lee, C.-H., and Kraume, M. (2006). Membrane fouling-a review on the role of EPS. Desalination *200*, 186-188.

[59] Guo, W., Ngo, H.-H., and Li, J. (2012). A mini-review on membrane fouling. Bioresource technology *122*, 27-34.

[60] Thapa, B., Kc, A.K., and Ghimire, A. (2012). A review on bioremediation of petroleum hydrocarbon contaminants in soil. Kathmandu university journal of science, engineering and technology *8*, 164-170.

[61] Pardieck, D.L., Bouwer, E.J., and Stone, A.T. (1992). Hydrogen peroxide use to increase oxidant capacity for in situ bioremediation of contaminated soils and aquifers: A review. Journal of Contaminant Hydrology *9*, 221-242.

[62] Ahn, Y.-H. (2006). Sustainable nitrogen elimination biotechnologies: a review. Process Biochemistry *41*, 1709-1721.

[63] Chan, Y.J., Chong, M.F., Law, C.L., and Hassell, D. (2009). A review on anaerobic–aerobic treatment of industrial and municipal wastewater. Chemical Engineering Journal *155*, 1-18.

[64] Caldwell, D.E., Kieft, T.L., and Brannan, D.K. (1984). Colonization of sulfide-oxygen interfaces on hot spring tufa by Thermothrix thiopara. Geomicrobiology Journal *3*, 181-200.

[65] Zhulin, I.B., Bespalov, V.A., Johnson, M.S., and Taylor, B.L. (1996). Oxygen taxis and proton motive force in Azospirillum brasilense. J Bacteriol *178*, 5199-5204.

[66] Hayat, R., Ali, S., Amara, U., Khalid, R., and Ahmed, I. (2010). Soil beneficial bacteria and their role in plant growth promotion: a review. Annals of microbiology *60*, 579-598.

[67] Lewandowski, Z., Walser, G., and Characklis, W.G. (1991). Reaction kinetics in biofilms. Biotechnol Bioeng *38*, 877-882.

[68] Stolper, D.A., Revsbech, N.P., and Canfield, D.E. (2010). Aerobic growth at nanomolar oxygen concentrations. Proceedings of the National Academy of Sciences *107*, 18755-18760.

[69] Fleischmann, M., and Pons, S. (1987). The behavior of microelectrodes. Anal Chem *59*, 1391A-1399A.

[70] Davies, P.W., and Brink, F. (1942). Microelectrodes for measuring local oxygen tension in animal tissues. Rev Sci Instrum *13*, 524-533.

[71] Silver, I.A. (1973). Problems in the investigation of tissue oxygen microenvironment. In Chemical Engineering in Medicine (American Chemical Society), pp. 343-352.

CHAPTER FIVE: SPATIOTEMPORAL MAPPING OF OXYGEN IN A MICROBIALLY-IMPACTED PACKED BED USING ^{19}F NUCLEAR MAGNETIC RESONANCE OXIMETRY

Contribution of Authors and Co-Authors

Manuscript in Chapter 5

Author: Jeffrey W. Simkins

Contributions: Helped conceive and implement experimental system. Collected and analyzed data. Wrote manuscript. Incorporated revisions and provided feedback on reviewer comments.

Co-Author: Philip S. Stewart

Contributions: Helped conceive and implement experimental system. Secured funding. Provided feedback on manuscript.

Co-Author: Joseph D. Seymour

Contributions: Helped conceive and implement experimental system. Provided training on experimental methodology. Secured funding. Provided feedback on manuscript.

Manuscript Information Page

Jeffrey W. Simkins, Philip S. Stewart, and Joseph D. Seymour

The Journal of Magnetic Resonance

Status of Manuscript: (Put an x in one of the options below)
____ Prepared for submission to a peer-reviewed journal
____ Officially submitted to a peer-review journal
____ Accepted by a peer-reviewed journal
__X_ Published in a peer-reviewed journal

Elsevier
Vol 293, pages 123-133, August 2018

https://doi.org/10.1016/j.jmr.2018.06.008

SPATIOTEMPORAL MAPPING OF OXYGEN IN A MICROBIALLY-IMPACTED PACKED BED USING ^{19}F NUCLEAR MAGNETIC RESONANCE OXIMETRY

Abstract

^{19}F magnetic resonance has been used in the medical field for quantifying oxygenation in blood, tissues, and tumors. The ^{19}F NMR oximetry technique exploits the affinity of molecular oxygen for liquid fluorocarbon phases, and the resulting linear dependence of ^{19}F spin-lattice relaxation rate R_1 on local oxygen concentration. Bacterial biofilms, aggregates of bacteria encased in a self-secreted matrix of extracellular polymers, are important in environmental, industrial, and clinical settings and oxygen gradients represent a critical determinant of biofilm function. However, measurement of oxygen distribution in biofilms and biofouled porous media is difficult. Here the ability of ^{19}F NMR oximetry to accurately track oxygen profile development in microbial impacted packed bed systems without impacting oxygen transport is demonstrated. Time-stable and inert fluorocarbon-containing particles are designed which act as oxygen reporters in porous media systems. Particles are generated by emulsifying and entrapping perfluorooctylbromide (PFOB) into alginate gel, resulting in oxygen-sensing alginate beads that are then used as the solid matrix of the packed bed. ^{19}F oxygenation maps, when combined with ^{1}H velocity maps, allow for insight into the interplay between fluid dynamics and oxygen transport phenomena in these complex biofouled systems. Spatial maps of oxygen consumption rate constants are calculated. The growth characteristics of

two bacteria, a non-biofilm forming *Escherichia coli* and *Staphylococcus epidermidis*, a strong biofilm-former, are used to demonstrate the novel data provided by the method.

5.1 Introduction

Bacterial biofilms, aggregates of bacteria encased in a self-secreted matrix of polysaccharides, proteins, nucleic acids and other metabolic products, are ubiquitous in environmental, clinical, and industrial settings. In natural environments, biofilms can be found in habitats as diverse as hot springs [1] to glaciers [2]. In medical contexts, biofilms such as those formed by opportunistic pathogens like *Staphylococcus aureus* commonly colonize chronic wounds and medical devices. Once established, biofilm infections are often all but untreatable and represent a major burden to healthcare and patient quality of life [3]. In industry, biofilms can be a hindrance, for instance in the biofouling of filtration membranes [4], ship hulls [5], and petroleum pipelines [6], but may be useful in other contexts, such as in bioremediation [7] or microbially-aided wastewater treatment [8]. In all of these cases, oxygen availability is one of the most critical parameters governing biofilm presentation [9].

Current methods for oxygen quantification within a biofilm, even in a laboratory context, are limited. The current standard for oxygen measurement in biofilm systems is the microelectrode [10; 11], which enjoys the advantage of high sensitivity. However, the microelectrode has three limitations. First, measurement is restricted to a single spatial point at a time [12], making it time consuming and unfeasible for dynamic tracking of oxygenation in non-steady state systems. Second, microelectrodes are invasive; the

biofilm must be physically penetrated to obtain a reading, potentially causing influx of oxygen during electrode insertion [13]. Finally, microelectrodes are ill-suited to contained systems such as packed bed columns, where introduction of the oxygen sensor becomes cumbersome.

^{19}F Nuclear Magnetic Resonance (NMR) and imaging (MRI) oximetry has the potential to overcome the characteristic setbacks of the electrode in biofilm oxygenation measurement. The technique, which has been successfully used in the medical literature to quantify oxygenation in blood [14], tumors [15], and tissues [16-18], exploits the linear relationship between ^{19}F spin-lattice relaxation rate R_1 and local oxygen concentration in perfluorocarbon (PFC) phases. While the presence of molecular oxygen hastens the relaxation rate of all nuclei due to its unpaired electrons, the high solubility of oxygen in PFC phases encourages the close proximity of oxygen atoms to the fluorine atoms of PFCs which facilitates strong hyperfine coupling [19]. This provides excellent sensitivity to oxygen changes as compared to ^{1}H NMR [20]. Using this approach, NMR can non-invasively resolve spatial oxygen gradients and, coupled with the fact that NMR is one of the most useful techniques for investigating fluid flow and molecular transport in porous media [21-29], can provide comprehensive analysis of the transport phenomena. To better understand the role of oxygen transport in biofilm-impacted systems, it is critical to elucidate the interactions between fluid flow dynamics, oxygen transport, and biofilm behavior in porous media, as the presented method does.

The present work develops a methodology to investigate the spatiotemporal evolution of oxygen distribution in a packed bed column porous medium contaminated

by either non-biofilm forming *Escherichia coli* [30] or biofilm-forming *Staphylococcus epidermidis* [31]. To facilitate these measurements, time-stable and inert PFC-containing particles are designed that report local oxygen concentration. This was accomplished by entrapping an aqueous emulsion of the PFC perfluorooctylbromide (PFOB) in alginate, resulting in oxygen-reporting alginate beads that can be incorporated as the solid matrix into the packed bed, thus allowing for oxygen to be monitored without impacting its transport or influencing fluid flow. PCF-loaded alginate beads have previously been used to evaluate oxygen delivery to encapsulated foreign cells implanted into rat tissues [32; 33]. As validation that the technique can provide accurate and precise measurements in a packed bed column with a heterogeneous oxygen sink, it is demonstrated that ^{19}F NMR oximetry accurately tracks oxygen distribution in a controlled system experiencing rapid evolution in oxygen profile over time and space. Despite applications to imaging oxygen in tumors and animal models [14-18], to our knowledge there exist no experiments confirming that the presence of the high oxygen-soluble PFCs does not significantly enhance, hinder, or otherwise alter oxygen transport. In order to quantitatively determine the impact of PFC on oxygen transport, time dependent oxygen diffusion into two samples, a neat liquid sample of the PFC hexafluorobenzene and an agarose gel containing dispersed HFB, was stimulated by pressurizing the samples. The pO_2 is monitored over time and the data compared to the analytical equation governing the conditions of the experiment. Concordance of the experimental results and theory demonstrate the quantitative nature of the measurement and verify the addition of PFC does not alter oxygen diffusion in the gel phase of the beads. This validation coupled with

the MRI measurements of bacterially-induced oxygen gradients provide a new NMR-based technique for studying microbial and biofilm systems. Note this research examines the evolution of oxygen gradients on the mesoscale of porous media, *i.e.* lengthscales on the order of hundreds of microns. Investigation of microscale variability in oxygen concentration as within individual biofilm colonies is an extension of this method which will require further refinement of the fluorinated hydrocarbon dispersion properties.

5.2 Methods

5.2.1 pO_2 vs R_1 Calibration Curve for HFB and PFOB

All experiments were performed on a 7 T vertical-bore magnet with an actively shielded micro2.5 gradient probe providing 1.5 T/m at 60 A, under the control of a Bruker Avance III MRI spectrometer. To construct a calibration curve for the R_1 of HFB as a response to pO_2 in the range of 18 to 180 kPa (85 kPa atmospheric pressure in Bozeman, MT, USA to 850 kPa pressure with 21% oxygen), a neat liquid-phase aliquot of HFB was loaded into a 3 mm ID/5 mm OD polyether ether ketone pressure cell designed to safely maintain the sample under high pressure. The sample was inserted into a 5 mm $^{1}H/^{19}F$ dual tuning coil and connected to a Teledyne Isco Model 500D syringe pump filled with laboratory air at atmospheric pressure. A bulk spin-lattice relaxation rate R_1 (=1/T_1) was collected and the overall pressure was adjusted to 2.5, 5, 7.5, and 10 times atmospheric pressure. After reaching equilibrium (~8 hours), an R_1 was collected for each pressure point. This process was repeated for three HFB samples to yield triplicate values for each measurement. R_1 was measured using an Inversion Recovery (IR) sequence with

the time domain sampled logarithmically at six points (TI = 25, 100, 300, 600, 1000, 3000, 5000 ms). Time-domain data was fit using Levenberg-Marquardt least-squares regression to a three-parameter mono-exponential formula governing the IR pulse sequence, yielding values for both signal intensity and R_1.

To construct a calibration curve for the R_1 of PFOB as a function of pO_2 in the anoxic to atmospheric range, 0 to 18 kPa, relevant to bacterial growth conditions, we followed the procedure outlined by Mason *et al* [15]. Alginate beads containing 90% w/v dispersed PFOB were prepared as described in section 5.2.4. The beads were placed into a 25 mL sample bottle immersed in DI water, and gases of variable oxygen content (100% air, 75% air/25% N_2, 50% air/50% N_2, 25% air/75% N_2, 100% N_2) were bubbled through the solution vigorously for 30 min. The area immediately above the liquid line was flooded with the appropriate gas, and the bottle was immediately sealed. The bottle was then loaded into a 25 mm dual tuning $^1H/^{19}F$ rf coil and R_1 for the CF_3 group was monitored over time. R_1 at t = 1 hour was recorded, as R_1 was found to be equilibrated by this point. Three replicates were acquired for each point using different aliquots. Selective excitation of the CF_3 peak was accomplished using a 2 ms rf excitation pulse.

5.2.2 Agarose Gel Containing Dispersed HFB

To verify dispersed PFCs can be used to quantitatively measure the temporal evolution of pO_2 gradients and evaluate the impact of the presence of high oxygen soluble PFC on transport, O_2 diffusion was stimulated into a neat aliquot of HFB and a gel containing dispersed HFB droplets. A 0.5 g low-gelling agarose powder (Sigma;

A0701) was mixed in 25 mL DI water to form a 2% agarose gel solution, autoclaved for 20 minutes, and maintained at 40 ºC on a hot plate with stirring. 2 mL HFB was added to make a 13% w/v solution and the mixture was mixed for 30 minutes at 15,000 rpm using a Heidolph SilentCrusher M shear mixer to form a liquid dispersion. It was then immediately quenched in an ice bath, locking in HFB droplet structure. Once cooled, a plug of gel was extracted and loaded into a PEEK cell constructed for high pressure gas studies. The sample was then connected to an Isco pump filled with laboratory air at atmospheric pressure and a ^{19}F one-dimensional sagittal R_1 profile was recorded (FOV: 15 mm, resolution: 234 μm, TE: 10 ms, TR: 10 s, 14 averages, AQ time: 14 min). To stimulate oxygen diffusion into the sample, the system was then pressurized from ambient pressure (85 kPa in Bozeman, MT, USA) to 850 kPa and continuous 1D spatial ^{19}F R_1 profiles were recorded to observe the evolution in spatiotemporal oxygen distribution. This experiment was also conducted on a sample of neat HFB.

5.2.3 Bacterial Cultivation

Two bacterial species were used in these experiments. The first was an *Escherichia coli* HB101 strain containing plasmid pMF440 (provided by Dr. Michael Franklin; Addgene plasmid #62550). The plasmid confers strong constitutive expression of red fluorescent protein (RFP) recombinant mCherry, allowing for ease of strain identification, along with co-expressed ampicillin resistance gene. Inocula were grown overnight at 37 ºC with shaking in full-strength tryptic soy broth (TSB) and 100 μg/mL ampicillin to promote retention of the plasmid. This *E. coli* strain does not form biofilms

[30]. The second bacterium was *S. epidermidis* strain RP62A, a model biofilm-former [31]. *S. epidermidis* was cultured in the same manner as *E. coli*, but in the absence of ampicillin.

5.2.4 Oxygen-Sensing Alginate Beads

To make the ^{19}F oxygen-sensing particles, 0.4 g α-phosphatidylcholine surfactant (Sigma; P3556) and 0.2 g low-viscosity sodium alginate (Sigma; A1112) was dissolved in 10 mL DI water. Then 9 g PFOB (Aurum Pharmatech; K-8801) was added and the solution was emulsified at 15,000 rpm for 30 minutes using a shear mixer to form a stable, 90% w/v emulsion of PFOB in a 2% w/v sodium alginate solution. The emulsion was divided into two aliquots, and the first aliquot was dripped into a 50 mM solution of calcium chloride (Sigma; C1016), generating spherical alginate beads approximately 3 mm in diameter containing dispersed PFC (Figure 5.1). The second aliquot was inoculated with either *E. coli* or *S. epidermidis* and the solution was prepared into alginate beads as described above. Alginate gel immobilization of biological cells is a widely used technique [34-39], and as the alginate structure is chemically and biologically inert, we do not anticipate any negative effects of entrapment on the growth of *E. coli* or *S. epidermidis*. A 1 mL aliquot of overnight culture was centrifuged at 6,000 rpm for 4 minutes, the supernatant was removed, and cells were resuspended in phosphate buffered saline and diluted 1:200. 100μL of this inoculant was then added to 5 mL of the second emulsion aliquot for a total dilution of 1:10,000. Both sterile beads and inoculated beads were incubated overnight in 1/10 strength TSB nutrient solution

containing 50 mM calcium chloride. All glassware and the shear mixer downshaft were autoclaved prior to bead production, and all operations were carried out in a biological cabinet with airflow to minimize contamination by environmental microbes.

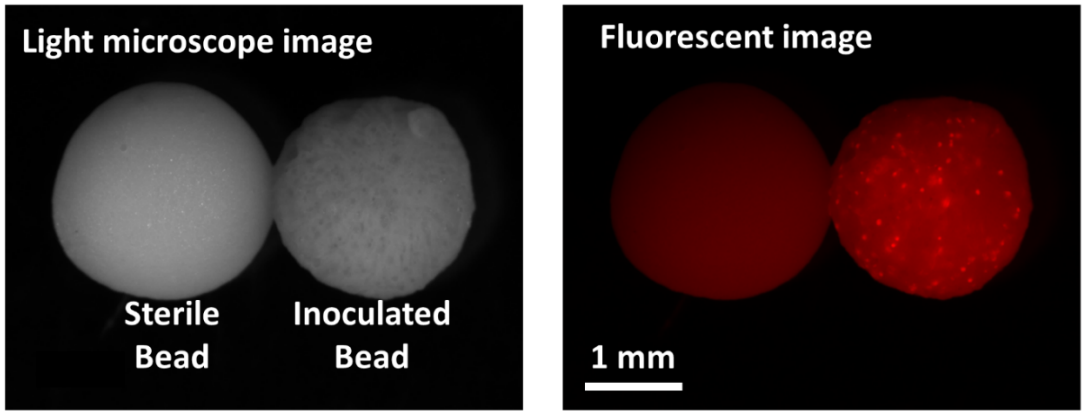

Figure 5.1. Light microscope and fluorescent microscope images of 3 mm diameter oxygen-sensing alginate beads. A 90% w/v emulsion of PFOB is contained within the alginate matrix of each bead, permitting for oxygen measurement via the R_1 of the PFOB CF_3 group. The bead on the right has been inoculated with an RFP-expressing *E. coli* mutant, allowing for visualization of biofilm growth on the bead surface. Scale bar indicates 1 mm.

5.2.5 Alginate Beads Stacked in Tube

Sterile incubated beads were removed from the incubating flask and placed on a paper towel to remove excess nutrient broth. A 5 mm NMR tube was filled with 200 µL DI water and 3 sterile beads were placed into the tube. A single inoculated bead, identified by its pink color, was wet loaded above the sterile beads, and three more sterile beads were placed above it. The tube was capped and loaded into the 5 mm coil and 1D ^{19}F sagittal R_1 profile (parameters in section 5.2.2) was recorded continuously to track oxygen profile development. Once conditions were uniformly anoxic due to bacterial

oxygen consumption, a ^{19}F sagittal image (FOV: 15 x 5 mm^2, resolution: 117 x 156 μm^2, TE: 8 ms, 8 echoes, TR: 1 s, 1 mm slice, 32 averages, AQ time: 17 min) and ^{1}H sagittal image (FOV: 15 x 5 mm^2, resolution: 117 x 78 μm^2, TE: 8 ms, 16 echoes, TR: 1 s, 1 mm slice, 8 averages, AQ time: 8.5 min) were recorded. R_1 was measured using inversion recovery with six inversion times as described in section 5.2.1, and the CF_3 peak was imaged selectively by using a chemically-selective excitation pulse and a slice-selective refocusing pulse.

5.2.6 Packed Bed Column Containing Alginate Beads

Sterile incubated beads were removed from the incubating flask and placed on a paper towel to remove excess nutrient broth. A freshly autoclaved, 10 mm ID liquid chromatography column (Omnifit Labware) with 30 µm filters at both ends was filled with DI water and the beads were wet loaded into the column. A single inoculated bead was loaded and its position manipulated using a spatula to the region of the column corresponding to the isocenter once inserted into the coil. The column was then filled to the top with sterile beads and connected to a High Performance Liquid Chromatography Pharmacia P-500 pump with 1.9 mm ID Teflon tubing, inserted into the coil, loaded into the magnet, and maintained at 22.8 ºC.

The feed stream for the packed bed column consisted of 2 L of 1/100 strength TSB with 50 mM calcium chloride, with the inclusion of calcium chloride in the feed preventing dissolution of the alginate structure over long periods due to calcium ion diffusion out of the alginate gel matrix. The solution was prepared by autoclave, allowed

several hours to cool, and laboratory air was bubbled through the carboy for one hour to replenish the dissolved oxygen lost in the autoclave process. Bacterial air filters were incorporated into the feed bottle inlet and offgas tubing to prevent introduction of bacteria during bubbling.

The feed reservoir was connected to the pump and the outlet of the packed bed column was connected to a waste collection bottle, forming an open flowthrough loop (Figure 5.2). The dilute nutrient feed was pumped through the bed at 25 mL/hr with a superficial velocity of 0.08 mm/sec. Oxygen was monitored over the course of bacterial growth by rotating through 1D sagittal profile, 2D axial, and 2D sagittal ^{19}F R_1 maps. 1D profile parameters are given in section 5.2.2, while the 2D R_1 maps (both sagittal and axial) sampled only 3 points along the IR curve (TI = 25, 1000, 3000 ms) to reduce acquisition time (FOV: 15 x 12 mm^2, resolution: 469 x 375 μm^2, TE: 8 ms, 1 echo, TR: 15 s, 3 mm slice, 8 averages, AQ time: 192 min). Pixels were only assigned an R_1 value if they met a threshold signal value (10^5) and the associated standard error for the R_1 parameter fit was below 20%.

Fluid flow velocity distribution was measured with two ^1H sagittal velocity maps, one with velocity sensitivity in the slice direction and one in the read direction, both with no-flow correction (FOV: 15 x 12 mm^2, resolution: 117 x 187.5 μm^2, TE: 13.8 ms, TR: 1 s, 1 mm slice, 8 averages, δ: 1 ms, Δ: 8.5 ms, $G_{flow\ encode}$: 0.51 T/m, AQ time: 17 min) and 3 axial velocity maps centered around the location of the inoculated bead with velocity encoded in the axial slice direction (FOV: 12 x 12 mm^2, resolution: 93 x 187.5 μm^2, TE:

13.8 ms, TR: 1 s, 1 mm slice, 8 averages, δ: 1 ms, Δ: 8.5 ms, $G_{flow\ encode}$: 0.51 T/m, AQ time: 17 min).

To demonstrate that the source of oxygen consumption was in fact bacterial activity, following the complete evacuation of oxygen from the column the feed reservoir was replaced with a 50mM calcium chloride solution with no nutrient present. Oxygen profiles were then acquired to observe the return of oxygen to the sample in the absence of an energy source to sustain bacterial respiration.

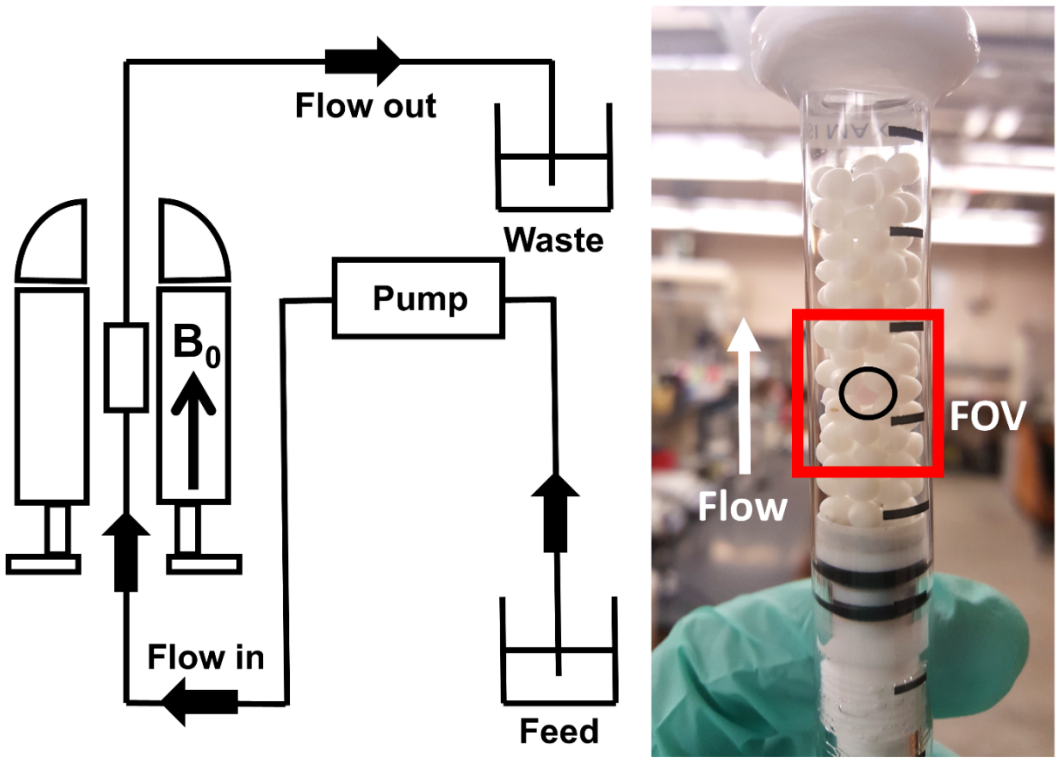

Figure 5.2. Schematic for flowthrough loop setup (left) and image of 10 mm ID chromatography column filled with oxygen-sensing alginate beads as the solid matrix. The single inoculated bead, placed at the location corresponding to the isocenter of the coil, is located within the black circle.

5.3. Results and Discussion

5.3.1 pO_2 vs R_1 Calibration Curves

HFB and PFOB exhibit strong sensitivity to changes in oxygen concentration (Figure 5.3) and relatively low sensitivity to temperature [15]. All experiments were conducted at 22.8 ºC with fluctuations on the order of ±0.5 C, such that accuracy and precision of pO_2 measurements are not impacted by variation in temperature. The calibration data are shown in Fig. 3. The ability to detect small changes in pO_2 is a function of both sensitivity of R_1 to pO_2 and inherent PFC signal to noise ratio. The relative precisions of different PFCs in oxygen measurement and how to compare them has been discussed at length by Thomas *et al*. [40]. They showed that to minimize fractional uncertainty in pO_2, the fractional sensitivity η (defined as slope/intercept), should be as large as possible. With an η of 25.2, HFB exhibited higher sensitivity to pO_2 than PFOB with an η of 4.7, consistent with the literature [15], and with theoretical considerations [19]. HFB also provides a single resonance with high spin density, yielding much greater signal to noise ratios. It should be noted that, due to the higher overall T_1 range of HFB (>9 sec to ~1.9 sec in the 0 to 18 kPa pO_2 range), some of the benefits of this signal increase are lost due to longer acquisition time as larger TR values must be used relative to PFOB (<3 sec to <1.5 sec T_1 range).

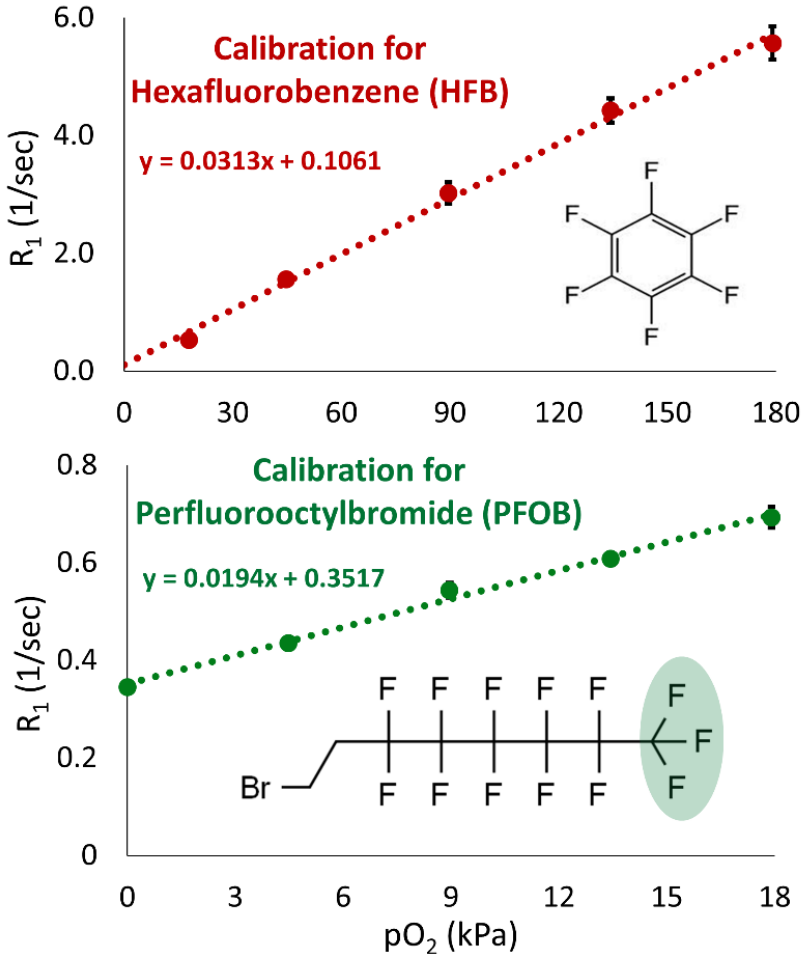

Figure 5.3. Calibration curves relating the response of spin-lattice relaxation R_1 to pO_2 for (top) pure HFB and (bottom) PFOB encapsulated in alginate beads at 7 T and 22.8 °C. All points were measured in triplicate, and error bars denote standard deviation. Where error bars are not apparent, standard deviation is smaller than the marker size. The selected peak for PFOB (CF_3 group) is highlighted in green.

Due to HFB's stronger single resonance signal, fractional sensitivity, and high oxygen solubility, it was selected to verify the ability to quantify the transient diffusion of oxygen. By running this study in the range of 85 kPa to 850 kPa (18 to 180 kPa pO_2), where T_1 values are shorter for HFB (~1.9 sec to 0.2 sec), prohibitively long TR times were avoided and high temporal resolution of O_2 diffusion into the samples was achieved.

In addition, HFB is volatile, so conducting the experiment at elevated pressure prevented evaporation. HFB was determined to be unsuitable for use in the packed bed column due to the inability to form stable HFB-in-water emulsions [41]. Therefore PFOB, which readily forms stable high-concentration emulsions in water, was used for this application.

5.3.2 Transient Diffusion of Oxygen

Pressurizing a sample of neat liquid HFB to 10 times atmospheric pressure resulted in forced diffusion into the sample. Figure 5.4A shows an example 1D ^{19}F R_1 depth profile taken soon after sample pressurization to 850 kPa (t = 70 min). Near the gas interface, R_1 has already achieved its steady state value corresponding to a pO_2 of 180 kPa. However, at greater depths, *i.e.* further from the gel-air interface, R_1 values are still lower, as oxygen has not yet had enough time to diffuse down. Transforming R_1 values for all time and spatial coordinates according to the calibration curve (Figure 5.3), we observe that for each depth coordinate, oxygen concentration exponentially increases from its initial condition (pO_2 = 18 kPa) to its steady state value (pO_2 = 850 kPa), but the timescale of transience increases with increasing depth in the gel (Fig 4B). Results for the agarose gel containing dispersed HFB (Fig 4C) are similar; however, in this sample, it takes longer for oxygen to fully permeate the sample. This is due to the slower rate of diffusion in the aqueous phase relative to the pure HFB phase.

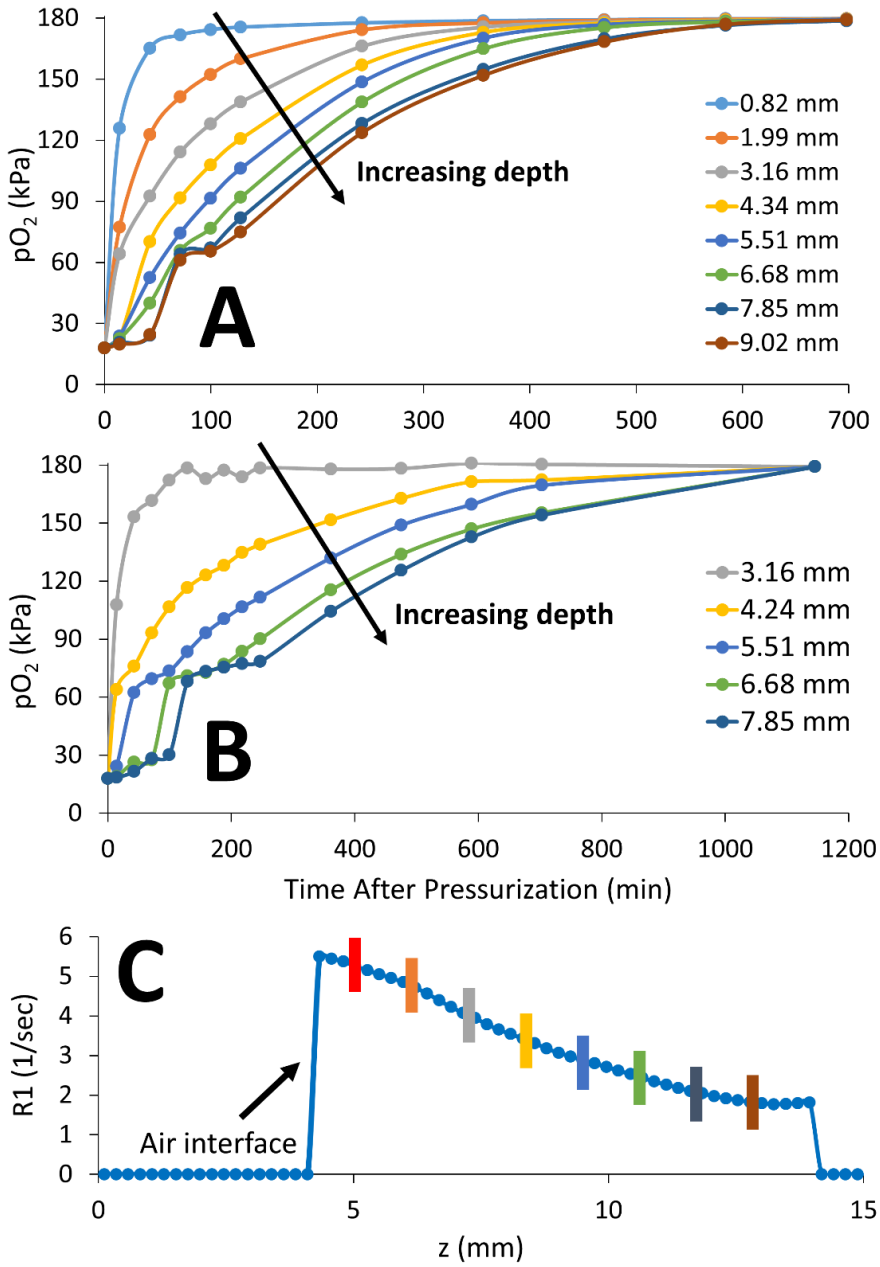

Figure 5.4. Calculated oxygen depth profiles over time for (A) pure HFB and (B) a 2% w/v agarose gel containing 12% w/v HFB after stimulating oxygen diffusion into the sample by pressurizing from 85 to 850 kPa. An example profile R_1 for pure HFB, this one collected at t = 78 min after sample pressurization, is shown in (C). The resolution is 234 µm/pixel. These R_1 profiles were transformed according to the HFB R_1 vs pO_2 calibration curve to yield oxygen concentration values as a function of time and depth coordinate. Oxygen values over time for several example depth coordinates are plotted. Note that the time axis is different for the two samples due to reduced rate of diffusion in the gel sample relative to the pure HFB sample.

The transport phenomenon being observed in the experiment described above is the transient diffusion of a dilute species in a finite medium of known length [42]. Assuming constant diffusivity, the governing mass conservation equation is:

$$\frac{\partial C_A}{\partial t} = D_{AB}\nabla^2 C_A \qquad \text{(Eq 5.1)}$$

where C_A is the concentration of species A and D_{AB} is the diffusivity of species A in medium B. Taking species A to be molecular oxygen and averaging signal contribution over the x-y plane (*i.e.* taking a 1D profile), the governing equation reduces to its one dimensional form:

$$\frac{\partial C_{O2}}{\partial t} = D_{O2,B}\frac{\partial^2 C_{O2}}{\partial z^2} \qquad \text{(Eq 5.2)}$$

subject to an initial condition of 18 kPa throughout the medium, a no flux boundary condition at the bottom of the sample tube, and a fixed concentration boundary condition at the gas interface:

$$C_{O2}(t=0) = 18\ kPa \text{ for all } 0 \le z < a$$

$$\frac{\partial C_{O2}}{\partial z}(z=0) = 0$$

$$C_{O2}(z=a) = 180\ kPa$$

The analytical solution is:

$$\frac{C_{surf}-C_{O2}}{C_{surf}-C_o} = \frac{4}{\pi}\sum_{n=0}^{\infty}\frac{(-1)^n}{(2n+1)}e^{\left[\frac{-D_{O2,B}(2n+1)^2\pi^2 t}{4a^2}\right]}\cos\frac{(2n+1)\pi z}{2a} \qquad \text{(Eq 5.3)}$$

where C_{surf} is the concentration at the surface, C_o is the initial concentration in the medium (18 kPa in this case), and a is the height of the sample. Thus, the technique's ability to accurately measure oxygen distribution in complex and rapidly evolving systems can be evaluated by comparing the empirically calculated oxygen profiles with

the above theoretical solution, with the only experimental unknown being the diffusion coefficient.

Agreement between the two datasets is found for both pure HFB and the two-phase agarose gel system, with an observed R^2 of 0.99 for pure HFB and 0.97 for the gel (Figure 5.5). The fit value for the diffusion coefficient of oxygen into neat HFB was 5.5 x 10^{-9} m^2/s. To our knowledge, the direct measurement of the mutual diffusion $D_{O2\text{-}HFB}$ of oxygen into HFB has not been previously reported in the literature. The fit value for the diffusion coefficient of oxygen into the gel is 2.1 x 10^{-9} m^2/s. Han and Bartels provide a practical formula to estimate oxygen diffusivity in pure water that suggests a diffusivity of around 1.9 x 10^{-9} m^2/sec at our operating temperature of 22.8 ºC [43]. The observed diffusion coefficient represents about an 11% increase over that expected for water, indicating modest transport enhancement. Treating the sample as a two-phase system of spheres of HFB in a continuous water phase, we can formulate an estimate for the expected effective diffusion coefficient using Maxwell's approach, summarized in Stewart 1998 [44; 45]. This yields an estimated effective diffusivity of 2.07 x 10^{-9} m^2/sec, very close to our experimental value of 2.1 x 10^{-9} m^2/sec for the gel. This further validates the quantitative accuracy of the measurement in rapidly evolving systems, and demonstrates that the presence of HFB has small impact on the transport properties of the system being probed.

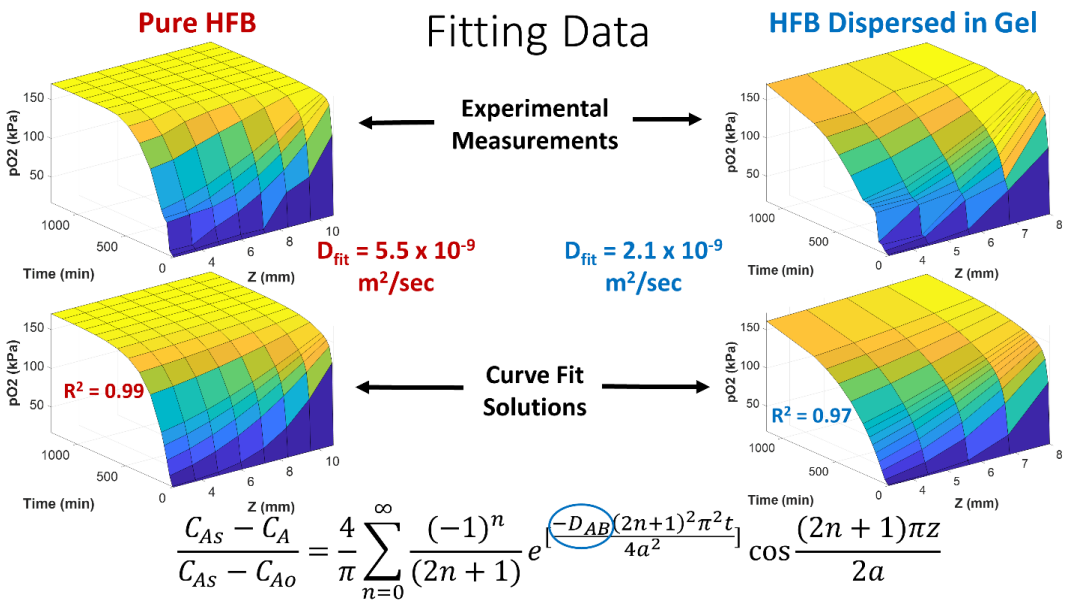

Figure 5.5. (Top experimental data and (bottom) curve fit solutions to the transient diffusion of oxygen through a finite medium of (left) pure HFB and (right) agarose gel containing dispersed HFB. The equation of fit is shown at the bottom, with the experimental unknown (diffusion coefficient) circled in blue.

5.3.3 Bacterial O_2 Consumption in Stacked Alginate Beads without Flow

Oxygenation measurements in bacterial growth experiments were conducted using PFOB which readily forms stable emulsions. This allows the oxygen sensor to remain fixed in flowing systems via encapsulation into alginate beads. The oxygen-sensing alginate beads are stable for at least two weeks (bead behavior over longer periods of incubation has not been investigated), and PFOB R_1 remains constant over this period provided the beads are refrigerated and immersed in a 50 mM solution of calcium chloride to prevent leaching of calcium ions from the alginate matrix. These beads were made to be 3 mm in diameter using a burette of 1 mm aperture to allow for ease of identifying the oxygen sink (a single bead) both visually and via ^{19}F signal. However, the size of the beads can be modified by adjusting the inner diameter of the aperture from

which the emulsion is dripped into the calcium chloride solution, for instance by using a needle tip and coaxial air flow [46]. In addition to PFC encapsulation, alginate beads are also a model system for bacterial culturing due to their simplicity, reproducibility, and ability to replicate characteristics commonly encountered in real-world biofilms such as diffusion limitation, heterogeneous gene expression, antibiotic resistance, and the establishment of steep oxygen gradients [39; 47]

To demonstrate spatial distribution capability, oxygen was monitored in a system consisting of several beads immersed in water and stacked vertically in a 5 mm NMR tube, with the center bead hosting *E. coli* colonies (Figure 5.6). There was no flow in this experiment. No nutrient needed to be added, as there was sufficient TSB remaining within the beads after incubation to stimulate enough growth to fully deplete oxygen within the tube. The inoculated bead was identified both visually by its pink color, and by its reduced signal in the ^{19}F T_1-weighted sagittal image shown at the top of Figure 5.6. Sagittal 1D calculated oxygen profiles indicate that the biofilm acts as a strong oxygen sink even immediately after loading. This is because the 37 ºC overnight incubation period allowed for substantial colonization of the bead before the experiment. The curvature of the oxygen sink also indicates that the biofilm is not able to use all of the available oxygen initially present in the system, *i.e.* there is a finite, nonzero flux *into* the bead. Over time, oxygen in the inoculated bead is depleted entirely and later, throughout the entire sample.

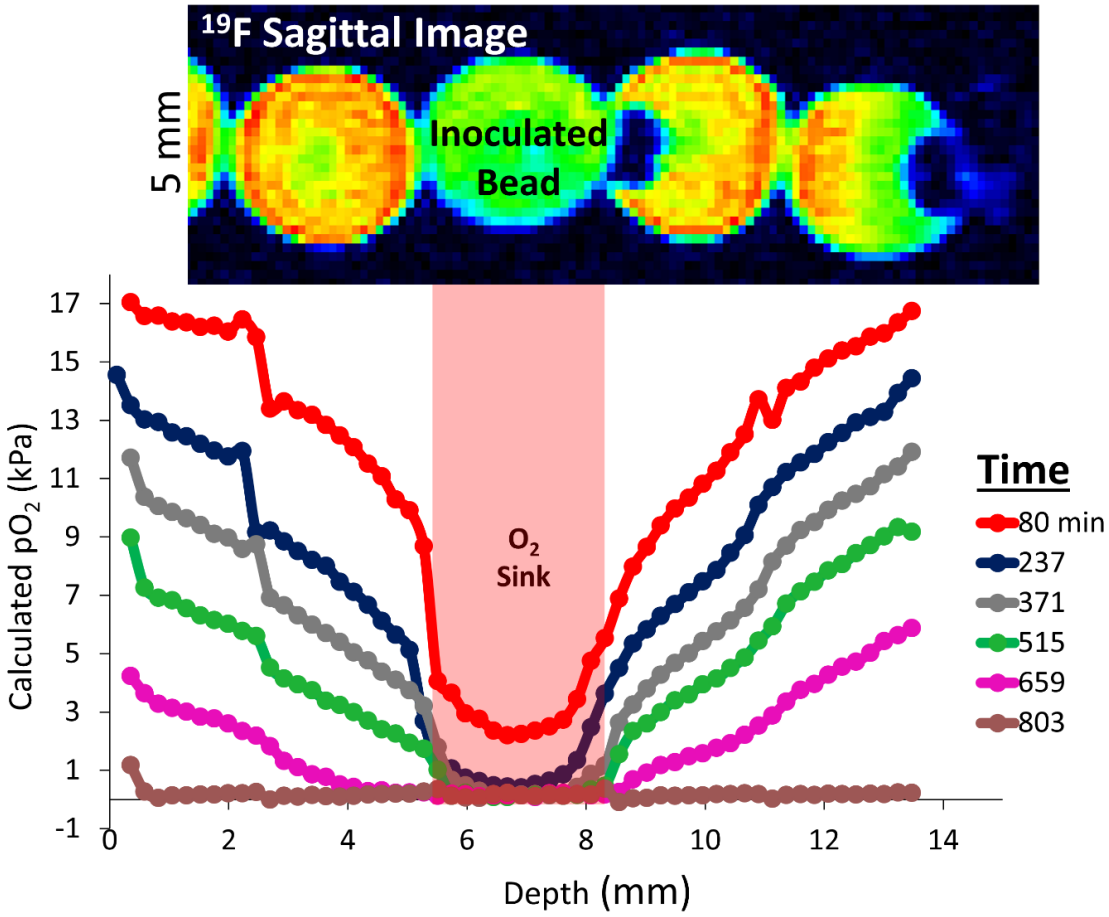

Figure 5.6. Oxygen profile over time in a system of five alginate beads stacked vertically in a 5 mm NMR tube (image and chart have been rotated 90º for ease of viewing). The reduced signal amplitude of the center bead in the T_1-weighted ^{19}F sagittal image (top) identify it as the one containing bacteria.

5.3.4 Bacterial O_2 Consumption in Packed Bed Columns with Flow

In the packed bed system, the single inoculated bead could be easily identified by the location of the oxygen sink in the 1D sagittal profile (Figure 5.7) or 2D sagittal oxygen map (Figure 5.8). Reynolds number for each pack was calculated using bead diameter as the characteristic length, and taking the mean v_z obtained from all axial ^1H velocity images as the fluid velocity. All packed beds were studied with a Reynold's

number on the order of $Re = \frac{\rho v_z D_p}{\mu} \sim 3$, indicating laminar flow [48]. Figure 5.7 shows that for a packed bed inoculated with *E. coli*, the oxygen sink is initially weak, with oxygen depletion proceeding slowly. However, the depth of the oxygen sink accelerates over time, as seen by the stark difference between the oxygen profiles at 912 and 1356 minutes, relative to the 24 and 468 min data. In effect, the exponential growth of the bacteria leads to a tipping point at which bacterial respiration suddenly overwhelms the rate of oxygen replenishment, after which oxygen concentration crashes within the bead. Over the course of 30-35 hours, oxygen levels throughout the field of view drop and result in fully anoxic conditions throughout the column.

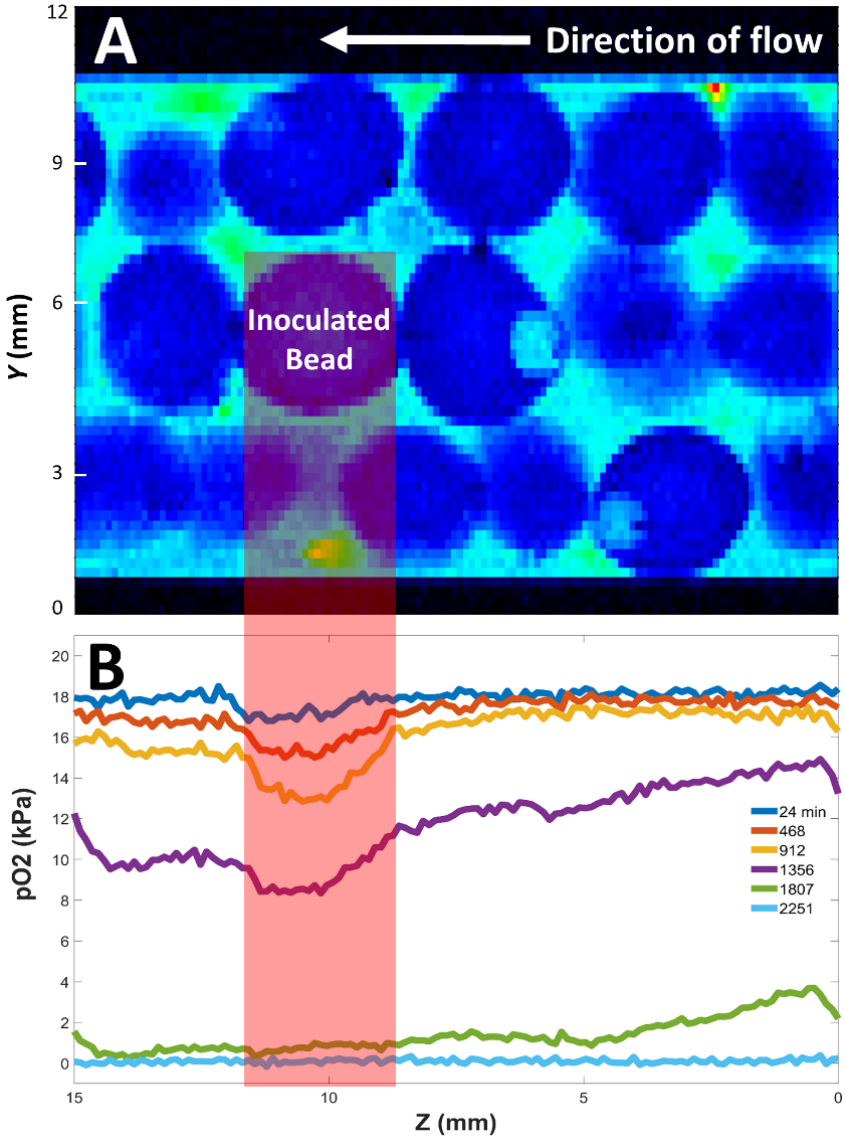

Figure 5.7. (A) ^{1}H sagittal image (117 µm x 187 µm/pixel) of a packed bed column with a single inoculated bead near the isocenter experiencing low Reynolds number flow ($v_{superficial}$ = 0.08 mm/sec) of dilute aerated TSB media (1/100x). (B) Calculated 1D sagittal O_2 profile over time. The strength of the O_2 sink grows over time, and eventually the entire column becomes oxygen depleted.

The 2D sagittal oxygenation maps of the *E. coli* packed bed clearly show the discrete location of the oxygen sink (Figure 5.8). At 264 minutes, oxygen levels within the inoculated bead are between 5 and 10 kPa, indicating incomplete respiration by the

bacteria. The oxygen levels drop to zero over time as the bacteria proliferate. A striking feature is the emergence of an oxygen shadow in the region immediately downstream of the inoculated bead, where incoming fluid pathlines have been stripped of oxygen by the bacteria. The 2D axial oxygenation maps, centered on the *z* coordinate of the oxygenated bead, further support these observations (Figure 5.9). The inoculated bead goes anoxic first, and the depletion spreads out in the radial dimension according to the developing concentration gradient. To demonstrate the sensitivity of the measurement to bacterial metabolism, the feed is then changed from TSB nutrient to a calcium chloride solution. This results in the oxygen slowly returning to the sample, as no respiration can occur in the absence of an electron donor (Figure 5.10). The oxygen recovery data of Figure 5.10 also demonstrate that the quantitation of oxygen concentration is insensitive to the spatial resolution applied, and that the ^{19}F R_1 measurement is insensitive to the presence of the bacterial cells themselves. A consistent characteristic of *E. coli* packed beds is that the oxygen sink, while growing in strength, remains spatially static. Oxygen depletion radiates outward slowly in the radial dimension, while very little upstream translation is observed, as shown in the sagittal O_2 maps of Figure 5.8.

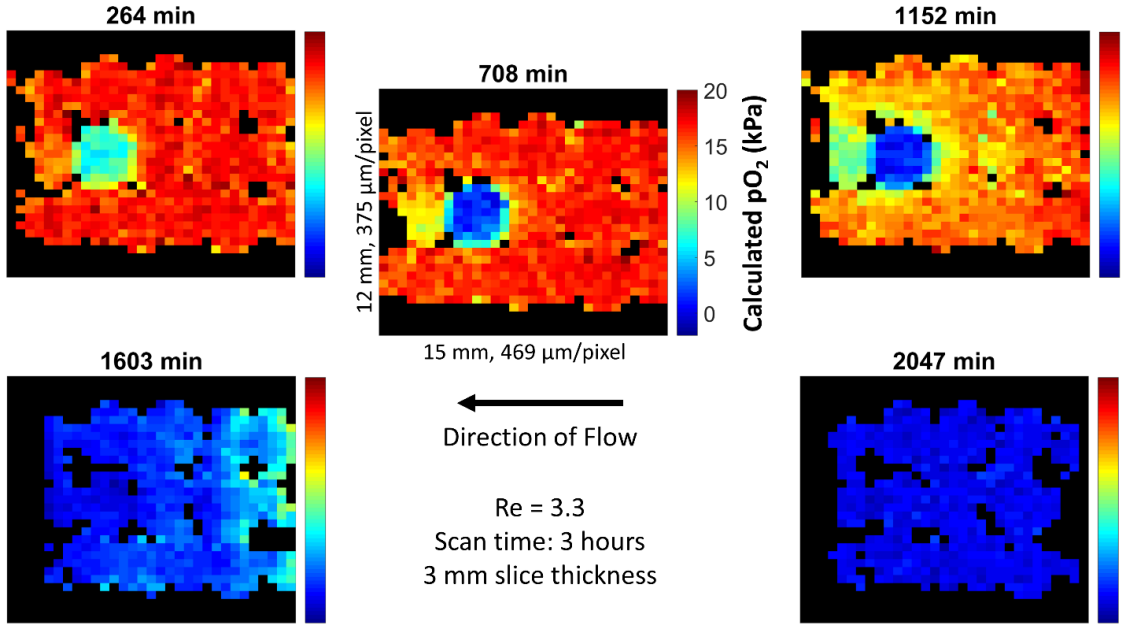

Figure 5.8. Sagittal map of calculated pO_2 values over time within a packed bed column inoculated with *E. coli*.

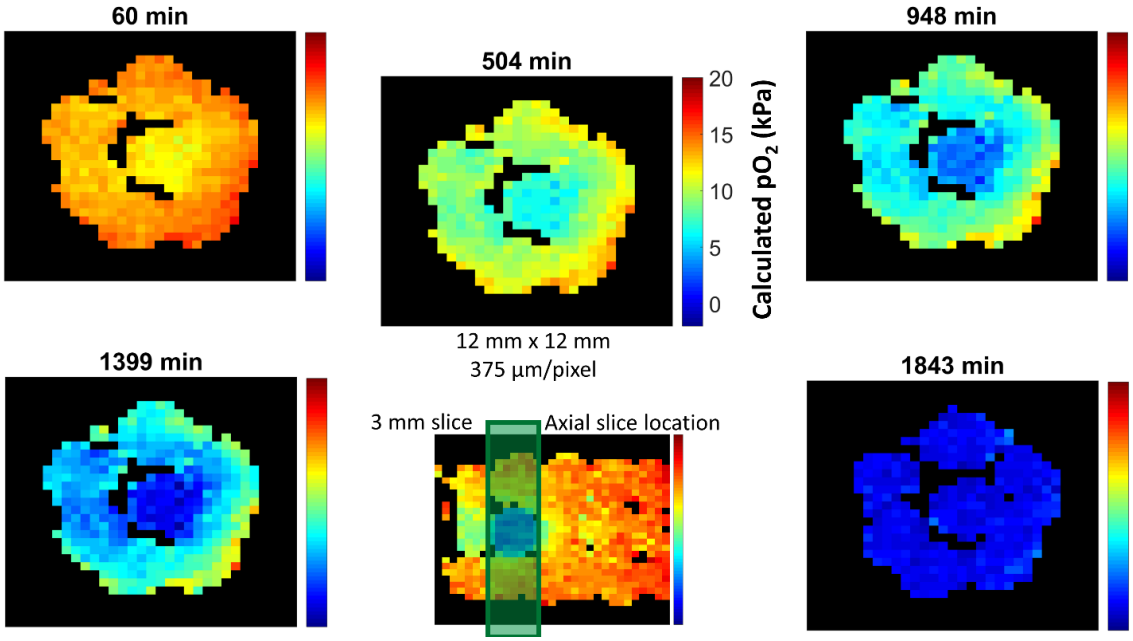

Figure 5.9. Axial map of calculated pO_2 values over time within a packed bed column inoculated with *E. coli*. The slice was taken right at the height coordinate of the inoculated bead.

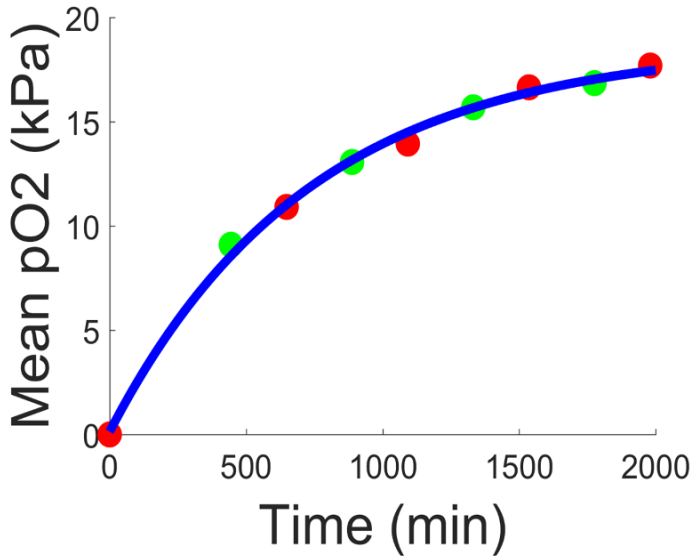

Figure 5.10. Recovery of oxygenation in *E coli* packed bed column after switching feed from a 1/100 strength TSB solution to a 50 mM calcium chloride solution containing no carbon source to sustain respiration. Each data point represents the mean calculated oxygen level. Red dots were acquired from 1D profile O_2 maps and green dots were acquired from 2D sagittal O_2 maps. Axial maps were not included as they acquired signal from only the region near the inoculated bead. Curve fitting reveals an exponential recovery with time constant 0.0014 ± 0.0002)/min.

The behavior of *E. coli* contrasts with the behavior of *S. epidermidis*, a strong biofilm former [31]. Packed beds inoculated with *S. epidermidis* exhibit an increased rate of oxygen consumption shown in the axial O_2 profile at 1018 minutes (Figure 5.11), by which point the image plane is almost completely oxygen deprived. More strikingly, the *S. epidermidis* biofilm is not static, and quickly colonizes the column. The sagittal O_2 profile at 778 min (Figure 5.12) shows a new O_2 sink developing upstream from the original inoculated bead, indicating the dispersal of bacterial cells from the source. This dispersal and colonization is further demonstrated by axial ^1H velocity maps taken at the beginning of the experiment and 44 hours later (Figure 5.13). After 44 hours of bacterial

growth, the porosity of the pack and distribution of z-component velocities in the plane of the inoculated bead remains essentially unchanged when *E coli* is grown. In contrast, over the course of 44 hours of *S. epidermidis* growth, the porosity of the pack decreases by 20%, and average fluid velocity within the remaining pore space spikes by 30%, as a result of biofilm layer formation on the inoculated bead surface. The development of a gel-like biofilm layer is further evidenced by the observation that the pressure drop increased dramatically after around two days of *S. epidermidis* growth, but not *E. coli* growth. This pressure drop spike exhibited a rapid onset and continued until tubing failure at 4 MPa (or until flow was discontinued), occurring on average within 6 hours of complete oxygen depletion in the column. The PFOB alginate beads thus allow us to quantify and observe fundamental differences in how different bacterial species establish oxygen gradients and modify flow.

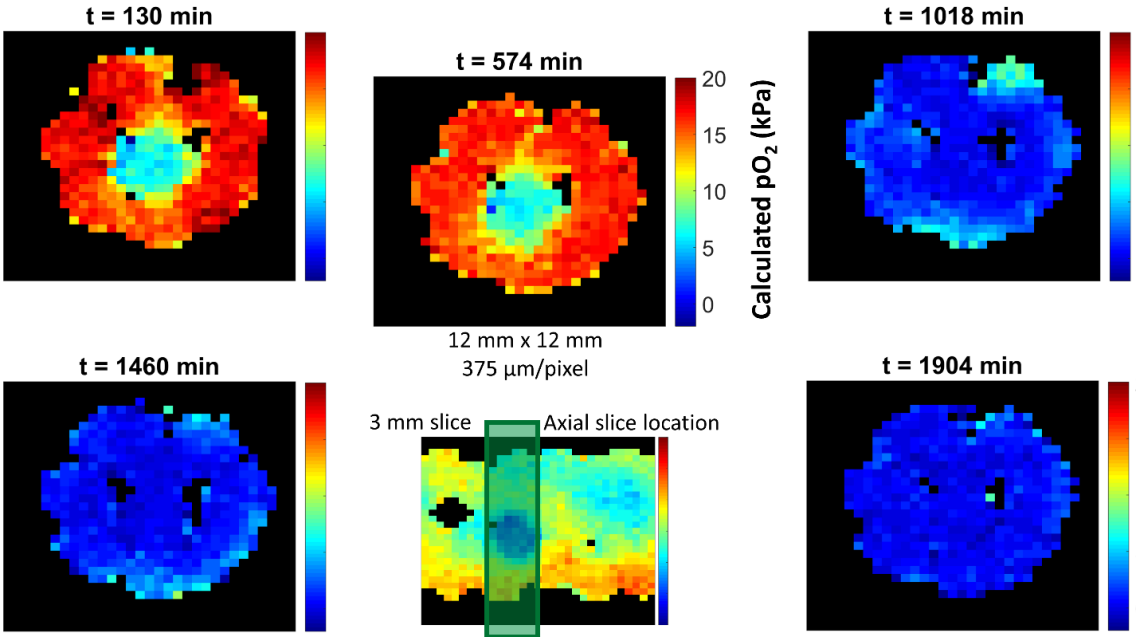

Figure 5.11. Axial map of calculated pO_2 values over time within a packed bed column inoculated with *S. epidermidis*. The slice was taken right at the height coordinate of the inoculated bead.

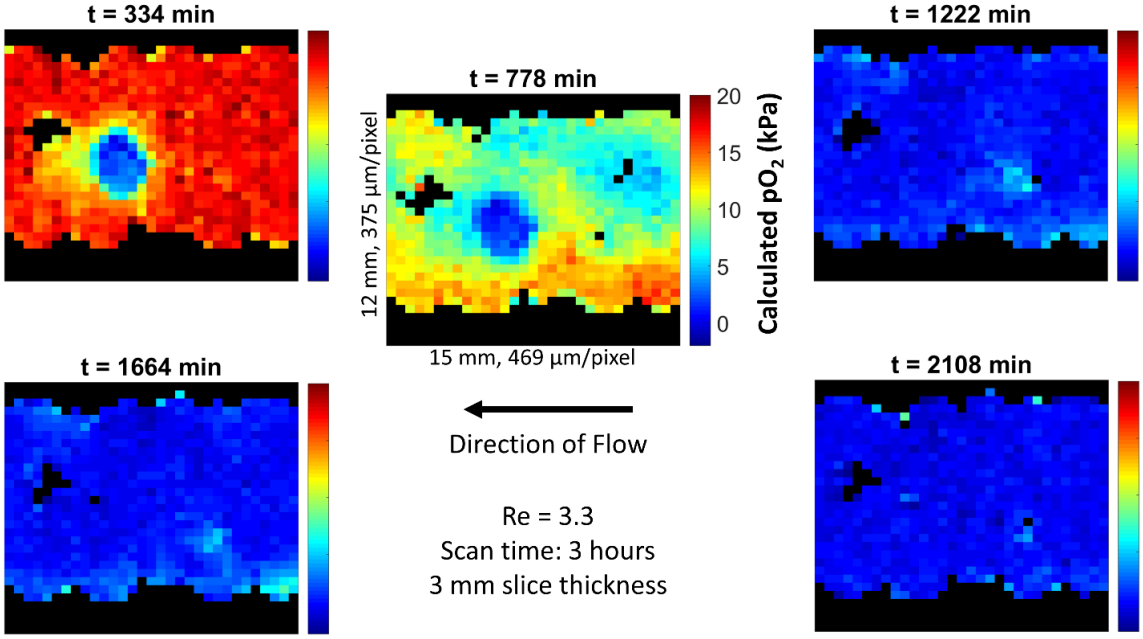

Figure 5.12. Sagittal map of calculated pO_2 values over time within a packed bed column inoculated with *S. epidermidis*.

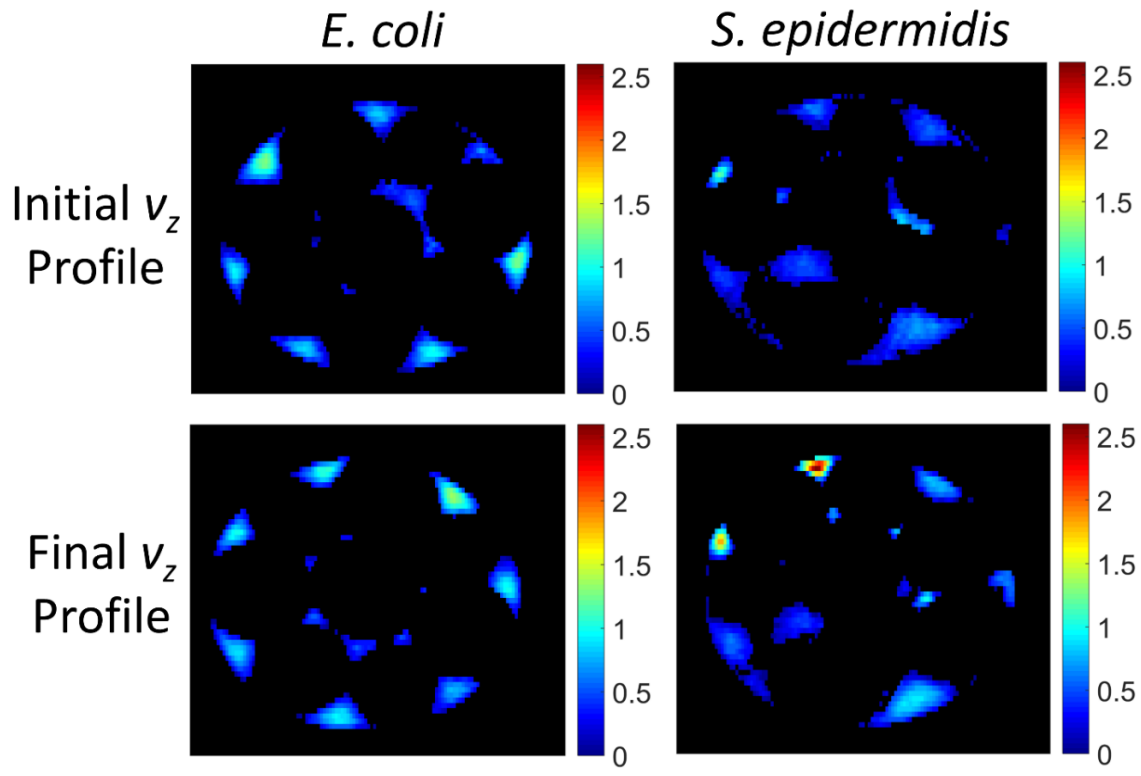

Figure 5.13. Axial ^{1}H v_z velocity maps taken at beginning of growth immediately after loading (top row) and 44 hours later, after establishment of uniform anoxic conditions (bottom row), for two bacterial species, *E. coli* (left column) and *S. epidermidis* (right column). All units are in mm/sec.

A useful attribute of this technique is that it imparts an unprecedented ability to correlate fluid flow dynamics measured with ^{1}H velocity maps, with scalar oxygen transport, measured with ^{19}F R_1 maps. For instance, Figure 5.14 shows a skew in the axial oxygenation profile around the *E. coli* inoculated bead at 1399 minutes, with the bottom-left side of the column experiencing faster oxygen depletion. The hydrogen velocity maps identify a large fluid flow path at this location. This is by far the largest fluid flow path in direct contact with the inoculated bead, as the small D_{column}/D_{bead} ratio encourages flow along the column edges. This region of the bead notably exhibits significantly increased

oxygen consumption, indicating enhanced growth in the proximity of flow. These data are therefore able to discern local variations in both fluid flow and time-dependent oxygen utilization, and to correlate the two measurements.

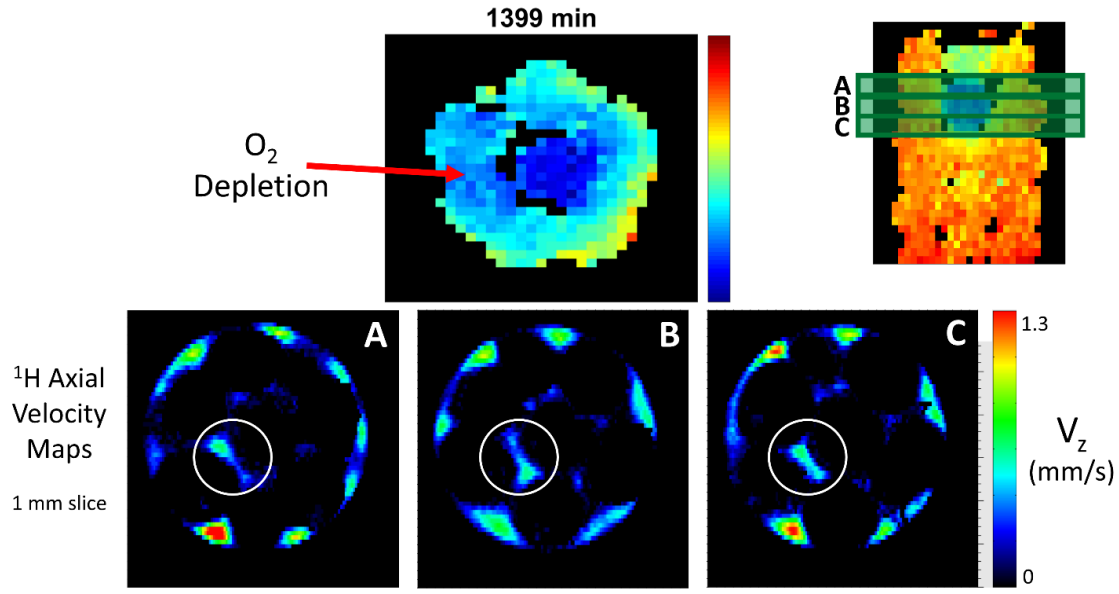

Figure 5.14. (Top) Axial distribution of oxygen at inoculated bead location, indicating accelerated depletion on left side of column. (Bottom) Axial velocity maps showing fluid streamline on left side of column in direct contact with inoculated bead. (Top right) Sagittal oxygen map showing the location of each of the three axial velocity maps.

Another application of the oxygen maps is the ability to fit oxygen decay data to models to determine the spatial distribution of reaction kinetics for bacterial growth, and to extract associated rate constants. Tracking oxygen concentration over time for each pixel reveals an apparent first-order reaction rate, and fitting the data to the corresponding equation extracted a rate constant for each pixel, generating a spatial map detailing bacterial metabolic activity (Figure 5.15). Substantial heterogeneity in oxygen

consumption within the bead is observed, an unsurprising result given the variability in access to fluid pathlines and the stochastic clustering of bacterial colonies in the bead. Bacterial oxygen consumption rates outside of the inoculated bead were found to be negligible.

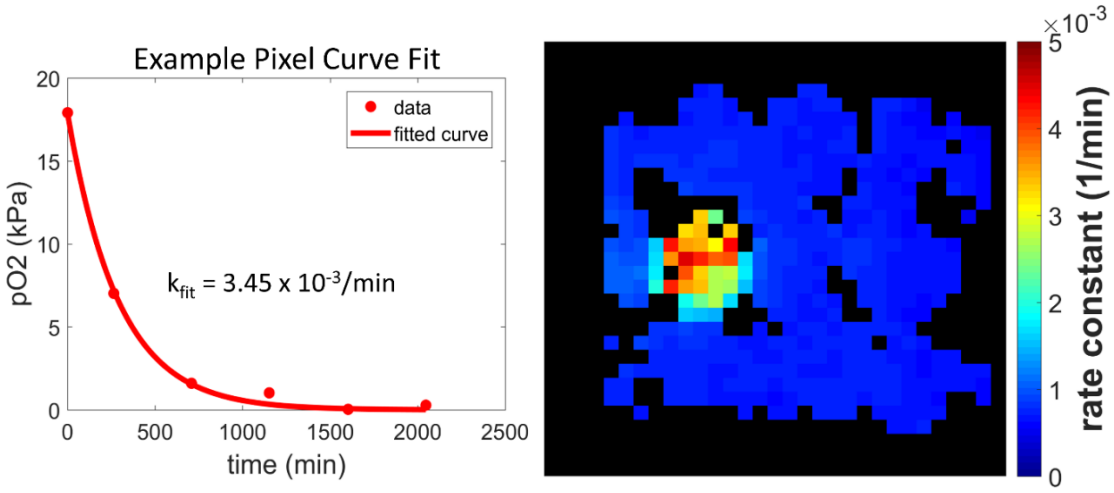

Figure 5.15. (Left) oxygen concentration over time for an arbitrary pixel in the *E. coli* inoculated bead region. (Right) spatial map of oxygen consumption rate obtained by fitting each pixel's oxygen decay data to a first order reaction rate equation. Pixels in the inoculated bead region exhibited high fidelity, with R^2 typically above 0.95 and never below 0.9, the threshold for calculation.

5.4 Conclusion

Oxygen availability is one of the most critical parameters governing microbial and biofilm growth behavior but is difficult or in some cases intractable to measure. In this work, the effectiveness of fluorine magnetic resonance oximetry to measure oxygen distribution in microbial and biofilm systems without impacting oxygen transport is demonstrated. The technique spatiotemporally tracks oxygen concentration in dynamic,

complex systems and is able to extract important parameters such as diffusion coefficient. Alginate beads are designed which entrap the oxygen-sensing fluorocarbon, and are incorporated as the solid matrix of a packed bed column, allowing spatially-resolved noninvasive mesoscale oximetry in these porous media systems. This method has been applied to packed bed columns inoculated with *E. coli* and *S. epidermidis*, and fundamental differences in establishment of oxygen gradients and alteration of flow distribution based on microbial physiology are observed. Combining fluid flow and oxygen transport information allows for generation of a spatial map of bacterial growth rate.

References

[1] Hall-Stoodley, L., Costerton, J.W., and Stoodley, P. (2004). Bacterial biofilms: from the Natural environment to infectious diseases. Nat Rev Micro *2*, 95-108.

[2] Smith, H.J., Schmit, A., Foster, R., Littman, S., Kuypers, M.M., and Foreman, C.M. (2016). Biofilms on glacial surfaces: hotspots for biological activity. npj Biofilms and Microbiomes *2*, 16008.

[3] Percival, S.L., Hill, K.E., Williams, D.W., Hooper, S.J., Thomas, D.W., and Costerton, J.W. (2012). A review of the scientific evidence for biofilms in wounds. Wound Repair Regen *20*, 647-657.

[4] Herzberg, M., and Elimelech, M. (2007). Biofouling of reverse osmosis membranes: Role of biofilm-enhanced osmotic pressure. Journal of Membrane Science *295*, 11-20.

[5] Townsin, R.L. (2003). The Ship Hull Fouling Penalty. Biofouling *19*, 9-15.

[6] Rajasekar, A., Anandkumar, B., Maruthamuthu, S., Ting, Y.-P., and Rahman, P.K.S.M. (2010). Characterization of corrosive bacterial consortia isolated from petroleum-product-transporting pipelines. Appl Microbiol Biotechnol *85*, 1175-1188.

[7] Edwards, S.J., and Kjellerup, B.V. (2013). Applications of biofilms in bioremediation and biotransformation of persistent organic pollutants, pharmaceuticals/personal care products, and heavy metals. Appl Microbiol Biotechnol *97*, 9909-9921.

[8] Adav, S.S., Lee, D.-J., Show, K.-Y., and Tay, J.-H. (2008). Aerobic granular sludge: Recent advances. Biotechnology Advances *26*, 411-423.

[9] Stewart, P.S., and Franklin, M.J. (2008). Physiological heterogeneity in biofilms. Nature Reviews Microbiology *6*, 199-210.

[10] Rasmussen, K., and Lewandowski, Z. (1998). Microelectrode measurements of local mass transport rates in heterogeneous biofilms. Biotechnol Bioeng *59*, 302-309.

[11] Lewandowski, Z., Altobelli, S.A., and Fukushima, E. (1993). NMR and Microelectrode Studies of Hydrodynamics and Kinetics in Biofilms. Biotechnol Prog *9*, 40-45.

[12] Davies, P.W., and Brink, F. (1942). Microelectrodes for Measuring Local Oxygen Tension in Animal Tissues. Rev Sci Instrum *13*, 524-533.

[13] Silver, I.A. (1973). Problems in the Investigation of Tissue Oxygen Microenvironment. In Chemical Engineering in Medicine (American Chemical Society), pp. 343-352.

[14] Eidelberg, D., Johnson, G., Barnes, D., Tofts, P.S., Delpy, D., Plummer, D., and McDonald, W.I. (1988). ^{19}F NMR imaging of blood oxygenation in the brain. Magn Reson Med *6*, 344-352.

[15] Mason, R.P., Rodbumrung, W., and Antich, P.P. (1996). Hexafluorobenzene: A sensitive F-19 NMR indicator of tumor oxygenation. NMR Biomed *9*, 125-134.

[16] Liu, S., Shah, S.J., Wilmes, L.J., Feiner, J., Kodibagkar, V.D., Wendland, M.F., Mason, R.P., Hylton, N., Hopf, H.W., and Rollins, M.D. (2011). Quantitative tissue oxygen measurement in multiple organs using 19F MRI in a rat model. Magn Reson Med *66*, 1722-1730.

[17] Yu, J.-X., Hallac, R.R., Chiguru, S., and Mason, R.P. (2013). New Frontiers and Developing Applications in (19)F NMR. Progress in nuclear magnetic resonance spectroscopy *70*, 25-49.

[18] Raichle, M.E. (1998). Behind the scenes of functional brain imaging: A historical and physiological perspective. Proc Natl Acad Sci U S A *95*, 765-772.

[19] Delpuech, J.J., Hamza, M.A., Serratrice, G., and Stebe, M.J. (1979). Fluorocarbons as oxygen carriers. 1. An NMR study of oxygen solutions in hexafluorobenzene. J Chem Phys *70*, 2680-2687.

[20] Hunjan, S., Mason, R.P., Constantinescu, A., Peschke, P., Hahn, E.W., and Antich, P.P. (1998). Regional tumor oximetry: F-19 NMR spectroscopy of hexafluorobenzene. International Journal of Radiation Oncology Biology Physics *41*, 161-171.

[21] Seymour, J.D., and Callaghan, P.T. (1997). Generalized approach to NMR analysis of flow and dispersion in porous media. AIChE J *43*, 2096-2111.

[22] Seymour, J.D., Gage, J.P., Codd, S.L., and Gerlach, R. (2004). Anomalous fluid transport in porous media induced by biofilm growth. Phys Rev Lett *93*, 198103.

[23] Hornemann, J.A., Codd, S.L., Romanenko, K., and Seymour, J.D. (2009). T2–T2 exchange in biofouled porous media. Diffusion Fundamentals *10*, 1.1-1.3.

[24] Johns, M., Sederman, A., Bramley, A., Gladden, L., and Alexander, P. (2000). Local transitions in flow phenomena through packed beds identified by MRI. AIChE J *46*, 2151-2161.

[25] Manz, B., Alexander, P., and Gladden, L. (1999). Correlations between dispersion and structure in porous media probed by nuclear magnetic resonance. Physics of Fluids *11*, 259-267.

[26] Liaw, H.K., Kulkarni, R., Chen, S., and Watson, A.T. (1996). Characterization of fluid distributions in porous media by NMR techniques. AIChE J *42*, 538-546.

[27] Song, Y.-Q., Cho, H., Hopper, T., Pomerantz, A.E., and Sun, P.Z. (2008). Magnetic resonance in porous media: Recent progress. The Journal of chemical physics *128*, 02B618.

[28] Blümich, B., Casanova, F., Dabrowski, M., Danieli, E., Evertz, L., Haber, A., Van Landeghem, M., Haber-Pohlmeier, S., Olaru, A., and Perlo, J. (2011). Small-scale instrumentation for nuclear magnetic resonance of porous media. New Journal of Physics *13*, 015003.

[29] Vogt, S.J., Sanderlin, A.B., Seymour, J.D., and Codd, S.L. (2013). Permeability of a growing biofilm in a porous media fluid flow analyzed by magnetic resonance displacement-relaxation correlations. Biotechnol Bioeng *110*, 1366-1375.

[30] Wakimoto, N., Nishi, J., Sheikh, J., Nataro, J.P., Sarantuya, J., Iwashita, M., Manago, K., Tokuda, K., Yoshinaga, M., and Kawano, Y. (2004). Quantitative biofilm assay using a microtiter plate to screen for enteroaggregative Escherichia coli. The American journal of tropical medicine and hygiene *71*, 687-690.

[31] Sadovskaya, I., Vinogradov, E., Flahaut, S., Kogan, G., and Jabbouri, S. (2005). Extracellular carbohydrate-containing polymers of a model biofilm-producing strain, Staphylococcus epidermidis RP62A. Infect Immun *73*, 3007-3017.

[32] Nöth, U., Gröhn, P., Jork, A., Zimmermann, U., Haase, A., and Lutz, J. (1999). 19F-MRI in vivo determination of the partial oxygen pressure in perfluorocarbon-loaded alginate capsules implanted into the peritoneal cavity and different tissues. Magn Reson Med *42*, 1039-1047.

[33] Nöth, U., Rodrigues, L.M., Robinson, S.P., Jork, A., Zimmermann, U., Newell, B., and Griffiths, J.R. (2004). In vivo determination of tumor oxygenation during growth and in response to carbogen breathing using 15C5-loaded alginate capsules as fluorine-19 magnetic resonance imaging oxygen sensors. International Journal of Radiation Oncology• Biology• Physics *60*, 909-919.

[34] Smidsrød, O., and Skja, G. (1990). Alginate as immobilization matrix for cells. Trends Biotechnol *8*, 71-78.

[35] Cheetham, P.S., Blunt, K.W., and Bocke, C. (1979). Physical studies on cell immobilization using calcium alginate gels. Biotechnol Bioeng *21*, 2155-2168.

[36] Taipa, M., Cabral, J., and Santos, H. (1993). Comparison of glucose fermentation by suspended and gel-entrapped yeast cells: An in vivo nuclear magnetic resonance study. Biotechnol Bioeng *41*, 647-653.

[37] Duff, R.G. (1985). Microencapsulation technology: a novel method for monoclonal antibody production. Trends Biotechnol *3*, 167-170.

[38] Robinson, P., Goulding, K., Mak, A., and Trevan, M. (1986). Factors affecting the growth characteristics of alginate-entrapped Chlorella. Enzyme Microb Technol *8*, 729-733.

[39] Pabst, B., Pitts, B., Lauchnor, E., and Stewart, P.S. (2016). Gel-entrapped Staphylococcus aureus bacteria as models of biofilm infection exhibit growth in dense aggregates, oxygen limitation, antibiotic tolerance, and heterogeneous gene expression. Antimicrob Agents Chemother *60*, 6294-6301.

[40] Thomas, C.D., Chavaudra, N., Martin, L., and Guichard, M. (1994). Correlation between radiosensitivity, percentage hypoxic cells and pO2 measurements in one rodent and two human tumor xenografts. Radiat Res *139*, 1-8.

[41] Ruiz-Cabello, J., Barnett, B.P., Bottomley, P.A., and Bulte, J.W.M. (2011). Fluorine (19F) MRS and MRI in biomedicine. NMR Biomed *24*, 114-129.

[42] Bird, R.B., Stewart, W.E., and Lightfoot, E.N. (1960). Transport phenomena. 1960. Madison, USA.

[43] Han, P., and Bartels, D.M. (1996). Temperature dependence of oxygen diffusion in H2O and D2O. J Phys Chem *100*, 5597-5602.

[44] Stewart, P.S. (1998). A review of experimental measurements of effective diffusive permeabilities and effective diffusion coefficients in biofilms. Biotechnol Bioeng *59*, 261-272.

[45] Maxwell, J.C. (1881). A treatise on electricity and magnetism, Vol 1 (Clarendon press).

[46] Dulieu, C., Poncelet, D., and Neufeld, R.J. (1999). Encapsulation and immobilization techniques. In Cell encapsulation technology and therapeutics (Springer), pp. 3-17.

[47] Sønderholm, M., Kragh, K.N., Koren, K., Jakobsen, T.H., Darch, S.E., Alhede, M., Jensen, P.Ø., Whiteley, M., Kühl, M., and Bjarnsholt, T. (2017).

Pseudomonas aeruginosa aggregate formation in an alginate bead model system exhibits in vivo-like characteristics. Appl Environ Microbiol *83*, e00113-00117.

[48] Wilkes, J.O. (2006). Fluid Mechanics for Chemical Engineers with Microfluidics and CFD (Pearson Education).

CHAPTER SIX: NON-INVASIVE IMAGING OF OXYGEN CONCENTRATION IN A COMPLEX *IN VITRO* BIOFILM INFECTION MODEL USING ^{19}F MRI: PERSISTENCE OF AN OXYGEN SINK DESPITE PROLONGED ANTIBIOTIC THERAPY

Contribution of Authors and Co-Authors

Manuscript in Chapter 6

Author: Jeffrey W. Simkins

Contributions: Helped conceive and implement study design. Collected and analyzed data. Wrote manuscript. Incorporated revisions and provided feedback on manuscript.

Co-Author: Philip S. Stewart

Contributions: Helped conceive and implement study design. Secured funding. Provided feedback on manuscript.

Co-Author: Sarah L. Codd

Contributions: Assisted with pulse sequence design.

Co-Author: Joseph D. Seymour

Contributions: Helped conceive and implement study design. Secured funding. Provided feedback on manuscript.

Manuscript Information Page

Jeffrey W. Simkins, Philip S. Stewart, Sarah L. Codd, and Joseph D. Seymour

Magnetic Resonance in Medicine

Status of Manuscript: (Put an x in one of the options below)
____ Prepared for submission to a peer-reviewed journal
__X_ Officially submitted to a peer-review journal
____ Accepted by a peer-reviewed journal
____ Published in a peer-reviewed journal

Wiley
February 2019

NON-INVASIVE IMAGING OF OXYGEN CONCENTRATION IN A COMPLEX *IN VITRO* BIOFILM INFECTION MODEL USING ^{19}F MRI: PERSISTENCE OF AN OXYGEN SINK DESPITE PROLONGED ANTIBIOTIC THERAPY

Abstract

Purpose: Oxygen availability is a critical determinant of microbial biofilm activity and antibiotic susceptibility. However, measuring oxygen gradients in these systems remains difficult, with the standard microelectrode approach being both invasive and limited to single-point measurement. The goal of the study was to develop a ^{19}F Magnetic Resonance Imaging approach for two-dimensional oxygen mapping in biofilm systems and to visualize oxygen consumption behavior in real time during antibiotic therapy.

Methods: Oxygen-sensing beads were created by encapsulating an emulsion of oxygen-sensing fluorocarbon into alginate gel. *Escherichia coli* biofilms were grown in and on the alginate matrix which was contained inside a packed bed column subjected to nutrient flow, mimicking the complex porous structure of human wound tissue, and subjected to antibiotic challenge.

Results: The linear relationship between ^{19}F spin-lattice relaxation rate R_1 and local oxygen concentration permitted noninvasive spatial mapping of oxygen distribution in real-time over the course of biofilm growth and subsequent antibiotic challenge. This technique was used to visualize persistence of microbial oxygen respiration during continuous gentamicin administration, providing a time series of complete spatial maps

detailing the continued bacterial utilization of oxygen during prolonged chemotherapy in an *in vitro* biofilm model with complex spatial structure.

Conclusions: Antibiotic exposure temporarily causes oxygen consumption to enter a pseudo-steady state wherein oxygen distribution becomes fixed; oxygen sink expansion resumes quickly after antibiotic clearance. This technique may provide valuable information for future investigations of biofilms by permitting the study of complex geometries (typical of *in vivo* biofilms) and facilitating noninvasive oxygen measurement.

6.1. Introduction

Molecular oxygen plays a profound role in biofilm presentation [1], shaping microbial diversity [2], gene expression and metabolism [3], and in the case of medical biofilms, infection persistence [4]. Gradients in oxygen concentration arise in biofilm systems through the simultaneous reaction and diffusion of this electron acceptor [5]. Oxygen utilization by active bacterial and host cells generates anoxic zones [6-8], inducing bacteria contained therein to transition to a state of dormancy which imparts tolerance to antimicrobials [9; 10] and host immune defenses [11]. As a consequence, oxygen penetration into infected tissue is a strong predictor of clinical outcome [12], and therapies stimulating oxygen delivery into colonized wounds have proven effective [13]. However, despite the importance of oxygen in medical biofilms, mapping oxygen concentration in these systems remains a cumbersome endeavor, with the traditional

microelectrode approach being both invasive and limited to single-point measurement [14].

The spin-lattice relaxation rate R_1 of ^{19}F nuclei in perfluorocarbons (PFCs) is linearly proportional to local oxygen concentration. This relationship has been exploited in the medical literature to measure pO_2 in blood [15], tissues [16], and tumors [17], although its use in this context has been limited by uncertain distribution and clearance profile of the PFC by the body. To facilitate oxygen mapping in a biofilm system, we encapsulated an emulsion containing an oxygen-sensing PFC into alginate gel beads such that PFC is both fixed and evenly distributed throughout the experiment. Bacterial growth is stimulated in the PFC-laden alginate beads by inoculating the emulsion before gel solidification [18]. As bacterial growth inside an alginate gel matrix is frequently used as an *in vitro* biofilm model, this approach allows for the noninvasive mapping of oxygen inside a conventional and well-studied biofilm system with *in vivo* relevance [19-23]. Gel beads, one inoculated and the others sterile, are packed into a chromatography column and nutrient media is flowed through, yielding a complex porous media containing liquid flow amidst tissue-like occlusions, which better approximates the growth conditions of real *in vivo* biofilms than planar biofilm models and may thus better capture their behavior.

The objective of the present study was to utilize these novel oxygen-sensing alginate beads to facilitate noninvasive, two-dimensional spatial mapping of oxygen profile in a clinically-relevant biofilm system undergoing chemical challenge by a broad-spectrum antibiotic. Successful application of this technique would exhibit distinct

advantages over conventional approaches, namely the ability to visualize oxygen distribution in multiple dimensions, the ability to quantify oxygenation in biofilm systems characterized by complex geometry (similar to real biofilms encountered in medicine), and the ability to measure transient responses to changes in chemical environment due to the lack of invasiveness and simultaneous sample-wide signal acquisition.

6.2. Methods

6.2.1 Bacterial Cultivation

The bacterium used in these experiments was an *Escherichia coli* HB101 strain containing plasmid pMF440 (provided by Dr. Michael Franklin; Addgene plasmid #62550), conferring constitutive expression of red fluorescent protein (RFP) recombinant mCherry, in addition to an ampicillin resistance gene. Inocula were cultured overnight at 37 ºC in a shaking incubator with full-strength tryptic soy broth (TSB) and 100 µg/mL ampicillin to promote retention of the plasmid. To demonstrate the efficacy of gentamicin against planktonic cells, a subset overnight cultures were grown in the presence of 50 µg/mL GEN. No growth was observed (data not shown).

6.2.2 Oxygen-Sensing Alginate Beads

Perfluorooctylbromide (PFOB) was selected as the oxygen-sensing PFC as it readily forms stable emulsions in water. ^{19}F oxygen-sensing alginate gel beads were created by dissolving 0.4 g α-phosphatidylcholine surfactant (Sigma; P3556) and 0.2 g low-viscosity sodium alginate (Sigma; A1112) in 10 mL of deionized water. 9g PFOB

(Aurum Pharmatech; K-8801) was introduced into the beaker and the solution was homogenized at 15,000 rpm for 30 minutes with a shear mixer to generate a 90% w/v emulsion of a PFOB in an aqueous solution containing 2% w/v sodium alginate. The emulsion was divided into two aliquots, with the first aliquot then dripped into a 50mM solution of calcium chloride (Sigma; C1016) with a burette. The dripping process generated spherical alginate beads with an average diameter of 3.42 ± 0.23 mm containing dispersed PFC. A 1 mL aliquot of the overnight culture was centrifuged at 6,000 rpm for 4 minutes, resuspended in sterile phosphate-buffered saline, and used to inoculate the second emulsion aliquot at a final dilution of 1:10,000. The inoculated emulsion aliquot was then dripped into the calcium chloride bath to generate beads containing the oxygen-sensing PFC as well as gel-entrapped bacterial colonies, a common *in vitro* biofilm model [19-21]. All glassware and the shear mixer downshaft were autoclaved prior to alginate bead creation, and all steps in the protocol were conducted in a sterile biological safety cabinet under laminar airflow to prevent contamination by ambient microbes.

6.2.3 pO_2 vs R_1 Calibration Curve for PFOB

Nuclear Magnetic Resonance (NMR) calibration experiments were conducted as described previously [18]. All experiments were performed on a 7 T vertical-bore magnet with an actively shielded micro2.5 gradient probe providing 1.5 T/m at 60 A, under the control of a Bruker Avance III MRI spectrometer. To construct a calibration curve for the R_1 of PFOB as a function of pO_2 in the anoxic to atmospheric range (0 to 18 kPa; 85 kPa

atmospheric pressure in Bozeman, MT, USA with 21% oxygen) relevant to bacterial growth conditions, we followed the procedure outlined by Mason *et al* [17]. Alginate beads containing 90% w/v dispersed PFOB were prepared as described in section 6.2.2. The beads were placed into a 25 mL sample bottle immersed in DI water, and gases of variable oxygen content (100% air, 75% air/25% N_2, 50% air/50% N_2, 25% air/75% N_2, 100% N_2) were bubbled through the solution vigorously for 30 min. The area immediately above the liquid line was flooded with the appropriate gas, and the bottle was immediately sealed. The bottle was then loaded into a 25 mm dual tuning $^{1}H/^{19}F$ rf coil and bulk spin-lattice relaxation rate R_1 (=1/T_1) for the CF_3 peak was collected every 30 minutes. Equilibrium was achieved within 1 hour, and therefore R_1 value at t = 1 hour was recorded. Three replicates were acquired for each point using different aliquots. R_1 was measured using the Inversion Recovery (IR) method with the time domain sampled logarithmically at six points (TI = 25, 100, 300, 600, 1000, 3000, 5000 ms). Time-domain data was fit using Levenberg-Marquardt least-squares regression to a three-parameter mono-exponential formula governing the IR pulse sequence, yielding values for both signal intensity and R_1. Selective excitation of the CF_3 peak was accomplished using a 2 ms rf pulse.

6.2.4 Packed Bed Column Containing Alginate Beads

Immediately following alginate bead creation, excess calcium chloride solution was poured into a freshly autoclaved, 10 mm ID liquid chromatography column (Omnifit Labware) with 50 µm filters at both ends. Sterile beads were then wet-loaded into the

column using a spatula. A single inoculated bead was loaded and moved into the center of the column at a height corresponding to the isocenter of the NMR coil. The column was filled with additional sterile beads and connected to a High Performance Liquid Chromatography Column (GE Healthcare; High Precision Pump P-500) with freshly autoclaved 1.9 mm ID Teflon tubing. The column outlet was connected to a waste collection bottle, forming an open flowthrough loop. The sample was then inserted into the coil and loaded into the magnet. Gradient cooling water was fixed at 22.8 ºC to ensure constant temperature in the magnet bore. A sterile solution containing full-strength TSB and 50 mM calcium chloride (to maintain alginate crosslinking) was flowed through the bed at a constant volumetric flowrate of 25 mL/hr (superficial velocity = 0.08 mL/s). Immediately prior to this, laboratory air was bubbled through the feed solution to restore the dissolved oxygen lost during autoclaving. Bacterial air filters were attached to the feed bottle inlet and outlet tubing to maintain sterile conditions during bubbling. Oxygen distribution was tracked over the course of biofilm growth by continuous acquisition of 2D longitudinal R_1 maps which sampled three points along the inversion recovery curve (TI = 25, 1000, 3000 ms). NMR acquisition parameters consisted of a 15 x 12 mm^2 field-of-view, 469 x 375 μm^2 spatial resolution, 8 ms echo time, 15 s repetition time to prevent T_1 weighting, slice thickness of 3 mm, 8 averages, and a total acquisition time of 192 min. Pixels were only assigned an R_1 if they achieved a threshold signal value of 10^5 and the associated standard error of the measurement for the R_1 parameter fit was below 30%.

To investigate the well-documented phenomenon of infection persistence under antibiotic treatment, a subset of columns were subjected to a feed containing 50 µg/mL

gentamicin (GEN), a broad-spectrum antibiotic that we found to completely inhibit planktonic *E. coli* growth when amended to the standard nutrient regimen (data not shown). Three experimental conditions were studied: a negative control with the entire protocol conducted in the absence of GEN treatment, a positive control with GEN administered throughout the experiment, and an experimental regimen wherein GEN administration began after about 20 hours of growth (at which point a substantial oxygen sink had developed), was continued for approximately 24 hours, and then was removed from the feed. Oxygen monitoring continued after removal of GEN from the feed reservoir.

6.2.5 Cell count experiments

Viable cell counts were measured at three different points in the packed bed experiment: immediately after bead creation (initial cell count), immediately before GEN exposure, and after 24 hours of GEN treatment. The initial cell count was carried out immediately after bead creation; ten sterile beads and ten inoculated beads were each dissolved in 10 mL of a 50 mM sodium citrate solution. Each was serially diluted to $1{:}10^6$ and 5 drops of 10 μL from each dilution were plated on tryptic soy agar. This was performed in triplicate for each dilution. Plates were incubated at 37 ºC for 6 to 8 hours until colonies were easily visible but well separated and counted.

It was discovered that over the course of the packed bed experiment, most colonies (or at least the fastest growing colonies) shed their RPF plasmid, making it impossible to identify the inoculated bead for cell counting. Thus for the later time points,

an additional step fluorescent tagging step was incorporated into the emulsion creation protocol to allow the inoculated beads to be distinguished. This was accomplished using the fluorescent tag PKH-26, which in addition to its uses for tagging cell membranes, is also known to tag the phosphatidylcholine surfactant used in the PFC emulsion [24]. A PKH-26 Fluorescent Cell Linker kit was obtained from Sigma (MINI26). For these beads, PFOB and the surfactant were dissolved in water and emulsified in the absence of sodium alginate. The emulsion was separated into 2 aliquots (a 10mL and a 1 mL), and centrifuged at 4700 rpm for 4 minutes. The 10 mL emulsion was resuspended in DI water while the 1 mL aliquot was resuspended in the diluent C provided with the linker kit which optimizes PKH-26 binding. 10 μL of the ethanolic dye was dissolved in 0.25 mL of diluent, and this solution was mixed with the emulsion and mixed with gentle pipetting and shaking. The emulsion was incubated for 15 minutes to allow for binding, and then both emulsion aliquots were again centrifuged at 4700 rpm for 4 minutes and resuspended in DI water. 2% w/v sodium alginate were added to both and allowed to dissolve fully, and the 1 mL aliquot was inoculated as described above. Beads were then created from each as normal. The PKH-26 tagging step resulted in brightly fluorescent inoculated beads that were easily distinguishable with the naked eye, but otherwise identical to non-tagged beads.

Packed bed columns for use in cell counting were operated outside the magnet but otherwise followed the same procedure. At the appropriate time point, the column was disconnected from the tubing and emptied out in a biological safety cabinet. The inoculated bead and 10 beads adjacent to the inoculated bead were dissolved in 1 mL and

10 mL of 50 mM sodium citrate, respectively. Plate counts for each were conducted as described above.

6.3. Results

The emulsion of PFOB in water exhibited a strong sensitivity to changes in oxygen partial pressure (Figure 6.1) and due to the tight temperature tolerances provided by the NMR gradient cooling water (T = 22.8 ± 0.5 °C), the accuracy and precision of pO_2 measurements are not impacted by temperature uncertainty. This is reflected in the high fidelity of the pO_2 vs R_1 curve fit.

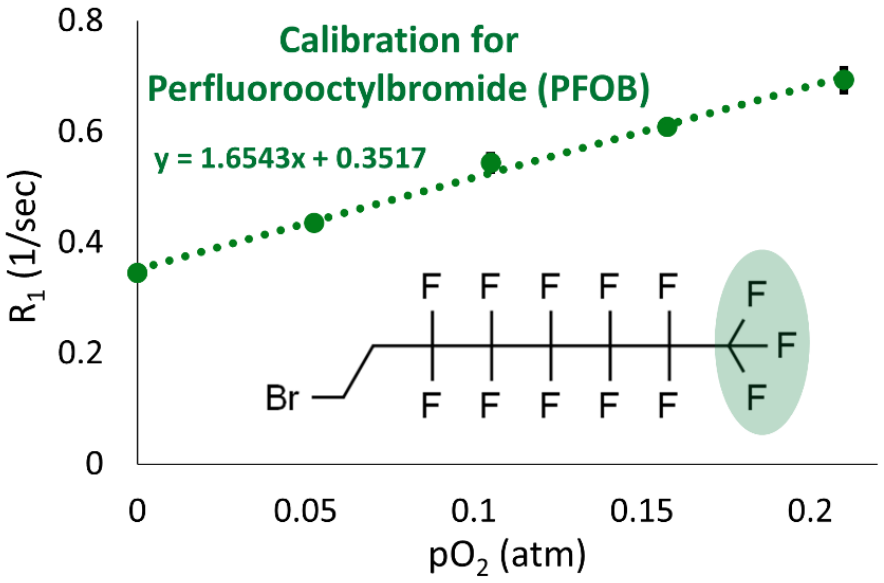

Figure 6.1. Calibration curve relating the response of spin-lattice relaxation R_1 to pO_2 for PFOB encapsulated in alginate beads at 7 T and 22.8 °C. All points were measured in triplicate, and error bars denote standard deviation. Where error bars are not apparent, standard deviation is smaller than the marker size. The resonance peak chosen to measure R_1 for PFOB (CF_3 group) is highlighted in green.

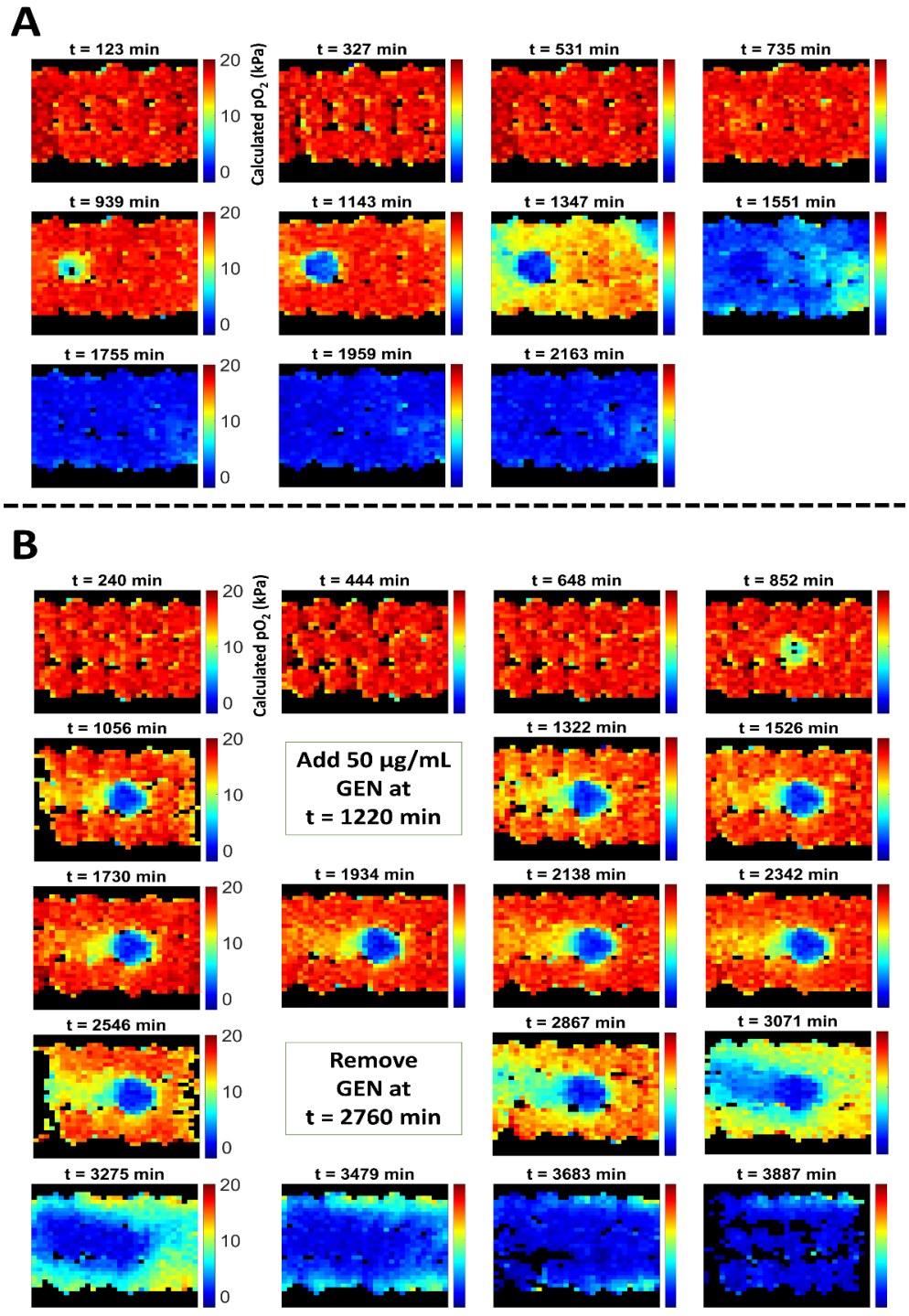

Figure 6.2. A: longitudinal map of calculated pO_2 values over time within a packed bed column containing a single alginate bead inoculated with *E. coli*. B: longitudinal map of calculated pO_2 values for a similar packed bed column exposed to a 24 hour treatment of 50 µg/mL gentamicin, a broad-spectrum antibiotic.

In the absence of GEN (negative control), the column was characterized by an extended period (~8 hours) in which oxygen levels remained at saturation levels (Figure 6.2). In this phase, bacterial counts were low and the total oxygen consumption rate was small enough to be overwhelmed by the rate of oxygen replenishment due to flow. Around the 750-850 min mark, a modest oxygen sink developed and, due to the exponential growth of the immobilized bacteria, rapidly grew in strength, with oxygen levels within the inoculated bead dropping to zero shortly after. The oxygen sink then spread through the rest of the column as *E. coli* colonies relocated to adjacent beads where oxygen was still available through bead contact points, rendering the entire column anoxic. The behavior of the negative control is also evident in Figure 6.3, which presents the average oxygen value of the inoculated bead for the various experimental conditions over time.

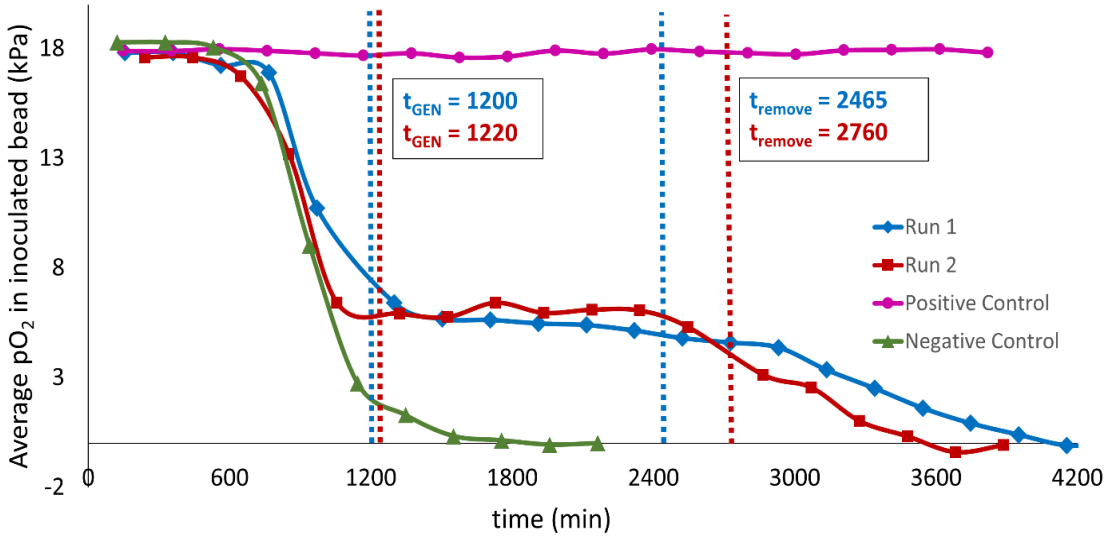

Figure 6.3. Average calculated pO_2 in inoculated bead for negative control (no GEN treatment; green triangles), positive control (GEN treated throughout experiment; pink circles), and experimental regimen (GEN treated from t = 20 hours to t = 44 hours; red squares and blue diamonds).

In the positive control, GEN administration began at the start of the experiment and continued uninterrupted throughout. This condition resulted in no bacterial growth and the absence of an oxygen sink. In the experimental condition, the bacteria were allowed 20 hours of growth to establish a biofilm before GEN administration. Plate counts revealed that over this time period bacterial counts in the inoculated bead rose from the initial inoculum concentration of ~$\log_{10}$ 5.4 CFU/mL to about $\log_{10}$ 9.2 CFU/mL (Figure 6.4), while beads adjacent to the inoculated bead experienced a growth from 0 to $\log_{10}$ 4.4 CFU/mL. After this point, in contrast to the rapid depletion of oxygen in the absence of antibiotic, the onset of GEN exposure coincided with a "freezing" of the oxygen sink, characterized by ongoing oxygen usage but a complete lack of sink spatial expansion. This forced steady state persisted throughout the 24 hour exposure period.

Cell counts conducted after the GEN treatment regimen indicated that cell viability was only weakly affected, with an average log reduction of 0.23 for the inoculated bead and 0.09 for the adjacent beads. Following GEN removal, the oxygen sink resumed its spread throughout the column, albeit at a slower rate than that which was observed for biofilms never exposed to the antibiotic, underscoring the difficulty that a well-established infectious biofilm presents for effective treatment.

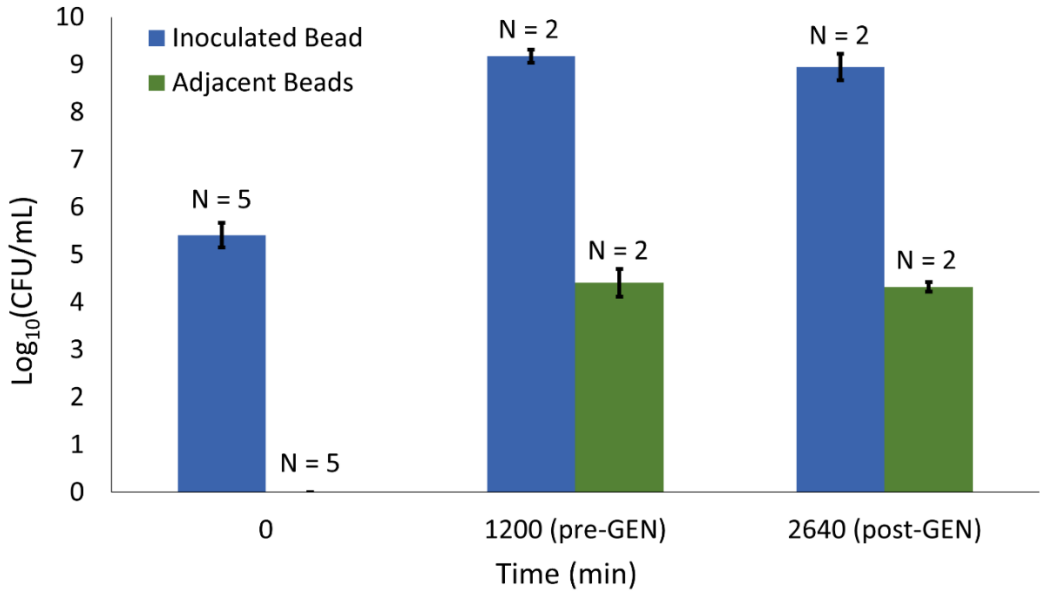

Figure 6.4. Viable cell counts for inoculated bead and adjacent beads at beginning of experiment, immediately prior to GEN treatment, and after 24 hours of GEN treatment. Error bars represent standard deviation.

6.4. Discussion and Conclusion

As with other aminoglycosides, GEN targets the bacterial ribosome, interfering with protein synthesis, and exhibits dose-dependent bacteriostatic or bactericidal activity

[25]. Literature reports of *E. coli* susceptibility to GEN range significantly depending on strain, with a minimum inhibitory concentration ranging from 4 to 256 μg/mL [26]. Minimum biofilm eradication concentration is typically (but not always) higher, ranging from 4 to >1024 μg/mL. The concentration used in the present study of 50 μg/mL, in the middle of this range, was found to completely inhibit planktonic growth (data not shown) but was insufficient to generate even a single log reduction in viable cell counts. These results are consistent with and enrich the long-standing observations *in vitro* and *in vivo* that aggressive antibiotic treatment of mature biofilms is often insufficient to eradicate bacterial respiration [27-29], even in cases where viable cell counts are affected, and that following cessation of antimicrobial therapy biofilms often regrow [30-32].

Traditional investigations of biofilm oxygen usage are typically conducted on steady state biofilms wherein oxygen penetration no longer changes with time, and studies examining the effect of antibiotic administration often infer continued oxygen utilization by identifying anoxic conditions at the biofilm base or by probing the one-dimensional oxygen profile, with the exact response of the oxygen sink to antibiotic challenge unknown. Here we have demonstrated the temporary bacteriostatic effect of a high dose of broad-spectrum antibiotic on a developing biofilm exhibiting a dynamic oxygen sink using a novel, MRI-based technique in real time. We show that gentamicin administration to a model infection results in establishment of a pseudo-steady state wherein oxygen consumption continues but oxygen sink development is halted indefinitely. Further, we have demonstrated the advantages and unique benefits afforded by this approach by achieving oxygen concentration mapping entirely noninvasively for a

model clinical biofilm in two spatial dimensions, providing comprehensive snapshots of transient oxygen profile that would be intractable with traditional oximetry methods. This method thus serves as a novel means to visualize the proliferation and dispersion of actively growing cells and to probe the interactions between oxygen gradients and chemical environment. The thorough oxygen distribution measurements provided by this technique may prove invaluable for further study of antibiotic efficacy and bacterial metabolism in biofilm systems that are more representative of real clinically-relevant biofilms, which are often characterized by non-planar geometry [33-35], porous structure [36], and the presence of flow [37; 38], and which may be inaccessible to conventional microelectrode approaches.

References

[1] Stewart, P.S., and Franklin, M.J. (2008). Physiological heterogeneity in biofilms. Nature Reviews Microbiology *6*, 199-210.

[2] Costerton, J.W., Lewandowski, Z., Caldwell, D.E., Korber, D.R., and Lappin-Scott, H.M. (1995). Microbial biofilms. Annu Rev Microbiol *49*, 711-745.

[3] Prigent-Combaret, C., Vidal, O., Dorel, C., and Lejeune, P. (1999). Abiotic surface sensing and biofilm-dependent regulation of gene expression in Escherichia coli. J Bacteriol *181*, 5993-6002.

[4] Schobert, M., and Tielen, P. (2010). Contribution of oxygen-limiting conditions to persistent infection of Pseudomonas aeruginosa. Future Microbiol *5*, 603-621.

[5] Stewart, P.S., Zhang, T., Xu, R., Pitts, B., Walters, M.C., Roe, F., Kikhney, J., and Moter, A. (2016). Reaction–diffusion theory explains hypoxia and heterogeneous growth within microbial biofilms associated with chronic infections. npj Biofilms and Microbiomes *2*, 16012.

[6] Worlitzsch, D., Tarran, R., Ulrich, M., Schwab, U., Cekici, A., Meyer, K.C., Birrer, P., Bellon, G., Berger, J., and Weiss, T. (2002). Effects of reduced mucus oxygen concentration in airway Pseudomonas infections of cystic fibrosis patients. The Journal of clinical investigation *109*, 317-325.

[7] Cowley, E.S., Kopf, S.H., LaRiviere, A., Ziebis, W., and Newman, D.K. (2015). Pediatric cystic fibrosis sputum can be chemically dynamic, anoxic, and extremely reduced due to hydrogen sulfide formation. MBio *6*, e00767-00715.

[8] Kolpen, M., Hansen, C.R., Bjarnsholt, T., Moser, C., Christensen, L.D., van Gennip, M., Ciofu, O., Mandsberg, L., Kharazmi, A., and Döring, G. (2010). Polymorphonuclear leukocytes consume oxygen in sputum from chronic Pseudomonas aeruginosa pneumonia in cystic fibrosis. Thorax *65*, 57-62.

[9] Borriello, G., Werner, E., Roe, F., Kim, A.M., Ehrlich, G.D., and Stewart, P.S. (2004). Oxygen limitation contributes to antibiotic tolerance of Pseudomonas aeruginosa in biofilms. Antimicrob Agents Chemother *48*, 2659-2664.

[10] Kolpen, M., Lerche, C.J., Kragh, K.N., Sams, T., Koren, K., Jensen, A.S., Line, L., Bjarnsholt, T., Ciofu, O., and Moser, C. (2017). Hyperbaric oxygen sensitizes anoxic Pseudomonas aeruginosa biofilm to ciprofloxacin. Antimicrob Agents Chemother *61*, 1-9.

[11] Jesaitis, A.J., Franklin, M.J., Berglund, D., Sasaki, M., Lord, C.I., Bleazard, J.B., Duffy, J.E., Beyenal, H., and Lewandowski, Z. (2003). Compromised host defense on Pseudomonas aeruginosa biofilms: Characterization of neutrophil and biofilm interactions. J Immunol *171*, 4329-4339.

[12] Schreml, S., Szeimies, R.M., Prantl, L., Karrer, S., Landthaler, M., and Babilas, P. (2010). Oxygen in acute and chronic wound healing. Br J Dermatol *163*, 257-268.

[13] Ueno, T., Omi, T., Uchida, E., Yokota, H., and Kawana, S. (2014). Evaluation of hyperbaric oxygen therapy for chronic wounds. Journal of Nippon Medical School *81*, 4-11.

[14] Davies, P.W., and Brink, F. (1942). Microelectrodes for measuring local oxygen tension in animal tissues. Rev Sci Instrum *13*, 524-533.

[15] Eidelberg, D., Johnson, G., Barnes, D., Tofts, P.S., Delpy, D., Plummer, D., and McDonald, W.I. (1988). ^{19}F NMR imaging of blood oxygenation in the brain. Magn Reson Med *6*, 344-352.

[16] Liu, S., Shah, S.J., Wilmes, L.J., Feiner, J., Kodibagkar, V.D., Wendland, M.F., Mason, R.P., Hylton, N., Hopf, H.W., and Rollins, M.D. (2011). Quantitative tissue oxygen measurement in multiple organs using 19F MRI in a rat model. Magn Reson Med *66*, 1722-1730.

[17] Mason, R.P., Rodbumrung, W., and Antich, P.P. (1996). Hexafluorobenzene: A sensitive F-19 NMR indicator of tumor oxygenation. NMR Biomed *9*, 125-134.

[18] Simkins, J.W., Stewart, P.S., and Seymour, J.D. (2018). Spatiotemporal mapping of oxygen in a microbially-impacted packed bed using 19 F Nuclear magnetic resonance oximetry. J Magn Reson *293*, 123-133.

[19] Smidsrød, O., and Skja, G. (1990). Alginate as immobilization matrix for cells. Trends Biotechnol *8*, 71-78.

[20] Cheetham, P.S., Blunt, K.W., and Bocke, C. (1979). Physical studies on cell immobilization using calcium alginate gels. Biotechnol Bioeng *21*, 2155-2168.

[21] Pabst, B., Pitts, B., Lauchnor, E., and Stewart, P.S. (2016). Gel-entrapped Staphylococcus aureus bacteria as models of biofilm infection exhibit growth in dense aggregates, oxygen limitation, antibiotic tolerance, and heterogeneous gene expression. Antimicrob Agents Chemother *60*, 6294-6301.

[22] Sønderholm, M., Koren, K., Wangpraseurt, D., Jensen, P.Ø., Kolpen, M., Kragh, K.N., Bjarnsholt, T., and Kühl, M. (2018). Tools for studying growth patterns and chemical dynamics of aggregated Pseudomonas aeruginosa exposed to different electron acceptors in an alginate bead model. NPJ biofilms and microbiomes *4*, 3.

[23] Sønderholm, M., Kragh, K.N., Koren, K., Jakobsen, T.H., Darch, S.E., Alhede, M., Jensen, P.Ø., Whiteley, M., Kühl, M., and Bjarnsholt, T. (2017). Pseudomonas aeruginosa aggregate formation in an alginate bead model system exhibits in vivo-like characteristics. Appl Environ Microbiol *83*, e00113-00117.

[24] Smith, D., Kornbrust, E., and Lane, T. (1994). Phagocytosis of a fluorescently labeled perflubron emulsion by a human monocyte cell line. Artificial Cells, Blood Substitutes, and Biotechnology *22*, 1215-1221.

[25] Yoshizawa, S., Fourmy, D., and Puglisi, J.D. (1998). Structural origins of gentamicin antibiotic action. The EMBO journal *17*, 6437-6448.

[26] Olson, M.E., Ceri, H., Morck, D.W., Buret, A.G., and Read, R.R. (2002). Biofilm bacteria: formation and comparative susceptibility to antibiotics. Can J Vet Res *66*, 86.

[27] von Ohle, C., Gieseke, A., Nistico, L., Decker, E.M., and Stoodley, P. (2010). Real-time microsensor measurement of local metabolic activities in ex vivo dental biofilms exposed to sucrose and treated with chlorhexidine. Appl Environ Microbiol *76*, 2326-2334.

[28] Kiamco, M.M., Atci, E., Mohamed, A., Call, D.R., and Beyenal, H. (2017). Hyperosmotic agents and antibiotics affect dissolved oxygen and pH concentration gradients in Staphylococcus aureus biofilms. Appl Environ Microbiol, AEM. 02783-02716.

[29] Kiamco, M.M., Atci, E., Khan, Q.F., Mohamed, A., Renslow, R.S., Abu-Lail, N., Fransson, B.A., Call, D.R., and Beyenal, H. (2015). Vancomycin and maltodextrin affect structure and activity of Staphylococcus aureus biofilms. Biotechnol Bioeng *112*, 2562-2570.

[30] Haagensen, J., Verotta, D., Huang, L., Engel, J., Spormann, A.M., and Yang, K. (2017). Spatiotemporal pharmacodynamics of meropenem-and tobramycin-treated Pseudomonas aeruginosa biofilms. J Antimicrob Chemother *72*, 3357-3365.

[31] Ito, A., Taniuchi, A., May, T., Kawata, K., and Okabe, S. (2009). Increased antibiotic resistance of Escherichia coli in mature biofilms. Appl Environ Microbiol *75*, 4093-4100.

[32] Anwar, H., Strap, J., Chen, K., and Costerton, J. (1992). Dynamic interactions of biofilms of mucoid Pseudomonas aeruginosa with tobramycin and piperacillin. Antimicrob Agents Chemother *36*, 1208-1214.

[33] Klapper, I. (2004). Effect of heterogeneous structure in mechanically unstressed biofilms on overall growth. Bull Math Biol *66*, 809-824.

[34] Bjarnsholt, T., Alhede, M., Alhede, M., Eickhardt-Sørensen, S.R., Moser, C., Kühl, M., Jensen, P.Ø., and Høiby, N. (2013). The in vivo biofilm. Trends Microbiol *21*, 466-474.

[35] Wu, Y., Klapper, I., and Stewart, P.S. (2018). Hypoxia arising from concerted oxygen consumption by neutrophils and microorganisms in biofilms. Pathogens and disease *76*, fty043.

[36] Høiby, N. (2002). Understanding bacterial biofilms in patients with cystic fibrosis: current and innovative approaches to potential therapies. Journal of Cystic Fibrosis *1*, 249-254.

[37] Grubb, S.E., Murdoch, C., Sudbery, P.E., Saville, S.P., Lopez-Ribot, J.L., and Thornhill, M.H. (2009). Adhesion of Candida albicans to endothelial cells under physiological conditions of flow. Infect Immun *77*, 3872-3878.

[38] Stewart, P.S. (2014). Biophysics of biofilm infection. Pathogens and disease *70*, 212-218.

CHAPTER SEVEN: MICROBIAL GROWTH RATES AND LOCAL EXTERNAL MASS TRANSFER RESISTANCE IN A POROUS BED BIOFILM SYSTEM MEASURED BY ^{19}F MAGNETIC RESONANCE IMAGING OF STRUCTURE, OXYGEN CONCENTRATION, AND FLOW VELOCITY

Contribution of Authors and Co-Authors

Manuscript in Chapter 6

Author: Jeffrey W. Simkins

Contributions: Helped conceive and implement study design. Collected and analyzed data. Wrote manuscript. Incorporated revisions and provided feedback on manuscript.

Co-Author: Philip S. Stewart

Contributions: Helped conceive and implement study design. Provided feedback on manuscript.

Co-Author: Joseph D. Seymour

Contributions: Helped conceive and implement study design. Provided feedback on manuscript.

Manuscript Information Page

Jeffrey W. Simkins, Philip S. Stewart, and Joseph D. Seymour

Biotechnology and Bioengineering

Status of Manuscript: (Put an x in one of the options below)
__X_ Prepared for submission to a peer-reviewed journal
____ Officially submitted to a peer-review journal
____ Accepted by a peer-reviewed journal
____ Published in a peer-reviewed journal

Wiley

MICROBIAL GROWTH RATES AND LOCAL EXTERNAL MASS TRANSFER RESISTANCE IN A POROUS BED BIOFILM SYSTEM MEASURED BY ^{19}F MAGNETIC RESONANCE IMAGING OF STRUCTURE, OXYGEN CONCENTRATION, AND FLOW VELOCITY

Abstract

Oxygen availability has a profound impact on biofilm structure and metabolism in diverse contexts, from medicine to industry to the environment. However, spatially-resolved measurement of oxygen distribution remains a technological challenge. ^{19}F nuclear magnetic resonance (NMR) oximetry and ^{1}H NMR velocimetry were combined with numerical simulation to characterize in detail macroscopic microbial respiration and growth behavior and to quantify local external mass transfer resistance in a model packed bed biofilm system in the presence and absence of flow. The spatiotemporal oxygen distribution, as measured by NMR, could be accurately simulated using a simple numerical model which demonstrated that only a few bacterial growth parameters, namely specific growth rate, inoculum cell density, and lag phase duration, can completely account for system-scale oxygen sink development. Localized experimental Sherwood numbers were calculated for flow experiments using NMR data and compared to correlation-based estimates. The oxygen concentration profile across a reactive biofilm particle was asymmetric with respect to flow direction with Sherwood numbers on the leading edge (Sh = 7) being larger than the trailing edge (Sh = 3.5).

7.1 Introduction

Biofilm systems, from wastewater treatment processes to localized infections, are characterized by heterogeneity at multiple length scales. Heterogeneity has been described at the microscale (*e.g.*, within a biofilm cell aggregate), at the mesoscale (*e.g.*, in and around multiple biofilm particles or aggregates), and macroscale (*e.g.*, gradients along a flow path in a pipe or wound bed). Heterogeneities can be anticipated in physical structure, hydrodynamics, metabolite concentrations, and microbial reactivity, creating complex systems in which structure, fluid flow, and reaction are coupled. These heterogeneities in turn have profound impacts on a variety of biofilm-related processes of high relevance to industry, medicine, and ecology, by shaping the local mass transfer environment.

One of the most important chemical species governing biofilm behavior is oxygen, which by virtue of its electron-accepting capacity, has a strong impact on microbial species composition and growth rate. Examples of biofilm-related phenomena that are profoundly influenced by oxygen transport include tolerance to antibiotics [1-4] and host immune defenses [5], virulence [6; 7], chemical conversion in wastewater treatment [8; 9], bioremediation [10; 11], and biofouling [12; 13]. Oxygen mass transfer rates, typically measured using microelectrodes [14; 15], have been used to explain spatial heterogeneity in biofilm structure [16], growth rate [17], protein expression and metabolic state [18], and to propose fluid flow phenomena such as flow channeling. Measurements of mass transfer coefficient and boundary layer thickness in biofilms have been reported [19; 20]. However, oxygen gradients are notoriously challenging to

measure, and measurements are often necessarily limited to either macroscopic measurements or 1D profiles along a single axis, which can be repeated at multiple sites to yield rudimentary spatial maps of local mass transfer coefficient. In both cases, invasiveness is a concern [21], and in the latter, a tradeoff must be made between detection of heterogeneity and acquisition time [19].

Here we report the application of nuclear magnetic resonance (NMR) imaging (MRI) and oximetry to a model packed bed biofilm system to elucidate in detail both macroscopic microbial respiration and growth dynamics as well as local external mass transfer resistance. This is achieved by measuring fluid flow patterns and velocities using ^{1}H NMR velocity mapping and by analyzing the spatiotemporal distribution of oxygen around biofilm-containing gel beads, at a resolution of approximately 117 μm, using ^{19}F NMR oximetry. Long-term noninvasive oxygen mapping is accomplished by encapsulation of emulsion containing an oxygen-sensitive perfluorocarbon (PFC) in alginate beads as described in [22]. Encapsulation of PFC in alginate has previously been used for oxygen monitoring in biological tissues [23].

7.2 Methods

7.2.1 Magnetic Resonance Imaging System

All experiments were performed on a 7 T vertical-bore magnet with an actively shielded micro2.5 gradient probe providing 1.5 T/m magnetic field gradients at 60 A, under the control of a Bruker Avance III MRI spectrometer.

7.2.2 pO_2 vs R_1 Calibration Curve for Perfluorooctylbromide

Oxygen measurement was accomplished using the oxygen-sensing perfluorocarbon perfluorooctylbromide (PFOB). The spin-lattice relaxation rate R_1 of PFOB is strongly and linearly sensitive to local oxygen concentration, and in addition, PFOB readily forms stable emulsions which permit incorporation of the oxygen-sensor into the biofilm system and a static ^{19}F signal spatial distribution. A calibration curve relating the R_1 of PFOB to pO_2 in the anoxic to atmospheric range (0 to 17.8 kPa; 85 kPa atmospheric pressure in Bozeman, MT, USA with 20.9% oxygen), relevant to bacterial growth conditions, was constructed. Alginate beads containing 90% w/v dispersed PFOB were prepared as described in section 7.2.3 and immersed in DI water. Gases of variable oxygen content (100% air, 75% air/25% N_2, 50% air/50% N_2, 25% air/75% N_2, 100% N_2) were bubbled through the sample for 30 min and the bottle was immediately sealed. The sample was loaded into a 25 mm dual-tuning $^{1}H/^{19}F$ radiofrequency (rf) coil and R_1 for the CF_3 group was recorded after 1 hour. R_1 was measured using an Inversion Recover (IR) sequence with the time domain sampled logarithmically at six points (inversion time = 25, 100, 300, 600, 1000, 3000, 5000 ms) [24]. Time-domain data was fit using Levenberg-Marquardt least-squares regression to a three-parameter mono-exponential formula governing the IR pulse sequence, yielding values for both signal intensity and rate constant R_1. Three replicates, each using a different aliquot of the beads, were acquired and averaged. Selective excitation of the CF_3 peak was accomplished using a chemically-selective 2 ms rf excitation pulse [24; 25].

7.2.3 Bacterial Cultivation

The bacterial species used in the present work was an *Escherichia coli* HB101 strain (a hybrid of *E. coli* strains B and K-12) containing plasmid pMF440 (provided by Dr. Michael Franklin; Addgene plasmid #62550) which confers strong constitutive expression of red fluorescent protein (RFP) recombinant mCherry, allowing for ease of strain identification, along with a co-expressed ampicillin resistance protein allowing for strain selection. Inocula were grown overnight in a shaker at 37 °C in full-strength Tryptic Soy Broth (TSB) and 100 μg/mL ampicillin to enforce retention of the plasmid. Resuspended bacteria were then introduced into the PFOB emulsion and encapsulated into alginate gel as described in section 7.2.4. This *E. coli* strain does not naturally form biofilms [26]. Nonetheless, alginate gel immobilization of bacteria is a widely-used laboratory biofilm model [27] due to the structural similarity of alginate and extracellular polymeric substance (EPS) and the ability to replicate biofilm phenomena such as antibiotic tolerance [28-31] and oxygen limitation [3; 4]. Use of a non-biofilm forming bacterium was critical as biofilm-forming species such as *Staphylococcus epidermidis* migrated rapidly from their inoculum bead and expanded throughout the column, making the spatial distribution of biofilm during the experiment unclear.

7.2.4 Oxygen-Sensing Alginate Beads

Oxygen measurement was facilitated by emulsifying PFOB in water and encapsulating the emulsion into alginate beads as described in detail previously [22]. Briefly, 0.4 g α-phosphatidylcholine surfactant (Sigma; P3556) and 0.2 g low-viscosity

sodium alginate (Sigma; A1112) was dissolved in 10 mL DI water. Then 9 g PFOB (Aurum Pharmatech; K-8801) was added and the solution was emulsified at 15,000 rpm for 30 minutes using a shear mixer to form a stable, 90% w/v emulsion of PFOB in a 2% w/v sodium alginate solution. An aliquot of the emulsion was inoculated with *E. coli* while the remainder was not, and both were dripped into a 50 mM solution of calcium chloride (Sigma; C1016) using a burette, generating spherical alginate beads of average diameter 3.42 mm (± 0.23) containing dispersed PFC (Figure 7.1). Inoculation of the PFOB emulsion was carried out as follows: a 1 mL aliquot of overnight culture was centrifuged at 6,000 rpm for 4 min, the supernatant was removed, and cells were resuspended in phosphate buffered saline (PBS). The inocula was then introduced into the PFOB emulsion at a final dilution of 1:10,000. All glassware and the shear mixer downshaft were autoclaved prior to bead production, and all processes were conducted in a biological cabinet with airflow to prevent contamination by environmental microbes.

7.2.5 Measurement of Growth Rate and Inoculum Cell Concentration

Specific bacterial growth rate μ and viable inoculum cell concentration were measured using the plate count method. 1 mL from an overnight culture was resuspended in PBS and used to inoculate a fresh solution of 25 mL of full-strength TSB at a final dilution of 1:10,000 which was then incubated on the shaker at 22.8 °C, the temperature used for all MRI experiments. At $t = 0$ hours, and every hour thereafter for 8 hours, a 1 mL aliquot was removed and a serial tenfold dilution was performed out to 10^{-6}. From each dilution, 5 drops of 10 µL were plated on tryptic soy agar. This was performed in

triplicate for each dilution. Plates were incubated at 37 ºC for 6 to 8 hours until colonies were easily visible but well separated and counted, and the dilution with the most colonies that were still well separated was selected for cell counting. This entire growth curve was repeated in triplicate. The cell counts at $t = 0$ hours provided X_o, the initial inoculum cell concentration, while the slope of the growth curve on a semilog plot following the lag phase yielded μ (see Eq 7.11 below).

Separate measurements (2) for X_o were also obtained by digestion of a subset of inoculated beads immediately after bead creation. Following gelation in the calcium chloride solution, 10 inoculated beads were blotted on paper towel to remove excess fluid and dissolved in 50 mM sodium citrate, and the resulting solution was subjected to a plate count as described above. Values obtained for X_o from the beads themselves were found to be in good agreement with values obtained from the planktonic growth curve.

7.2.6 Biofilm System: Column Packed with Alginate Beads

Experiments were carried out on a packed bed column wherein the alginate beads were used as the solid packing (Figure 7.1). The protocol for packed bed loading and for NMR scans generally follow [22] but with changes. Excess calcium chloride solution used for bead gelation was poured into a freshly autoclaved, 10 mm ID liquid chromatography column (Omnifit Labware) with 30 μm filters at both ends. Sterile beads were removed from the calcium chloride bath and wet-loaded into the column. A single inoculated bead was loaded and its position manipulated using a spatula to the region of the column corresponding to the isocenter once inserted into the MRI coil. The column

was then filled to the top with sterile beads and connected to a high performance liquid chromatography (HPLC) Pharmacia P-500 pump with 1.9 mm ID Teflon tubing, inserted into the rf coil, loaded into the magnet, and maintained at 22.8 ºC.

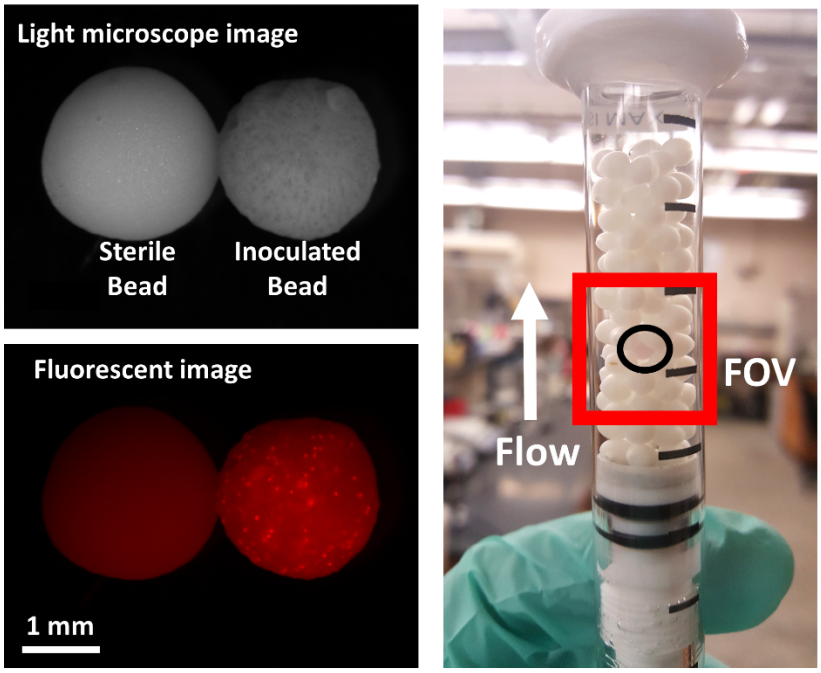

Figure 7.1. Top left: light microscope image of 3.42 mm diameter oxygen-sensing alginate beads. A 90% w/v emulsion of PFOB was encapsulated within the alginate matrix of each bead, and the linear dependence of R_1 of the CF_3 group on local pO_2 allows for oxygen mapping. The bead on the right was inoculated with an RFP-expressing *E. coli* strain, and colonies were observed as regions of decreased transparency. Bottom left: fluorescent microscope image of the same beads, where expressed RFP allows for identification of intended microbe and visualization of biofilm growth. Right: experimental system consisting of a 10 mm ID chromatography column with oxygen-sensing beads used as the solid packing. A single inoculated bead were placed at the isocenter of the field of view, located within the black circle. Experiments were run both in the presence and absence of flow (25 mL/h). Used with permission from [22].

The feed stream for the packed bed column consisted of 2 L of full-strength TSB with 50 mM calcium chloride, with the inclusion of calcium chloride in the feed

preventing dissolution of the alginate structure over long periods due to calcium ion diffusion out of the alginate gel matrix. The solution was prepared by autoclave, allowed several hours to cool, and laboratory air was bubbled through the carboy for one hour to replenish the dissolved oxygen lost in the autoclave process. Bacterial air filters were incorporated into the feed bottle inlet and offgas tubing to prevent introduction of bacteria during bubbling.

The feed reservoir was connected to the pump and the outlet of the packed bed column was connected to a waste collection bottle, forming an open flowthrough loop (Figure 7.1). For a subset of packed bed samples, the nutrient feed was pumped through the bed at 25 mL/h with a superficial velocity of 0.08 mm/sec. For another subset, the nutrient was pumped only until it had filled the column, following which flow was turned off. Oxygen was monitored over the course of bacterial growth by continuous acquisition of 2D sagittal ^{19}F R_1 maps. These R_1 maps sampled only 3 points along the IR curve (TI = 25, 1000, 3000 ms) to reduce acquisition time (FOV: 15 x 12 mm^2, resolution: 469 x 375 μm^2, TE: 8 ms, 1 echo, TR: 15 s, 3 mm slice, 8 averages, AQ time: 192 min).

Following complete depletion of oxygen throughout the column, fluid flow velocity distribution was measured with two ^{1}H sagittal velocity maps, one with velocity sensitivity in the slice direction and one in the read direction, both with no-flow correction (FOV: 15 x 12 mm^2, resolution: 117 x 187.5 μm^2, TE: 13.8 ms, TR: 1 s, 1 mm slice, 8 averages, δ: 1 ms, Δ: 8.5 ms, $G_{\text{flow encode}}$: 0.51 T/m, AQ time: 17 min) and 3 axial velocity maps centered around the location of the inoculated bead with velocity encoded in the axial slice direction (FOV: 12 x 12 mm^2, resolution: 93 x 187.5 μm^2, TE: 13.8 ms,

TR: 1 s, 1 mm slice, 8 averages, δ: 1 ms, Δ: 8.5 ms, $G_{flow\ encode}$: 0.51 T/m, AQ time: 17 min).

7.2.7 Oxygen Distribution as a Function of *r* and *z* and Experimental Sherwood Number

All processing of MRI scans were carried out in MATLAB. Each ^{19}F sagittal image was zero-filled to a matrix size of 128 x 128, yielding an apparent resolution of 117 x 94 μm^2. R_1 maps were generated by fitting signal intensity of each pixel to the inversion recovery equation as described in section 7.2.2. Pixels were only assigned an R_1 value if they met a threshold signal intensity (10^5) and the associated standard error for the R_1 parameter fit was below 15%. Mean pO_2 for the active (inoculated) bead was calculated by applying a circular mask with radius 1.71 mm (the average radius of an alginate bead) and centered at the active bead center and computing the mean nonzero value of all pixels within the mask. These values were then converted from kPa to mol/m^3 and exported to COMSOL for comparison with numerical simulations as described in the next section.

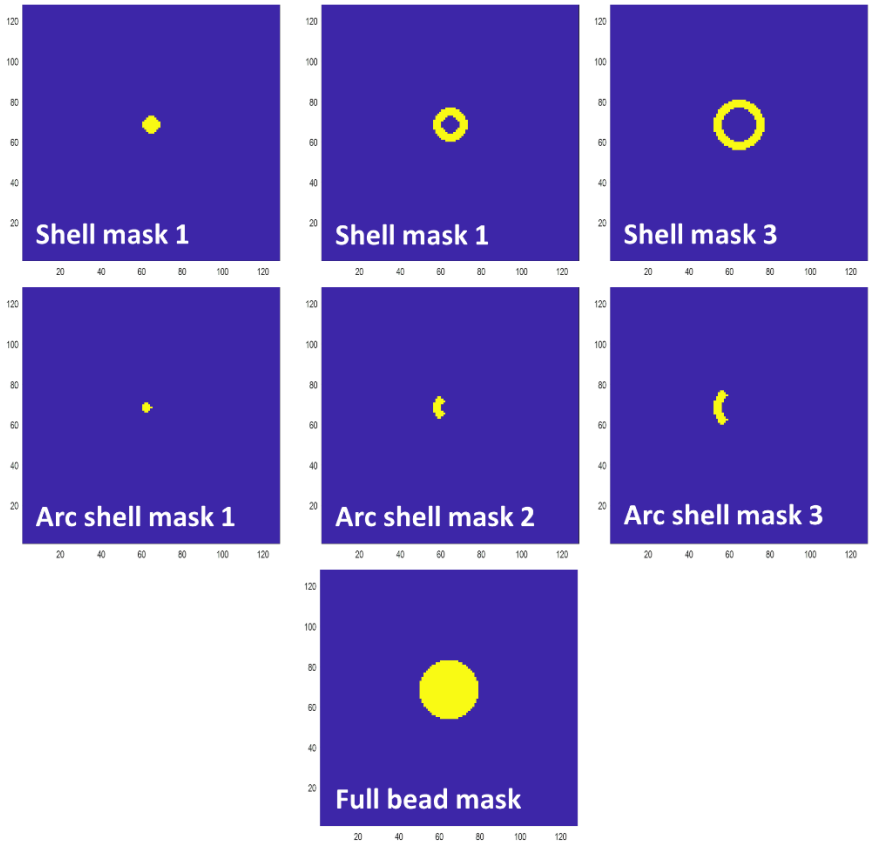

Figure 7.2. Top row: circular shell masks of successively larger radial coordinate used for calculating overall pO_2 as a function of R. Masks were centered about the inoculated bead center and each mask had a radial thickness of 489 μm, corresponding to ¼ the total radius of the bead. Middle row: circular arc masks used for calculating pO_2 as a function of r for leading and trailing edge separately. Circular masks were multiplied by a circular segment such that only values from the trailing or leading edge were averaged. Bottom: Circular mask with radial thickness 1.71 mm (equal to the inoculated bead radius), used for calculation of average pO_2 within the active bead over time.

pO_2 as a function of r was calculated by applying several circular masks of increasing area centered on the active bead center, and subtracting the previous smaller mask from the current mask to generate "shell" masks wherein only values within a ring-shaped slice around the active bead are averaged (Figure 7.2). The mean pO_2 values from each shell were then plotted as a function of radial distance from the active bead center r

and over time. Radial coordinates represent the center of the shell, i.e. a value plotted at r = 0.24 represents the mean pO_2 value obtained from averaging from r = 0 to r = 0.48. To evaluate oxygenation as a function of radial coordinate for the trailing and leading edges of the active bead with respect to flow direction separately, an additional circular "arc" mask was applied specifying the range of θ values over which to average. With the θ = 0 axis defined as aligned with the leading edge, only values between θ = -π/4 and π/4 were averaged for the leading edge measurement and only values between θ = 3π/4 and 5π/4 were averaged for the trailing edge measurement. Overall mean pO_2 in the active bead was calculated by averaging over a circular mask with radius exactly equal to the inoculated bead diameter.

Experimental Sherwood numbers for trailing and leading edges were calculated by identifying the radial coordinate corresponding to the bead surface (r_s) and the coordinate corresponding to a pO_2 value of 99% of the bulk value (r_b). In practice, identification of the point corresponding to r_b was accomplished by marking the radial coordinate at which the pO_2 profile became flat. The distance between these two points is then defined as δ, the thickness of the external mass transfer resistance layer (also called the concentration boundary layer) [32]. The external mass transfer coefficient is then given by:

$$k_c = \frac{D_{aq}}{\delta} \qquad \text{(Eq 7.1)}$$

Normalizing to the characteristic lengthscale, we obtain the Sherwood number [33]:

$$Sh = \frac{k_c l}{D_{aq}} = \frac{l}{\delta} \qquad \text{(Eq 7.2)}$$

where l in this case is the average diameter of an alginate bead.

It should be noted that the method for calculating Sherwood number naturally introduces binning into the computation process, as selection of the width of the averaging shells dictates the possible values that can be obtained for δ. Using thin shells for averaging allows one to plot more values on the pO_2 vs r curve but also results in few pixels being averaged for each point, introducing more variability in the obtained values and potentially obscuring the shape of the pO_2 curve. This could lead to misidentification of the boundary layer thickness. Conversely, using thick averaging shells augments the precision of the measurement but results in fewer points being plotted on the pO_2 vs r curve, leading to binning during the calculation of δ and Sh.

An additional source of uncertainty in the boundary layer measurement is identification of the exact location of r_b. The pO_2 vs r curves at different times for a single experiment are not necessarily in exact agreement on the location of r_b. However for the flow experiments it was observed that pO_2 vs r curves at different time points were generally in good agreement, and thus the potential error introduced by this analysis operation was minimized. When the point identified as r_b differed between successive maps in a single experiment, the profile exhibiting the largest total oxygen gradient was selected for r_b identification, as signal-to-noise is expected to be highest when oxygen gradient is strongest. The two considerations above have the potential to influence the absolute values obtained for δ and Sh. However, differences observed between experiments at different conditions and between trailing and leading edges are not affected as the same procedure is followed in all analyses.

7.2.8 Sherwood Number Estimation Using Empirical Correlations

To determine a range of expected Sherwood numbers with which to compare to measured Sherwood values, we examined three theoretical or empirical formulations for *Sh*. In the present experiment, bead diameter is large relative to column diameter ($D_p/D_{col} \approx 3$), and thus we are unlikely to satisfy criteria for a random beadpack wherein flow channeling is assumed to be stochastic [34]. However, the experimental system also likely deviates from the assumption of laminar flow over a single suspended sphere due to the presence of adjacent beads. We therefore used correlations for both a single sphere experiencing laminar forced convection and for a random packed bed experiencing forced convection to determine bounds on expected Sherwood number dependent on assumptions. It was observed that the different formulations for *Sh* nonetheless converged on similar values, relaxing the need for strict adherence to the individual criteria of each correlation.

All empirical correlations for expected *Sh* required computation of Reynolds number and Schmidt number. The Schmidt number, given by [35]:

$$Sc = \frac{\mu}{\rho D} \qquad \text{(Eq 7.3)}$$

is constrained for our experimental system given the fixed temperature, fluid composition, and characteristic lengthscale (bead diameter), and was determined to be Sc = 492. Reynolds number for a packed bed column is given by [36]:

$$Re = \frac{\rho V_o D_p}{(1-\varepsilon)\mu} \qquad \text{(Eq 7.4)}$$

where the void fraction ε can be estimated by the geometry of the packing material and the nature of the packing (e.g. loose, poured) or computed specifically for the system. For

our system ε was determined by collecting five axial ^{1}H velocity maps (pulse sequence parameters given in section 7.2.6) spaced throughout the column and computing the fraction of pixels exhibiting nonzero flow, yielding a value of 0.374. Using the superficial velocity of 0.14 mm/sec calculated for our column (25 cm^3/h with ID = 10 mm), *Re* was determined to be 0.8, in the laminar regime $Re < 10$ for packed beds [36].

Since v_z velocity distribution measurements were collected for the columns, we were also able to calculate *Re* directly instead of formulating an effective V_o using volumetric flowrate and void fraction for a packed bed column. The mean v_z in the region round the inoculated bead was taken to be the fluid velocity and *Re* calculated for a single sphere as:

$$Re = \frac{\rho V_o D_p}{\mu} \qquad \text{(Eq 7.5)}$$

This results in $Re = 1.1$, which is not in the creeping flow regime for a single sphere ($Re \ll 1$) [37]. Both *Re* calculations were used in computation of Sherwood number to yield a range of expected values.

Three correlations were used to determine *Sh* for the experimental system. The first is a theoretical consideration of creeping flow around a single solid sphere as summarized in Bird, Stewart, and Lightfoot [32]. The result is:

$$Sh = 2 + 0.991(ReSc)^{1/3} \qquad \text{(Eq 7.6)}$$

and is most accurate for $Re \ll 1$. The second, formulated from the theoretical consideration of forced convection around a single sphere, is the mass transfer analogue of the Ranz-Marshall correlation [38]:

$$Sh = 2 + 0.6Re^{1/2}Sc^{1/3} \qquad \text{(Eq 7.7)}$$

which is most accurate for $Re < 200$, $Sc < 250$. The final correlation is applicable specifically to packed bed columns and arises not from theoretical considerations but rather empirical fitting of experimental *Sh* values across a range of *Re* and *Sc* values. Details about the correlation may be found in Karabelas et al [39].

$$Sh = [(4.58Re^{\frac{1}{3}}Sc^{\frac{1}{3}})^6 + (2.39Re^{0.56}Sc^{\frac{1}{3}})^6]^{\frac{1}{6}} \qquad \text{(Eq 7.8)}$$

This equation is accurate for a wide range of *Re* values ($0.4 < Re < 2000$).

7.2.9 Bacterial Growth Numerical Model Assumptions

To determine whether the macroscale behavior of the oxygen sink could be comprehensively accounted for by intrinsic bacterial growth parameters (namely X_o, μ, and lag phase duration), a numerical model of the experimental system was built using the Transport of Dilute Species module in COMSOL (v5.3) and compared to the experimental datasets. Several assumptions were employed in the model. First, that growth is restricted to the inoculated bead, an assumption consistent with previous observations in these columns. Second, that oxygen diffusivity within the alginate beads is approximately equal to oxygen diffusivity in water:

$$D_{alg} \approx D_{aq} \qquad \text{(Eq 7.9)}$$

This assumption is well supported by a study by Kurosawa *et al.* [40] that determined the oxygen diffusivity in 2% agarose gel beads containing entrapped bacterial cells was 92% of the aqueous diffusivity, and was insensitive to cell density. The influence of the discrepancy between the assumption and the true, slightly reduced diffusivity was investigated in the model, and it was determined that minor changes to the

diffusion coefficient had little effect on the numerical solution. The exact diffusion coefficient used in the model was 1.9 x 10^{-9} m^2/sec, as predicted for our operating temperature of 22.8 °C by Han and Bartels [41].

The third assumption was that oxygen consumption obeyed zero-order kinetics, wherein reaction rate is unaffected by oxygen concentration:

$$\frac{-dC}{dt} = k_o \qquad \text{(Eq 7.10)}$$

This assumption is satisfied whenever oxygen concentration values are well above K_s, the Monod half-saturation coefficient for oxygen uptake. In *Pseudomonas aeruginosa*, K_s for oxygen has been measured to be 0.25 mg/L [42] while K_s for *E. coli* strain K-12 has been reported as 3.84 μg/L [43]. With saturation dissolved oxygen values of 7.25 mg/L in our experiments (calculated from Benson and Krause 1980 [44] and adjusted for our operating elevation of 1,461 m), the zero-order kinetic model is a valid approximation.

Fourth, that bacterial cells are in exponential growth phase throughout the experiment and that as a consequence biomass density X grows exponentially with rate constant μ and initial condition X_o:

$$X = X_o \exp(\mu t) \qquad \text{(Eq 7.11)}$$

Inoculating beads with a diluted overnight culture ensures that cells are in exponential phase at the beginning of the experiment. Bacteria do not transition to stationary phase until either an essential nutrient has become depleted or an inhibitory product has accumulated enough to interfere with growth. In the experimental system, oxygen eventually becomes fully depleted. However, the low value of K_s for *E. coli*

indicates that oxygen levels must be very close to zero to cause deviation from the exponential growth model. Thus, this approximation is well-supported for most of the oxygen decay curve, but is likely increasingly violated as oxygen levels in the site of growth approach zero.

The fifth assumption, related to the previous, states that oxygen reaction rates are uniform throughout the active bead. This is valid for most of the experiment but becomes violated as cell density becomes large enough that the penetration depth of oxygen falls below the radius of the inoculated bead. At this point, cells in the interior of the active bead become nutrient limited and experience a reduction in growth rate. At this point oxygen reaction rate becomes a function of radius *r*. This transition is not captured in the numerical model, and thus the uniform reaction rate assumption is also violated as oxygen depletion dominates.

For no-flow columns, it was additionally assumed that no natural convection was present, given the gradient cooling water at 22.8 °C circulating the probe within the magnet bore prevents the development of significant temperature gradients across the sample. For flow experiments, a limiting-case assumption was made wherein the oxygen concentration at the bead surface takes on its bulk value throughout the experiment:

$$C(r_s) = C_b = 17.8kPa \qquad \text{(Eq 7.12)}$$

This limiting-case assumption is termed the 'perfect mixing' case, and is postulated to represent the upper-bound, where external mass transfer is negligible throughout the experiment. This assumption provides a basis for examining the influence of external mass transfer on the numerical solution.

7.2.10 Parameter Values for Numerical Model

Oxygen transport in the column can be generally described by a diffusion-advection-reaction balance:

$$\frac{\partial C}{\partial t} + \nabla \cdot (\boldsymbol{v}c) = \nabla \cdot (\boldsymbol{D}^* \nabla C) + R \qquad \text{(Eq 7.13)}$$

where R denotes reaction rate. Assumption of isotropic diffusion coefficient simplifies the diffusive flux term. For the no-flow experiments the advective term is eliminated, while for flow experiments, perfect mixing replaces the advective term with an advective mass transfer boundary condition at the bead surface (Eq 7.12). This leaves a simple diffusion model:

$$\frac{\partial C}{\partial t} = D\nabla^2 C + R(t) \qquad \text{(Eq 7.14)}$$

For zero-order kinetics, the reaction rate is:

$$R(t) = \frac{-\mu}{Y_{XO2}} X_o exp(\mu t) \qquad \text{(Eq 7.15)}$$

where Y_{XO2} represents the yield coefficient for biomass created per gram oxygen consumed. Y_{XO2} for aerobic *E. coli* growth was obtained from Carlson and Srienc, who compiled published experimental values and identified the linear dependence of Y_{XO2} on maximum specific growth rate [45]. Our growth rate of 0.618/h yielded an expected Y_{XO2} value of 1.073 g biomass/g O_2.

For input into the numerical model, all values were converted into units of mol/m^3. To determine biomass *X*, it was necessary to convert viable cell counts into biomass. The dry weight of a single bacterium can vary significantly even within a single strain, with much of the variation attributed to growth rate (faster growing colonies typically exhibit reduced size). To determine a suitable value for the average dry weight

of an *E. coli* HB101 cell, we used a study by Basan et al which compared growth rate and dry mass of the closely related *E. coli* strain K-12 [46]. Our experimentally-measured growth rate of 0.618/h corresponded to a dry weight of 0.3 pg, and this value was selected for conversion from viable cell count to live biomass. Incorporation of all elements and unit conversion into the reaction term yielded a final reaction rate of -3.33 x 10^{-7} mol $O_2/m^3 \cdot s$. Lag phase was accounted for in the model by introducing a time delay in the emergence of the reaction term. Average oxygen concentration within the active bead from the numerical model was plotted over time against the experimental results. Values of the variables governing bacterial growth, μ, and X_o, were systematically varied to determine the parameters yielding the best fit to the experimental data and to observe the nature of their influence on the simulated oxygen profile. All time coordinates were converted from s to min and all oxygenation values converted from mol/m^3 back to kPa before plotting to provide consistency in data presentation.

7.3 Results and Discussion

7.3.1 pO_2 vs R_1 Calibration Curve for Perfluorooctylbromide

The ^{19}F spin-lattice relaxation rate R_1 of the CF_3 group of PFOB encapsulated in alginate beads exhibited a linear dependence on oxygen partial pressure (Figure 7.3), and the constant temperature of the NMR gradient cooling water (T = 22.8 ± 0.5 °C) ensured no temperature impact on the R_1 measurements. Even in anoxic conditions, PFOB

possesses a relatively high R_1 value, which allows for faster R_1 measurements due to the requirement that TR > $5/R_1$. For more detail on calibration curve construction, see [22].

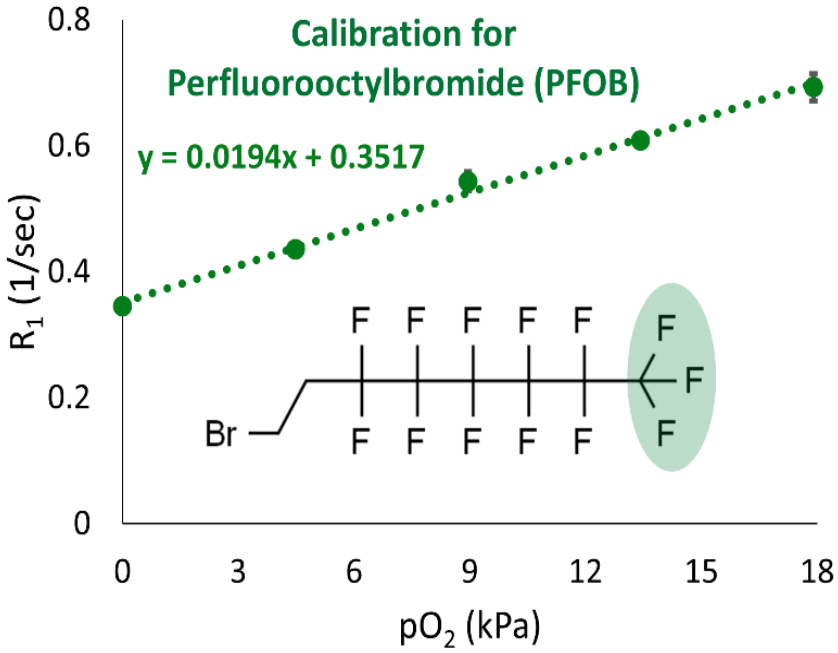

Figure 7.3. Standard curve of the response of ^{19}F R_1 to pO_2 for 90% w/v PFOB dispersed in 2% w/v alginate beads at 7 T and 22.8 °C. All points were measured in triplicate using different bead samples and error bars denote standard deviation. Where error bars are not apparent, standard deviation is smaller than the marker size. The resonance peak used to measure R_1 (CF_3 group) is highlighted in green.

7.3.2 Measurement of Growth Rate and Inoculum Cell Concentration

Triplicate measures of planktonic growth parameters are given in Figure 7.4. The lag phase was four hours for each of the three runs. Maximum specific growth rate was quantified by fitting the natural logarithm of cell count from t = 4 to 8 hours to a line using least-squares regression, and inoculum cell density was taken to be the bacterial concentration obtained at the t = 0 time point. Two additional measurements were

obtained for X_o without running a full growth curve. Separate measurements were obtained for each run and then averaged together for use in the numerical model. Estimates for population parameter values were μ = 0.618 ± 0.02/h and X_o = 259,111 ± 70,000 CFU/mL, where uncertainty denotes standard error. In the absence of nutrient limitation, specific growth rate is expected to be an intrinsic property of bacterial strain and nutrient conditions, a proposition supported by the low variability among the μ measurements. X_o measurements showed significantly higher uncertainty, likely in part due to variability in the overnight culture incubation time (18-20 h), and in general X_o is expected to differ between individual experiments.

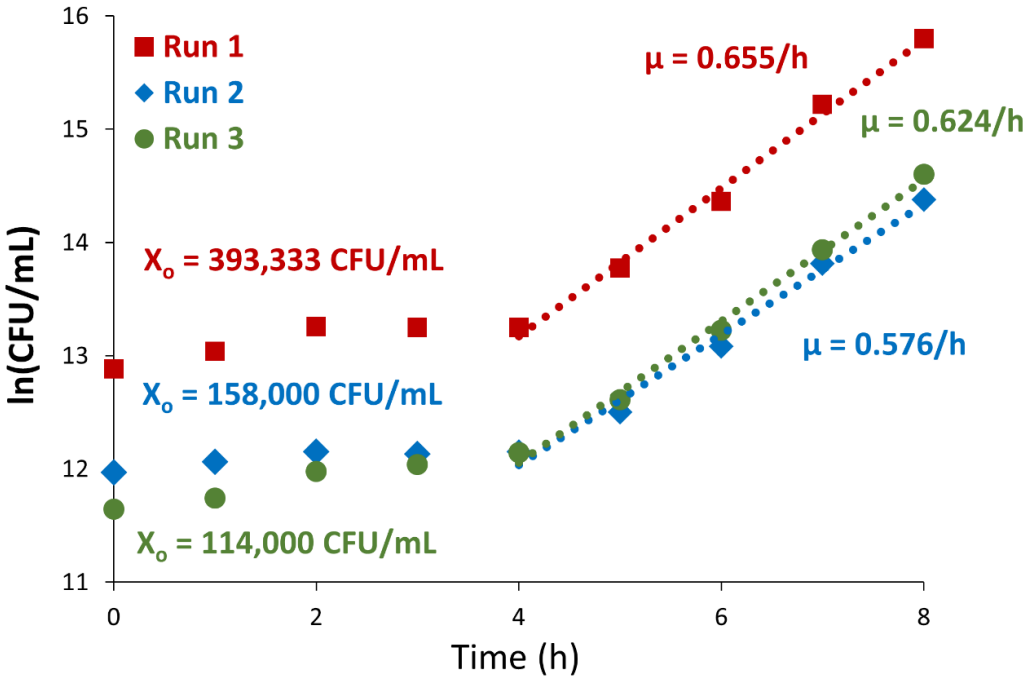

Figure 7.4. Planktonic growth curves for *E. coli* HB101 quantified by viable cell count, along with associated measurements inoculum cell density X_o and specific growth rate μ during exponential phase. Two additional measurements of X_o in the absence of a full growth curve yielded X_o = 152,781 and 477,441 CFU/mL.

7.3.3 Oxygen Maps for Flow and No-Flow Packed Bed Columns

Oxygenation data for a representative packed bed column in the absence of flow ("No Flow" run) is shown in Figure 7.5. For all columns, the location of the inoculated bead was determined by comparison of the developing oxygen sink with high-resolution ^{19}F sagittal and ^{1}H sagittal images showing the distribution of beads within the bed. No Flow columns exhibited static oxygenation profiles for several hours, the first portion of which can be attributed to bacterial cells being in lag phase. Following initiation of growth, oxygen levels remained steady at saturation values of 17.8 kPa as the initial bacterial population was too small to deplete local O_2. As bacterial counts increased exponentially, a miniscule oxygen sink developed; for No Flow #2, this sink is barely evident in the center of the t = 560 min oxygen map. Thereafter the total respiration rate surged and oxygen levels within the bead crashed, followed by complete depletion of oxygen throughout the field of view.

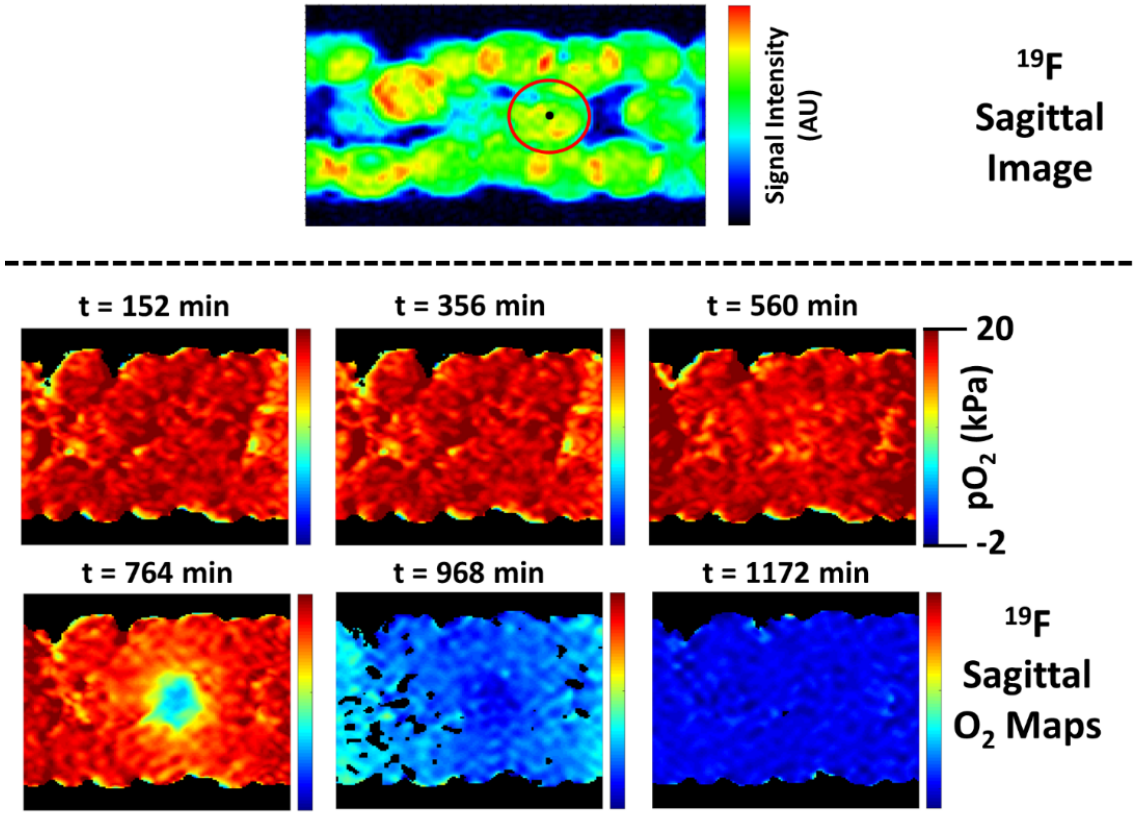

Figure 7.5. Top: high-resolution ^{19}F sagittal signal intensity image of No Flow column #2. The center of the inoculated bead is marked with a black dot, and its size is denoted with a red ring. Bottom: corresponding time series of sagittal oxygenation maps in kPa. Field of view for both the sagittal image and the oxygen maps are 15 x 12 mm^2 with a matrix size of 128 x 128, yielding a resolution of 117 x 94 μm^2/pixel.

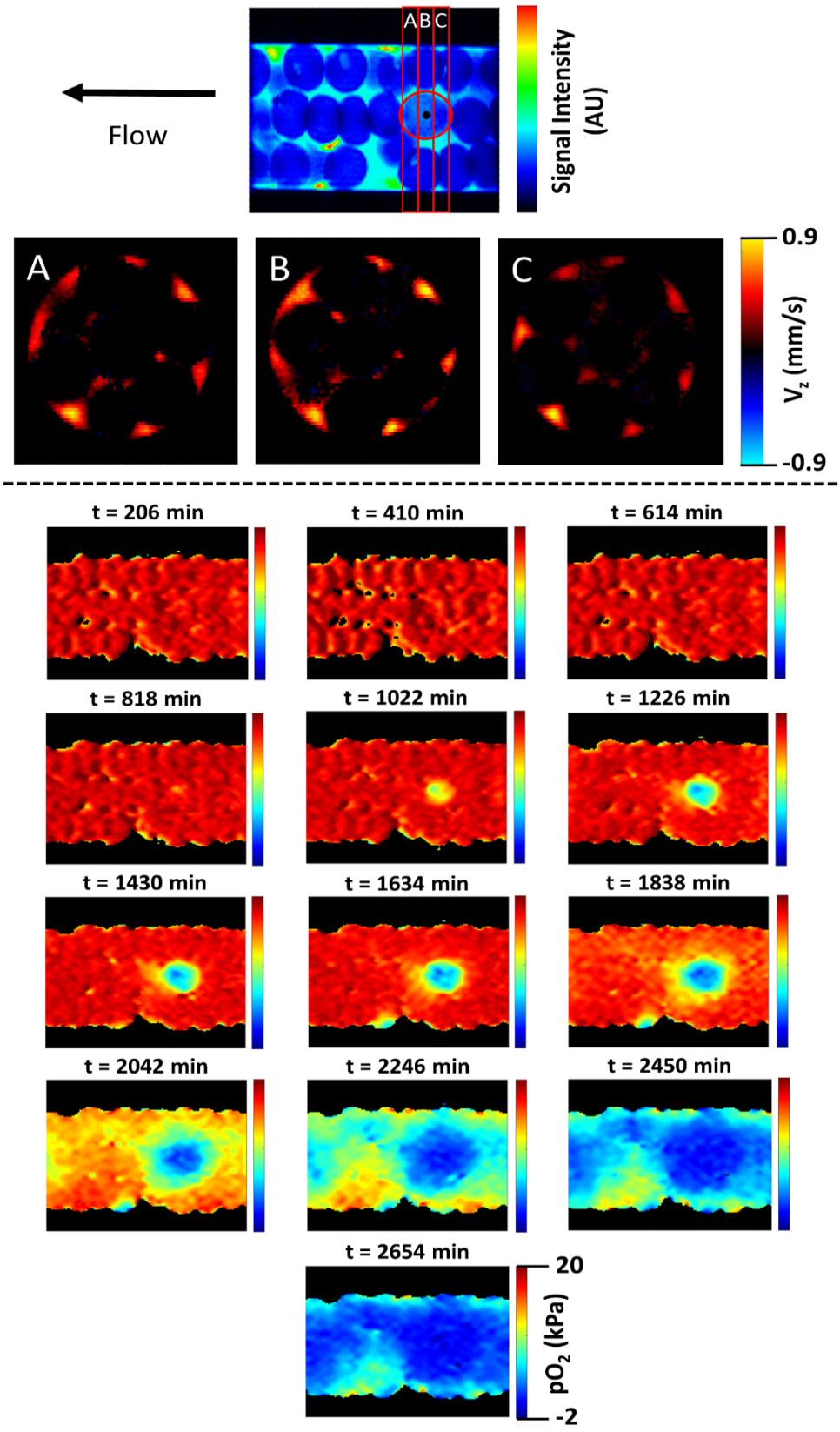
Flow
A B C
Signal Intensity (AU)
A
B
C
0.9
V_z (mm/s)
-0.9
t = 206 min
t = 410 min
t = 614 min
t = 818 min
t = 1022 min
t = 1226 min
t = 1430 min
t = 1634 min
t = 1838 min
t = 2042 min
t = 2246 min
t = 2450 min
t = 2654 min
20
pO_2 (kPa)
-2

Figure 7.6. Top: T_2-weighted ^{1}H sagittal image (rotated 90°) showing the distribution of alginate beads in a 1 mm thick longitudinal slice of the column which provides contrast between water in pore space and within the alginate. The inoculated bead is marked with a black dot (center) and red circle (outer edge). Vertical red rectangles represent the locations of the ^{1}H axial V_z velocity maps shown below. Middle row: ^{1}H axial V_z velocity maps centered around the active bead, with the position of each relative to the sagittal image above denoted using letters A-C. Bottom: corresponding time series of sagittal oxygenation maps in kPa. Field of view for both the sagittal image and the oxygen maps are 15 x 12 mm^2 with a matrix size of 128 x 128, yielding a resolution of 117 x 94 μm^2/pixel.

Oxygenation data for a representative packed bed column subjected to 25 mL/h nutrient solution flow is shown in Figure 7.6. The position of the inoculated bead was identified by comparing the oxygenation maps to high-resolution ^{1}H sagittal (top) and ^{19}F sagittal (not shown) images. ^{1}H axial v_z velocity profiles centered about the active bead reveal that most of the flow occurred along the column edges due to the increased pore size at these locations. Mass transport enhancement at the walls is expected due to the large D_p/D_{col} ratio in these columns. However, small flow channels can be observed surrounding the active bead, with typical velocity values ranging from 0 to 0.5 mm/s and a mean v_z value of 0.31 mm/sec. This experimental $\bar{v}_z$ value yielded a measured Reynolds number of 1.13. No flow was detected within the gel beads, consistent with the observation in natural biofilms that bacterial biofilm aggregates have very low hydraulic permeability [47; 48].

Relative to No Flow runs, Flow columns exhibited a slower emergence of the oxygen sink, with oxygen consumption for Flow column #2 becoming visible only around 1000 minutes, a significant delay compared to the No Flow experiments. There is also a substantial reduction in the rate at which the oxygen sink strengthens and expands

to adjacent regions, which is partially explained by replenishment of oxygen by fluid flow adjacent to the active bead.

7.3.4 Numerical Model of Bacterial Oxygen Consumption

The experimentally measured values for *E. coli* HB101 growth parameters (intrinsic growth rate, inoculum cell density, and lag phase duration) and literature estimates for the remaining unknown parameters (yield coefficient, dry cell weight, oxygen diffusivity) were combined to formulate a simple reaction rate which was used in simulations. The experimental mean oxygen concentration in the active bead was plotted against the corresponding value obtained from the simulation. A fitting factor (additional coefficient) was introduced into either X_o or μ, modifying the model's reaction rate to adjust the timescale and magnitude of the simulated oxygen decay curve. This fitting factor was calibrated until simulation and experimental data were in agreement, detailing the discrepancy between observed and expected oxygen consumption rates and quantifying the variability among replicate runs. An X_o fitting factor of 1.5, for instance, would indicate that the reaction term in the numerical model required an additional constant coefficient of 1.5 to provide best fit, while a μ fitting factor of 1.5 would indicate the need for a 1.5x multiplier on both the front coefficient and the exponential term (see Eq 7.15).

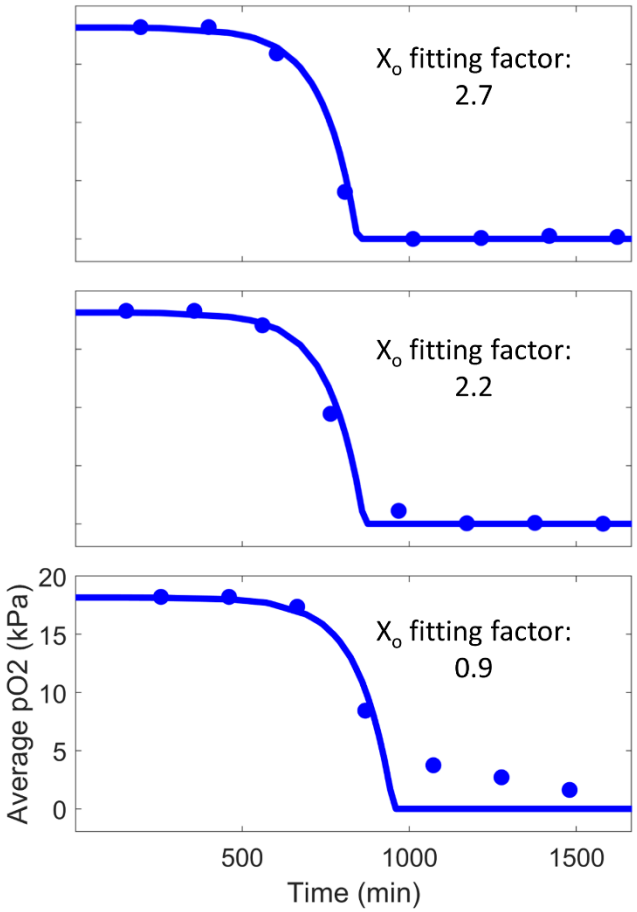

Figure 7.7. Time series of average oxygen concentration in inoculated bead for three No Flow columns. Empirical datasets are shown with blue circles, while simulation results are shown with blue lines. With μ and lag phase duration fixed at their independently-measured values, a fitting factor (constant coefficient) for X_o was introduced to each simulation and adjusted until experiment and model were in agreement, allowing for quantification of the variability between runs.

Results for No Flow experiments with fitting of the X_o parameter are shown in Figure 7.7. Best fit for the simulation was achieved by fixing μ and lag phase duration at their naïve, independently-measured values and fitting X_o to the experimental dataset. The timescale over which oxygen crashed within the active bead was somewhat variable, as exemplified by the range of fitting factors from 0.9 to 2.7 for the three replicate

datasets. This threefold range in the reaction strength yielding best fit is reasonable given the scatter of the X_o values obtained from lab bench experiments, which fluctuated from 114,000 to 477,441 CFU/mL (a fourfold increase). However, the scatter in the relative reaction strength among the datasets had a modest effect on the timescale of complete oxygen depletion, with the best fit simulations all reaching anoxic conditions between 850 and 1000 minutes. The overall shape of the simulated oxygen decay curve matched well with the experimental data, suggesting that lab bench measurements of X_o, μ, and lag phase duration reasonably represent the growth characteristics of *E. coli* during the packed bed column experiment. For two of the columns (#2 and #3), the model began to diverge with experimental data at later time points whereby mean oxygen concentration was low. This is likely due to violation of the model assuming cell density grows exponentially throughout the experiment and that reaction rate is uniform throughout the inoculated bead. As cell density spikes, the penetration depth of oxygen into the bead decreases due to reaction rate overwhelming diffusional transport capabilities, leading to both an overall reduction in growth rate and spatially-dependent oxygen utilization, neither of which are captured by the model. The numerical model should be most accurate in the early and mid-stages of oxygen usage, a prediction supported by Figure 7.7.

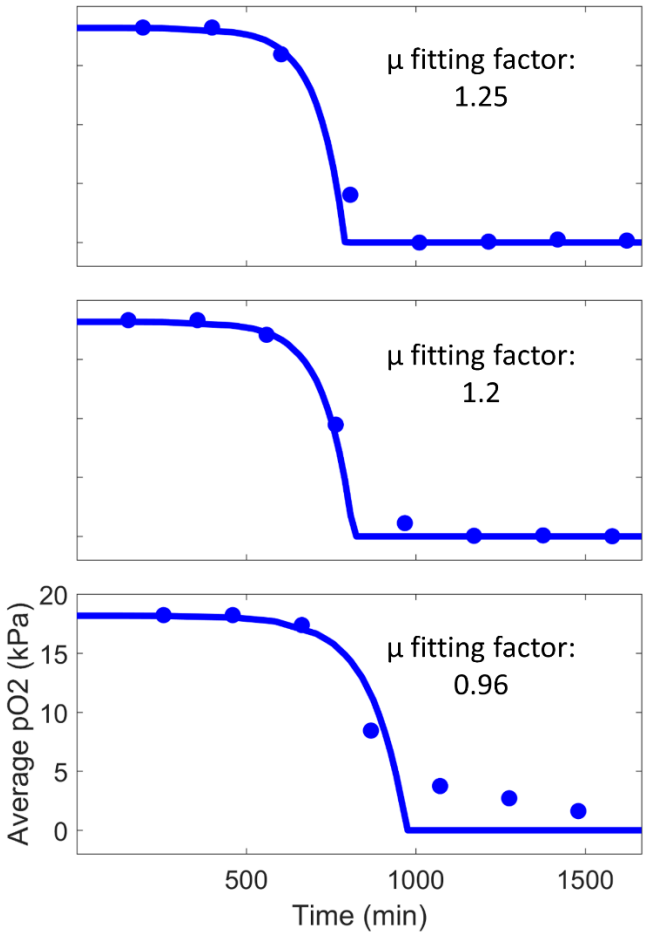

Figure 7.8. Time series of average oxygen concentration in inoculated bead for three No Flow columns with μ as the fitting parameter. Empirical datasets are shown with blue circles, while simulation results are shown with blue lines.

Best fit results for No Flow columns using μ as the fitting parameter are shown in Figure 7.8. Fixing X_o and lag phase duration and modifying μ to provide best fit reduced the variability in fitting factors required to well-represent the replicate datasets. This is due to both the dominance of exponential coefficients on the overall solution as well as the fact that μ appears both in the exponential term and the leading coefficient (Eq 7.15). The mean fitting factor obtained was 1.14, corresponding to a specific growth rate of 0.7, representing a modest discrepancy. This is because μ is typically assumed to be a

constant for a given strain under uniform environmental conditions [49], in contrast to the expected variability in X_o which is verified by our measurements. X_o is thus the preferred fitting parameter.

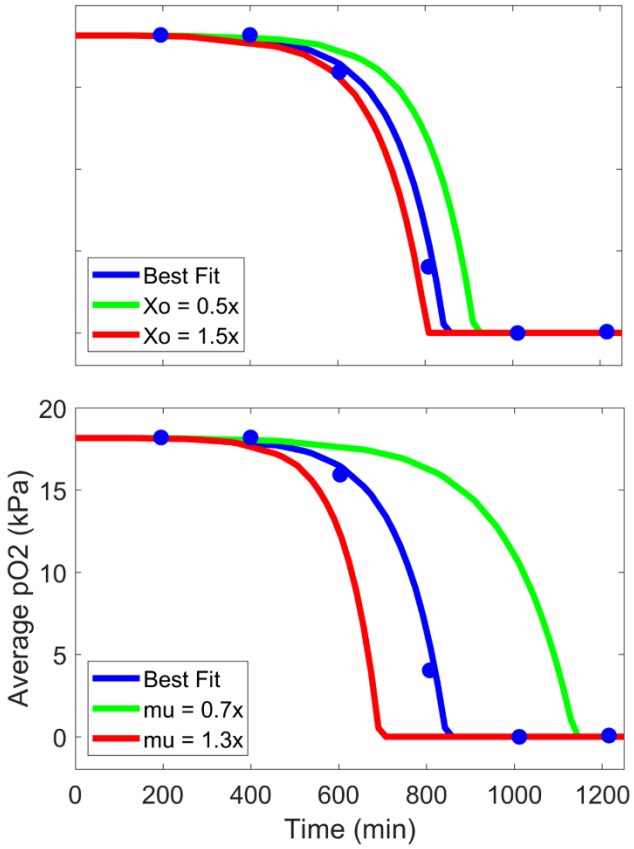

Figure 7.9. Top: experimental measurement of mean pO_2 in inoculated bead over time (blue circles) along with best fit simulation using X_o as the fitting parameter (blue line), and simulation results when model inoculum cell concentration X_o is decreased by 50% (green line) and increased by 50% (red line). Bottom: the same dataset but with growth rate μ varied by 30%.

To evaluate the influence of the different experimentally measured growth parameters on the behavior of the numerical solution, X_o, μ, and lag phase duration were

systematically varied within a single experiment using the "best fit" X_o as the base case (Figure 7.7), with the results for No Flow #1 shown in Figure 7.9. Increasing X_o in the numerical model by a factor of 50% relative to its initial value resulted in a modest decrease in the simulated timescale of complete oxygen depletion in the active bead, with anoxic conditions being achieved in approximately 810 minutes, down from the 'best fit' case of 850 minutes. Decreasing X_o by the same percentage relative to the 'best fit' case increased the timescale to about 925 min. It is evident that the shape of the oxygen depletion profile is identical for the three, with the only development resulting from modifying X_o being a translational shift in the position of the exponential decline. This demonstrates that variation in the initial cell concentration is functionally equivalent to variation in the lag phase duration, a result of the properties of the exponential growth model. With a specific growth rate of 0.618/h, a doubling of the inoculum cell density X_o is mathematically identical to a reduction in the lag phase of 67 minutes. While the influence of lag phase duration and inoculum cell concentration cannot be distinguished by the numerical model, we note that lag phase duration was found to be 4 hours for all growth rate experiment runs while X_o was found to vary significantly. Thus scatter in X_o is the more likely source of variability in the No Flow experiments.

In contrast to the limited influence of changes to X_o and lag phase duration on the simulated timescale of oxygen depletion, modest changes to the specific growth rate μ were sufficient to cause significant changes in the behavior. A 30% increase in μ changed the timescale of complete oxygen depletion from 850 to 700 minutes, while a corresponding increase resulted in a timescale of 1150 minutes. These adjustments to μ

cause significant changes to the exponential which shapes the oxygen decay curve, an effect absent from the No Flow experimental curves. Thus the simulations suggest that variability across replicate runs is likely caused by fluctuation in X_o at the beginning of the experiments, a conclusion reinforced by the growth curves. Overall, the results indicate that bacterial growth in complex media systems can be reasonably modeled with knowledge of just a few intrinsic growth parameters. Additionally, these data suggest that it may be possible to extract intrinsic growth rate, a fundamental characteristic of microbial behavior, from growth in complex media by fitting spatiotemporal oxygen distribution to a simple mathematical model of bacterial growth. In such an approach, X_o should be used as the initial fitting parameter to synchronize the timescale of early oxygen sink development with experimental data, with the understanding that variance in initial cell density is high and likely to account for most of the variability between replicate experiments. From this point, μ can be fitted to match the shape of the oxygen depletion curve, as this shape is entirely determined by μ and not X_o and thus should be relatively constant across replicates relative to X_o scatter.

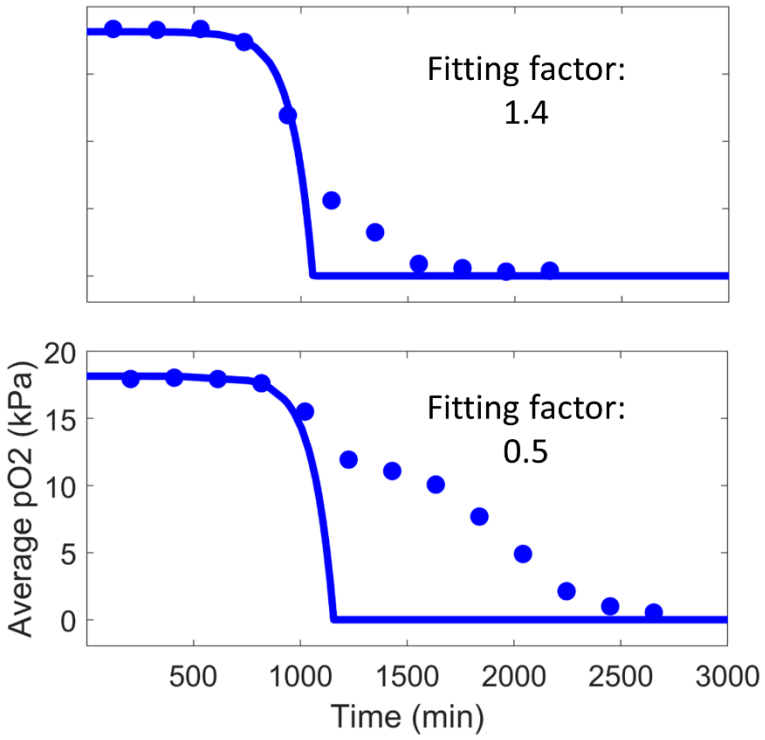

Figure 7.10. Time series of average oxygen concentration in inoculated bead for two Flow columns. Experimental datasets are shown with blue circles, while simulation results are shown with blue lines. An X_o fitting factor was introduced to each simulation, allowing for quantification of the variability between runs. For Flow #2, a poor fit to the model was observed regardless of the fitting factor used.

Time series of mean oxygenation in the inoculated bead for Flow columns are shown in Figure 7.10. Note the time axis is longer than for the corresponding No Flow plots (Figures 7.7 and 7.8) due to the longer timescales required for oxygen depletion. Relative to No Flow runs, Flow columns exhibited both a delay in the emergence of the oxygen sink and a substantial reduction in the rate of oxygen depletion. This is partially explained by increased replenishment of oxygen by the fluid flow, a key difference accounted for in the perfect mixing model described in section 7.2.9. The perfect mixing assumption imposes a fixed bulk concentration boundary condition at the bead surface,

and thus represents an upper-bound limiting case wherein no external mass transfer resistance exists. This assumption did slow the progression of the simulated oxygen sink, increasing the timescale required to reach oxygen conditions by about 170 min for the naïve model (i.e. when fitting factor is left at 1). However, as evident in Figure 7.10, even this limiting case was insufficient to capture the slow development of the oxygen sink exhibited by the flow columns. Thus the effect was too strong to be accounted for by transport physics alone, and we speculate that the stagnation observed in the development of the oxygen sink was likely a biological effect; for instance fluid flow may result in the removal of metabolic products which aid in growth, product stimulation, as documented by Sakata *et al* [50]. There was also noticeable variability between the two flow runs, which could be due to the additional variability introduced under flow conditions in a randomly packed column. In No Flow columns, the locations of adjacent beads are unimportant to growth as diffusion in the alginate gel is approximately equal to diffusion in the void spaces, whereas when subjected to flow, random packing geometry can lead to large stochastic differences in the advective transport experienced by the active bead.

7.3.5 Correlational Estimates and Experimental Determination of Sherwood Number

The range of predicted Sherwood numbers spanned approximately a factor of two, from 6.3 to 11.5, as presented in Table 7.1. Two methods were used to calculate *Re*: first, by assuming a single sphere and using the mean V_z velocity calculated near the active bead using ^{1}H axial velocity maps (Eq 7.5) and second, by assuming a random packed bed and using the superficial velocity of the column, corrected for void fraction as

measured by ^{1}H axial velocity maps (Eq 7.4). Three correlations were used to estimate *Sh*, with the first and second applicable to forced convection across single spheres. The first correlation (rows 1 and 2 of Table 7.1) is most accurate for creeping flow *(Re* $\ll 1$), an assumption not truly satisfied by our experiments. The second (rows 3 and 4 of Table 7.1) is applicable to a wider range of *Re* values ($Re < 200$) but is most accurate for values of *Sc* below 250. While the assumptions of neither were fully met, the estimates nonetheless predict similar values. The third correlation (rows 5 and 6) was an empirical fitting of *Sh* values for forced convection in randomly packed beds and is valid across a wide range of *Re* values ($0.4 < Re < 2000$). This formulation produced Sherwood estimates similar to the previous single sphere treatments, indicating general agreement in the predicted behavior and a narrow range of *Sh* values expected for the Flow experiments.

Method for Re	Form of Re	Re	Method for Sh	Form of Sh	Sh
General definition, $\bar{V}$ measured from ^{1}H axial V map	$\frac{\rho \bar{V} D}{\mu}$	1.1	Flow past single solid sphere	$2 + 0.991 Re^{1/3} Sc^{1/3}$	10.1
Packed bed, $\bar{V}$ represents superficial velocity	$\frac{\rho \bar{V} D_p}{(1-\varepsilon)\mu}$	0.8	Flow past single solid sphere	$2 + 0.991 Re^{1/3} Sc^{1/3}$	9.3
General definition, $\bar{V}$ measured from ^{1}H axial V map	$\frac{\rho \bar{V} D}{\mu}$	1.1	Mass analogue of Ranz-Marshall Correlation for sphere	$2 + 0.6 Re^{1/2} Sc^{1/3}$	7.0
Packed bed, $\bar{V}$ represents superficial velocity	$\frac{\rho \bar{V} D_p}{(1-\varepsilon)\mu}$	0.8	Mass analogue of Ranz-Marshall Correlation for sphere	$2 + 0.6 Re^{1/2} Sc^{1/3}$	6.3
General definition, $\bar{V}$ measured from ^{1}H axial V map	$\frac{\rho \bar{V} D}{\mu}$	1.1	Forced convection in packed bed	$[(4.58 Re^{\frac{1}{3}} Sc^{\frac{1}{3}})^6 + (2.39 Re^{0.56} Sc^{\frac{1}{3}})^6]^{\frac{1}{6}}$	10.1
Packed bed, $\bar{V}$ represents superficial velocity	$\frac{\rho \bar{V} D_p}{(1-\varepsilon)\mu}$	0.8	Forced convection in packed bed	$[(4.58 Re^{\frac{1}{3}} Sc^{\frac{1}{3}})^6 + (2.39 Re^{0.56} Sc^{\frac{1}{3}})^6]^{\frac{1}{6}}$	11.5

Table 7.1. Description of six formulations used to calculate expected Sherwood number for experimental flow columns. Two different experimental *Re* values were calculated and three different *Sh* correlations were used. Details regarding the sources of these correlations can be found in section 7.2.8.

To determine experimental Sherwood number for both trailing and leading edges of the Flow experiments, oxygen concentration was plotted as a function of radial coordinate *r* as described in section 7.2.7. The same procedure was carried out for the three No Flow columns, as we expect that in the absence of flow, the calculated boundary

layer thickness δ should be the same for trailing and leading edges, and that δ for these experiments should, in general, be larger than observed for Flow columns due to the lack of advective transport enhancement. The terms 'trailing' and 'leading' have no physical meaning for No Flow experiments due to the lack of flow orientation, but are used to facilitate comparison with flow columns by indicating the same region of the sphere.

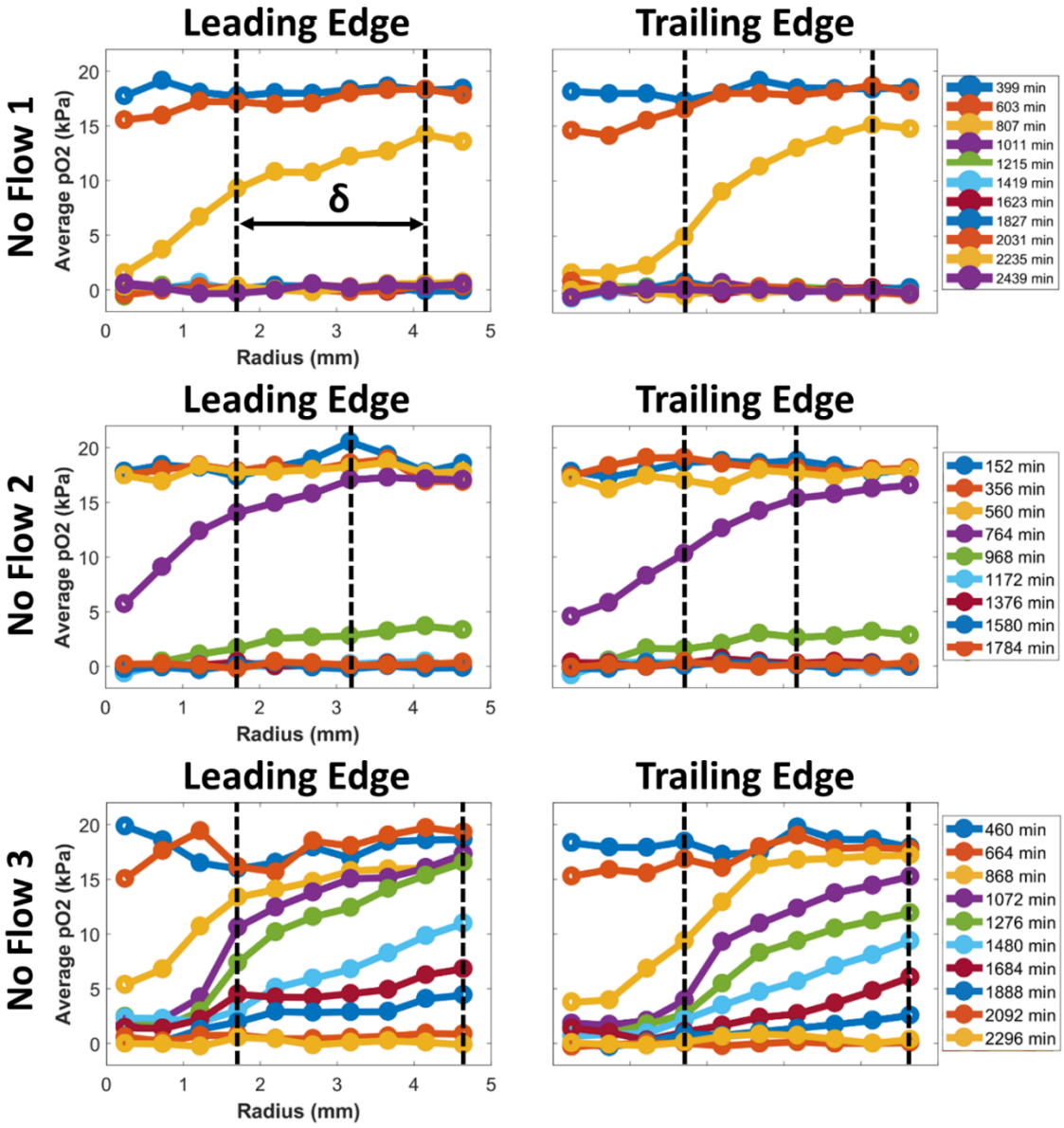

Figure 7.11. Mean oxygen concentration as a function of radius r for three No-Flow columns for both leading and trailing edges. Mean oxygen for each radial coordinate was calculated by averaging values over shells of thickness 489 μm about the center of the inoculated bead. Values were calculated separately for trailing and leading edges by specifying the θ domain over which averaging took place ($-\pi/4$ to $\pi/4$ for leading and $3\pi/4$ to $5\pi/4$ for trailing). Because these experiments have no flow, trailing and leading do not refer to location with respect to flow but rather indicate the same region as in Flow experiments. Black dotted lines indicate the location of the bead surface at $r = 1.71$ mm and the location of the bulk oxygen concentration (the point exterior to the bead surface at which oxygenation profile becomes flat). The distance between these two points is δ, the boundary layer thickness, and is labelled in the first plot for clarity.

pO_2 as a function of radial coordinate and resulting Sherwood number analysis for the No Flow columns are shown in Figure 7.11. Within a single experiment, successive pO_2 profiles were in general agreement as to the location of r_b, the radial coordinate external to the bead surface at which oxygenation takes on a constant bulk value, although some natural variability was evident. During the transient period of progressive oxygen depletion, all columns exhibited substantial external mass transfer resistance, with δ ranging from 1.5 to 2.9 mm, corresponding to experimental Sherwood numbers ranging from 1.2 to 2.3. Correlations for Sherwood number generally express *Sh* as the sum of a constant value (Sh_o; representing the no flow case) and a term describing the transport contribution of flow ($Re^m Sc^n$), with Sh_o typically ascribed a value of two [32]. The experimental measurements are in good agreement with correlation estimates for expected *Sh* in the absence of flow. Additionally, calculated Sherwood numbers showed no asymmetry as expected. The No Flow analysis thus provides validation that experimental *Sh* determination reliably produces expected results.

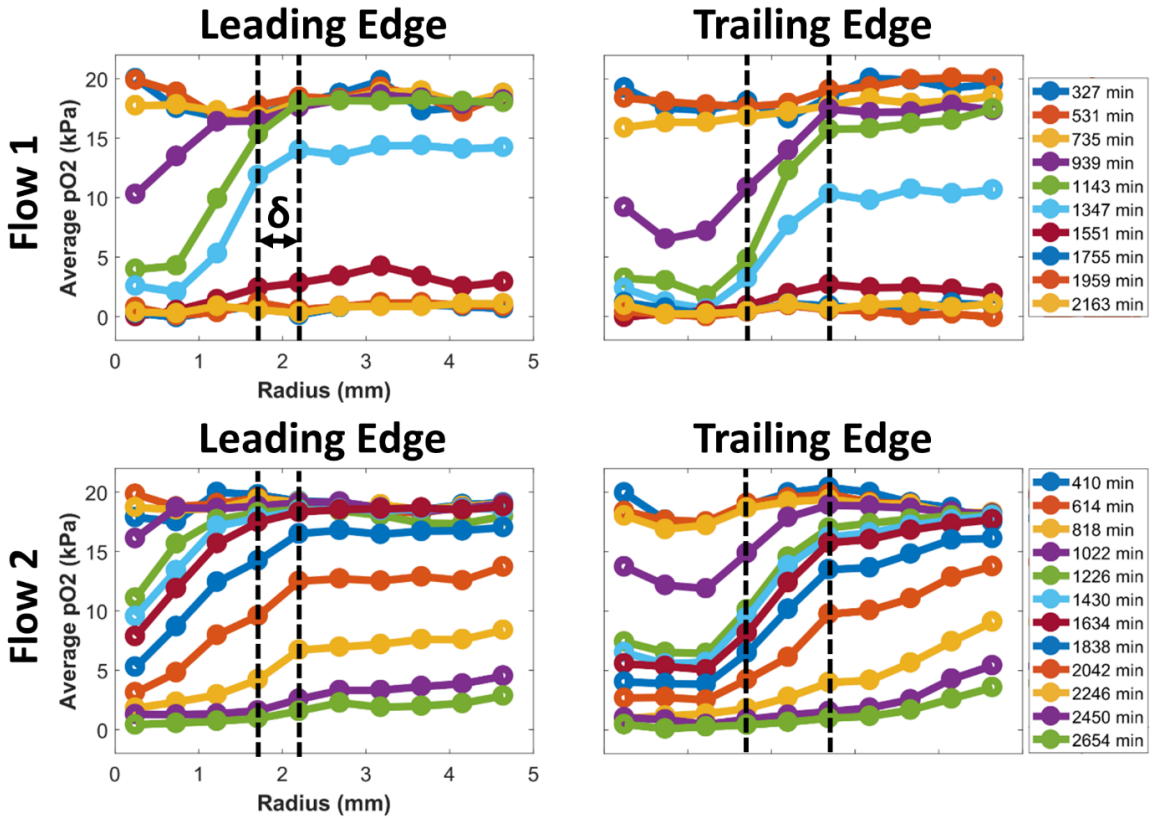

Figure 7.12. Mean oxygen concentration as a function of radius r for two Flow columns for both leading and trailing edges with respect to flow direction. Mean oxygen for each radial coordinate was calculated by averaging values over shells of thickness 489 μm about the center of the inoculated bead. Values were calculated separately for trailing and leading edges by specifying the θ domain over which averaging took place ($-\pi/4$ to $\pi/4$ for leading and $3\pi/4$ to $5\pi/4$ for trailing; the $\theta = 0$ axis is defined as aligning with the leading edge). Black dotted lines indicate the location of the bead surface at $r = 1.71$ mm and the location of the bulk oxygen concentration, the point exterior to the bead surface at which oxygenation profile becomes flat. The distance between these two points is δ, the boundary layer thickness, and is labelled in the first plot for clarity.

pO_2 as a function of radial coordinate and resulting Sherwood number analysis for the Flow columns is shown in Figure 7.12. Compared to No Flow experiments, Flow experiments exhibited smaller overall oxygen gradients external to the active bead, indicating expected lower levels of external mass transport limitation consistent with smaller δ values. Further, a different value of δ was consistently obtained from the

trailing and leading edges, indicating that boundary layer thickness is asymmetric, varying along flow direction. Replicates gave identical results, with a leading edge δ of 489 μm (corresponding to Sh = 7) and trailing edge δ of 978 μm (corresponding to Sh = 3.5). These values were consistent with correlation-based estimates, with a range of Sh = 6.3 to 11.5. The methodology for quantifying boundary layer thickness in this study involves error in the identification of the bulk concentration radial coordinate r_b and discretization of radial shell thickness over which to average. The absolute numbers measured are expected to vary, but relative differences in leading and trailing edges are robust. The influence of binning and bulk concentration coordinate selection on calculated boundary layer thickness and Sherwood number is discussed in section 7.2.7.

An interesting observation is that at the trailing edge, a slight concave-up pO_2 profile was present within the inoculated bead. This indicates that pO_2 at the exact center of the inoculated bead was actually slightly higher than in the region immediately downstream. The same observation is evident in Figure 7.6, which shows that the developing oxygen sink was greatest in magnitude slightly downstream of the bead center. This downstream oxygen depletion can be explained by streamlines being stripped of oxygen as they flow over the active bead, resulting in a lower oxygen replenishment rate in the downstream stagnation region of the bead and therefore a more rapid approach to anoxic conditions.

Localized Sherwood number is difficult to measure experimentally. Due to the difficulty inherent to quantification of small concentration gradients in multiple dimensions, the mass transfer thin film thickness must often be estimated. Mass transfer

correlations implicitly assume constant boundary layer thickness. Our demonstrate that boundary layer thickness for advection across a sphere varies along the direction of flow, an intuitively unsurprising observation but one with important implications for the use of mass transfer correlation estimates. This discrepancy can likely be explained by localized velocity fluctuations that arise both from the geometry of the active bead and from the distribution of streamlines due to random packing of the column. The consistent result of a higher *Sh* at the upstream edge in both Flow experiments, despite their random, unique packing, suggests a predictable dependence of *Sh* on flow direction, even in the presence of complex fluid paths.

As our experimental system focused on a simple, model biofilm geometry (sphere), we might expect that divergence between correlation determinations of *Sh* and true values would increase as geometry becomes more complex or as relative spatial fluctuations to velocity grow larger, for instance at higher Reynolds numbers. In such cases, *Sh* values along trailing and leading edges, or more generally in distinct localized regions, may differ by significantly more than observed here, altering the nature of mass transfer at the local scale. In the case of biofilms, fluid flow typically takes tortuous paths through void spaces in microcolonies exhibiting complex structures such as mushrooms and streamers. Variable boundary layer thicknesses around these cell and EPS networks may induce striking variability in nutrient transport at the microscale, affecting cell metabolism and behavior, shaping the development of the biofilm structure. Conventional *Sh* correlations do not capture this local effect, introducing error. The same inaccuracy has implications for mass transport-sensitive process operations in complex media, such

as chemical conversion (*e.g.* aerobic sludge wastewater treatment, heterogeneous catalysis) or separation processes (*e.g.* chromatography). Although this limitation is difficult to circumvent and the use of dimensionless numbers for macroscale systems is inherently inexact, awareness of potential sources of error and identification of imperfect assumptions may prove useful as our understanding of transport phenomena is refined. Finally, the ability to noninvasively measure boundary layer thickness for oxygen transport independently for trailing and leading edges is a useful tool for future studies, for instance to investigate how boundary layer thickness variability is affected by perturbations to model geometries, or as a means to experimentally measure *Sh* in systems where correlation estimates are poor predictors of system behavior.

7.4 Conclusion

^{19}F NMR oximetry was used in combination with conventional ^{1}H NMR velocity mapping to investigate the oxygen utilization dynamics of *E. coli* in a packed bed column. Encapsulation of the perfluorocarbon PFOB in alginate gel beads permits noninvasive oxygen mapping by maintaining a static distribution of the oxygen sensor, facilitating long-term monitoring over the course of bacterial growth. The microbial growth rate measured *in situ* during biofilm development phase is quantitatively indistinguishable from the growth rate of the organism measured in planktonic conditions in the same medium. Only a few intrinsic bacterial growth parameters (X_o, μ, and lag phase duration) are needed to comprehensively describe the behavior of the oxygen sink.

The mechanistic simplicity of macroscale oxygen consumption in this system may even facilitate the ability to extract an unknown specific growth rate from such datasets due to the shape of the oxygen depletion curve being entirely determined by μ but not X_o, although this has yet to be investigated directly. When growth parameters are known *a priori*, the numerical model can discern correct growth rate with high sensitivity, with true μ easily distinguished from values 30% higher or lower.

Fluid flow patterns were consistent with flow around, but not through hydrogel beads. Local fluid velocities in the region adjacent to the active bead ranged from 0 to 0.5 mm/s and varied markedly. Direct calculation of Reynolds number using the mean value from this dataset yielded a value consistent with an estimate of effective Reynolds number using the superficial velocity. These values in turn were employed in calculation of a range of approximate Sherwood numbers based on different assumptions, where it was discovered that the different correlations and methods for *Re* calculation nonetheless converged on similar values.

External mass transfer resistance was visualized as a concentration boundary layer around individual gel beads. The boundary layer was found to be asymmetric, being smaller on the leading edge and larger on the trailing edge in Flow experiments. This asymmetry was absent for no Flow Experiments. Experimental Sherwood numbers were calculated from boundary layer thickness measurements and were in approximate agreement with values predicted by established correlations, with *Sh* ranging from 3.5 to 7. Our results demonstrate that boundary layer thickness varies locally, as has been reported previously for biofilms [19; 20], with velocity fluctuations a likely cause.

Furthermore, our findings suggest that local *Sh* may exhibit a consistent dependence on relative orientation with respect to system-scale flow direction, even when microscale flow dynamics are complex. Strong variance in external mass transfer resistance at small scales may exert a strong influence in the development of complex structures of voids and mushroom-like cell clusters observed in biofilms by dictating nutrient availability and thus localized growth rate, and may also play a role in other mass transport-sensitive processes such as heterogeneous catalysis and separation processes in complex media such as chromatography. The present technique allows both for macroscale monitoring of oxygen reaction rate over long periods and the direct, noninvasive measurement of localized external mass transfer resistance, and may prove useful for evaluating the role of transport limitation in applications such as the above. Future work could investigate the dependence of localized *Sh* number variation on system geometry, as we might expect that more complex geometry would induce greater velocity fluctuations.

References

[1] Borriello, G., Werner, E., Roe, F., Kim, A.M., Ehrlich, G.D., and Stewart, P.S. (2004). Oxygen Limitation Contributes to Antibiotic Tolerance of Pseudomonas aeruginosa in Biofilms. Antimicrob Agents Chemother *48*, 2659-2664.

[2] Kolpen, M., Lerche, C.J., Kragh, K.N., Sams, T., Koren, K., Jensen, A.S., Line, L., Bjarnsholt, T., Ciofu, O., and Moser, C. (2017). Hyperbaric oxygen sensitizes anoxic Pseudomonas aeruginosa biofilm to ciprofloxacin. Antimicrob Agents Chemother, AAC. 01024-01017.

[3] Pabst, B., Pitts, B., Lauchnor, E., and Stewart, P.S. (2016). Gel-entrapped Staphylococcus aureus bacteria as models of biofilm infection exhibit growth in dense aggregates, oxygen limitation, antibiotic tolerance, and heterogeneous gene expression. Antimicrob Agents Chemother *60*, 6294-6301.

[4] Tresse, O., Jouenne, T., and Junter, G.A. (1995). The role of oxygen limitation in the resistence of agar-entrapped, sessile-like escherichia coli to aminoglycoside and beta lactam antibiotics. J Antimicrob Chemother *36*, 521-526.

[5] Jesaitis, A.J., Franklin, M.J., Berglund, D., Sasaki, M., Lord, C.I., Bleazard, J.B., Duffy, J.E., Beyenal, H., and Lewandowski, Z. (2003). Compromised host defense on Pseudomonas aeruginosa biofilms: Characterization of neutrophil and biofilm interactions. J Immunol *171*, 4329-4339.

[6] Ahn, S.-J., Wen, Z.T., and Burne, R.A. (2007). Effects of oxygen on virulence traits of Streptococcus mutans. J Bacteriol *189*, 8519-8527.

[7] Marteyn, B., Scorza, F.B., Sansonetti, P.J., and Tang, C. (2011). Breathing life into pathogens: the influence of oxygen on bacterial virulence and host responses in the gastrointestinal tract. Cell Microbiol *13*, 171-176.

[8] Casey, E., Glennon, B., and Hamer, G. (1999). Review of membrane aerated biofilm reactors. Resources, conservation and recycling *27*, 203-215.

[9] Chan, Y.J., Chong, M.F., Law, C.L., and Hassell, D. (2009). A review on anaerobic–aerobic treatment of industrial and municipal wastewater. Chemical Engineering Journal *155*, 1-18.

[10] Thapa, B., Kc, A.K., and Ghimire, A. (2012). A review on bioremediation of petroleum hydrocarbon contaminants in soil. Kathmandu university journal of science, engineering and technology *8*, 164-170.

[11] Pardieck, D.L., Bouwer, E.J., and Stone, A.T. (1992). Hydrogen peroxide use to increase oxidant capacity for in situ bioremediation of contaminated soils and aquifers: A review. Journal of Contaminant Hydrology *9*, 221-242.

[12] Drews, A., Lee, C.-H., and Kraume, M. (2006). Membrane fouling-a review on the role of EPS. Desalination *200*, 186-188.

[13] Lee, W., Lewandowski, Z., Nielsen, P.H., and Hamilton, W.A. (1995). Role of sulfate-reducing bacteria in corrosion of mild steel: a review. Biofouling *8*, 165-194.

[14] Rasmussen, K., and Lewandowski, Z. (1998). Microelectrode measurements of local mass transport rates in heterogeneous biofilms. Biotechnol Bioeng *59*, 302-309.

[15] Lewandowski, Z., Altobelli, S.A., and Fukushima, E. (1993). NMR and Microelectrode Studies of Hydrodynamics and Kinetics in Biofilms. Biotechnol Prog *9*, 40-45.

[16] De Beer, D., Stoodley, P., Roe, F., and Lewandowski, Z. (1994). Effects of biofilm structures on oxygen distribution and mass transport. Biotechnol Bioeng *43*, 1131-1138.

[17] Xu, K.D., Stewart, P.S., Xia, F., Huang, C.-T., and McFeters, G.A. (1998). Spatial Physiological Heterogeneity inPseudomonas aeruginosa Biofilm Is Determined by Oxygen Availability. Appl Environ Microbiol *64*, 4035-4039.

[18] Prigent-Combaret, C., Vidal, O., Dorel, C., and Lejeune, P. (1999). Abiotic surface sensing and biofilm-dependent regulation of gene expression in Escherichia coli. J Bacteriol *181*, 5993-6002.

[19] Yang, S., and Lewandowski, Z. (1995). Measurement of local mass transfer coefficient in biofilms. Biotechnol Bioeng *48*, 737-744.

[20] Stoodley, P., Yang, S., Lappin-Scott, H., and Lewandowski, Z. (1997). Relationship between mass transfer coefficient and liquid flow velocity in heterogenous biofilms using microelectrodes and confocal microscopy. Biotechnol Bioeng *56*, 681-688.

[21] Silver, I.A. (1973). Problems in the investigation of tissue oxygen microenvironment. In Chemical Engineering in Medicine (American Chemical Society), pp. 343-352.

[22] Simkins, J.W., Stewart, P.S., and Seymour, J.D. (2018). Spatiotemporal mapping of oxygen in a microbially-impacted packed bed using 19 F Nuclear magnetic resonance oximetry. J Magn Reson *293*, 123-133.

[23] Nöth, U., Rodrigues, L.M., Robinson, S.P., Jork, A., Zimmermann, U., Newell, B., and Griffiths, J.R. (2004). In vivo determination of tumor oxygenation during growth and in response to carbogen breathing using 15C5-loaded alginate capsules as fluorine-19 magnetic resonance imaging oxygen sensors. International Journal of Radiation Oncology• Biology• Physics *60*, 909-919.

[24] Blumich, B. (2000). NMR imaging of materials, Vol 57 (OUP Oxford).

[25] Callaghan, P.T. (1993). Principles of nuclear magnetic resonance microscopy (Oxford University Press on Demand).

[26] Wakimoto, N., Nishi, J., Sheikh, J., Nataro, J.P., Sarantuya, J., Iwashita, M., Manago, K., Tokuda, K., Yoshinaga, M., and Kawano, Y. (2004). Quantitative biofilm assay using a microtiter plate to screen for enteroaggregative Escherichia coli. The American journal of tropical medicine and hygiene *71*, 687-690.

[27] Strathmann, M., Griebe, T., and Flemming, H.-C. (2000). Artificial biofilm model–a useful tool for biofilm research. Appl Microbiol Biotechnol *54*, 231-237.

[28] Whitham, T., and Gilbert, P. (1993). Evaluation of a model biofilm for the ranking of biocide performance against sulphate-reducing bacteria. J Appl Bacteriol *75*, 529-535.

[29] Coquet, L., Junter, G., and Jouenne, T. (1998). Resistance of artificial biofilms of Pseudomonas aeruginosa to imipenem and tobramycin. The Journal of antimicrobial chemotherapy *42*, 755-760.

[30] Clutterbuck, A.L., Cochrane, C.A., Dolman, J., and Percival, S.L. (2007). Evaluating antibiotics for use in medicine using a poloxamer biofilm model. Ann Clin Microbiol Antimicrob *6*, 2.

[31] WerthÉn, M., Henriksson, L., Jensen, P.Ø., Sternberg, C., Givskov, M., and Bjarnsholt, T. (2010). An in vitro model of bacterial infections in wounds and other soft tissues. APMIS *118*, 156-164.

[32] Bird, R.B., Stewart, W.E., and Lightfoot, E.N. (1960). Transport phenomena. 1960. Madison, USA.

[33] Sherwood, T.K. (1959). Mass transfer between phases (Pennsylvania State University).

[34] De Klerk, A. (2003). Voidage variation in packed beds at small column to particle diameter ratio. AIChE J *49*, 2022-2029.

[35] Bergman, T.L., Incropera, F.P., DeWitt, D.P., and Lavine, A.S. (2011). Fundamentals of heat and mass transfer (John Wiley & Sons).

[36] Wilkes, J.O. (2006). Fluid Mechanics for Chemical Engineers with Microfluidics and CFD (Pearson Education).

[37] Batchelor, C.K., and Batchelor, G. (1967). An introduction to fluid dynamics (Cambridge university press).

[38] Ranz, W., and Marshall, W.R. (1952). Evaporation from drops. Chem Eng Prog *48*, 141-146.

[39] Karabelas, A.J., Wegner, T.H., and Hanratty, T.J. (1971). Use of asymptotic relations to correlate mass transfer data in packed beds. Chem Eng Sci *26*, 1581-1589.

[40] Kurosawa, H., Matsumura, M., and Tanaka, H. (1989). Oxygen diffusivity in gel beads containing viable cells. Biotechnol Bioeng *34*, 926-932.

[41] Han, P., and Bartels, D.M. (1996). Temperature dependence of oxygen diffusion in H2O and D2O. J Phys Chem *100*, 5597-5602.

[42] Lewandowski, Z., Walser, G., and Characklis, W.G. (1991). Reaction kinetics in biofilms. Biotechnol Bioeng *38*, 877-882.

[43] Stolper, D.A., Revsbech, N.P., and Canfield, D.E. (2010). Aerobic growth at nanomolar oxygen concentrations. Proceedings of the National Academy of Sciences *107*, 18755-18760.

[44] Benson, D.M., Knopp, J.A., and Longmuir, I.S. (1980). Intracellular oxygen measurements of mouse liver cells using quantitative fluorescence video microscopy. Biochimica et Biophysica Acta (BBA)-Bioenergetics *591*, 187-197.

[45] Carlson, R., and Srienc, F. (2004). Fundamental Escherichia coli biochemical pathways for biomass and energy production: creation of overall flux states. Biotechnol Bioeng *86*, 149-162.

[46] Basan, M., Zhu, M., Dai, X., Warren, M., Sévin, D., Wang, Y.P., and Hwa, T. (2015). Inflating bacterial cells by increased protein synthesis. Mol Syst Biol *11*, 836.

[47] Stewart, P.S. (2012). Mini-review: convection around biofilms. Biofouling *28*, 187-198.

[48] Vogt, S.J., Sanderlin, A.B., Seymour, J.D., and Codd, S.L. (2013). Permeability of a growing biofilm in a porous media fluid flow analyzed by magnetic resonance displacement-relaxation correlations. Biotechnol Bioeng *110*, 1366-1375.

[49] Monod, J. (1949). The growth of bacterial cultures. Annual Reviews in Microbiology *3*, 371-394.

[50] Sakata, N., Usui, Y., and Kogure, T. (1999). Extracellular product(s) of Staphylococcus aureus stimulate their own growth. Zentralbl Bakteriol Parasitenkd Infektionskr Hyg *289*, 339-345.

CHAPTER EIGHT: CONCLUSION

The work that encompasses this thesis introduces a new technique for the quantification of oxygen distribution in biofilm systems. We have developed methodology for the incorporation and fixation of PFC into biofilm systems of interest, consisting of emulsifying the oxygen-sensor in water using an appropriate surfactant and immobilizing the dispersed PFC droplets by mixing the emulsion with sodium alginate and gelling it via dropwise introduction into a calcium chloride solution. The result is spherical alginate gel capsules containing a stable emulsion of oxygen-sensing PFC which allows for the long-term monitoring of oxygen distribution in relevant systems. The PFC used in our studies, PFOB, exhibits very low toxicity and does not adversely affect microbial growth processes. We have additionally demonstrated that the inclusion of PFC into hydrogels such as alginate or the EPS naturally formed by biofilms does not significantly impact oxygen transport phenomena, and measurements therefore reliably reflect intrinsic system behavior. The compounds required for alginate bead generation are extremely inexpensive and easily obtained with the exception of PFC itself, and thus this method is an accessible option for biofilm oximetry due to the small sample volumes.

In addition to method development and verification, ^{19}F NMR oximetry was used for a variety of applications with high-relevance to biofilm science. In our 2018 *Journal of Magnetic Resonance* article, we demonstrated the reversibility of the oxygen measurements, showing that removal of a carbon source results in restoration of oxygen saturation into the column and that the dependence of PFC R_1 exhibits no temporal hysteresis. Additionally, we characterized distinct oxygen consumption behavior for

different bacterial species, correlated fluid flow distribution with localized oxygen reaction rates, and generated spatial maps of apparent oxygen consumption rate constant.

In our *Magnetic Resonance in Medicine* article, currently under review, we utilized the method to produce multiple time series detailing the oxygen consumption behavior of biofilms under antibiotic challenge. We verified that early antimicrobial exposure is sufficient to prevent growth entirely, but that established biofilms exhibit dramatically increased resilience, a long-standing observation in the literature. More importantly, due to the two-dimensional nature of the measurement, the oxygenation maps yielded a unique insight: that antibiotic administration to a mature biofilm induces a temporary pseudo-steady state wherein the oxygen sink does not expand but respiration rates endure. Following clearance, the oxygen sink quickly resumes its expansion. This technique therefore represents a novel means for visualization of infection persistence, with the measurements providing spatial information that is both highly-relevant to biofilm research and unique to this method. ^{19}F NMR oximetry thus offers an emerging opportunity to enrich scientific understanding of antimicrobial tolerance and other oxygen-dependent biofilm processes.

In the *Biotechnology and Bioengineering* manuscript, about to be submitted, ^{19}F NMR oximetry was used for engineering applications, most notably the mathematical modeling of microbial growth on the macroscale, and the quantification of localized mass transfer rates. We demonstrated that *a priori* knowledge of just a few microbial growth parameters, namely specific growth rate, inoculum cell density, and lag phase duration, is sufficient to comprehensively describe the macroscopic behavior of the oxygen sink. The

numerical model could easily discern correct growth rate from the oxygen decay curve, suggesting it may be possible to extract an unknown specific growth rate from such a dataset. External mass transfer resistance for flow systems was analyzed by evaluating the thickness of the concentration boundary layer around the bacteria-laden bead. Experimental Sherwood numbers calculated using the oxygen maps were in good agreement with correlational estimates, indicating that the technique may be useful for mass transfer analyses, which are notoriously difficult. The boundary layer was found to be asymmetric under flow, being smaller on the leading edge and larger on the trailing edge, suggesting that local *Sh* exhibits a consistent dependence on the relative orientation of system geometry with respect to flow direction, even when microscale flow dynamics are complex. The strong spatial variation of local external mass transfer resistance documented here may have important implications for biofilm structure, which is characterized by complex geometry consisting of mushroom-like cell clusters amidst interstitial voids. As nutrient transport limitation is perhaps the greatest contributing factor to the establishment of heterogeneity in biofilms, variability in *Sh* across the biofilm may exert a strong influence in the development of these structures. In addition to the demonstration that ^{19}F NMR can provide measurements of localized oxygen boundary layer thickness, which have been historically difficult to obtain, this study also suggests that the technique could be used more generally for evaluation of how geometry for an arbitrary system of interest influences the magnitude of spatial *Sh* variability, which would have broad relevance for a variety of engineering applications such as heterogeneous catalysis and affinity chromatography.

The oximetry technique pioneered in this work has several distinct advantages and disadvantages when compared to the traditional microelectrode approach. Fundamentally, the NMR phenomenon exhibits low signal-to-noise, with MRI functionally constrained to a maximum resolution of about 10 x 10 μm^2/pixel due to the miniscule population excess in spin states and molecular motion constraints. For applications that require resolution of oxygen profile at the lengthscale of an individual cell cluster (tens to hundreds of microns), ^{19}F NMR oximetry is currently impractical and traditional methods must be employed. The same signal-to-noise limitation introduces modest variability into the R_1 fitting process, resulting in lower precision than the Clark electrode. To compensate for the intrinsic low sensitivity, signal averaging must be employed, causing a reduction in temporal resolution which may limit the range of transient phenomena that can be effectively probed with this method. Finally, the technique requires access to a high-field NMR spectrometer, an expensive piece of equipment, and thus measurements that require on-site field analysis are ill-suited to this approach. The microelectrode, in contrast, is inexpensive, portable, and accurate, and is the superior option for data collection in the field at this time.

^{19}F NMR oximetry, however, enjoys a few important advantages over microelectrodes. First, it is entirely noninvasive, making it an appealing option for flow systems where physical introduction of a needle has the potential to alter intrinsic transport behavior either via introduction of substrate down the puncture path or by alteration of fluid flow. These problems are nontrivial and have long been concerns for analyses of, for instance, concentration boundary layers. The NMR method therefore

provides a unique ability to obtain such measurements with full assurance that the system's integrity remains intact. Second, ^{19}F NMR oximetry allows for the spatial mapping of oxygen across two-dimensions simultaneous, providing a snapshot of oxygen distribution across an entire plane. As microelectrodes are limited to single-point acquisition, applying them to measure oxygen spatial distribution across multiple dimensions is extremely time consuming and introduces potential error due to the fact that each observation is being collected at a different time. For dynamic systems such as the ones featured in this work, it is the transient changes to oxygen gradient which are of fundamental interest, and microelectrodes are unable to characterize such behavior. For the many experimental systems that violate the steady state assumption, ^{19}F NMR oximetry may provide a unique means of investigating spatiotemporal evolution of oxygen. The two-dimensional resolution also permits the examination of complicated geometries without having to rely on assumptions of homogeneity, which are often wildly inaccurate. In biofilms, which exhibit complex structure, this capability is nontrivial, and it is likely that other systems with similar spatial heterogeneity could benefit as well. Finally, NMR is able to probe closed-walled systems that would be intractable using a microelectrode, such as the packed bed columns employed in the current work. Applications such as heterogeneous catalysis and affinity chromatography which are inherently enclosed systems are poor candidates for microelectrode examination but are readily accessible by the NMR approach.

The unique advantages of ^{19}F NMR oximetry thus strongly suggest that this method may provide invaluable insights into a wide range of systems exhibiting oxygen-

sensitive behavior and it is our hope that the technique will be applied to these contexts. The primary challenge, of course, is the introduction of the oxygen-sensing PFC into the sample of interest. One significant technological advancement that could greatly simplify this endeavor would be the emulsification of PFC at smaller spatial scales, ideally to the point where single microdroplets can be emulsified individually. When introduced into liquid systems, the high solubility of this microemulsion would allow it to fully permeate the sample, facilitating oxygen measurement across the whole system. In solid-like systems such as gels or, for instance, wastewater flocs, the microdroplets could be immobilized in alginate gel following the same procedure as the macroscale beads, and these microbeads could be easily incorporated into a sample without significantly altering system geometry.

For this reason, development of a microfluidic approach for oxygen-sensing bead generation is an ongoing research focus at the Center for Biofilm Engineering, in a collaboration between the microfluidic lab, run by Dr. Connie Chang, and the magnetic resonance lab, run by Dr. Joseph Seymour and Dr. Sarah Codd. Currently in the early stages of process development, the goal of this project is to design microfluidic devices which can downscale the production of PFC bead generation to the size of an individual PFC microdroplet. This advancement would allow for the mass production of microscopic or near-microscopic dispersions of PFC which could be easily incorporated into liquid or solid samples, providing a wide spatial distribution of PFC without disturbing system geometry. In addition to dramatically improving the ease of production, this process would also ensure that the emulsion is monodisperse, with

properties such as size, shape, and phase ratio uniform. Current work has focused on the selection of an appropriate microfluidic device material to ensure solubility, selection of optimal PFC (with PFOB and hydrofluoroether being investigated primarily), and optimization of surfactant and device geometry to encourage stability and structural integrity during downstream processing. Successful development of this production technique will significantly reduce the barrier to entry for ^{19}F NMR oximetry, and it is our hope that it will facilitate the expansion of the technique to other systems that would benefit from comprehensive oxygen monitoring.

A specific potential application for the ^{19}F NMR oximetry method pioneered by the current work and one that we expect to be relatively straightforward, especially pending the success of microfluidic production, is the evaluation of oxygen delivery into chronic wounds. Oxygen penetration into infected tissues is a significant predictor of clinical outcome, and thus a simple clinical method for assessing oxygen distribution in patients in clinical settings could aid substantially in treatment strategy. However, due to their invasiveness and single-point acquisition, the microelectrode is a poor candidate for this measurement. We propose that ^{19}F NMR oximetry is uniquely suited for this application; an emulsion of PFOB or other appropriate PFC is likely to easily permeate human wound tissue, following which NMR oximetry could provide a comprehensive depth profile of oxygen penetration into the wound. NMR analysis could be either accomplished through a conventional miniature borehole spectrometer, or, more likely, using a surface analysis NMR tool such as the NMR-MOUSE, a permanent electromagnet that generates a B_o magnetic field in the sample it is placed against. We

contend that this approach could have strong potential for aiding in the determination of wound healing prognosis, and recommend that this possibility be investigated in an *in vivo* animal infection model.

This thesis pioneers the application of ^{19}F NMR oximetry to bacterial biofilms, where oxygen gradients are a critical determinant of microbial presentation and behavior but have been historically difficult to measure. We have developed methodology for incorporation and fixation of an oxygen-sensitive PFC to a complex model biofilm system, and utilized spatiotemporal oxygen monitoring to generate unique insights into bacterial physiology, localized oxygen consumption rates, the interplay between fluid flow and growth, infection persistence, and external mass transfer resistance.

REFERENCES CITED

[1] Characklis, W.G., and Marshall, K.C. (1990). Biofilms (Wiley).

[2] Donlan, R.M. (2002). Biofilms: microbial life on surfaces. Emerg Infect Dis *8*, 881.

[3] Stewart, P.S. (2003). Diffusion in biofilms. J Bacteriol *185*, 1485-1491.

[4] Stewart, P.S., and Franklin, M.J. (2008). Physiological heterogeneity in biofilms. Nature Reviews Microbiology *6*, 199-210.

[5] Xu, K.D., Stewart, P.S., Xia, F., Huang, C.-T., and McFeters, G.A. (1998). Spatial physiological heterogeneity inPseudomonas aeruginosa biofilm is determined by oxygen availability. Appl Environ Microbiol *64*, 4035-4039.

[6] Lee, W., Lewandowski, Z., Nielsen, P.H., and Hamilton, W.A. (1995). Role of sulfate-reducing bacteria in corrosion of mild steel: a review. Biofouling *8*, 165-194.

[7] Marteyn, B., Scorza, F.B., Sansonetti, P.J., and Tang, C. (2011). Breathing life into pathogens: the influence of oxygen on bacterial virulence and host responses in the gastrointestinal tract. Cell Microbiol *13*, 171-176.

[8] Borriello, G., Werner, E., Roe, F., Kim, A.M., Ehrlich, G.D., and Stewart, P.S. (2004). Oxygen Limitation Contributes to Antibiotic Tolerance of Pseudomonas aeruginosa in Biofilms. Antimicrob Agents Chemother *48*, 2659-2664.

[9] Prigent-Combaret, C., Vidal, O., Dorel, C., and Lejeune, P. (1999). Abiotic surface sensing and biofilm-dependent regulation of gene expression in Escherichia coli. J Bacteriol *181*, 5993-6002.

[10] Worlitzsch, D., Tarran, R., Ulrich, M., Schwab, U., Cekici, A., Meyer, K.C., Birrer, P., Bellon, G., Berger, J., and Weiss, T. (2002). Effects of reduced mucus oxygen concentration in airway Pseudomonas infections of cystic fibrosis patients. The Journal of clinical investigation *109*, 317-325.

[11] Cowley, E.S., Kopf, S.H., LaRiviere, A., Ziebis, W., and Newman, D.K. (2015). Pediatric cystic fibrosis sputum can be chemically dynamic, anoxic, and extremely reduced due to hydrogen sulfide formation. MBio *6*, e00767-00715.

[12] Kolpen, M., Hansen, C.R., Bjarnsholt, T., Moser, C., Christensen, L.D., van Gennip, M., Ciofu, O., Mandsberg, L., Kharazmi, A., and Döring, G. (2010).

Polymorphonuclear leukocytes consume oxygen in sputum from chronic Pseudomonas aeruginosa pneumonia in cystic fibrosis. Thorax *65*, 57-62.

[13] Kolpen, M., Lerche, C.J., Kragh, K.N., Sams, T., Koren, K., Jensen, A.S., Line, L., Bjarnsholt, T., Ciofu, O., and Moser, C. (2017). Hyperbaric oxygen sensitizes anoxic Pseudomonas aeruginosa biofilm to ciprofloxacin. Antimicrob Agents Chemother *61*, 1-9.

[14] Jesaitis, A.J., Franklin, M.J., Berglund, D., Sasaki, M., Lord, C.I., Bleazard, J.B., Duffy, J.E., Beyenal, H., and Lewandowski, Z. (2003). Compromised host defense on Pseudomonas aeruginosa biofilms: Characterization of neutrophil and biofilm interactions. J Immunol *171*, 4329-4339.

[15] Silver, I.A. (1973). Problems in the investigation of tissue oxygen microenvironment. In Chemical Engineering in Medicine (American Chemical Society), pp. 343-352.

[16] Davies, P.W., and Brink, F. (1942). Microelectrodes for measuring local oxygen tension in animal tissues. Rev Sci Instrum *13*, 524-533.

[17] Stewart, P.S. (2012). Mini-review: convection around biofilms. Biofouling *28*, 187-198.

[18] Delpuech, J.J., Hamza, M.A., Serratrice, G., and Stebe, M.J. (1979). Fluorocarbons as oxygen carriers. 1. An NMR study of oxygen solutions in hexafluorobenzene. J Chem Phys *70*, 2680-2687.

[19] Eidelberg, D., Johnson, G., Barnes, D., Tofts, P.S., Delpy, D., Plummer, D., and McDonald, W.I. (1988). ^{19}F NMR imaging of blood oxygenation in the brain. Magn Reson Med *6*, 344-352.

[20] Mason, R.P., Rodbumrung, W., and Antich, P.P. (1996). Hexafluorobenzene: A sensitive F-19 NMR indicator of tumor oxygenation. NMR Biomed *9*, 125-134.

[21] Liu, S., Shah, S.J., Wilmes, L.J., Feiner, J., Kodibagkar, V.D., Wendland, M.F., Mason, R.P., Hylton, N., Hopf, H.W., and Rollins, M.D. (2011). Quantitative tissue oxygen measurement in multiple organs using 19F MRI in a rat model. Magn Reson Med *66*, 1722-1730.

[22] Simkins, J.W., Stewart, P.S., and Seymour, J.D. (2018). Spatiotemporal mapping of oxygen in a microbially-impacted packed bed using 19 F Nuclear magnetic resonance oximetry. J Magn Reson *293*, 123-133.

[23] Purcell, E.M., Torrey, H.C., and Pound, R.V. (1946). Resonance absorption by nuclear magnetic moments in a solid. Physical review *69*, 37.

[24] Bloch, F. (1946). Nuclear induction. Physical review *70*, 460.

[25] Callaghan, P.T. (1993). Principles of nuclear magnetic resonance microscopy (Oxford University Press on Demand).

[26] Callaghan, P.T. (2011). Translational dynamics and magnetic resonance: principles of pulsed gradient spin echo NMR (Oxford University Press).

[27] Blumich, B. (2000). NMR imaging of materials, Vol 57 (OUP Oxford).

[28] Slichter, C.P. (2013). Principles of magnetic resonance, Vol 1 (Springer Science & Business Media).

[29] Fukushima, E. (2018). Experimental pulse NMR: a nuts and bolts approach (CRC Press).

[30] Halliwell, B., and Gutteridge, J. (1984). Oxygen toxicity, oxygen radicals, transition metals and disease. Biochem J *219*, 1.

[31] Navari, R.M., Rosenblum, W.I., Kontos, H.A., and Patterson, J.L. (1977). Mass transfer properties of gases in fluorocarbons. Res Exp Med (Berl) *170*, 169-180.

[32] Mason, R.P. (1994). Noninvasive physiology - 19F NMR of perfluorocarbons. Artificial Cells Blood Substitutes and Immobilization Biotechnology *22*, 1141-1153.

[33] Yntema, G. (1955). Superconducting winding for electromagnet. Paper presented at: Physical Review (American Physical Society One, College PK, MD 20740 USA).

[34] Torrey, H.C. (1956). Bloch equations with diffusion terms. Physical review *104*, 563.

[35] Brigham, E.O. (1988). The fast Fourier transform and its applications, Vol 448 (prentice Hall Englewood Cliffs, NJ).

[36] Carr, H.Y., and Purcell, E.M. (1954). Effects of diffusion on free precession in Nuclear Magnetic Resonance experiments. Physical Review *94*, 630-638.

[37] Hahn, E.L. (1950). Spin echoes. Physical Review *80*, 580-594.

[38] Meiboom, S., and Gill, D. (1958). Modified spin-echo method for measuring nuclear relaxation times. Rev Sci Instrum *29*, 688-691.

[39] Keeler, J. (2011). Understanding NMR spectroscopy (John Wiley & Sons).

[40] Lauterbur, P.C. (1973). Image formation by induced local interactions: examples employing nuclear magnetic resonance. Nature *242*, 190-191.

[41] Mansfield, P., and Grannell, P.K. (1973). NMR 'diffraction' in solids? Journal of Physics C: solid state physics *6*, L422-L426.

[42] Stehling, M.K., Turner, R., and Mansfield, P. (1991). Echo-planar imaging: magnetic resonance imaging in a fraction of a second. Science *254*, 43-50.

[43] Glover, G.H., Pauly, J.M., and Bradshaw, K.M. (1992). Boron-11 imaging with a three-dimensional reconstruction method. J Magn Reson Imaging *2*, 47-52.

[44] Brateman, L. (1986). Chemical shift imaging: a review. AJR Am J Roentgenol *146*, 971-980.

[45] Bellon, E.M., Haacke, E.M., Coleman, P.E., Sacco, D.C., Steiger, D.A., and Gangarosa, R.E. (1986). MR artifacts: a review. American Journal of Roentgenology *147*, 1271-1281.

[46] Kärger, J., and Heink, W. (1983). The propagator representation of molecular transport in microporous crystallites. Journal of Magnetic Resonance (1969) *51*, 1-7.

[47] Stejskal, E.O., and Tanner, J.E. (1965). Spin diffusion measurements: spin echoes in the presence of a time-dependent field gradient. The journal of chemical physics *42*, 288-292.

[48] Callaghan, P., Eccles, C., and Xia, Y. (1988). NMR microscopy of dynamic displacements: k-space and q-space imaging. Journal of Physics E: Scientific Instruments *21*, 820.

[49] Mansuripur, M. (1999). The van Leeuwenhoek microscope. Optics and Photonics News *10*, 39-42.

[50] Smit, P., and Heniger, J. (1975). Antoni van Leeuwenhoek (1632–1723) and the discovery of bacteria. Antonie Van Leeuwenhoek *41*, 217-228.

[51] Mack, W., Mack, J., and Ackerson, A. (1975). Microbial film development in a trickling filter. Microb Ecol *2*, 215-226.

[52] Monds, R.D., and O'Toole, G.A. (2009). The developmental model of microbial biofilms: ten years of a paradigm up for review. Trends Microbiol *17*, 73-87.

[53] Rupp, C.J., Fux, C.A., and Stoodley, P. (2005). Viscoelasticity of Staphylococcus aureus biofilms in response to fluid shear allows resistance to detachment and facilitates rolling migration. Appl Environ Microbiol *71*, 2175-2178.

[54] Flemming, H.-C., and Wingender, J. (2010). The biofilm matrix. Nature reviews microbiology *8*, 623.

[55] Parsek, M.R., and Greenberg, E. (2005). Sociomicrobiology: the connections between quorum sensing and biofilms. Trends Microbiol *13*, 27-33.

[56] Madsen, J.S., Burmølle, M., Hansen, L.H., and Sørensen, S.J. (2012). The interconnection between biofilm formation and horizontal gene transfer. FEMS Immunol Med Microbiol *65*, 183-195.

[57] Sutherland, I.W. (2001). The biofilm matrix–an immobilized but dynamic microbial environment. Trends Microbiol *9*, 222-227.

[58] Stewart, P.S., Zhang, T., Xu, R., Pitts, B., Walters, M.C., Roe, F., Kikhney, J., and Moter, A. (2016). Reaction–diffusion theory explains hypoxia and heterogeneous growth within microbial biofilms associated with chronic infections. Npj Biofilms And Microbiomes *2*, 16012.

[59] Fux, C., Costerton, J.W., Stewart, P.S., and Stoodley, P. (2005). Survival strategies of infectious biofilms. Trends Microbiol *13*, 34-40.

[60] Tuomanen, E., Cozens, R., Tosch, W., Zak, O., and Tomasz, A. (1986). The rate of killing of Escherichia coli byβ-lactam antibiotics is strictly proportional to the rate of bacterial growth. Microbiology *132*, 1297-1304.

[61] Stewart, P.S., and Costerton, J.W. (2001). Antibiotic resistance of bacteria in biofilms. The lancet *358*, 135-138.

[62] Leid, J.G. (2009). Bacterial biofilms resist key host defenses. Microbe *4*, 66-70.

[63] Murphy, T.F., and Kirkham, C. (2002). Biofilm formation by nontypeable Haemophilus influenzae: strain variability, outer membrane antigen expression and role of pili. BMC Microbiol *2*, 7.

[64] Wimpenny, J., Manz, W., and Szewzyk, U. (2000). Heterogeneity in biofilms. FEMS Microbiol Rev *24*, 661-671.

[65] Flemming, H.-C., and Wuertz, S. (2019). Bacteria and archaea on Earth and their abundance in biofilms. Nature Reviews Microbiology, 17, 247-260.

[66] Smith, H.J., Schmit, A., Foster, R., Littman, S., Kuypers, M.M., and Foreman, C.M. (2016). Biofilms on glacial surfaces: hotspots for biological activity. npj Biofilms and Microbiomes *2*, 16008.

[67] Hall-Stoodley, L., Costerton, J.W., and Stoodley, P. (2004). Bacterial biofilms: from the Natural environment to infectious diseases. Nat Rev Micro *2*, 95-108.

[68] Akers, K.S., Mende, K., Cheatle, K.A., Zera, W.C., Yu, X., Beckius, M.L., Aggarwal, D., Li, P., Sanchez, C.J., and Wenke, J.C. (2014). Biofilms and persistent wound infections in United States military trauma patients: a case–control analysis. BMC Infect Dis *14*, 190.

[69] Herzberg, M., and Elimelech, M. (2007). Biofouling of reverse osmosis membranes: Role of biofilm-enhanced osmotic pressure. Journal of Membrane Science *295*, 11-20.

[70] Townsin, R.L. (2003). The ship hull fouling penalty. Biofouling *19*, 9-15.

[71] Rajasekar, A., Anandkumar, B., Maruthamuthu, S., Ting, Y.-P., and Rahman, P.K.S.M. (2010). Characterization of corrosive bacterial consortia isolated from petroleum-product-transporting pipelines. Appl Microbiol Biotechnol *85*, 1175-1188.

[72] Edwards, S.J., and Kjellerup, B.V. (2013). Applications of biofilms in bioremediation and biotransformation of persistent organic pollutants, pharmaceuticals/personal care products, and heavy metals. Appl Microbiol Biotechnol *97*, 9909-9921.

[73] Adav, S.S., Lee, D.-J., Show, K.-Y., and Tay, J.-H. (2008). Aerobic granular sludge: Recent advances. Biotechnology Advances *26*, 411-423.

[74] Monroe, D. (2007). Looking for chinks in the armor of bacterial biofilms. PLoS Biol *5*, e307.

[75] Beloin, C., Valle, J., Latour-Lambert, P., Faure, P., Kzreminski, M., Balestrino, D., Haagensen, J.A., Molin, S., Prensier, G., and Arbeille, B. (2004). Global impact of mature biofilm lifestyle on Escherichia coli K-12 gene expression. Mol Microbiol *51*, 659-674.

[76] Kostakioti, M., Hadjifrangiskou, M., and Hultgren, S.J. (2013). Bacterial biofilms: development, dispersal, and therapeutic strategies in the dawn of the postantibiotic era. Cold Spring Harb Perspect Med *3*, a010306.

[77] Melo, L. (2005). Biofilm physical structure, internal diffusivity and tortuosity. Water science and Technology *52*, 77-84.

[78] Sauer, K., Cullen, M., Rickard, A., Zeef, L., Davies, D.G., and Gilbert, P. (2004). Characterization of nutrient-induced dispersion in Pseudomonas aeruginosa PAO1 biofilm. J Bacteriol *186*, 7312-7326.

[79] Hong, S.H., Lee, J., and Wood, T.K. (2010). Engineering global regulator Hha of Escherichia coli to control biofilm dispersal. Microbial biotechnology *3*, 717-728.

[80] Monod, J. (1949). The growth of bacterial cultures. Annual Reviews in Microbiology *3*, 371-394.

[81] Stewart, P.S. (1998). A review of experimental measurements of effective diffusive permeabilities and effective diffusion coefficients in biofilms. Biotechnol Bioeng *59*, 261-272.

[82] De Beer, D., Srinivasan, R., and Stewart, P.S. (1994). Direct measurement of chlorine penetration into biofilms during disinfection. Appl Environ Microbiol *60*, 4339-4344.

[83] Thiele, E.W. (1939). Relation between catalytic activity and size of particle. Ind Eng Chem *31*, 916-920.

[84] Characklis, W.G. (1981). Bioengineering report: fouling biofilm development: a process analysis. Biotechnol Bioeng *23*, 1923-1960.

[85] Sherwood, T.K. (1959). Mass transfer between phases (Pennsylvania State University).

[86] Sommerfeld, A. (1909). Ein beitrag zur hydrodynamischen erklaerung der turbulenten fluessigkeitsbewegungen.

[87] Wilhelm, S.E.H. (1955). Production of steam under pressure (Google Patents).

[88] Gekas, V., and Hallström, B. (1987). Mass transfer in the membrane concentration polarization layer under turbulent cross flow: I. Critical literature review and adaptation of existing sherwood correlations to membrane operations. Journal of Membrane Science *30*, 153-170.

[89] Wang, G., Yuan, X., and Yu, K. (2005). Review of mass-transfer correlations for packed columns. Ind Eng Chem Res *44*, 8715-8729.

[90] Thompson, B. (1967). A critical review of existing methods of calculating the turbulent boundary layer (HM Stationery Office).

[91] Incropera, F.P., Lavine, A.S., Bergman, T.L., and DeWitt, D.P. (2007). Fundamentals of heat and mass transfer (Wiley).

[92] Valentine, J.S., Foote, C.S., Greenberg, A., and Liebman, J.F. (2012). Active oxygen in biochemistry, Vol 3 (Springer Science & Business Media).

[93] Bekker, A., Holland, H., Wang, P.-L., Rumble Iii, D., Stein, H., Hannah, J., Coetzee, L., and Beukes, N. (2004). Dating the rise of atmospheric oxygen. Nature *427*, 117.

[94] Anbar, A.D., Duan, Y., Lyons, T.W., Arnold, G.L., Kendall, B., Creaser, R.A., Kaufman, A.J., Gordon, G.W., Scott, C., and Garvin, J. (2007). A whiff of oxygen before the great oxidation event? Science *317*, 1903-1906.

[95] Dorado, G., Rey, I., Sánchez-Cañete, F.J.S., Luque, F., Jiménez, I., Morales, A., Gálvez, M., Sáiz, J., Sánchez, A., and Hernández, P. (2010). Biological mass extinctions on planet Earth. Archaeobios, 53.

[96] Phelan, V.V., Liu, W.-T., Pogliano, K., and Dorrestein, P.C. (2012). Microbial metabolic exchange—the chemotype-to-phenotype link. Nat Chem Biol *8*, 26.

[97] Liu, X., Roe, F., Jesaitis, A., and Lewandowski, Z. (1998). Resistance of biofilms to the catalase inhibitor 3-amino-1, 2, 4-triazole. Biotechnol Bioeng *59*, 156-162.

[98] Britigan, B.E., and Cohen, M.S. (1986). Effects of human serum on bacterial competition with neutrophils for molecular oxygen. Infect Immun *52*, 657-663.

[99] Schreml, S., Szeimies, R.M., Prantl, L., Karrer, S., Landthaler, M., and Babilas, P. (2010). Oxygen in acute and chronic wound healing. Br J Dermatol *163*, 257-268.

[100] Ueno, T., Omi, T., Uchida, E., Yokota, H., and Kawana, S. (2014). Evaluation of hyperbaric oxygen therapy for chronic wounds. Journal of Nippon Medical School *81*, 4-11.

[101] Drews, A., Lee, C.-H., and Kraume, M. (2006). Membrane fouling-a review on the role of EPS. Desalination *200*, 186-188.

[102] Guo, W., Ngo, H.-H., and Li, J. (2012). A mini-review on membrane fouling. Bioresource technology *122*, 27-34.

[103] Thapa, B., Kc, A.K., and Ghimire, A. (2012). A review on bioremediation of petroleum hydrocarbon contaminants in soil. Kathmandu university journal of science, engineering and technology *8*, 164-170.

[104] Pardieck, D.L., Bouwer, E.J., and Stone, A.T. (1992). Hydrogen peroxide use to increase oxidant capacity for in situ bioremediation of contaminated soils and aquifers: A review. Journal of Contaminant Hydrology *9*, 221-242.

[105] Ahn, Y.-H. (2006). Sustainable nitrogen elimination biotechnologies: a review. Process Biochemistry *41*, 1709-1721.

[106] Chan, Y.J., Chong, M.F., Law, C.L., and Hassell, D. (2009). A review on anaerobic–aerobic treatment of industrial and municipal wastewater. Chemical Engineering Journal *155*, 1-18.

[107] Caldwell, D.E., Kieft, T.L., and Brannan, D.K. (1984). Colonization of sulfide-oxygen interfaces on hot spring tufa by Thermothrix thiopara. Geomicrobiology Journal *3*, 181-200.

[108] Zhulin, I.B., Bespalov, V.A., Johnson, M.S., and Taylor, B.L. (1996). Oxygen taxis and proton motive force in Azospirillum brasilense. J Bacteriol *178*, 5199-5204.

[109] Hayat, R., Ali, S., Amara, U., Khalid, R., and Ahmed, I. (2010). Soil beneficial bacteria and their role in plant growth promotion: a review. Annals of microbiology *60*, 579-598.

[110] Lewandowski, Z., Walser, G., and Characklis, W.G. (1991). Reaction kinetics in biofilms. Biotechnol Bioeng *38*, 877-882.

[111] Stolper, D.A., Revsbech, N.P., and Canfield, D.E. (2010). Aerobic growth at nanomolar oxygen concentrations. Proceedings of the National Academy of Sciences *107*, 18755-18760.

[112] Fleischmann, M., and Pons, S. (1987). The behavior of microelectrodes. Anal Chem *59*, 1391A-1399A.

[113] Percival, S.L., Hill, K.E., Williams, D.W., Hooper, S.J., Thomas, D.W., and Costerton, J.W. (2012). A review of the scientific evidence for biofilms in wounds. Wound Repair Regen *20*, 647-657.

[114] Rasmussen, K., and Lewandowski, Z. (1998). Microelectrode measurements of local mass transport rates in heterogeneous biofilms. Biotechnol Bioeng *59*, 302-309.

[115] Lewandowski, Z., Altobelli, S.A., and Fukushima, E. (1993). NMR and Microelectrode Studies of Hydrodynamics and Kinetics in Biofilms. Biotechnol Prog *9*, 40-45.

[116] Yu, J.-X., Hallac, R.R., Chiguru, S., and Mason, R.P. (2013). New Frontiers and Developing Applications in (19)F NMR. Progress in nuclear magnetic resonance spectroscopy *70*, 25-49.

[117] Raichle, M.E. (1998). Behind the scenes of functional brain imaging: A historical and physiological perspective. Proc Natl Acad Sci U S A *95*, 765-772.

[118] Hunjan, S., Mason, R.P., Constantinescu, A., Peschke, P., Hahn, E.W., and Antich, P.P. (1998). Regional tumor oximetry: F-19 NMR spectroscopy of hexafluorobenzene. International Journal of Radiation Oncology Biology Physics *41*, 161-171.

[119] Seymour, J.D., and Callaghan, P.T. (1997). Generalized approach to NMR analysis of flow and dispersion in porous media. AIChE J *43*, 2096-2111.

[120] Seymour, J.D., Gage, J.P., Codd, S.L., and Gerlach, R. (2004). Anomalous fluid transport in porous media induced by biofilm growth. Phys Rev Lett *93*, 198103.

[121] Hornemann, J.A., Codd, S.L., Romanenko, K., and Seymour, J.D. (2009). T2–T2 exchange in biofouled porous media. Diffusion Fundamentals *10*, 1.1-1.3.

[122] Johns, M., Sederman, A., Bramley, A., Gladden, L., and Alexander, P. (2000). Local transitions in flow phenomena through packed beds identified by MRI. AIChE J *46*, 2151-2161.

[123] Manz, B., Alexander, P., and Gladden, L. (1999). Correlations between dispersion and structure in porous media probed by nuclear magnetic resonance. Physics of Fluids *11*, 259-267.

[124] Liaw, H.K., Kulkarni, R., Chen, S., and Watson, A.T. (1996). Characterization of fluid distributions in porous media by NMR techniques. AIChE J *42*, 538-546.

[125] Song, Y.-Q., Cho, H., Hopper, T., Pomerantz, A.E., and Sun, P.Z. (2008). Magnetic resonance in porous media: Recent progress. The Journal of chemical physics *128*, 02B618.

[126] Blümich, B., Casanova, F., Dabrowski, M., Danieli, E., Evertz, L., Haber, A., Van Landeghem, M., Haber-Pohlmeier, S., Olaru, A., and Perlo, J. (2011). Small-scale instrumentation for nuclear magnetic resonance of porous media. New Journal of Physics *13*, 015003.

[127] Vogt, S.J., Sanderlin, A.B., Seymour, J.D., and Codd, S.L. (2013). Permeability of a growing biofilm in a porous media fluid flow analyzed by magnetic resonance displacement-relaxation correlations. Biotechnol Bioeng *110*, 1366-1375.

[128] Wakimoto, N., Nishi, J., Sheikh, J., Nataro, J.P., Sarantuya, J., Iwashita, M., Manago, K., Tokuda, K., Yoshinaga, M., and Kawano, Y. (2004). Quantitative biofilm assay using a microtiter plate to screen for enteroaggregative Escherichia coli. The American journal of tropical medicine and hygiene *71*, 687-690.

[129] Sadovskaya, I., Vinogradov, E., Flahaut, S., Kogan, G., and Jabbouri, S. (2005). Extracellular carbohydrate-containing polymers of a model biofilm-producing strain, Staphylococcus epidermidis RP62A. Infect Immun *73*, 3007-3017.

[130] Nöth, U., Gröhn, P., Jork, A., Zimmermann, U., Haase, A., and Lutz, J. (1999). 19F-MRI in vivo determination of the partial oxygen pressure in perfluorocarbon-loaded alginate capsules implanted into the peritoneal cavity and different tissues. Magn Reson Med *42*, 1039-1047.

[131] Nöth, U., Rodrigues, L.M., Robinson, S.P., Jork, A., Zimmermann, U., Newell, B., and Griffiths, J.R. (2004). In vivo determination of tumor oxygenation during growth and in response to carbogen breathing using 15C5-loaded alginate capsules as fluorine-19 magnetic resonance imaging oxygen sensors. International Journal of Radiation Oncology• Biology• Physics *60*, 909-919.

[132] Smidsrød, O., and Skja, G. (1990). Alginate as immobilization matrix for cells. Trends Biotechnol *8*, 71-78.

[133] Cheetham, P.S., Blunt, K.W., and Bocke, C. (1979). Physical studies on cell immobilization using calcium alginate gels. Biotechnol Bioeng *21*, 2155-2168.

[134] Taipa, M., Cabral, J., and Santos, H. (1993). Comparison of glucose fermentation by suspended and gel-entrapped yeast cells: An in vivo nuclear magnetic resonance study. Biotechnol Bioeng *41*, 647-653.

[135] Duff, R.G. (1985). Microencapsulation technology: a novel method for monoclonal antibody production. Trends Biotechnol *3*, 167-170.

[136] Robinson, P., Goulding, K., Mak, A., and Trevan, M. (1986). Factors affecting the growth characteristics of alginate-entrapped Chlorella. Enzyme Microb Technol *8*, 729-733.

[137] Pabst, B., Pitts, B., Lauchnor, E., and Stewart, P.S. (2016). Gel-entrapped Staphylococcus aureus bacteria as models of biofilm infection exhibit growth in dense aggregates, oxygen limitation, antibiotic tolerance, and heterogeneous gene expression. Antimicrob Agents Chemother *60*, 6294-6301.

[138] Thomas, C.D., Chavaudra, N., Martin, L., and Guichard, M. (1994). Correlation between radiosensitivity, percentage hypoxic cells and pO2 measurements in one rodent and two human tumor xenografts. Radiat Res *139*, 1-8.

[139] Ruiz-Cabello, J., Barnett, B.P., Bottomley, P.A., and Bulte, J.W.M. (2011). Fluorine (19F) MRS and MRI in biomedicine. NMR Biomed *24*, 114-129.

[140] Bird, R.B., Stewart, W.E., and Lightfoot, E.N. (1960). Transport phenomena. 1960. Madison, USA.

[141] Han, P., and Bartels, D.M. (1996). Temperature dependence of oxygen diffusion in H2O and D2O. J Phys Chem *100*, 5597-5602.

[142] Maxwell, J.C. (1881). A treatise on electricity and magnetism, Vol 1 (Clarendon press).

[143] Dulieu, C., Poncelet, D., and Neufeld, R.J. (1999). Encapsulation and immobilization techniques. In Cell encapsulation technology and therapeutics (Springer), pp. 3-17.

[144] Sønderholm, M., Kragh, K.N., Koren, K., Jakobsen, T.H., Darch, S.E., Alhede, M., Jensen, P.Ø., Whiteley, M., Kühl, M., and Bjarnsholt, T. (2017). Pseudomonas aeruginosa aggregate formation in an alginate bead model system exhibits in vivo-like characteristics. Appl Environ Microbiol *83*, e00113-00117.

[145] Wilkes, J.O. (2006). Fluid Mechanics for Chemical Engineers with Microfluidics and CFD (Pearson Education).

[146] Costerton, J.W., Lewandowski, Z., Caldwell, D.E., Korber, D.R., and Lappin-Scott, H.M. (1995). Microbial biofilms. Annu Rev Microbiol *49*, 711-745.

[147] Schobert, M., and Tielen, P. (2010). Contribution of oxygen-limiting conditions to persistent infection of Pseudomonas aeruginosa. Future Microbiol *5*, 603-621.

[148] Sønderholm, M., Koren, K., Wangpraseurt, D., Jensen, P.Ø., Kolpen, M., Kragh, K.N., Bjarnsholt, T., and Kühl, M. (2018). Tools for studying growth patterns and chemical dynamics of aggregated Pseudomonas aeruginosa exposed to different electron acceptors in an alginate bead model. NPJ biofilms and microbiomes *4*, 3.

[149] Smith, D., Kornbrust, E., and Lane, T. (1994). Phagocytosis of a fluorescently labeled perflubron emulsion by a human monocyte cell line. Artificial Cells, Blood Substitutes, and Biotechnology *22*, 1215-1221.

[150] Yoshizawa, S., Fourmy, D., and Puglisi, J.D. (1998). Structural origins of gentamicin antibiotic action. The EMBO journal *17*, 6437-6448.

[151] Olson, M.E., Ceri, H., Morck, D.W., Buret, A.G., and Read, R.R. (2002). Biofilm bacteria: formation and comparative susceptibility to antibiotics. Can J Vet Res *66*, 86.

[152] von Ohle, C., Gieseke, A., Nistico, L., Decker, E.M., and Stoodley, P. (2010). Real-time microsensor measurement of local metabolic activities in ex vivo dental biofilms exposed to sucrose and treated with chlorhexidine. Appl Environ Microbiol *76*, 2326-2334.

[153] Kiamco, M.M., Atci, E., Mohamed, A., Call, D.R., and Beyenal, H. (2017). Hyperosmotic agents and antibiotics affect dissolved oxygen and pH concentration gradients in Staphylococcus aureus biofilms. Appl Environ Microbiol, AEM. 02783-02716.

[154] Kiamco, M.M., Atci, E., Khan, Q.F., Mohamed, A., Renslow, R.S., Abu-Lail, N., Fransson, B.A., Call, D.R., and Beyenal, H. (2015). Vancomycin and maltodextrin affect structure and activity of Staphylococcus aureus biofilms. Biotechnol Bioeng *112*, 2562-2570.

[155] Haagensen, J., Verotta, D., Huang, L., Engel, J., Spormann, A.M., and Yang, K. (2017). Spatiotemporal pharmacodynamics of meropenem-and tobramycin-treated Pseudomonas aeruginosa biofilms. J Antimicrob Chemother *72*, 3357-3365.

[156] Ito, A., Taniuchi, A., May, T., Kawata, K., and Okabe, S. (2009). Increased antibiotic resistance of Escherichia coli in mature biofilms. Appl Environ Microbiol *75*, 4093-4100.

[157] Anwar, H., Strap, J., Chen, K., and Costerton, J. (1992). Dynamic interactions of biofilms of mucoid Pseudomonas aeruginosa with tobramycin and piperacillin. Antimicrob Agents Chemother *36*, 1208-1214.

[158] Klapper, I. (2004). Effect of heterogeneous structure in mechanically unstressed biofilms on overall growth. Bull Math Biol *66*, 809-824.

[159] Bjarnsholt, T., Alhede, M., Alhede, M., Eickhardt-Sørensen, S.R., Moser, C., Kühl, M., Jensen, P.Ø., and Høiby, N. (2013). The in vivo biofilm. Trends Microbiol *21*, 466-474.

[160] Wu, Y., Klapper, I., and Stewart, P.S. (2018). Hypoxia arising from concerted oxygen consumption by neutrophils and microorganisms in biofilms. Pathogens and disease *76*, fty043.

[161] Høiby, N. (2002). Understanding bacterial biofilms in patients with cystic fibrosis: current and innovative approaches to potential therapies. Journal of Cystic Fibrosis *1*, 249-254.

[162] Grubb, S.E., Murdoch, C., Sudbery, P.E., Saville, S.P., Lopez-Ribot, J.L., and Thornhill, M.H. (2009). Adhesion of Candida albicans to endothelial cells under physiological conditions of flow. Infect Immun *77*, 3872-3878.

[163] Stewart, P.S. (2014). Biophysics of biofilm infection. Pathogens and disease *70*, 212-218.

[164] Tresse, O., Jouenne, T., and Junter, G.A. (1995). The role of oxygen limitation in the resistence of agar-entrapped, sessile-like escherichia coli to aminoglycoside and beta lactam antibiotics. J Antimicrob Chemother *36*, 521-526.

[165] Ahn, S.-J., Wen, Z.T., and Burne, R.A. (2007). Effects of oxygen on virulence traits of Streptococcus mutans. J Bacteriol *189*, 8519-8527.

[166] Casey, E., Glennon, B., and Hamer, G. (1999). Review of membrane aerated biofilm reactors. Resources, conservation and recycling *27*, 203-215.

[167] De Beer, D., Stoodley, P., Roe, F., and Lewandowski, Z. (1994). Effects of biofilm structures on oxygen distribution and mass transport. Biotechnol Bioeng *43*, 1131-1138.

[168] Yang, S., and Lewandowski, Z. (1995). Measurement of local mass transfer coefficient in biofilms. Biotechnol Bioeng *48*, 737-744.

[169] Stoodley, P., Yang, S., Lappin-Scott, H., and Lewandowski, Z. (1997). Relationship between mass transfer coefficient and liquid flow velocity in heterogenous

biofilms using microelectrodes and confocal microscopy. Biotechnol Bioeng *56*, 681-688.

[170] Strathmann, M., Griebe, T., and Flemming, H.-C. (2000). Artificial biofilm model–a useful tool for biofilm research. Appl Microbiol Biotechnol *54*, 231-237.

[171] Whitham, T., and Gilbert, P. (1993). Evaluation of a model biofilm for the ranking of biocide performance against sulphate-reducing bacteria. J Appl Bacteriol *75*, 529-535.

[172] Coquet, L., Junter, G., and Jouenne, T. (1998). Resistance of artificial biofilms of Pseudomonas aeruginosa to imipenem and tobramycin. The Journal of antimicrobial chemotherapy *42*, 755-760.

[173] Clutterbuck, A.L., Cochrane, C.A., Dolman, J., and Percival, S.L. (2007). Evaluating antibiotics for use in medicine using a poloxamer biofilm model. Ann Clin Microbiol Antimicrob *6*, 2.

[174] WerthÉn, M., Henriksson, L., Jensen, P.Ø., Sternberg, C., Givskov, M., and Bjarnsholt, T. (2010). An in vitro model of bacterial infections in wounds and other soft tissues. APMIS *118*, 156-164.

[175] De Klerk, A. (2003). Voidage variation in packed beds at small column to particle diameter ratio. AIChE J *49*, 2022-2029.

[176] Bergman, T.L., Incropera, F.P., DeWitt, D.P., and Lavine, A.S. (2011). Fundamentals of heat and mass transfer (John Wiley & Sons).

[177] Batchelor, C.K., and Batchelor, G. (1967). An introduction to fluid dynamics (Cambridge university press).

[178] Ranz, W., and Marshall, W.R. (1952). Evaporation from drops. Chem Eng Prog *48*, 141-146.

[179] Karabelas, A.J., Wegner, T.H., and Hanratty, T.J. (1971). Use of asymptotic relations to correlate mass transfer data in packed beds. Chem Eng Sci *26*, 1581-1589.

[180] Kurosawa, H., Matsumura, M., and Tanaka, H. (1989). Oxygen diffusivity in gel beads containing viable cells. Biotechnol Bioeng *34*, 926-932.

[181] Benson, D.M., Knopp, J.A., and Longmuir, I.S. (1980). Intracellular oxygen measurements of mouse liver cells using quantitative fluorescence video microscopy. Biochimica et Biophysica Acta (BBA)-Bioenergetics *591*, 187-197.

[182] Carlson, R., and Srienc, F. (2004). Fundamental Escherichia coli biochemical pathways for biomass and energy production: creation of overall flux states. Biotechnol Bioeng *86*, 149-162.

[183] Basan, M., Zhu, M., Dai, X., Warren, M., Sévin, D., Wang, Y.P., and Hwa, T. (2015). Inflating bacterial cells by increased protein synthesis. Mol Syst Biol *11*, 836.

[184] Sakata, N., Usui, Y., and Kogure, T. (1999). Extracellular product(s) of Staphylococcus aureus stimulate their own growth. Zentralbl Bakteriol Parasitenkd Infektionskr Hyg *289*, 339-345.